RED-OX ROBUST SOFC STACKS FOR AFFORDABLE, RELIABLE, DISTRIBUTED GENERATION POWER SYSTEMS

Award No. DE-FE0027897

Sponsoring Program Office: The Office of Fossil Energy

Performer: Redox Power Systems, LLC

Principle Investigator: Bryan M. Blackburn, Ph.D.

FINAL TECHNICAL REPORT

08/21/2022

Project Period: October 1, 2016 – March 31, 2022

ACKNOWLEDGMENT

This material is based upon work supported by the Department of Energy under Award Number DE-FE0027897.

DISCLAIMER

TABLE OF CONTENTS

LIST OF FIGURES

LIST OF TABLES

LIST OF ABBREVIATIONS

Acronym	Definition
AFL	Anode Functional Layer
ASL	Anode Support Layer
ASR	Area-Specific Resistance
CFL	cathode functional layer
Co-GDC	Cobalt-modified GDC
CTE	Coefficient of Thermal Expansion
DES	Discrete Event Simulator
DOE	Department of Energy
DoO	Degree of Oxidation
EDS	Energy Dispersive X-Ray Spectroscopy
GC	Gas Chromatography
GDC	Gadolinium Doped Ceria (typically 10GDC)
GNP	Glycine–Nitrate Process (GNP) combustion method
LCOE	Levelized Cost of Electricity
LPM	Liters per Minute
LSC	Lanthanum Strontium Cobaltite
LSCF	Lanthanum Strontium Cobalt Ferrite
MCO	Manganese Cobalt Oxide (in this work, $Mn_{1.5}Co_{1.5}O_4$)
MFC	mass flow controller
MS	Mass Spectrometry
NETL	National Energy Technology Laboratory
NiO	Nickel oxide
OCV	Open circuit potential
PO2	Partial pressure of oxygen
PPM	Parts Per Million
SCCM	Standard Cubic Centimeters per Minute
SEM	Scanning Electron Microscope

Acronym	Definition
SFCM	$SrFe_xCo_{1-x}Mo_{1-x}O_3$ (in this work, $SrFe_{0.2}Co_{0.4}Mo_{0.4}O_3$)
SOFC	Solid Oxide Fuel Cell
SRU	Stack repeat unit
SS	Stainless Steel
SSC	Samarium Strontium Cobaltite ($Sm_{0.5}Sr_{0.5}CoO_3$)
UMD	University of Maryland
UTM	Universal test machine
XRD	X-Ray Diffraction
YSZ	Yttria stabilized zirconia

EXECUTIVE SUMMARY

While SOFC systems are expected to operate reliably and with limited degradation in steady state or transient performance, SOFC stacks may ultimately fail due to the loss of structural integrity of one or several of the cells as a result of the weakening of the materials and interfaces due to physico-chemical changes that occur during continuous operation as a result of plastic and creep deformations, modification of the temperature profile, and/or degradation of the electrochemical performance of the cells [1-3]. The total degradation of the stack performance originates from the deterioration of individual components of the cell and stack as well as from mutual interactions between components. Degradation mechanisms originating from the cell components include coarsening of the microstructure over time; decomposition of materials; chemical reaction of electrode materials with electrolyte at the interface; delamination from each other; and for the anode, coking and sulfur poisoning [4]. Furthermore, the nickel cermet anodes are also prone to re-oxidation by various oxidants during operation (e.g., CO_2 and/or H_2O in a syngas fuel stream; air cross-over from the cathode stream; and air during a fuel outage), which causes a volume change of >60% that can mechanically damage the anode or other components [5].

Of all the reliability issues that may occur for SOFCs, the main limitation for Ni-based cermet anodes (e.g., NiO-YSZ) is the poor stability in red-ox cycling [6]. This instability is due, primarily, to the large volume change and coarsening of the Ni-phase in the cermet anode [7]. Such large volume changes of the Ni-phase produce considerable stress in the anode and electrolyte. Past approaches for enhanced red-ox robustness of SOFCs include modifications to Ni-based anode supports, designs incorporating metal supports, and alternative anode support materials. Unfortunately, such solutions either result in low power density and thus increased system cost; an incompatibility with advanced SOFC materials such as lower temperature GDC electrolytes or a requirement to be activated at very high temperature (e.g., 900 °C); or relatively bulky and expensive power system solutions including the use of backup gas. Therefore, new developments that overcome these limitations are desirable to enable stationary power applications that are more robust to challenges such as fuel outages, as well as in mobile/portable applications that can benefit from simpler system design and control.

In this project, Redox Power Systems, LLC (Redox) together with the University of Maryland Center for Advanced Life Cycle Engineering (CALCE) and the University of Maryland Energy Research Center (UMERC) developed a high-power density solid oxide fuel cell (SOFC) that is reduction-oxidation (red-ox) stable for robust, reliable, and lower cost distributed generation. The SOFC stacks had a target operating temperature of ~600 °C based on an advanced, conductive SFCM-based ceramic anode support. The objective of the overall project was to improve the red-ox stability of Redox stacks while reducing costs through the:

- Scale-up and optimization of ceramic anode material processing and cell fabrication for lower cost manufacturing;
- Determination of SFCM-based ceramic anode degradation mechanisms with an optimization of anode compositions and geometries for enhanced red-ox stability;
- Demonstration of stacks that are more robust for red-ox cycling; and
- Demonstration of a reduced lifetime cost compared to a system without a red-ox stable stack.

The scope of the project included:

a) The systematic study of degradation mechanisms of red-ox robust SOFCs and stacks and the development of relevant solutions to improve performance and durability;
b) The scaling of SFCM-based ceramic anode SOFCs to a large format cell size (approximately 5 cm by 5 cm to 10 cm by 10 cm) and utilization of fabrication methods that are compatible with high volume manufacturing;
c) The optimization of large format cell performance (target of 0.75 W/cm^2 at 0.75 V) at ~600 °C and red-ox robustness for at least 20 red-ox cycles; and
d) The demonstration of red-ox robust stacks utilizing large format SFCM-based ceramic anode SOFCs.

The project, which started on October 1, 2016 and ended March 31, 2022, consisted of the following five tasks:

- Task 1: Project Management and Planning
- Task 2: Optimization of a Large Format Red-Ox Stable SOFC
- Task 3: Development of a Red-Ox Robust Stack
- Task 4: Demonstration of 1-2 kW Red-Ox Robust Stacks

- Task 5: Economic Analysis for Reduced System and O&M Costs

Tasks 1, 3, and 4 were performed completely by Redox. For Task 2 UMERC investigated the fundamental characterization of SFCM materials and of SFCM-based ceramic anode SOFC (at the button cell level), whereas Redox mainly focused on the optimization of large format SFCM-based ceramic anode SOFCs with some materials investigations to understand degradation mechanisms and fabrication issues in the large format cells. In Task 2, CALCE also investigated the impact of storage conditions on SFCM-based ceramic anode materials. For Task 5, CALCE created a cost model and discrete event simulator model, working with Redox to choose the appropriate assumptions for the model simulations.

Task 1 was focused on the management of project work conducted at Redox as well as that performed at UMERC and CALCE. This included coordination of all activities; management of resources, including budget and personnel; and ensuring the achievement of technical objectives. Redox also managed project risks and provided regular progress reports to the Department of Energy.

Task 2 involved the scale-up of the SFCM-based ceramic anode SOFCs to a large format size (5 cm by cm to 10 cm by 10 cm) with an optimization in red-ox cycling robustness and cell performance. This involved the investigation of degradation and failure mechanisms associated with the SFCM-based ceramic anode cells at baseline conditions and with a focus on red-ox cycling.

Task 3 involved the assessment and improvement of the red-ox robustness of Redox's standard stack, including (as necessary) the development of optimized coatings, contacts, and seals that are robust to red-ox cycling. To achieve sufficient red-ox robustness, the mechanical design of the stack was optimized to accommodate the mechanical properties of the optimized cell and sealing arrangement. Redox's multi-physics model was updated to incorporate the mechanical properties of the SFCM-based ceramic anode and used as a tool to optimize the design of the cells and stack, as well as to understand test results.

Task 4 involved demonstrating that the optimized cell and stack can operate as desired and meet target performance metrics. A series of red-ox robustness stack evaluations were conducted to

demonstrate the improved cell/stack designs with an intermediate goal of characterizing a ~0.5 kW stack. The final goal was to demonstrate a 1-2 kW stack with the red-ox stable cells. Stack performance was to be evaluated using both hydrogen fuel and either reformed natural gas or simulated natural gas reformate. The primary objective of these tests was to demonstrate low voltage degradation rates (target: < 1% per 1,000 hours) and durability (target: < 2% after the completion of 20 red-ox cycles). Tests were to be conducted for up to 1,000 hours as necessary to assess durability.

Task 5 involved the demonstration that the optimized red-ox stable cell and stack can reduce the system capital costs, as well as operation and maintenance costs, that ultimately lower the levelized cost of electricity (LCOE) for a distributed generation product and further lower barriers to commercialization. The cost analysis included the cell production process flow and associated raw materials and handling costs.

The project ran for longer than originally intended due to unforeseen issues associated with the baseline (long-term) stability of large format SFCM-based ceramic anode SOFCs and difficulties in identifying the root cause for the issues. While stacks with as many as ten 10 cm by 10 cm SFCM-based ceramic anode cells were operated, the delays associated with solving the baseline-stability problem unfortunately prevented us from demonstrating the targeted 1-2 kW stack. Ultimately though, the project was successful in demonstrating a highly red-ox robust large format (5 cm by 5 cm) cell in smaller stacks. Moreover, the path for continued improvement has been described. For instance, SFCM-based ceramic anode cell performance was demonstrated as high as 0.6 W/cm^2 at 0.75 V, which would lead to a 1-kW stack requiring only around eighteen to twenty 10 cm by 10 cm cells. Key accomplishments across all tasks included:

- 5 cm by 5 cm and 10 cm by 10 cm SFCM-based ceramic anode SOFCs were fabricated using commercially produced tape cast layers and laminates to produce sintered half cells that met the target camber specification (i.e., maximum height between any high or low points across the cell).
- A 5 cm by 5 cm SFCM-based ceramic anode SOFC was optimized and demonstrated to have very high maximum power density (~0.9 W/cm^2) at ~600 °C with a power density of more than 0.6 W/cm^2 at 0.75 V in hydrogen.

- A stack of 10-cells using 10 cm by 10 cm SFCM-based ceramic anode SOFCs was assembled and tested at ~600 °C, and successfully demonstrated a red-ox cycle.
- A single cell, 10 cm by 10 cm SFCM-based ceramic anode cell was tested with reformed, pipeline natural gas and an abnormally high steam-to-fuel ratio (due to a limitation with the setup) and found to have no difference in performance at 0.75 V when using bottled hydrogen versus reformed natural gas.
- The red-ox robustness of stack components were fully evaluated and found to be very good, with only minor adjustments made to the stack assembly process to accommodate the relatively low strength of the SFCM-based ceramic anode cells.
- As the electrochemical performance of 5 cm by 5 cm and 10 cm by 10 cm cells was optimized, long-term degradation was seen to increase, and through an extensive set of studies the cause was found to be due to relatively low mechanical strength and weak bonding between the anode and electrolyte; ultimately this led to the optimization of a red-ox robust cell structure utilizing an SFCM-based ceramic anode support layer combined with a thin anode functional layer.
- The cell fabrication process was optimized to scale-up the size for various cell designs as the performance was optimized (e.g., using dilatometry) to achieve 5 cm by 5 cm and 10 cm by 10 cm cells that met the specifications for assembly in a stack — i.e., the cells were of sufficient quality to meet such criteria as flatness and level of defects such as cracks or electrolyte pinholes.
- The cell fabrication processes were optimized to achieve higher yields during batch processing of the SFCM-based ceramic anode cells — tape casting was improved with optimization of slurry delivery to the tape caster and more uniform bed temperature, while improved temperature uniformity in the high temperature furnace increased the yield of sintered cells during batch firing.
- Studied and found the optimal storage conditions (i.e., temperature and humidity) for Sr-containing SFCM and SFCM-based ceramic anode SOFCs.

- Built a discrete event simulator to assess the impact of various operational abnormalities (e.g., red-ox cycling) and other phenomena (e.g., different types of degradation) on operational costs and ultimately levelized cost of electricity (LCOE).
- Demonstrated the red-ox cycling robustness of a 3-cell stack of 5 cm by 5 cm SFCM-based ASL with an AFL SOFCs in hydrogen at 600 °C with no OCV or ASR degradation after ~40 cycles (target: < 2% after 20 red-ox cycles); the stack likely would have continued to operate without degradation, but several instances of unintentionally current loading the stack (e.g., while the anode was in an oxidized state as well as over-polarizing the cells in a reduced state) ultimately damaged the cells.

Redox Technical Staff Contributors to This Project

Redox Staff

- Bryan Blackburn (PI)
- Stelu Deaconu
- Kevin Doherty
- Yue Li
- Lei Wang
- Lenny Fischer

Former Redox Staff

- Sean Bishop
- Keji Pan
- Colin Gore
- Thomas Langdo
- Luis Correa

Other Contributors to This Project

University of Maryland, Energy Research Center
(Subaward Lead: Prof. Eric Wachsman)
Key contributions of UMERC included fundamental studies of cell degradation and assessing the red-ox cycling stability of the SFCM-based ceramic anode SOFCs with respect to button cells. This included characterization of materials (e.g., mechanical strength) and the fabrication and testing of button cells.

University of Maryland, Center for Advanced Lifecycle Engineering
(Subaward Lead: Prof. Peter Sandborn and Prof. Michael Pecht)
Key contributions of CALCE included the analysis of possible failure mechanisms associated with the SFCM-based ceramic anode SOFCs, especially with respect to red-ox cycling. CALCE evaluated the impact of storage conditions (i.e., temperature and humidity) on strontium-containing SOFC materials such as the SFCM-based ceramic anode material. CALCE also investigated the techno-economic impact of red-ox cycle robustness, which included an analysis of manufacturing cost and operating costs under various scenarios using a discrete event simulator model.

1. PROJECT OBJECTIVES AND OVERALL APPROACH

1.1. Project Objectives

In this project, Redox Power Systems, LLC (Redox) together with the University of Maryland Center for Advanced Life Cycle Engineering (CALCE) and the University of Maryland Energy Research Center (UMERC) developed a high-power density solid oxide fuel cell (SOFC) that is reduction-oxidation (red-ox) stable for robust, reliable, and lower cost distributed generation. The SOFC stacks had a target operating temperature of ~600 °C based on an advanced, conductive SFCM-based ceramic anode support. The objective of the overall project was to improve the red-ox stability of Redox stacks while reducing costs through the:

- Scale-up and optimization of ceramic anode material processing and cell fabrication for lower cost manufacturing;
- Determination of SFCM-based ceramic anode degradation mechanisms with an optimization of anode compositions and geometries for enhanced red-ox stability;
- Demonstration of stacks that are more robust for red-ox cycling; and
- Demonstration of a reduced lifetime cost compared to a system without a red-ox stable stack.

1.2. Approach

The focus of this project was on the development of large format SFCM-based ceramic anode SOFCs and demonstrating the red-ox robustness of such cells in stacks. The ceramic SFCM material has sufficiently high conductivity to be a good SOFC anode material, as well as excellent red-ox cycling stability with low volume expansion and little impact on electrical properties. As the SFCM is a relatively new material, some aspects of the project necessarily involved basic materials and device characterization as there was limited information available in the literature. However, the goal of the project was scaling the SFCM-based ceramic anode SOFCs to a large format size and demonstrating their red-ox robustness in a stack. This meant that the stack components had to first be characterized for red-ox robustness. Scale-up challenges for the SFCM-based ceramic anode cells had to be overcome, while optimizing the large format cells for compatibility with the stack and maintaining high electrochemical performance. After demonstration of the red-ox robustness of the SFCM-based ceramic anode SOFCs in stacks, cost

and lifecycle modeling allowed for an assessment of the impact of red-ox robustness on the overall cost of ownership for SOFC systems.

1.3. Description of Tasks

The project had 5 tasks and eight milestones. Task 1 was focused on project management and planning. Progress made during the project was measured against risks and adjustments were made as necessary in conjunction with NETL. Redox coordinated and worked closely with UMERC and CALCE throughout the project and delivered frequent technical reports to NETL. Task 2 involved scale-up of the SFCM-based ceramic anode SOFCs to a large format size (5 cm by 5 cm or larger) with an optimization in red-ox cycling robustness and cell performance. The following additional efforts were included in this task:

- optimize the shrinkage and constrained sintering parameters for a target cell camber of < 100 μm/cm;
- determine the impact of red-ox cycling on electrical, mechanical, catalytic, and electrocatalytic properties;
- determine the long-term stability of the materials for continuous cycles of reduction-oxidation using such techniques as dilatometry;
- determine the cell degradation of the anode under normal operating conditions (relevant to stack), under accelerated / life-cycle oriented conditions with a focus on red-ox cycling to more quickly determine the impact of operating conditions on cell/stack and catalyst life, and failure evaluation-oriented tests (extreme conditions); and
- characterize samples post-test using SEM and EDS and related techniques as necessary.

Task 3 and **4** involved the assessment and improvement of the red-ox robustness of Redox's standard stack, followed by a demonstration of red-ox cycling robustness of the SFCM-based ceramic anode SOFCs in stacks. As necessary, this including the development of optimized coatings, contacts, and seals that are robust to red-ox cycling. To achieve sufficient red-ox robustness, the mechanical design of the stack was optimized to accommodate the mechanical properties of the optimized cell and sealing arrangement. Redox's multi-physics model was updated to incorporate the mechanical properties of the SFCM-based ceramic anode and used as a tool to optimize the design of the cells and stack, as well as to understand test results. The following efforts were also included as part of these tasks:

- assess and optimize as necessary red-ox robust interconnect coatings, current collectors, and/or anode contact pastes for the anode-compartment;
- characterize and, if necessary, develop red-ox stable sealing configurations
- modify Redox's multi-physics model for the SFCM-based ceramic anode by incorporating related electrochemistry and mechanical properties under relevant conditions (ex. equivalent oxygen partial pressure of the anode, operation temperature, and fuel feeds type, etc.);
- perform thermo-mechanical studies related to residual stress between the ceramic anode and other SOFC layers as well as the ceramic anode SOFC within the stack upon assembly at relevant temperature conditions;
- study the thermal-related mechanical stress under the stack operation condition and red-ox cycling conditions (such as local increment of oxygen partial pressure);
- investigate long-term operation reliability with respect to how mechanical properties and resulting thermal-stress change under thermal cycling;
- test stacks under relevant conditions to validate the performance of optimized stack designs;
- perform the appropriate tests to analyze cycles and fully characterize cells and stacks; and
- conduct a series of red-ox robustness stack evaluations to demonstrate the improved cell/stack designs with an intermediate goal of characterizing a ~0.5 kW stack and a final goal of a 1-2 kW stack with low degradation (target: < 1% per 1,000 hours) and high durability (target: < 2% after the completion of 20 red-ox cycles).

Task 5 involved techno-economic cost modeling and the demonstration that the optimized red-ox stable cell and stack can reduce the system capital costs, as well as operation and maintenance costs, that ultimately lower the levelized cost of electricity (LCOE) for a distributed generation product and further lower barriers to commercialization. The cost analysis included the cell production process flow and associated raw materials and handling costs. To assess the impact of operation and maintenance costs, a discrete event modeling tool was created using Monte Carlo simulations to assess the impact of various events (e.g., unexpected red-ox cycling) on stack degradation and failure, and ultimately the resulting impact on the power system.

2. BACKGROUND DISCUSSION

During its operational lifetime an SOFC system is expected to operate reliably and with limited degradation in steady state or transient performance [1]. However, the end of life for an SOFC

stack may ultimately occur due to the loss of structural integrity of one or several of the cells as a result of the weakening of the materials and interfaces due to physical-chemical changes that occur during continuous operation as a result of plastic and creep deformations, modification of the temperature profile, and/or degradation of the electrochemical performance of the cells [2-3]. Degradation processes are complex and are influenced by both the instantaneous operating conditions and by the cumulative history of multi-modal degradation. Great efforts have been made worldwide to investigate SOFC degradation mechanisms. The total degradation of the stack performance originates from the deterioration of individual components of the cell and stack as well as from mutual interactions between components. Degradation mechanisms originating from the cell components include coarsening of the microstructure over time; decomposition of materials; chemical reaction of electrode materials with electrolyte at the interface; delamination from each other; and for the anode, coking and sulfur poisoning [4].

Chemical instability at the interfaces is one of the key issues in stationary applications, whereas the thermo-mechanical instability has tended to dominate degradation in transportation applications because of frequent thermal cycles. Advancement of key technologies increases the possibility to use SOFC systems for applications such as distributed generation (DG), in which realistic conditions require the ability to regularly experience load following, thermal cycling, and red-ox cycling with minimal degradation. An increased understanding of the degradation mechanisms for these modes of operation and improved cell and stack designs are therefore essential for the successful deployment of DG systems. Much work has been done to understand cathode and electrolyte degradation mechanisms, as well as to engineer solutions to improve reliability. To further improve reliability from a systems level standpoint, this project focused on improving the reliability of the anode, which for state-of-the-art SOFC designs acts simultaneously as the cell support, catalyst/electrocatalyst, electrical conduit, and reactant/product transport path.

Conventional SOFCs employ nickel-based cermet anodes, which exhibit good compatibility with electrolytes composed of yttrium stabilized zirconia (YSZ) or doped ceria, high activity toward the electrocatalytic oxidation of hydrogen, and high electronic conductivity [8-9]. The initial microstructure of Ni-based anode is also reported to change at elevated operating temperatures, which is closely associated with performance degradation phenomena. They most likely include

agglomeration of nickel, loss of Ni–Ni contacts, change of nickel surface morphology, the breakdown of the ceramic network, the change in anode porosity, and phase separation [10-11]. Further, conventional nickel anodes are prone to carbon deposition when operated on hydrocarbon fuels such as natural gas. Rapid solid carbon accumulation (coke) covering the anode is often observed and leads to degradation of SOFC performance, especially in conventional Ni-YSZ cermet anodes. The solid carbon can block fuel diffusion through pores in the anode, starving the cell and decreasing power output [8-9,11]. Also, sulfur in the fuel can induce serious poisoning effects on the nickel cermet anodes by forming nickel sulfides [12-13]. Furthermore, the nickel cermet anodes are also prone to re-oxidation by the oxidant (e.g., CO_2 and/or H_2O), which causes a volume change of >60% that can mechanically damage the anode or other components [5]. These extrinsic degradation modes usually dominate the entire degradation of the anode and are strongly dependent on the thermodynamics, actual natural gas composition, and H_2S concentration. In most state-of-the-art SOFC systems, the anode feed composition is tightly controlled via pretreatment steps to remove sulfur contaminants, followed by extensive fuel reforming to produce optimum conditions for prevention of carbon accumulation. Additional anode development can increase stability and reduce reliance on intensive anode feed composition control, thus reducing costs and improving system stability.

2.1. Red-Ox Cycling Robustness of SOFCs

Red-Ox Cycling. Of all the reliability issues that may occur for SOFCs, the main limitation for Ni-based cermet anodes (e.g., NiO-YSZ) is the poor stability in red-ox cycling [6]. This instability is due, primarily, to the large volume change and coarsening of the Ni-phase in the cermet anode [7]. Nickel-oxide experiences close to 40% contraction upon first reduction to Ni metal in the anode cermet (mostly resulting in an increase in anode porosity rather than in bulk NiO-YSZ ceramic dimensional changes), while Ni can undergo anywhere from 65-69% volume increase upon re-oxidation to NiO [14-15]. Such large volume changes of the Ni-phase produce considerable stress in the anode and electrolyte. When the porosity in the Ni–YSZ anode (anode support layer) cannot accommodate the volume change, the rigid YSZ network breaks and, invariably, the whole cell fails. In addition, such red-ox cycles can be expected during long-term fuel cell operation due to unexpected fuel supply interruptions, high fuel utilization under high

current loads, or gas sealing failures. For instance, researchers have shown the importance of the oxidation process for the thermo-mechanical behavior and failure modes of anode supported SOFCs [16-17]. While the investigated cells could tolerate a degree of oxidation of about 50% when exposed to air from the anode side flow supply, oxidation by oxygen ions arriving through the electrolyte resulted in cell failure even at degrees of oxidation as low as of 5%. Those results indicate that oxidation at the anode-electrolyte interface (where the anode is relatively dense) would be the least desirable mode of operation since this generates a peak stress at the electrolyte. This type of situation is possible during extreme cell loading when fuel utilization approaches 100% or when (for any reason) the local oxygen partial pressure exceeds that needed for the oxidation of Ni. To some extent, fast communication of oxygen may also take place through the backside of the anode support (through regions of higher porosity) to a denser anode region. The re-oxidation could also result from abnormal conditions in the fuel supply system which can lead to fuel starvation and a subsequent increase in the oxygen partial pressure above the Ni thermodynamic oxidation threshold, or from oxygen ingress into the anode through pinholes and other defects in the electrolyte, or through imperfect gas seals [18].

These issues do not occur exclusively only after prolonged use [19]. Improper control during unsteady operation, excessive electrical loading, harsh characterization procedures, thermal cycling, etc., can induce premature component and system failures [20-21]. Thus, in addition to steady-state durability, SOFCs must cope with transient situations such as start-up/shut-down, red-ox cycling, conditioning protocols (first operation), thermal cycling or thermal runaway conditions, reforming dynamics, and gas supply failures [22]. This is particularly the case for planar stacks, where different thin ceramic and metal layers alternate in a compact volume and are exposed to high temperature flows of reactive gases and to various pressure and temperature gradients. In addition, the SOFC cells and stacks are not subjected to these different adverse conditions independently, and therefore cycle durability studies must be performed using realistic operation protocols which simulate typical operational conditions [23].

Past Approaches To Red-Ox Robustness. Solutions for enhanced red-ox robustness of SOFCs include modifications to Ni-based anode supports, designs incorporating metal supports, and alternative anode support materials. For instance, Wood et al (2006) have studied the optimization

of SOFCs for better red-ox stability through micro-structural optimization (e.g., composite structures), while Fouquet et al. (2003) and Busawon et al. (2008) have shown improved red-ox stability of anodes infiltrated with Ni-based salt solutions [24-26]. However, there has been limited success in improving the red-ox stability for Ni-based anode supported cells using these methods. Commercial entities have approached the red-ox stability issue through the construction of cells with thin anodes deposited on top of a rigid stainless-steel support [27-28]. While promising, this comes at the expense of power density, which ultimately is a major contributor to the overall system cost. A key alternative anode material is $SrTi_{0.75}Nb_{0.25}O_3$ (SNT), which is an electronically conductive ceramic that is relatively red-ox stable in comparison to Ni-based anodes. However, the material is essentially incompatible with GDC, and therefore limited to use above ~800 °C. Of the known past solutions to a red-ox robust cell, there is considerable room for improvement.

In addition to cell-based improvements, several system solutions for mitigating or preventing SOFC degradation through red-ox cycling of have been suggested and demonstrated with varying degrees of success. Singhal (2003) describes methods for prevention of anode re-oxidation by employing special controls and safety cool-down subsystems (e.g., by utilizing purge gas systems), while Halinen et al. (2014) presents results from an experimental study of SOFC systems equipped with a steam pre-reformer and an anode off-gas recycling system designed to reduce the need for premixed safety gases [29-30]. However, these solutions add complexity and extra cost to the SOFC systems, and other operational failures remain a possibility.

The Impact Of A Red-Ox Robust System. Techno-economic analyses of the impact on cost from the addition of anode re-oxidation prevention/mitigation subsystems (e.g. the more common anode safety gas storage solutions) are generally scarce, however, the recent study by Halinen et al. (2014) points to the fact that the 10 kW demo SOFC stack at VTT Technical Research Centre, Finland would consume 5 bottles (50 liter, 200 bar) of premixed safety gas (4% H_2, 96%N_2) during a heat-up cycle which could span several hours [30]. Scaled for a high-performance 25-kW SOFC system, this type of anode re-oxidation prevention system would increase system volume by at least 50%, substantially add to the complexity and cost of the system, and still would only be able to provide anode protection during one shut-down (or start-up) event. In addition, an economic study prepared for the US Department of Energy, Weimar et al. (2013) concluded that factoring in

the risk of having to replace a stack after only 2-3 years of operation (due, for instance, to accidental failure) can more than double the levelized cost of electricity (LCOE) generated, even in large, mass-produced (270 kW) stationary power units (i.e., units which take advantage of the economies of scale) and would essentially render the technology unfeasible (noncompetitive) for commercial energy generation purposes [31]. While controls malfunctions, E-stops, and seal degradation are all reasons to pursue a red-ox robust stack, the potential for fuel supply disruption is also real [32-35]. Therefore, a more desirable (and economically advantageous) approach is to avoid the potential cell failure by improving the red-ox stability of anodes rather than by devising solutions to mitigate it. As such, this project focused on the development of a ceramic-anode based, red-ox stable SOFC and stack.

2.2. Ceramic-Anode Based SOFCs

To address the issues related to conventional Ni-based anodes, this project on the development of a ceramic-anode based SOFC, which was intended to become the core component of a new red-ox robust stack. The microstructures of a ceramic anode can offer very significant improvements in both mechanical robustness and red-ox stability. A red-ox robust stack will improve system reliability without the need for an expensive systems level solution. Therefore, a red-ox robust stack can ultimately reduce system capital cost and operating and maintenance (O&M) costs for a lower LCOE and a greater chance for widespread commercialization.

Red-ox processes have considerably fast kinetics at high temperatures, which means that Ni can oxidize rapidly. This oxidation can cause the Ni phase to expand as much as 60% while the YSZ (or GDC) phase of conventional cermet anodes will work to oppose the expansion. Such an event generates a large degree of strain within the anode and electrolyte, which can be accommodated through a combination of elastic and pseudoplastic deformation that will eventually be relaxed through microcracking in the anode and/or electrolyte. If the cracking does not cause failure of the cell immediately, the restoration of a fuel atmosphere will re-reduce the anode cermet. Due to irreversibility during red-ox cycles, the accumulation of such damage causes electrical conductivity loss and other contributions to degradation, as well as inevitable cell failure.

In contrast to Ni-based cermet anodes, ceramic anodes are advantageous for a number of reasons. First, minor oxygen non-stoichiometry in the ceramic anode creates only a slight dimensional

change in the presence of oxidizing and reducing conditions, which results in minimal internal stresses and thus excellent red-ox cycling stability. Second, the excellent chemical stability as well as coking and sulfur tolerant properties of ceramic anodes make them attractive for direct utilization of hydrocarbons at lower operating temperatures. Lastly, ceramic oxides can have considerable mechanical strength in both the oxidized and reduced state, and the thermal expansion coefficient can be engineered appropriately for improved compatibility most common electrolytes.

However, in the past there has been no single ceramic oxide material meeting all the requirements for a lower temperature red-ox robust SOFC that can operate on hydrocarbon fuels. The ceramic anode materials investigated in the literature have mainly focused on high-temperature SOFCs [36]. Known materials with some of the required characteristics can be broadly classified as titanates (e.g., $SrTi_{0.75}Nb_{0.25}O_3$), molybdates (e.g., Sr_2MgMoO_6), chromates (e.g., $La_{0.2}Sr_{0.7}Cr_{0.5}Mn_{0.5}O_{3-\delta}$) ferrites (e.g., $La_{0.6}Sr_{0.4}Fe_{0.9}Mn_{0.1}O_{3-\delta}$) and vanadates ($La_{0.8}Sr_{0.2}VO_{3-\delta}$) [37-45]. Among the studied materials, substituted double perovskites such as Sr_2MgMoO_6 (SMMO) have shown desirable electrode properties for direct hydrocarbon utilization at high-temperature operation [46]. And while SMMO can prevent carbon formation at 600 °C, the major limitation preventing its use in lower operating temperature SOFCs is the requirement for relatively high temperature pre-treatment (under low pO_2 conditions, > 900 °C) to achieve the required electronic conductivity. This problem is also true for other common conductive ceramic materials that have been investigated for use in the anode. For example, the conductivity of SNT pre-treated at 900 °C is 8.2 S/cm when measured at 400 °C (shown in **Figure 1**). However, when pre-treated at 650 °C, the value of conductivity reduced to 1.7 S/cm. Furthermore, many of these ceramic materials, such as SNT, are not compatible with GDC electrolytes which enable lower operating temperatures (e.g., ≤ 650 °C) due to high ionic conductivity. These factors limit the applicability of known conductive ceramic anode materials to high temperatures.

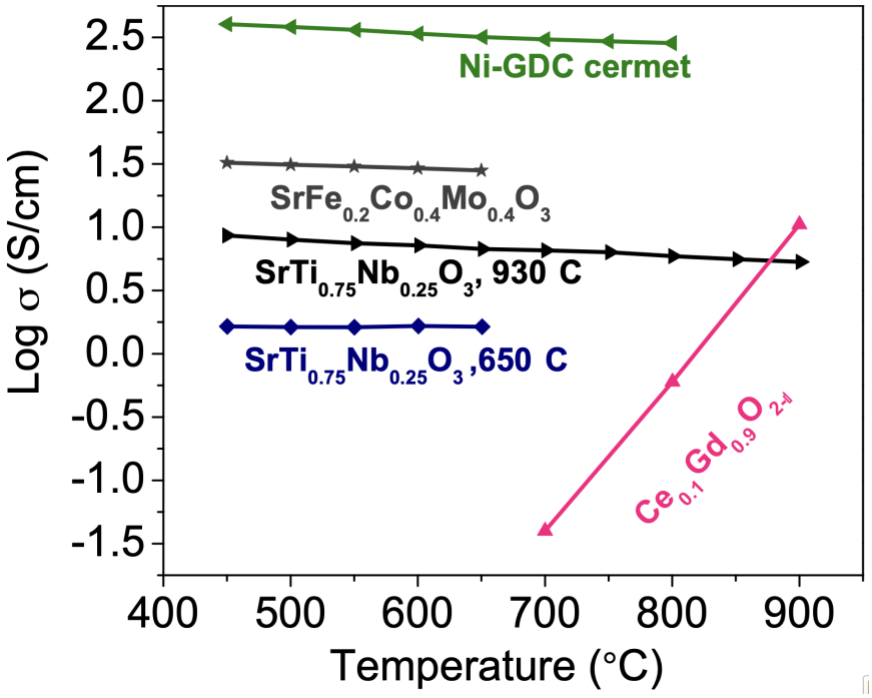

Figure 1. Temperature-dependent DC conductivity of ceramic anodes, including the SFCM-based material, compared to a standard Ni-GDC anode measured in reducing gases.

Of the ceramic anode materials developed by the project team, the most promising is $SrFe_xCo_{1-x}Mo_{1-x}O_3$ (SFCM, x=0.1-0.5) [47]. As shown in **Figure 1**, a high conductivity of ~ 30 S/cm was achieved for $SrFe_{0.2}Co_{0.4}Mo_{0.4}O_3$ (SFCM244) in reducing atmosphere, 10%H_2/N_2 at 650 °C. For comparison, the conductivity of a typical Ni-GDC cermet is shown along with that of SNT reduced at 900 °C or 650 °C. SFCM has a sufficiently high conductivity even when activated in a reducing atmosphere at 650 °C. Furthermore, SFCM is also chemically compatible with GDC up to the lower end of temperatures at which cells typically are fabricated (~1250-1300 °C). During the initial process development of a functional button cell, SFCM anode-supported SOFCs were fabricated at a low-sintering temperature of 1200 °C, which when compared to the normal 1400-1500 °C fabrication temperature typically needed for YSZ- and GDC-based cells has the potential to reduce the overall cell fabrication cost.

There is also evidence that SFCM has a high degree of red-ox stability, both as a single phase and in a composite with other oxides (e.g., GDC). Solid-state synthesized SFCM powder was prepared and mixed into a composite with GDC before being pressed into rectangular bars for conductivity measurements under red-ox cycling conditions. The samples were initially heated to at 650 °C in

N_2 and changed to 10% H_2/N_2. The samples were then allowed to stabilize in reducing gas conditions over a period of 50 hours and measurements were made by alternating the gas conditions between 10% H_2/N_2 and air. The red-ox stability of the conductivity in the reducing gas is shown in **Figure 2**. The baseline red-ox cycle (i.e., cycle 0) is the initial value before flowing air across the sample. After the first few cycles, there is a slight decrease in conductivity, which has been attributed to sample preparation rather than an intrinsic property of the material. After this decrease, and subsequent slight increase, the conductivity was very stable. These results indicate that the conductivity of an SFCM-GDC composite is red-ox stable for at least ~20 cycles.

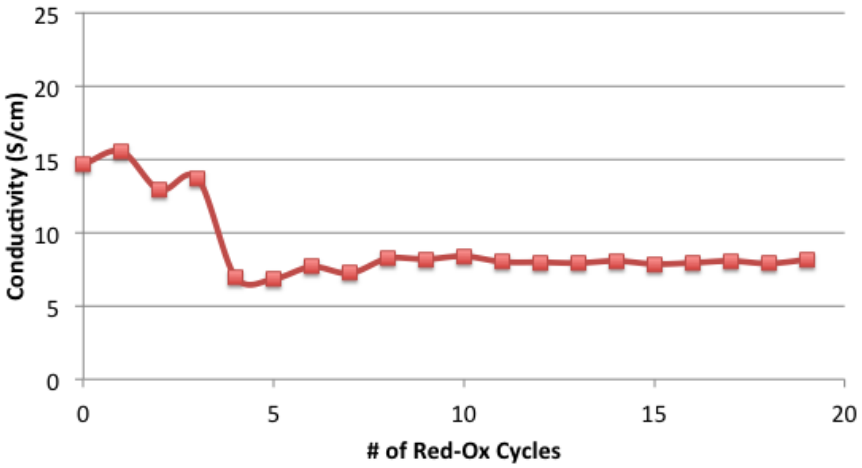

Figure 2. Electronic conductivity of SFCM-GDC composite after ~20 red-ox cycles at 650 °C.

SEM micrographs of SFCM before and after red-ox cycles are shown in **Figure 3**A and **Figure 3**B, respectively. No major changes were observed in the micrographs for SFCM before being exposed to a reducing gas (i.e., virgin state) and after ~10 red-ox cycles other than some minor texturing of the grains. This is in stark contrast with the changes that occur under comparable conditions for a Ni-YSZ anode (**Figure 3**C). This lends further evidence that the SFCM-based anode has superior red-ox stability.

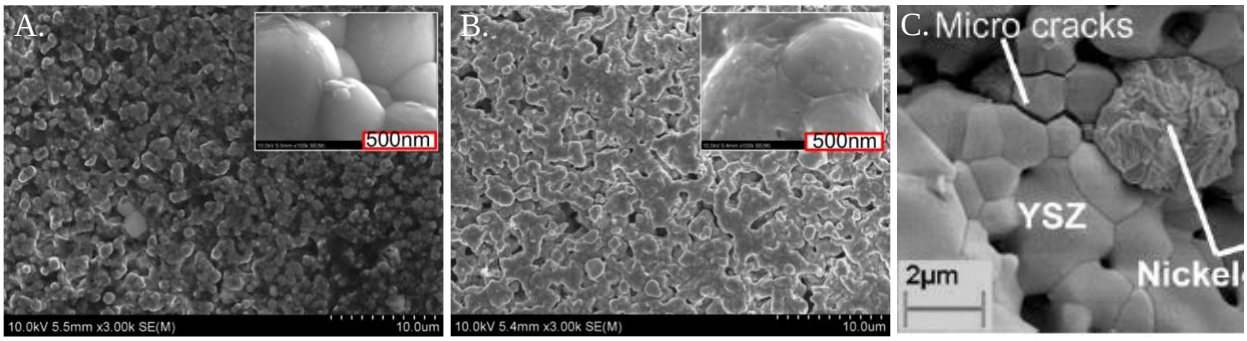

Figure 3. SEM micrographs showing A) SFCM microstructure before exposure to reducing gas; B) SFCM microstructure after 9 red-ox cycles (illustrating that no major reconstructions or other changes occur); and C) an example of a Ni-YSZ cermet microstructure with micro-cracks that formed during red-ox cycling [48].

An SFCM electrode was also deposited on a thick YSZ pellet in a three-electrode symmetric cell arrangement to determine the area specific resistance (ASR) from the measured impedance for successive red-ox cycles in air and 5%H_2/N_2. A nitrogen purge was used in between each change in gas composition. The sample was allowed to equilibrate in air for at least for one hour before a reducing gas environment was reintroduced. Sufficient time was provided for equilibration and the impedance spectrum was measured in the reducing condition after each cycle. The ohmic and non-ohmic portion of the impedance spectra are shown in the normalized plot of **Figure 4**.

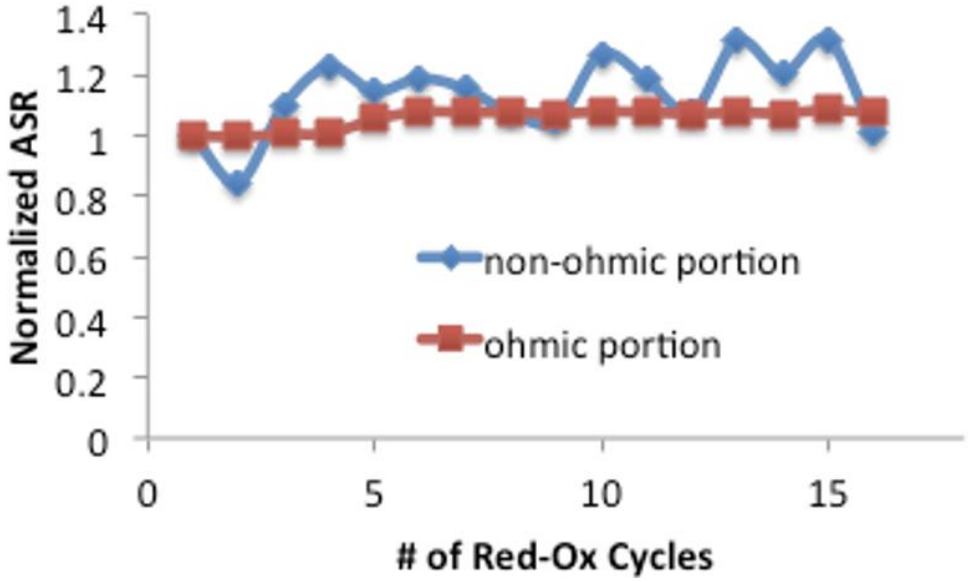

Figure 4. Normalized ASR versus number of red-ox cycles for a SFCM-based electrode deposited on a YSZ pellet.

2.3. SOFCs Based on Ceramic SFCM-Based Anode Materials

SFCM-GDC anode-support button cells were tested in both H_2 and H_2/CH_4 mixtures. SFCM alone is not very catalytically active for hydrogen oxidation at lower temperatures. Thus, Ni-GDC was infiltrated into SFCM scaffold. Such cells have been tested with both LSCF-GDC and SSC-GDC composite cathodes, where LSCF is Lanthanum Strontium Cobalt Ferrite and SSC is samarium strontium cobaltite. Owing in part to the high electronic conductivity of the SFCM-based anode, these cells have shown remarkably high performance, which is even better than most conventional Ni-GDC cermet supported cells. Note, these cells utilized SFCM powder synthesized using a glycine–nitrate process (GNP) combustion method, which resulted in a very fine particle size. The anode was infiltrated with ~10 wt% Ni-GDC catalyst loading. Additionally, a cobalt-modified GDC (Co-GDC) cathode functional layer (CFL) was arranged between the electrolyte and the cathode. As shown in **Figure 5**A, the cell with the SSC-GDC composite cathode achieved an open circuit potential (OCP) of ~0.9 V at 550 °C and ~1 V at 450 °C, which are both considerably higher than normal GDC cells with the same GDC thickness [47,49]. A peak power density of ~0.75 W/cm^2 and ~0.3 W/cm^2 were demonstrated at 550 °C and 450 °C, respectively. **Figure 5**B shows a Nyquist plot of the electrochemical impedance for the button cell. At 500 °C, the ohmic ASR of the cell was ~0.17 Ω-cm^2, while the total ASR was about 0.24 Ω-cm^2, which is excellent for this temperature.

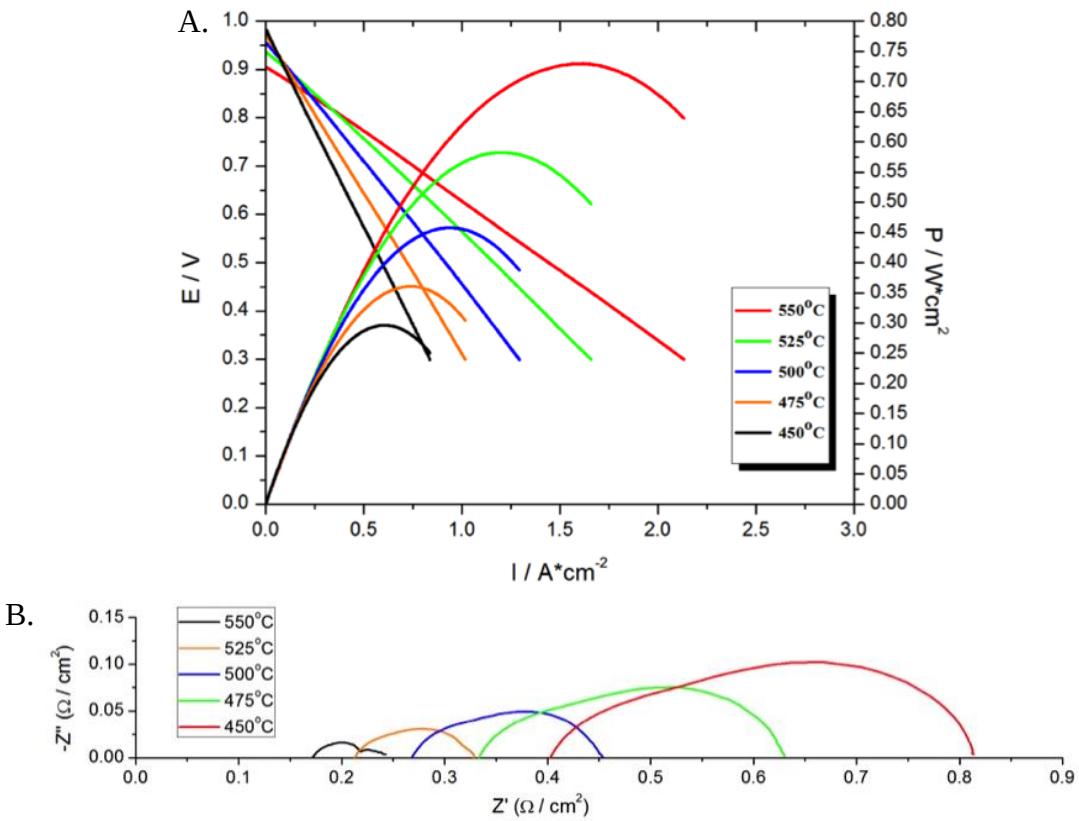

Figure 5. Characteristic performance curves for an SFCM-based anode-supported SOFC with a GDC electrolyte, Co-GDC CFL, and SSC-GDC cathode in humidified hydrogen, showing A) voltage and power density versus current density between 450 °C and 550 °C, and B) a Nyquist plot of the impedance spectra.

A long-term performance evaluation of a button cell with a composite SFCM-GDC ceramic anode was made using a simulated reformate composition consisting of 81% H_2, 16% CH_4, and 3% H_2O. As shown in **Figure 6**, the button cell showed less than 0.3% degradation per 1,000 hours over 225 hours after stable operation was reached with a fixed current density of 0.2 A/cm^2 and a furnace temperature of 500 °C. The measured local temperature was 489 °C, which is assumed to be a result of endothermic reforming reactions in the presence of CH_4.

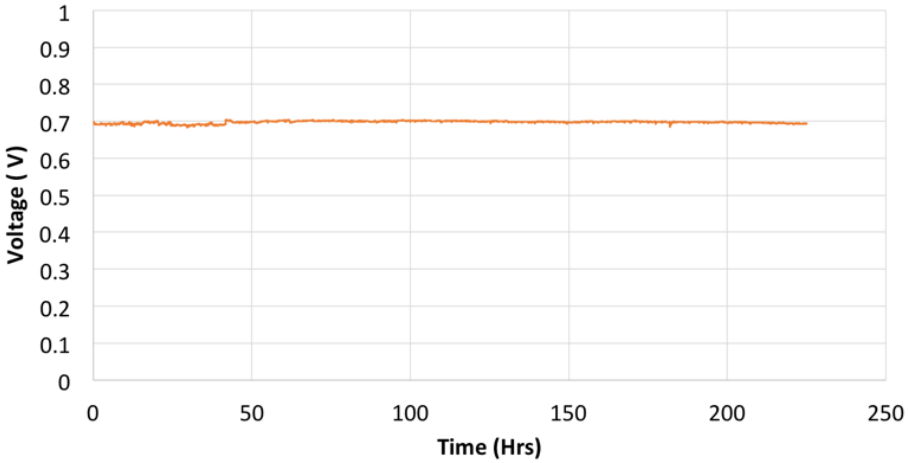

Figure 6. Long-term stability data for SFCM-GDC anode supported button cell using reformate gas mixture at ~500 °C with a fixed current density of 0.2 A/cm^2.

There is much evidence that SFCM has structural stability in both air and hydrogen. For example, after calcination, SFCM has tetragonal perovskite pure phase as shown in the XRD plot of **Figure 7**. When the sample was reduced at 650 °C in hydrogen for 24 hours, the phase did not change. The peaks shift to the left, indicating crystalline lattice expansion which occurs during reduction as the material loses a small amount of oxygen and the repulsion between cations increases. Furthermore, when the Mo^{6+} gets reduced to Mo^{5+}, the Mo ionic radii increase.

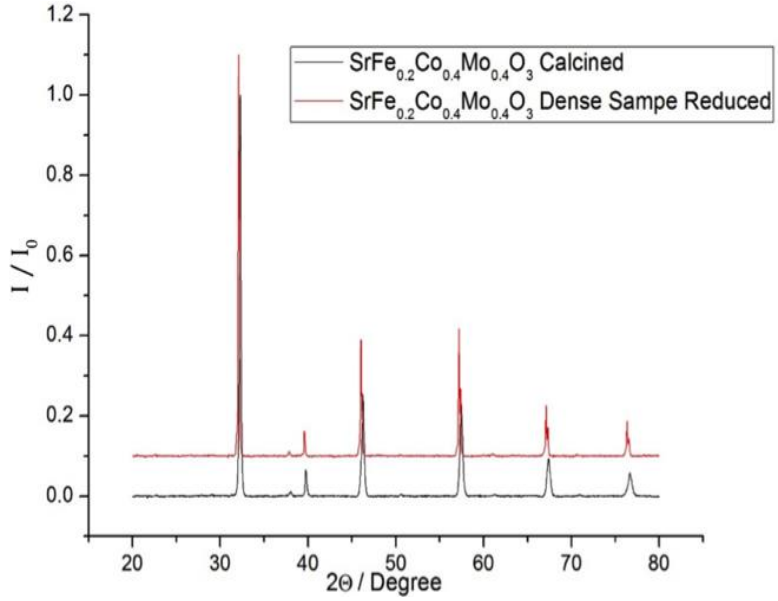

Figure 7. XRD of calcined (exposed to air) SFCM powder and a reduced SFCM (dense) pellet illustrating the absence of any impurity phases and thus good red-ox cycling structural stability.

2.4. Ceramic-Anode Cell Structures Used During the Project

During the project, several variations of the ceramic-anode cell architecture were used to balance electrochemical performance, general long-term stability, strength, scaled-up cell size requirements (e.g., flatness, defects, etc. at up to 10 cm by 10 cm), and red-ox robustness. The baseline SFCM-based cell structure (**Figure 8**A) is the basic cell architecture used during the initial development of button cells before this project. Note, in all cases, the cell may optionally include a cathode functional layer (CFL), which consists of a layer of cobalt-modified GDC (Co-GDC). This CFL has been shown to provide strong bonding to the cathode and to have a higher oxygen surface exchange coefficient than GDC (**Figure 9**), which improves mass transport of the dissociated oxygen ion into the GDC lattice for improved electrochemical performance. The baseline structure consists of an ASL layer (e.g., SFCM-GDC), an electrolyte layer (i.e., ceria-based materials, such as GDC), a CFL, and a cathode (e.g., LSCF-GDC or SSC-GDC composite). Another cell architecture pursued during this project is shown in **Figure 8**B and consists of two different types of ASL, an electrolyte, a CFL, and a cathode. The two different ASLs may consist of different materials, or proportions of materials for composites, or different microstructures (e.g., pore size). As shown in **Figure 8**C, the final basic cell architecture consists of an ASL and a thin AFL, an electrolyte, a CFL, and a cathode. In this case, the AFL typically has a finer pore structure, but may also consist of a different composition and/or particle size.

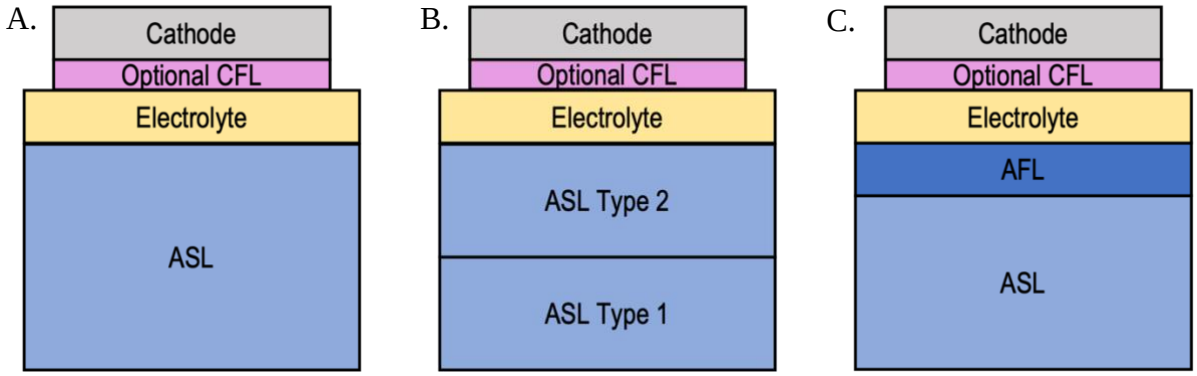

Figure 8. Basic cell architecture variations used during the project for the SFCM-based ceramic anode SOFC development showing A) single-type (uniform) ASL, B) multiple types of ASL, and C) an ASL combined with a thin AFL.

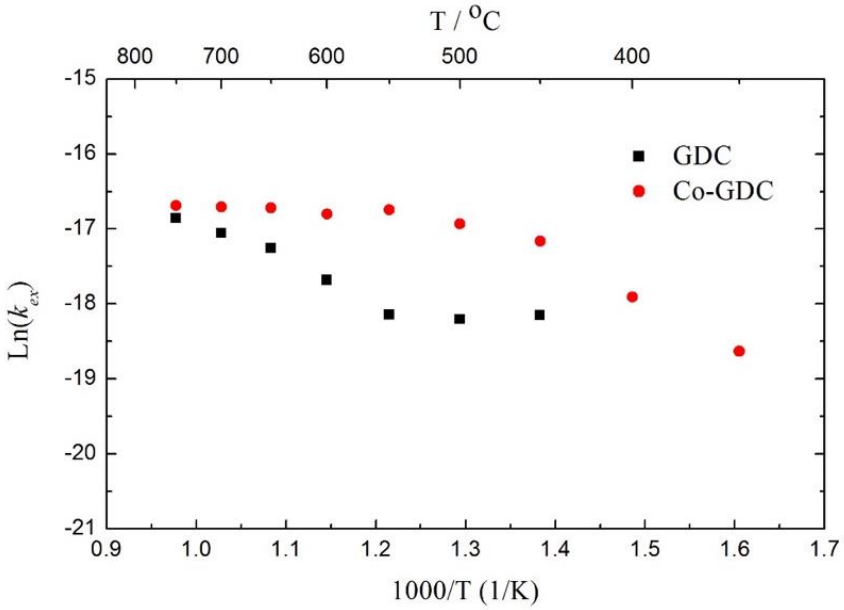

Figure 9. Oxygen surface exchange coefficients for GDC and Co-GDC versus temperature.

3. METHODS, TYPE OF MEASUREMENTS, AND INSTRUMENTATION

Throughout this project various methods, types of measurements, and related instrumentation were used to characterize the materials, fabricated SOFCs, and stacks. The type of measurements necessary to evaluate performance and infer reliability are typical to SOFC development and included electrical, mechanical, catalytic, and electro-catalytic measurements. Electrical measurements included DC and AC conductivity (electrochemical impedance spectroscopy, EIS), as well as current and voltage. Such measurements were used to assess open circuit voltage (OCV), area specific resistance (ASR), current-voltage characteristics, and performance stability over time. Mechanical measurements included 3-point and 4-point bend tests and nano-indenter measurements. Catalytic and electrocatalytic measurements included gas analysis via gas chromatograph and/or mass spectrometry, as well as the electrical measurements. Additionally, powder characterization methods yielded such information as particle size and distribution; surface area; phase purity; and crystal structure. The coefficient of thermal expansion (CTE) and sintering curves for each cell material were determined to optimize cell geometries and cell fabrication processes. Such characterizations techniques included thermal/chemical expansion (e.g., via dilatometry and X-ray Diffraction (XRD)). Other materials characterization equipment involved microstructural and chemical analysis via scanning electron microscopy (SEM) and SEM energy

dispersive X-ray spectroscopy (SEM-EDS). These tests were made at room temperature or elevated temperature (e.g., 550 °C to 700 °C). As appropriate, these measurements were also made in different gas conditions such as in air or fuel (e.g., humidified hydrogen or reformate gas such as mixtures containing H_2 and CH_4) and as a function of PO_2. Mass spectrometry (MS) and gas chromatography (GC) gas analysis methods were used to assess catalytic and electrocatalytic activity, seal quality, and other related characteristics.

3.1. Cell and Stack Testing

General Cell and Stack Testing. **Figure 10**A shows an example of a typical SOFC characterization setup used during the project for 10 cm by 10 cm single cell and stack testing. Multiple gases can be flowed to this setup, and the absolute flow as well as the relative feed concentration is controlled via mass flow controllers (MFCs). The setup allows for widely varying synthetic reformate compositions. Furthermore, the setup ensures that the gas feed to each electrode either flows through or bypasses a humidifier, which brings molar H_2O content as high as 67 vol. %, allowing the effect of water content on the electrode long-term performance to be investigated. An electrochemical test bench (frequency response analyzer and electronic load) is connected to the stack to perform conventional electrochemical performance evaluation (I-V and EIS) to assess extent of degradation resulting from bulk resistance increase and electrode area specific resistance increase, and current-voltage (I-V) performance deterioration corresponding to fuel feed composition. Cell temperatures and feed/effluent pressures are also monitored and recorded during operation. Button cell test setups used similar, scaled-down equipment as well as common alumina tube reactors wherein the cells are cemented to the alumina tube (e.g., anode side down) and electrical contact is made using a mesh current collector that is adhered with a contact paste (e.g., platinum or silver).

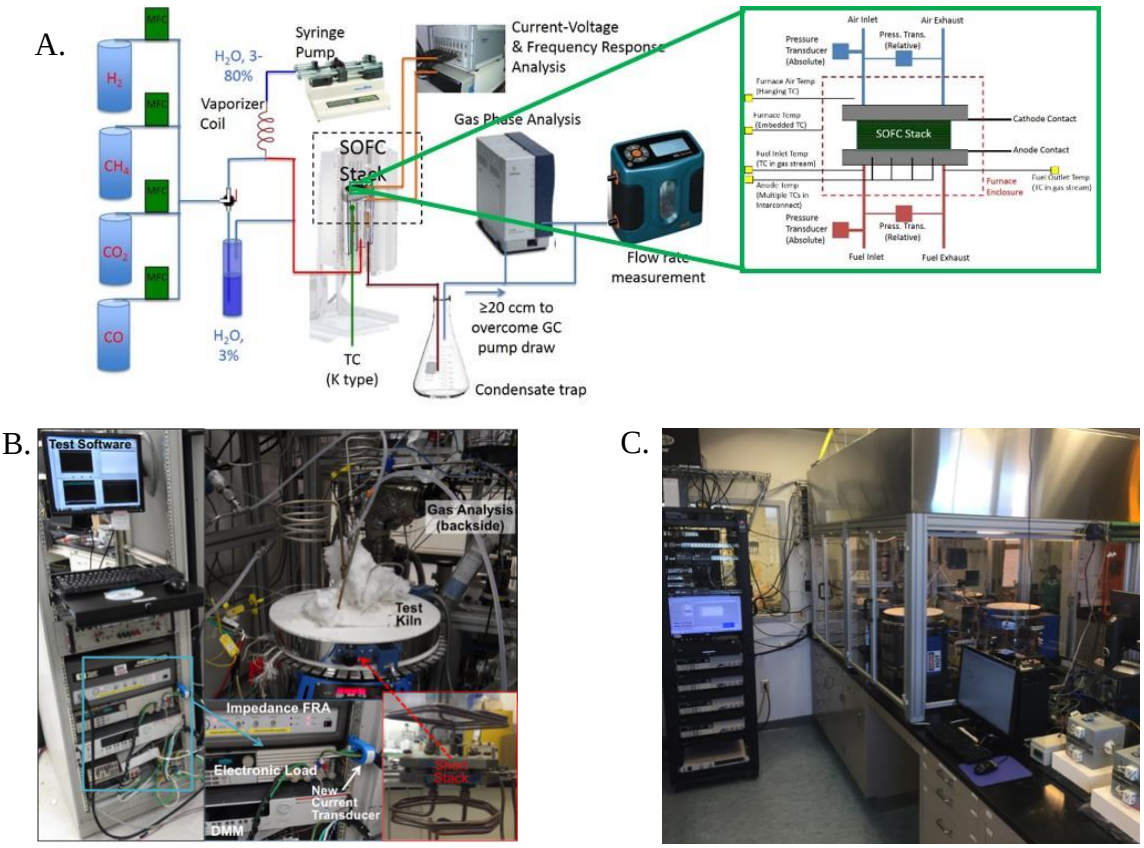

Figure 10. Large-format cell test setups showing A) a piping and instrumentation (P&ID) diagram, B) a 10 cm by 10 cm single cell/short stack, and C) multiple stack test bench facilities.

Simultaneous GC and MS measurement for the exhaust gas composition analysis and carbon balance calculations enables monitoring of coking as well as monitoring of degradation of anode catalytic performance during operation. Coke formation can be detected by performing a species balance of the inlet and exhaust gases. Composition analysis via GC further allows for the assessment of crossover leakage between fuel and oxidant channels due to mechanical degradation (camber, inelastic deformation, creep, etc.). Together with GC measurement, pressure sensors and a humidity sensor are attached to the piping lines for monitoring any changes in feed and effluent conditions. Post-test degradation analysis provides an opportunity to correlate any observed electrochemical performance degradation with a variety of measurable parameters including: 1) contact degradation of electrode and contact layers using measured resistance; 2) interdiffusion between electrode and electrolyte materials using microscopy and elemental analysis (SEM and

EDS); 3) coking or carbonating of anode using SEM, EDS and XRD; 4) delamination of cell layers using optical microscopy; 5) cell camber changes using, for example, an optical profilometer.

Natural Gas Test Facility (NGTF). In addition to general large format cell testing, larger size stacks and testing using reformed natural gas was conducted at Redox's Natural Gas Test Facility (NGTF). There is a large test bench with 10+ large-format cell/stack test setups within the facility as shown in the left side of **Figure 11**A. The facility also houses a subsystem and standalone system test hood (**Figure 11**A, right foreground) and a large stack test bench (**Figure 11**A, right background). The large stack test bench consists of a balance of plant (steam production/control, steam reformers, cathode recuperators, etc.) and two large stack hotbox modules as seen in **Figure 11**B and **Figure 11**C, respectively. While larger tube-in-shell reformers are available, the large stack test benches utilize a similar design (i.e., tube-in-kiln) with a computer-controlled kiln for heat input rather than the burner of the tube-in-shell reformer. The large stack test bench also uses a large electric boiler to produce steam for additional control during characterization and testing. Steam and (desulfurized) pipeline natural gas are mixed just prior to entering the reformer kiln where they pass through a preheating tube coil to bring them up to a thermocouple monitored temperature which will not coke the reformer catalyst. After reforming, the syngas steam mixture is piped to a larger kiln for stack anode feed. The tube-in-kiln reformer can support stacks with power outputs as high as 2.5 kW. Multiple electronic loads are available for testing cells and stacks up to 12 kWe. The two main test stations feature exhaust water condensation/recovery, full data logging and back-up and the facility retains multiple-point gas sampling and analysis capability.

A.

B.

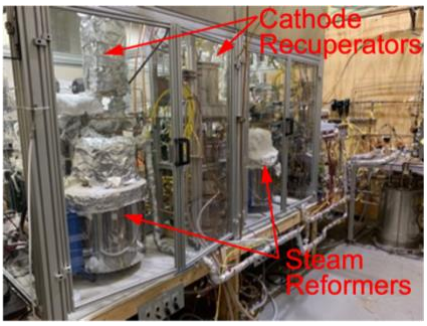

C.

Figure 11. Redox's Natural Gas Test Facility (NGTF) showing A) stack test benches (left), system test bench (right, foreground), and large stack test bench and balance of plant (right, back); B) balance of plant for large stack test bench, including cathode recuperators and steam reformers; and C) large stack test hotbox modules.

A micro gas chromatograph was used to characterize the effluent of both tube-in-kiln reformers. Example feed and effluent data for the tube-in-kiln reformer is presented in Table 1. The reformer was fed with desulfurized pipeline natural gas at 1.75 liters per minute, with a steam feed of 9.75 liters per minute. This steam value is the smallest stable value for the steam controller, as the reformers were designed for multi-kW scale demands. On a dry basis (H_2O removed), the natural gas reformate was 67.5% H_2 with only 10.1% CH_4 remaining, indicating that reforming was over 68.5% complete compared to thermodynamic equilibrium values. Equilibrium values were determined using Cantera v2.3 packages in Python, and degree of reformation was calculated based on a carbon balance. Complete reformation to equilibrium values is not necessary because additional reformation occurs within the stack.

Table 1. Composition of the feed to the tube-in-kiln reformer and the effluent measured by GC at ~600-650 °C. H_2, CH_4, CO, and CO_2 values are measured on a dry basis by GC (H_2O is removed prior to sampling).

	H_2	**CH_4**	**CO**	**CO_2**	***H_2O***
Feed to Reformer	0.0%	100%	0.0%	0.0%	*5.6:1 Steam:Carbon*
Feed to Stack	67.5%	10.1%	8.8%	13.2%	*Balance*
Thermodynamic Equilibrium Values	78.1%	0.1%	7.8%	13.7%	*Balance*

3.2. Dilatometry of Cell and Stack Components

During this project, Redox's dilatometer (**Figure 12**) was upgraded to accommodate atmosphere control capabilities for *in-situ* redox cycling of materials. The dilatometer has compatible quartz or alumina tubes and fixturing and can reach a temperature of 1600 °C. The sample is loaded into the test fixture and rests against a pushrod that is coupled to a sensitive linear variable differential transformer (LVDT). The transducer is calibrated using a standard such as alumina periodically to ensure accurate results. The dilatometer was used for various purposes during this project. For instance, the dilatometer was used to acquire sintering curves for different layers making up the ceramic anode SOFCs (e.g., the anode support layer). Generally, such samples produced by laminating several tape-cast green tape layers, burning off the organics, and lightly sintering before loading into the dilatometer. The dilatometer was also used to characterize the thermal expansion coefficient of the individual layers of the SOFC, the entire SOFC, and various stack materials (e.g., seals). Finally, the dilatometer was used to assess the chemical expansion and contraction of cell and stack materials when exposed to different gas environments, such as during red-ox cycling.

Figure 12. Redox's vertical pushrod dilatometer with atmosphere control for oxidizing and reducing conditions and more generally acquiring sintering curves and coefficients of thermal expansion for cell materials and stack components.

3.3. Mechanical Characterization of Ceramic Anode Materials

To determine mechanical strength and the impact of red-ox cycling, we utilized a Redox/UMD designed atmosphere/temperature-controlled fixture for testing the mechanical properties of SOFC materials (**Figure 13**). The setup consists of an alumina 3- or 4-point test fixture which connects to a Tinius Olsen 10ST universal test machine (UTM) with a 250 N load cell. The test fixture is housed in a stainless-steel chamber where air or a safety gas (e.g., 3% hydrogen with a balance of an inert gas such as nitrogen or argon) can be flowed for in-situ reduction of samples to determine the impact on mechanical strength. The design allows samples to be swapped at elevated temperature for rapid evaluation and relevant statistical analysis (e.g., Weibull distributions). The chamber is placed inside a furnace designed to fit within the UTM to allow heating to SOFC operating conditions. A setup such as this is useful for characterizing a variety of SOFC- and stack-relevant parameters. For example, the setup may be used to help determine if any mechanical creep occurs when the cells are under compression (as is done in a stack) and to determine if there is any impact to creep or mechanical strength as the cell undergoes red-ox cycling.

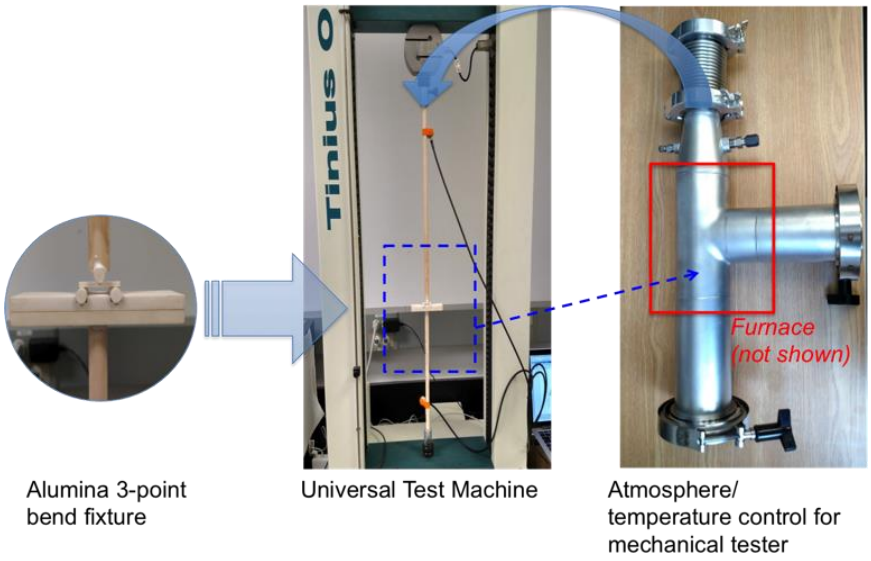

Figure 13. Atmosphere and temperature-controlled fixture for mechanical testing of cell materials under relevant conditions.

4. OPTIMIZATION OF RED-OX ROBUST CELLS

4.1. SFCM Conductivity

As part of the efforts to assess the red-ox stability of the SFCM-based ceramic anode SOFCs, the electrical conductivity was evaluated for SFCM-GDC/GDC half-cell samples before and after cycling. The reducing environment consisted of a 5% H_2 (balance argon) flow stream, which was either dry or humidified using a room temperature water bubbler. As shown in **Table 2**, the in-plane conductivity of two SFCM-GDC/GDC half-cell samples in air before and after red-ox cycling was stable and essentially identical, within experimental error. Furthermore, no cracks or other visual evidence of degradation was observed in the samples after red-ox cycling, as shown in **Figure 14**. Some foreign matter (e.g., dirt) is observed in the SEM image, while the Ag paste and leads for electrical contact are shown in the photographs.

Table 2. Conductivity of two SFCM-based ceramic-anode half cells consisting of SFCM-GDC/GDC and measured at 650 °C during red-ox cycling between air and 5% H_2 (balance argon).

Step	Log(pO_2 [atm])	Gas	Sample 1 Conductivity [S/cm]	Sample 2 Conductivity [S/cm]
1	-0.68	Dry air	1.3	1.5
2	Undef.	Dry 5% H_2	5.2	skipped
3	-0.68	Dry air	1.3	skipped
4	Undef.	Dry 5% H_2	5.6	skipped
5	-22.7	Wet 5% H_2	3.0	2.8
6	-25.3	Wet 100% H_2	6.4	6.3
7	-0.68	Dry air	1.2	1.3

Figure 14. Sample 1 from **Table 2** after measurement, showing no evidence for cracking after red-ox cycling.

We also evaluated the impact of red-ox cycling on the conductivity of an SFCM ceramic-anode half cell at 650 °C using 3% H_2 (balance nitrogen) instead of 5% H_2 (balance argon), as shown in **Figure 15**. The measurement starts in dry air (~1.2 S/cm), then as gas is switched to wet H_2, the conductivity first drops, then rises to ~2.2 S/cm. When air is switched back on, conductivity first drops to a low value, then rises back to the equilibrium air value. The drops are most likely a *p*-type to *n-type semiconductor behavior* transition. The conductivity in air is almost always at the same value, while in H_2 the conductivity only stabilizes at and after the 4th cycle. This latter point coincides with a doubling of the gas flow rate. The higher gas flow rate resulted in a more extensive purge of the O_2 from the system during the 3-hour hold. Over 9 red-ox cycles, conductivity remains

fairly constant, indicating good stability of the SFCM-based ceramic anode. Note, prior to 9 red-ox cycles shown the sample underwent an extra 2 red-ox cycles during equipment troubleshooting.

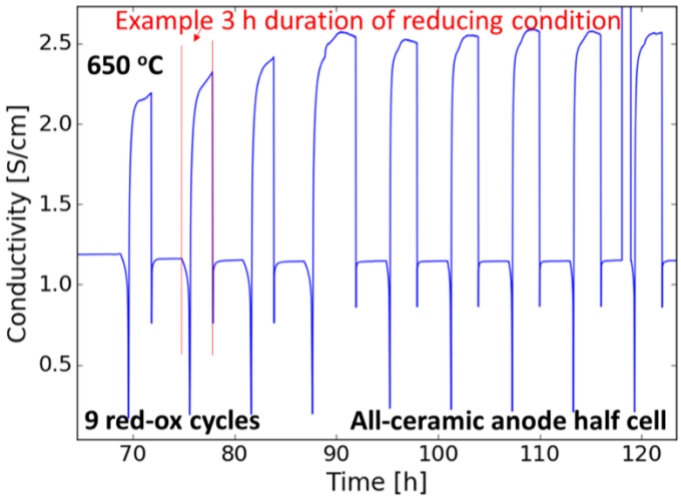

Figure 15. Conductivity of a ceramic-anode half-cell consisting of SFCM-GDC/GDC and measured at 650 °C during red-ox cycling between air and 3% H_2 (balance nitrogen).

Additional conductivity measurements were made using ceramic anode support layers (without an electrolyte), switching between reducing and partially oxidizing (N_2 with > 10 ppm O_2 expected) Even after 5 red-ox cycles, the conductivity of the anode support layers was found to be reasonably stable, as shown in **Figure 16**.

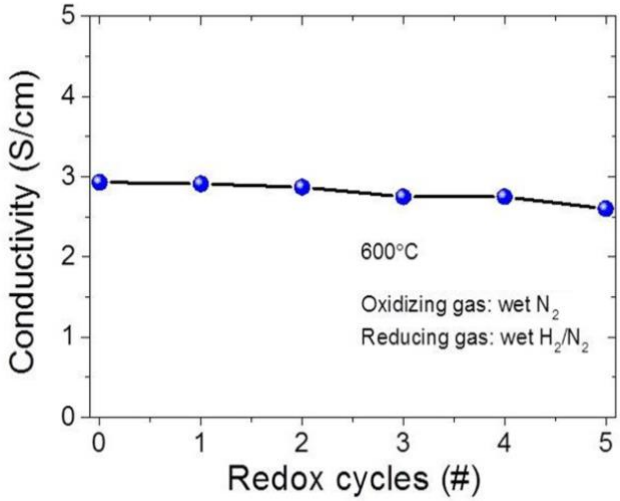

Figure 16. SFCM-based ceramic anode conductivity measured in humidified 10% H_2/N_2 at 600 °C between exposures to humidified N_2 (with O_2 impurity).

4.2. Chemical Expansion of Cell Materials During Red-Ox Cycling

Reduction-oxidation cycling was further evaluated using a combination of conductivity and chemical expansion measurements. The tests were initially performed switching between oxidizing and reducing conditions at 650 °C, which is a high enough temperature to accelerate any potential thermally activated processes, while not so high as to activate largely different degradation mechanisms. Moreover, this temperature remains within the reasonable operation range of the target operation temperature for SFCM-based ceramic anode cells in this project (i.e., ~600-650 °C). The oxidizing and reducing conditions are dry air and 3-5% H_2 (with 2.7% H_2O and balance N_2). Dry air is the highest oxygen activity expected during an unintentional oxidation cycle of the anode during operation, while 3-5% H_2 is highly reducing, but below the lower explosive limit when mixed with air. The latter condition facilitates cycling directly between the reducing and oxidizing gas without an inert purge gas, such as N_2. The reducing gas is humidified, fixing the partial pressure of oxygen (pO_2) to ~$10^{-22.5}$ atm, and thus creating reproducible pO_2 red-ox cycles with air ($pO_2 \sim 10^{-0.68}$ atm). A more aggressive red-ox cycling in humidified pure H_2 ($pO_2 \sim 10^{-25.3}$ atm) with a N_2 purge between cycles was also evaluated.

As shown in **Figure 17**A, only a small degree of shrinkage, followed by expansion, was observed during sample reduction in a conditioning process seen during typical Ni-cermet SOFC conditioning. However, a much larger expansion was observed during oxidation of the reduced cell, which is possible during a seal or fuel flow failure, for instance. This non-reversible expansion behavior (i.e., strain mainly during oxidation) is the likely reason for the electrolyte cracking in red-ox cycled Ni-cermet cells as shown in **Figure 17**B. In this project, the much smaller volume changes of the SFCM-based ceramic ASLs were expected to alleviate this mechanical degradation, and ultimately were shown to do so (e.g., see Section 5.4).

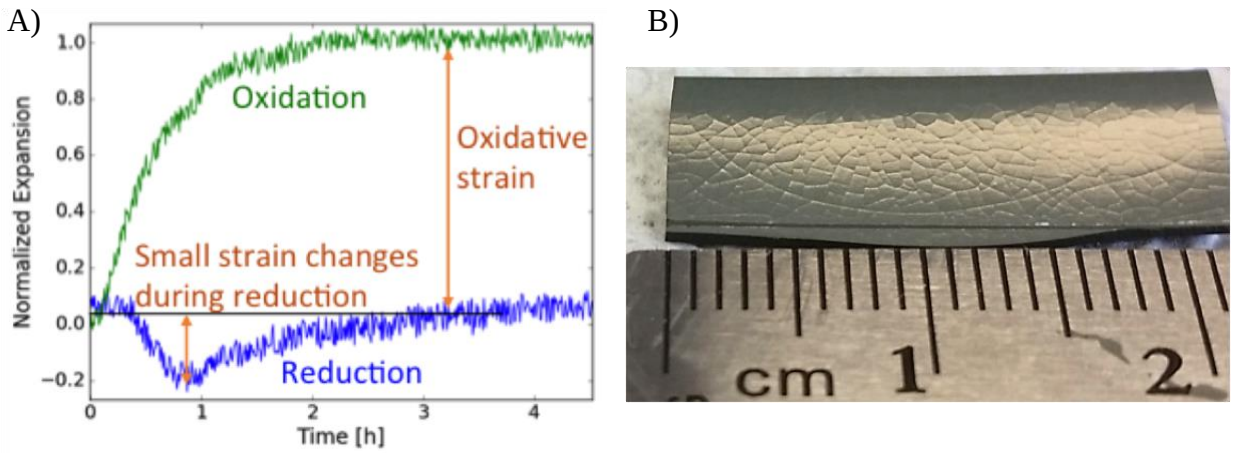

Figure 17. Red-ox cycling stability overview for Ni-cermet anodes, showing A) normalized expansion data measured via dilatometry (highlighting a small strain during reduction of porous NiO-YSZ ASL followed by more significant expansion during subsequent oxidation); and B) an optical image of electrolyte fracture (rough pattern on sample) observed after oxidation of a Ni-cermet half cell used in dilatometry assessments.

The results for *chemical* expansion measurements are shown in **Figure 18**, where the red vertical lines highlight the beginning and end of the reducing condition with a duration of 3 hours. Upon exposure to a reducing condition (5% H_2), the sample expanded by about 0.1%, and then reversibly contracted during exposure to oxidizing conditions (air). This is known as *chemical expansion* as the phenomenon is a result of changes in sample composition, namely loss (reduction) and gain (oxidation) of oxygen. The primary source of the expansion is likely from changes in cation radius during oxidation state changes, the reduced cation typically being larger than the oxidized version [50]. The sample did not immediately respond to the start of reducing conditions but did immediately respond to the oxidizing conditions. This likely was due to 1) a difference in reduction versus oxidation kinetics and 2) a slow purge of oxygen. Note that these measurements were made using a custom ceramic jig to support the ~2 cm long rectangular, thin half-cell sample vertically in the vertical pushrod dilatometer (**Figure 12**). After the red-ox cycle measurement, no cracks or other irregularities were found on the SFCM-based ceramic anode half cells using an optical microscope at 1000x magnification or less, demonstrating the robustness to red-ox cycling.

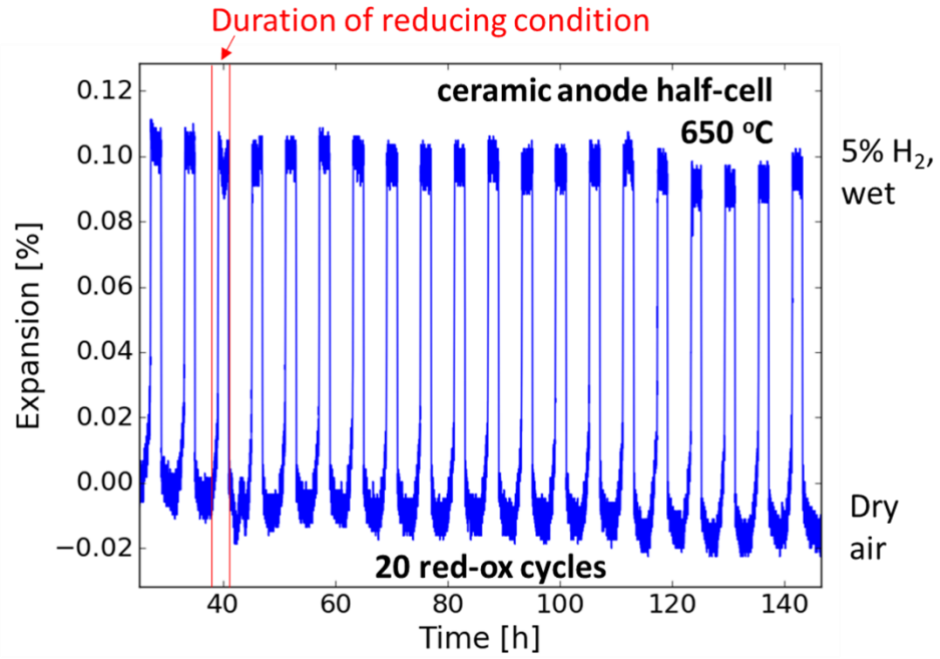

Figure 18. Isothermal linear expansion at 650 °C of the SFCM-based ceramic anode half-cell during cycling from dry air (~0% expansion) to humidified 5% H_2 balance N_2 (~0.1% expansion) every three hours for humidified 5% H_2 and dry air.

We also investigated changes in dilation and conductivity during red-ox cycles when catalyst was infiltrated into the ceramic anode of SFCM-based half cells as shown in **Figure 19** through **Figure 22**. The half cells were tested using various gas conditions (e.g., cycling between air and different concentrations of hydrogen, as well as CH_4) and at different temperatures from ~600-700 °C.

As seen in **Figure 19** and **Figure 20** for 600 °C, dilation and conductivity were largely reproducible between cycling between dry air and humidified (~2.7% H_2O) 5% H_2 (balance N_2) or 100% H_2, respectively. The data is highly reproducible (except for some long-term drift in dilatometry), indicating red-ox stability of the SFCM-based half cells. Consistent with the results in **Figure 18**, the sample expanded upon exposure to reducing conditions while conductivity increased. As described previously, the conductivity dipped during the switch from oxidizing to reducing atmosphere which likely resulted from a p-type to n-type transition. The dilatometry data exhibited some relaxation (shrinkage) after the initial spike in expansion upon reduction. While the origin of this behavior is not fully understood, in both the 5% and 100% H_2 cases at 600 °C, no cracking or other obvious mechanical damage was observed in the post-tested samples (as shown by optical microscopy of the surface in **Figure 23**).

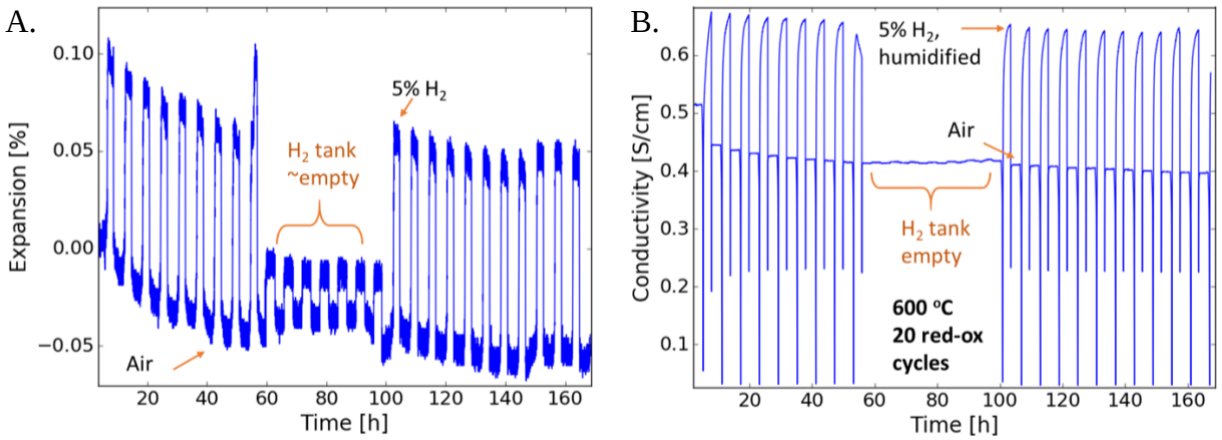

Figure 19. Chemical expansion and electrical behavior of an infiltrated SFCM-based ceramic anode half-cell at 600 °C with red-ox cycling between air and humidified 5% H_2 (balance N_2), showing A) dilation and B) conductivity.

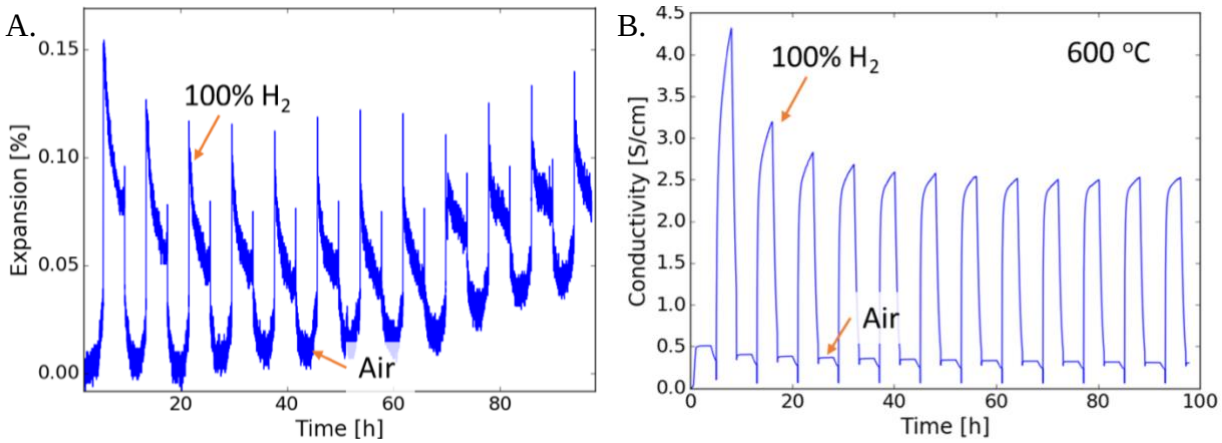

Figure 20. Chemical expansion and electrical behavior of an infiltrated SFCM-based ceramic anode half-cell at 600 °C with red-ox cycling between air and humidified 100% H_2, showing A) dilation and B) conductivity.

Figure 21 shows the dilation and conductivity measured in humidified pure (100%) H_2 at 700 °C. As with the data above, the conductivity and expansion were largely reproducible over the >20 cycles, though conductivity showed a slight decrease during the first ~5 cycles. However, the sample in post-test analysis exhibited cracks in the electrolyte, as shown in **Figure 23**. At higher temperatures, the sample will be more easily reduced due to the thermally activated nature of reduction. Therefore, a larger chemical expansion was expected and was indeed observed (~0.15% at 700 °C versus ~0.1% at 600 °C). The conductivity also increased at higher temperature in 100% H_2, also consistent with a higher number of charge carriers. The evidence of cracking suggests that

SFCM-based ceramic anode cells may not yield sufficient red-ox cycling robustness at operation temperatures ≥ 700 °C. The target operating temperature for this project was ~600 °C, where red-ox cycling of half-cells is stable, and therefore despite the observed mechanical issues at 700 °C, the initial cell design met the criteria for operation at the target temperature.

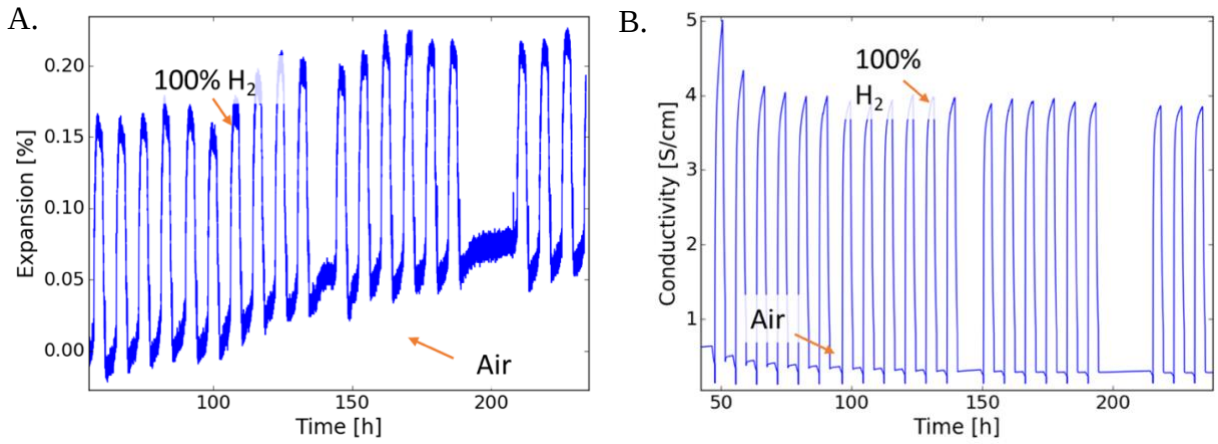

Figure 21. Chemical expansion and electrical behavior of an infiltrated SFCM-based ceramic anode half-cell at 700 °C with red-ox cycling between air and humidified 100% H_2, showing A) dilation and B) conductivity.

Figure 22 shows the dilation and conductivity measured at 600 °C in humidified 100% CH_4. Chemical expansion was highly reproducible after the first cycle. As expected, the conductivity increased upon exposure to reducing conditions. However, the conductivity increased to much higher-than-expected values (~10 times the value in H_2) even though the reduction potential of CH_4 is expected to be only slightly greater than H_2. Post-test analysis of the sample did not reveal any cracking of the samples, as shown in **Figure 23**. The large conductivity may arise from the formation of carbon in the sample, particularly deposition on infiltrated Ni-based catalyst. After oxidation, the carbon is burned away, and another reduction step leads to re-deposition. There was evidence of carbon formation after test at the bottom of the furnace tube, under the sample. A large part of this coke could have come from electrical leads, which had obvious coke formation on them, but some portion may have also come from the sample. However, note that in past long-term testing of SFCM-based SOFCs with CH_4 fuel (see **Figure 6**), coking was not observed. Despite the evidence for coking in this test, the sample did not fracture, indicating the extent of coking is minimal and the SFCM-based ceramic anode is mechanically tolerant to some degree of

coking. Regardless, in an operating system, the steam to carbon ratio will be much higher and any coking tendency will be suppressed.

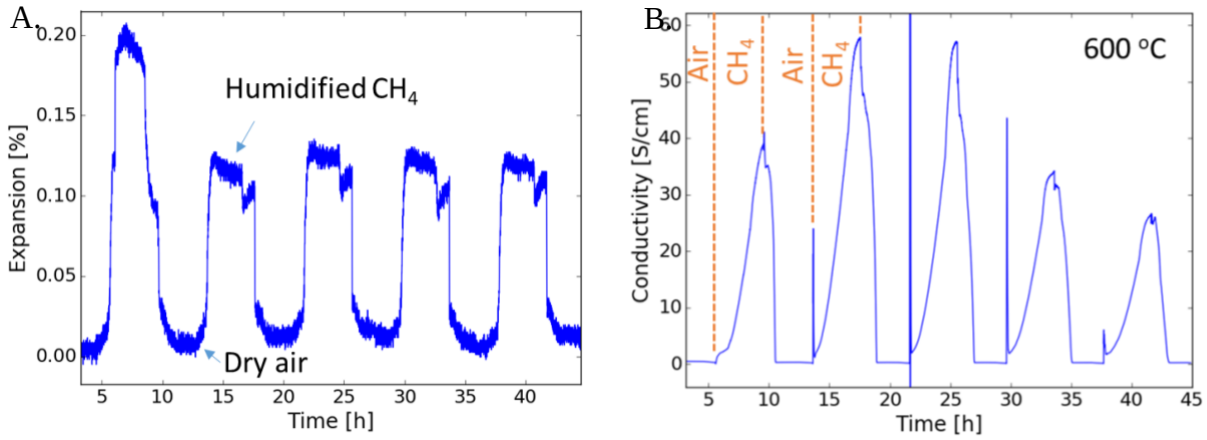

Figure 22. Chemical expansion and electrical behavior of an infiltrated SFCM-based ceramic anode half-cell at 600 °C under air and humidified pure CH_4 red-ox cycling, showing A) dilation and B) conductivity.

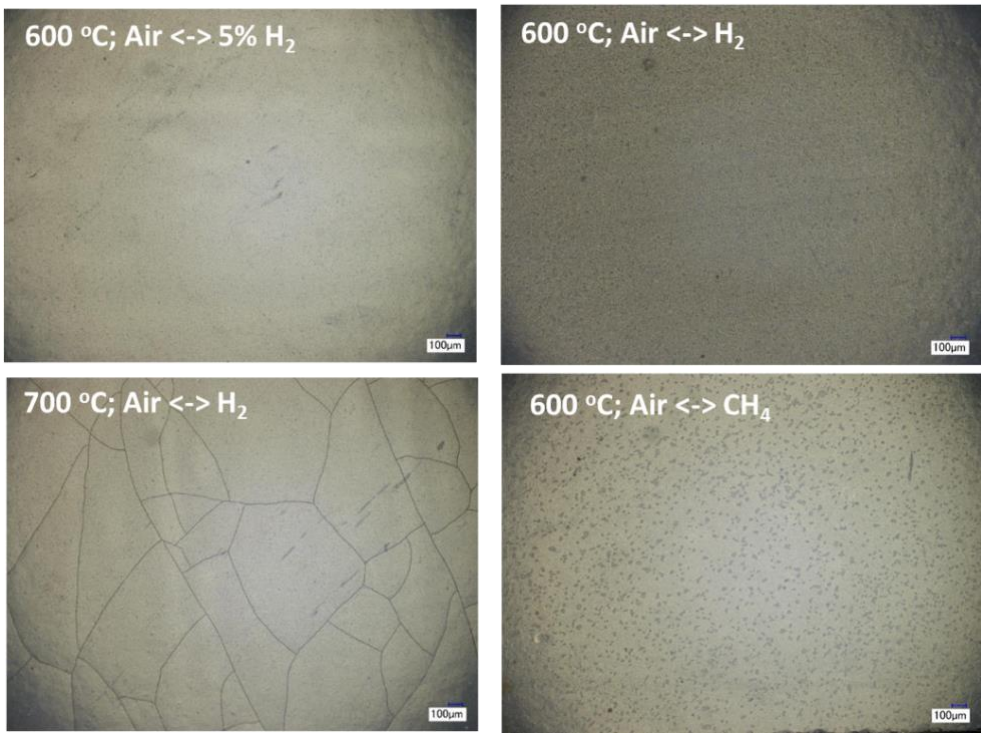

Figure 23. Electrolyte surface of post-tested red-ox cycled samples at 100x magnification, where only the 700 °C sample exhibited evidence (cracking) of red-ox cycling damage — spots or rough surfaces appear in the images on the right side, which is believed to arise from manufacturing related defects rather than red-ox cycling.

Mass loss was measured during red-ox cycles for SFCM, SFCM-GDC, and Ni-GDC samples using a thermogravimetric analyzer (TGA, Cahn D200 microbalance) with samples placed in a crucible suspended from a platinum wire inside an alumina tube enclosed in a temperature-controlled furnace. As seen in **Figure 24**A, when cycling between 50 sccm humidified (3% H_2O) reducing conditions (3% H_2, balance N_2) and 50 sccm 21% O_2 mixed with a balance of dry N_2 (oxidizing conditions), the mass change was less than 1%. Moreover, the behavior was very repeatable over 7 red-ox cycles. The oxidation step was relatively fast and took ~1 hour, while reduction took ~5 hours to complete. Even as a composite with GDC, SFCM-GDC only experienced a less than 1% change in mass (**Figure 24**B) and reached equilibrium in less than 2 hours. This is much less than a composite of NiO-GDC, which experienced ~87.5% mass loss as NiO reduced to Ni metal over the course of more than 30 hours.

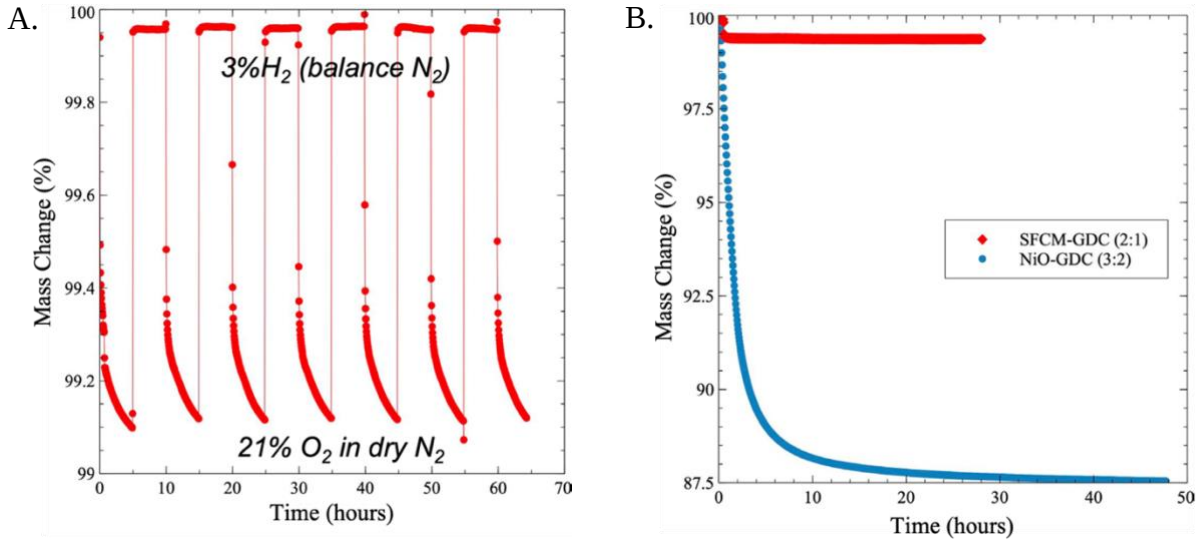

Figure 24. Change in mass (%) versus time measured using thermogravimetric analysis (TGA) for A) SFCM during red-ox cycles between humidified 3%H_2 (N_2 balance) and 21% O_2 in dry N_2 at 600 °C; and B) SFCM-GDC and NiO-GDC composites during reduction in humidified 3%H_2 (N_2 balance) at 650 °C.

4.3. Mechanical Strength of SFCM-Based SOFCs

Redox prepared sample sets of two different ceramic anode bar samples that were cut from large half-cells (IDs: B39C2 and C3-19) for evaluation of mechanical strength. Data for the stress at failure are shown in **Figure 25**. The non-overlapping t-test metrics indicate a significant difference between the two sample datasets. The dataset for sample C3-19 is a relatively lower porosity anode

support that yields testable cells, while that for sample B39C2 is for a different composite that showed very poor sintering characteristics and higher porosity (hence the lower strength). To aid in identifying sources of variation in the data, optical profilometry (Keyence VR-3200 Macroscope) was used evaluated the flatness of the samples. Samples that were at the extremes of the failure stresses (i.e., high or low failure stress) are indicated in **Figure 26**. For the low strength samples (B39C2), the flatter sample appears to have the highest strength. For the higher strength sample set (C3-19), there is no clear correlation of failure stress with profilometry.

A.

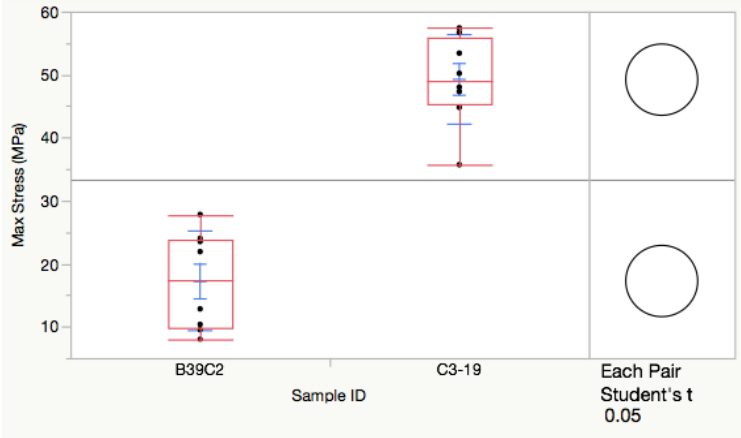

Means and Std Deviations

Level	Number	Mean	Std Dev	Std Err Mean	Lower 95%	Upper 95%
B39C2	8	17.2313	7.84412	2.7733	10.673	23.789
C3-19	8	49.1875	7.05882	2.4957	43.286	55.089

B.

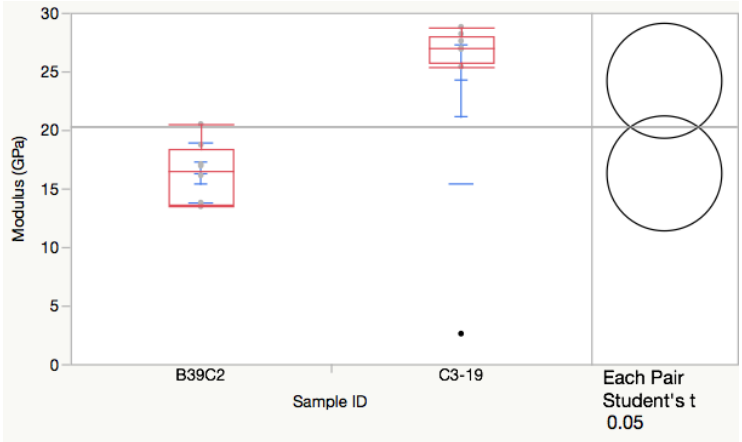

Means and Std Deviations

Level	Number	Mean	Std Dev	Std Err Mean	Lower 95%	Upper 95%
B39C2	8	16.2800	2.57209	0.9094	14.130	18.430
C3-19	8	24.1875	8.78057	3.1044	16.847	31.528

Figure 25. A) Maximum stress at failure and B) modulus for 4-point test bend bars of SFCM-based ceramic anode half-cells.

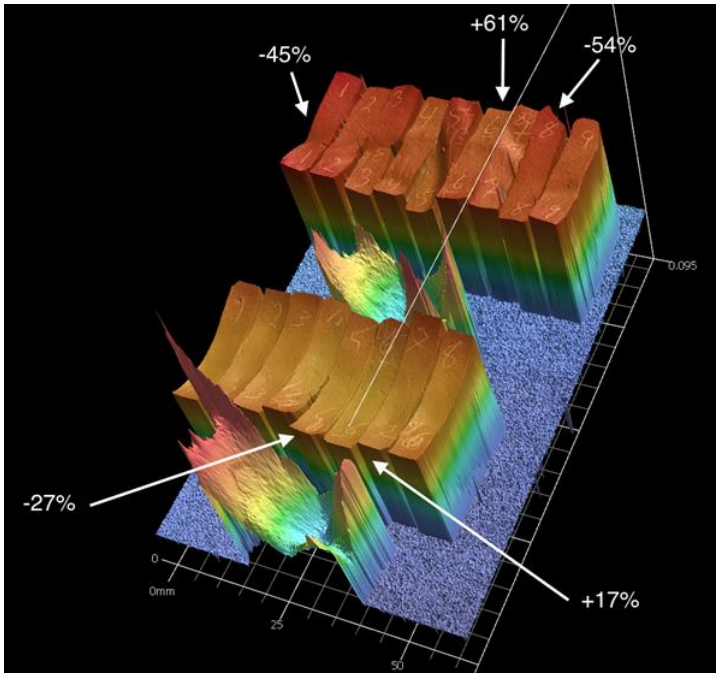

Figure 26. Optical profilometry of multiple bend bar samples placed adjacent to each other, magnified 1000x in the z-direction. The top row corresponds to the B39C2 samples, while the bottom row shows the C3-19 samples (see **Figure 25**). Note the large, noisy peaks shown at the bottom of each group of samples are caused by magnification of sample labeling and is not due to the samples themselves. Relative failure stresses are as indicated.

Fracture toughness was also evaluated. Bend bars of the dense SFCM-based ceramic anode single phase material were fabricated and tested under 4-point bending. The samples were chevron notched, consistent with ASTM standards for fracture toughness measurements. A typical fracture, showing the chevron notch, is shown in **Figure 27**. The measured fracture toughness of five samples was determined to be 1.11 MPa√m with a standard deviation of 0.04 MPa√m. This measurement is in the typical range for ceramics of this type and the loading profile exhibited the expected behavior for fracture toughness (i.e., stable crack extension through the maximum load, as the force peaks, then a slight decrease before dropping to zero). The fracture surfaces showed no undesired flaws in the chevron notch.

Figure 27. Fracture surface of single-phase dense SFCM bar, showing the notched areas (bottom left and right triangle features) and the region fractured during the test (i.e., top triangle area).

The fracture toughness was also evaluated at elevated temperature in-situ and found to decrease from 1.11 MPa√m at room temperature to 0.8 and 0.95 MPa√m at 400 °C and 600 °C, respectively. These values of fracture toughness are similar to other ceramics and glasses, though they are low in comparison with structural ceramics, such as alumina and silicon nitride (~5 MPa√m). A summary of the fracture toughness results is shown in **Figure 28**. Compared to room temperature, there is a decrease in fracture toughness at both 400 °C and 600 °C. This result suggests that a crack may propagate more easily through SFCM at elevated temperature than at room temperature. This is the opposite trend seen with strength, which relies on the microstructure due to the closing of cracks with thermal expansion. The decrease in fracture toughness is likely due to the added energy, allowing for the easier breakage of grains and boundaries.

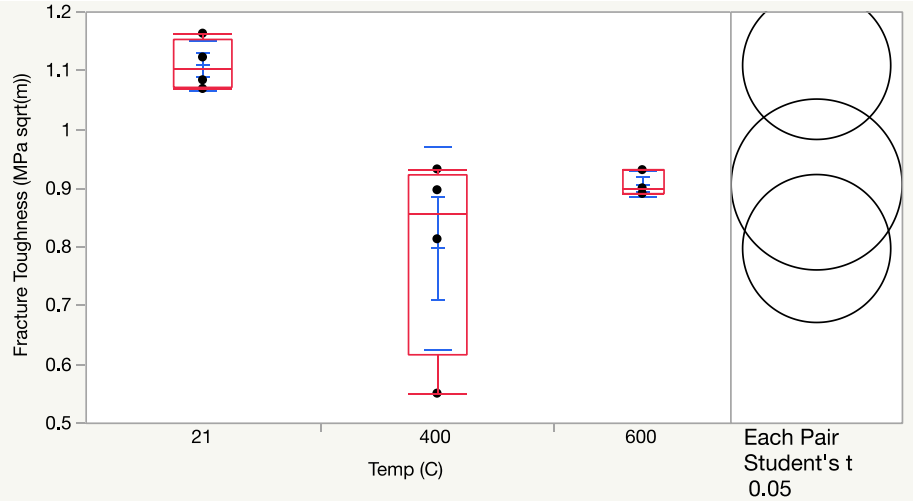

Figure 28. Fracture toughness of SFCM at room temperature (21 °C), 400 °C, and 600 °C.

The effect of red-ox cycling on mechanical strength and modulus of SFCM-GDC anode layers was also investigated. Samples were red-ox cycled at elevated temperature (~600 °C) 10 times before mechanical characterization at room temperature. As shown in **Figure 29**, fresh SFCM-GDC (0 red-ox cycles) had a strength of 34.3±7.2 MPa and modulus of 24.5±5.0 GPa. The red-ox cycled samples, on the other hand, had a strength of 22.4±4.9 MPa and modulus of 27.3±3.6 GPa. The Student's t-test results suggest no discernable difference in the modulus after cycling, but show that the samples weakened in strength after 10 red-ox cycles. SFCM-GDC based cells were found to tolerate cycling well because of phase stability but weaken from 34.3 to 22.4 MPa due to uniform growth of critical microstructural flaws.

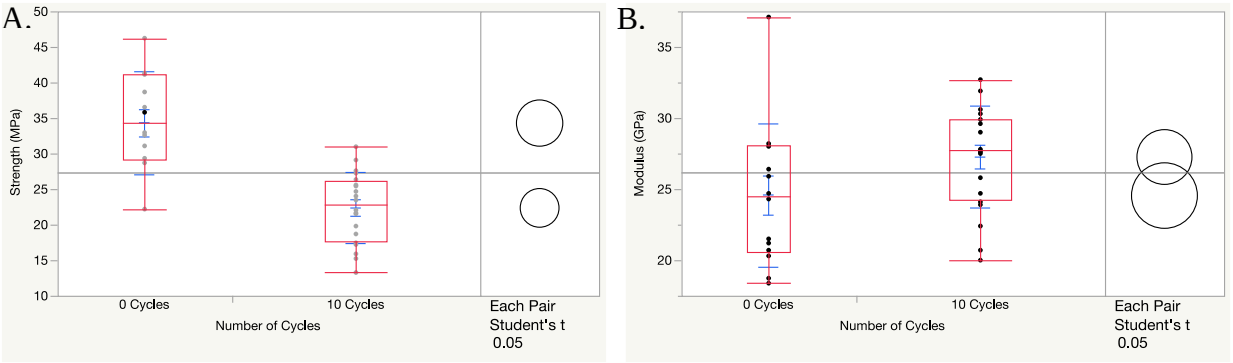

Figure 29. The impact of red-ox cycling on A) strength and B) modulus of an SFCM-GDC anode.

As shown in Section 4.2, the degree of chemical expansion of the SFCM-based ceramic anode cells is much less than that of a Ni-cermet cell (e.g., see **Figure 17**, **Figure 19**, and [15-16]). The SFCM-based ceramic anode half cells, however, have a mechanical strength that is about 4-10 times lower than Ni-YSZ cermet half cells [51]. Therefore, even the relatively small increase in chemical expansion observed for SFCM at 700 °C (see **Figure 20**, **Figure 21**, and **Figure 23**) combined with the relatively lower mechanical strength of the SFCM-based cells practically limits the operating temperature of the SOFC cells to below ~650 °C. These results also highlight the importance of finding ways to increase the mechanical strength of cells made using SFCM (while maintaining a high degree of porosity for catalyst infiltration) and/or decreasing the mechanical stress imparted to such cells when assembling and operating stacks.

4.4. SFCM-Based SOFC Electrochemical Performance and Red-Ox Robustness

The cell performance goals of this project included scaling up SFCM-based ceramic anode SOFCs

to large format size (e.g., 5 cm by 5 cm or 10 cm by 10 cm) with a high cell performance (e.g., ~0.75 W/cm^2 at 0.75 V) at ~600 °C. Moreover, the cells need to be capable of operation with hydrogen or reformed pipeline natural gas and robust to red-ox cycling (e.g., ≥ 20 red-ox cycles) based on anticipated red-ox cycle events due to gas outages for instance.

SFCM has relatively low-catalytic activity and therefore is not prone to coking in the presence of a hydrocarbon fuel. To boost catalytic and electro-catalytic activity for hydrocarbon reforming, a surface modification process is used to achieve a higher catalytic activity in the anode. The surface coating may consist of discrete particles, or a continuous thin film. These modifications can serve as a new functional layer, effectively utilizing the unique properties of ceramic anode substrate and coated catalysts and thus offering multi-functionality [52]. Unique morphology and microstructure through surface modification can not only bring in higher electrochemical catalytic property but also present excellent sulfur tolerance [53-54].

Infiltration of the SFCM-based ceramic anode with Ni and GDC based catalysts has been shown to lower the cell area-specific-resistance (ASR), leading to an increase in cell voltage for a given current. Infiltrates are added typically using a solvent-based approach to fill pores with metal catalyst solute after the cell has been fabricated with a cathode to avoid high temperature sintering of the infiltrate and to maintain high surface area catalyst structures. A low temperature burnout creates nano-sized particles of the metal catalyst dispersed on the surface of the porous anode which increase active surface area in addition to adding a catalyst. However, due to the small size of the catalyst, there is the possibility the catalyst particles may grow when exposed to elevated temperature during SOFC operation. Performance was therefore explored at the button cell level with respect to catalyst infiltration. The catalyst morphology was observed and correlated with any degradation of the cells as the best feedback to further optimize the entire infiltration process including the substrate microstructure, materials composition, solution concentration, and thermal treatment.

Ultimately, the shift was made toward exclusive performance optimization of large format SFCM-based ceramic anode SOFC. At various points during the performance optimization of the large format cells, we modified the cell architecture (e.g., see **Figure 8**) and processing conditions (e.g.,

see Section 6) to adjust various parameters, including the shrinkage of the different half-cell layers during sintering, porosity, and strength.

Performance of Button Cells. The growth of Ni-GDC catalyst particles during long-term operation of SFCM-based ceramic anode SOFC button cells was evaluated and correlated with electrochemical performance results. The performance of three cells were compared in both humidified hydrogen and a humidified mixture of H_2/CH_4 (5:1) between 550 °C and 650 °C. Each cell had an approximately 400 μm porous SFCM-GDC anode, 20 μm dense GDC electrolyte, 12 μm Co-GDC CFL, and a 15 μm SSC-GDC cathode. The button cells were sealed to alumina tube reactor using ceramic cement using silver current collectors. The first cell (#BC1) had a Ni-to-GDC infiltrate ratio of 1:10, whereas the second cell (#BC2) had an infiltrate ratio of 5:10. The third cell (#BC3) had only Ni infiltrate (i.e., no GDC). The catalyst loading was ~5 wt% in each cell. The performance of cell #BC1 is shown in **Figure 30** between 550 °C and 650 °C in both humidified H_2 and a mixture of H_2/CH_4. Total ASR near OCV was around 0.18 Ω-cm^2 (0.23 Ω-cm^2), 0.32 Ω-cm^2 (0.41 Ω-cm^2), 0.67 Ω-cm^2 (0.84 Ω-cm^2) in H_2 (H_2/CH_4) at 650 °C, 600 °C, and 550 °C, respectively. The lower performance in the H_2/CH_4 mixture versus in humidified hydrogen may have resulted from the relatively low infiltrate catalyst loading (~5 wt%).

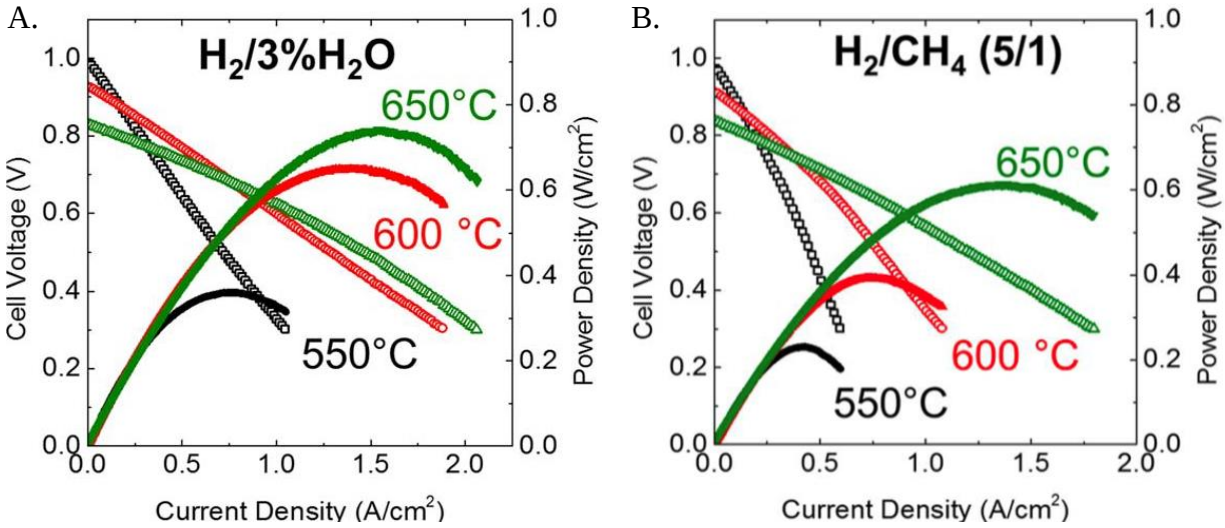

Figure 30. Current-voltage-power density characteristics for an SFCM-based ceramic anode button cell with a Ni-to-GDC infiltrate ratio of 1:10, operated between 550-650 °C in A) humidified hydrogen and B) a humidified H_2/CH_4 mixture (5:1).

The three types of button cells were compared to each other while being held at a constant current of 0.2 A/cm^2 in the humidified H_2/CH_4 mixture at 600 °C. As shown in **Figure 31**, the cells each displayed different initial performance (e.g., current-power density characteristics and impedance spectra). Moreover, the cells also had differences in stability over time from 0-200 hours of operation. Cell #BC3 had the highest initial OCV and power density (**Figure 31**E) due to the higher catalytic activity associated with the relatively high catalyst loading of Ni (i.e., no GDC infiltrate was used). Comparing **Figure 31**B and **Figure 31**F, button cells #BC1 and #BC3 had similar initial non-Ohmic ASRs (~0.12 Ω-cm^2), but cell #BC1 had a lower OCV (**Figure 31**A). Button cell #BC3 also had the highest degree of degradation with a decrease in OCV and an increase in ASR (**Figure 31**E and **Figure 31**F). Button cell #BC1 had almost no change in OCV over the 200 hours (**Figure 31**A), whereas cell #BC2 experienced a small decrease in OCV (**Figure 31**C). Button cell #BC3 also had the largest initial non-Ohmic ASR and showed the greatest increase in ASR over the 200 hours (**Figure 31**D). However, due to the mostly stable OCV during the test, button cell #BC2 ended up with a slightly higher peak power density than cell #BC3. The total ASR initially was ~0.47 Ω-cm^2, ~0.48 Ω-cm^2, and 0.33 Ω-cm^2 for #BC1, #BC2, and #BC3, respectively. After 200 hours of operation at 0.2 A/cm2, the total ASR had increased to 0.54 Ω-cm^2, 0.56 Ω-cm^2, and 0.48 Ω-cm^2.

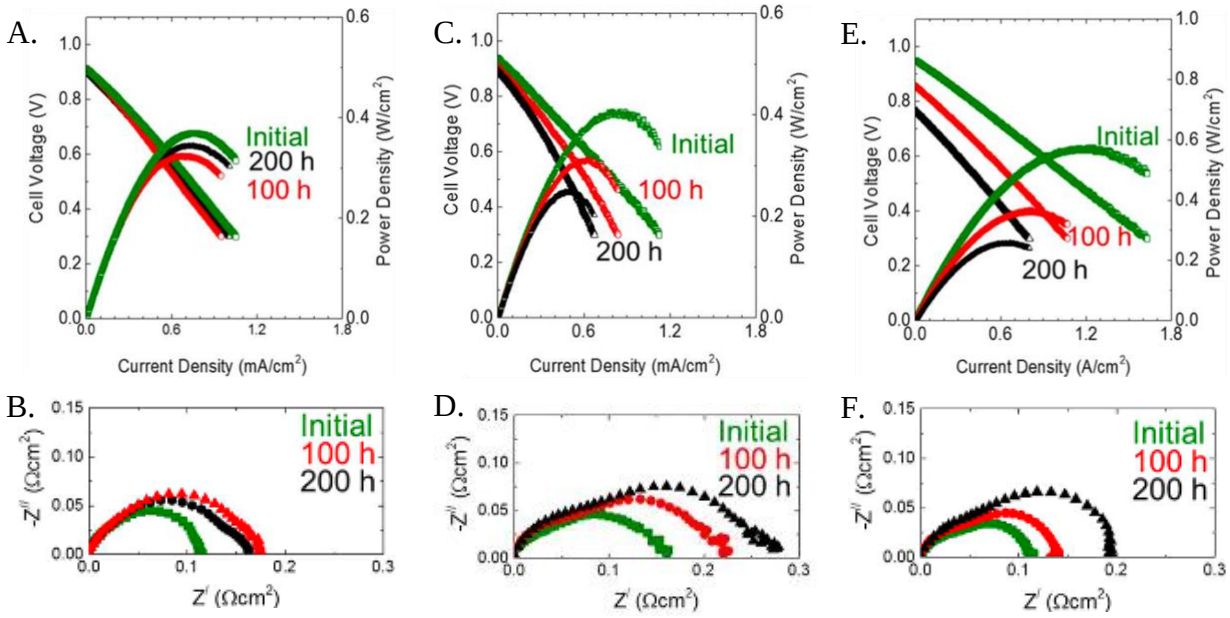

Figure 31. Button cell results for SFCM-based ceramic anode SOFC with different infiltration compositions (total Ni content < 5 wt%) for time at 0 hours (green), 100 hours (red), and 200 hours (black) of operation in a humidified H_2/CH_4 mixture (5:1) at 600 °C, showing A) cell voltage and power density versus current density characteristic and B) non-Ohmic impedance spectra for a cell with a Ni-to-GDC infiltrate ratio of 1:10; C) cell voltage and power density versus current density characteristic and D) non-Ohmic impedance spectra for a cell with a Ni-to-GDC infiltrate ratio of 5:10; and C) cell voltage and power density versus current density characteristic and D) non-Ohmic impedance spectra for a cell with 100% Ni infiltrate.

Figure 32 summarizes the results of the three different Ni-GDC infiltrate compositions that were investigated with the SFCM-based ceramic anode button cells. Comparing the operating voltage versus time (fixed current density of 0.2 A/cm^2 in humidified H_2/CH_4 at 600 °C) in **Figure 32**A and **Figure 32**C, infiltrate composition #1 (i.e., #BC1) resulted in a lower initial operating voltage (~0.8 V) than composition #3 (~0.85 V), but after 200 hours button cell #BC1 retained its original voltage while button cell #BC3 dropped below ~0.7. Additionally comparing the initial and final particle sizes of the infiltrate (**Figure 32**D) shows that the large drop in voltage with time for button cell #BC3 correlates with a significant growth in Ni particle size, while particle size remained constant for button cell #BC1. The GDC is believed to prevent the coarsening and agglomeration of the Ni infiltrate. This effect was less apparent in button cell #BC2 which had more Ni infiltrate and less GDC infiltrate than button cell #BC1. This is because button cell #BC2 shows a large

growth in Ni particle size after the 200 hour test (e.g., comparing the initial SEM micrograph in **Figure 32**E with in **Figure 32**F).

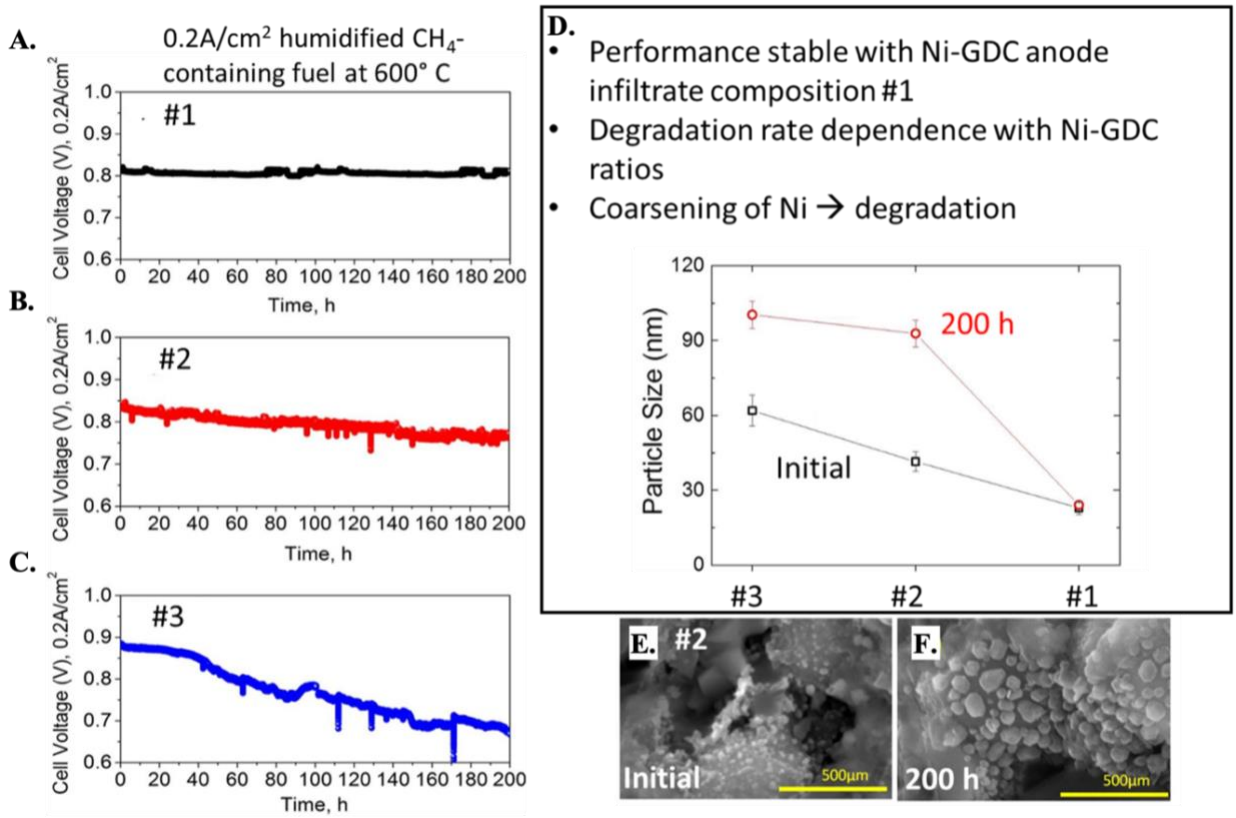

Figure 32. Summary of results for infiltrated button cells operated for 200 hours at a fixed current density of 0.2 A/cm^2 in humidified H_2/CH_4 at 600 °C showing cell voltage versus time for A) button cell #BC1 (1:10 Ni-to-GDC infiltrate), B) button cell #BC2 (5:10 Ni-to-GDC infiltrate), and C) button cell #BC3 (Ni only infiltrate); D) particle size before and after measurement for the different Ni-GDC ratios; and the corresponding morphology change of Ni in cell #BC2 E) before and F) after the 200 hour test.

Different button cells (#BC4 and BC#5) were prepared used to investigate the red-ox cycling stability of the SFCM anode. **Figure 33** shows the cell voltage of an SFCM-based ceramic anode button cell (#BC4) at 600 °C with a fixed current density of 0.1 A/cm^2. This cell had ~6 wt% of Ni and GDC infiltrate. Note, the cell was under load only while in the reduced state (i.e., with humidified hydrogen flowing). During the oxidizing state, dry air was flowing. The operating voltage at 0.1 A/cm^2 was very stable over the 20 cycles. Exposure time to each gas was approximately 5 minutes, though there were a few instances where the intervals were up to 1-2 hours. This result demonstrates good red-ox stability for the SFCM-based ceramic anode.

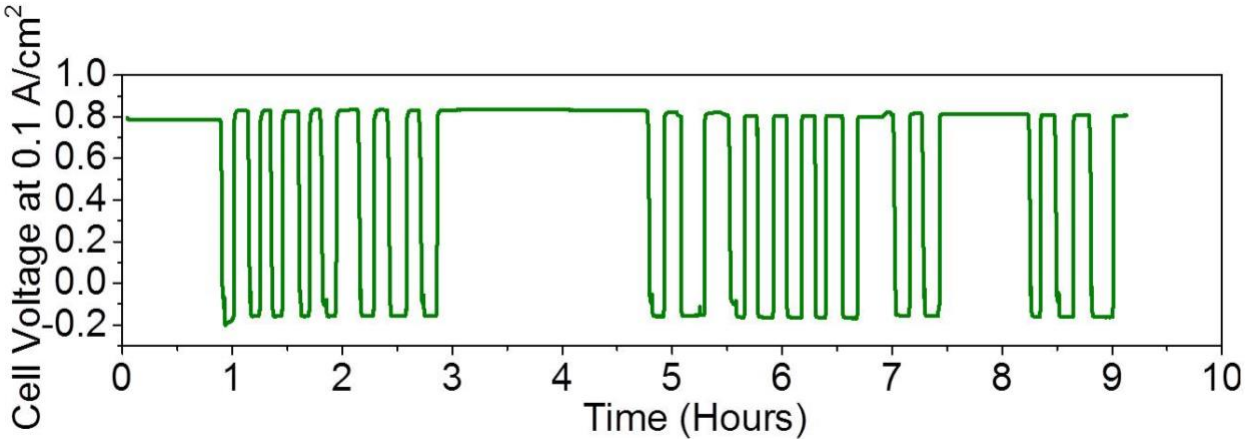

Figure 33. Cell voltage of an SFCM-based ceramic anode button cell (#BC4) at a fixed current of 0.1 A/cm^2 (while in the reduced state) during red-ox cycling between humid H_2 and dry air at 600 °C.

A different SFCM-based ceramic anode button cell (#BC5) was tested at 600 °C and underwent red-ox cycles switching between hydrogen and industrial nitrogen. This cell had 10 wt% of Ni and GDC infiltrate. While in the reduced state (hydrogen flowing), the cell was held constant at 0.2 A/cm^2. The cell microstructure before (as prepared) and after 30 cycles is shown in **Figure 34**A and **Figure 34**B, respectively. No obvious changes in microstructure can be seen after red-ox cycles. Similarly, the cell operating voltage under 0.2 A/cm^2 (when in the reduced state with hydrogen flowing) is essentially unchanged during the 30 red-ox cycles as shown in **Figure 34**C. **Figure 34**D compares cell voltage and power density versus current density for every 5 red-ox cycles (from the 10th cycle to the 30th cycle).

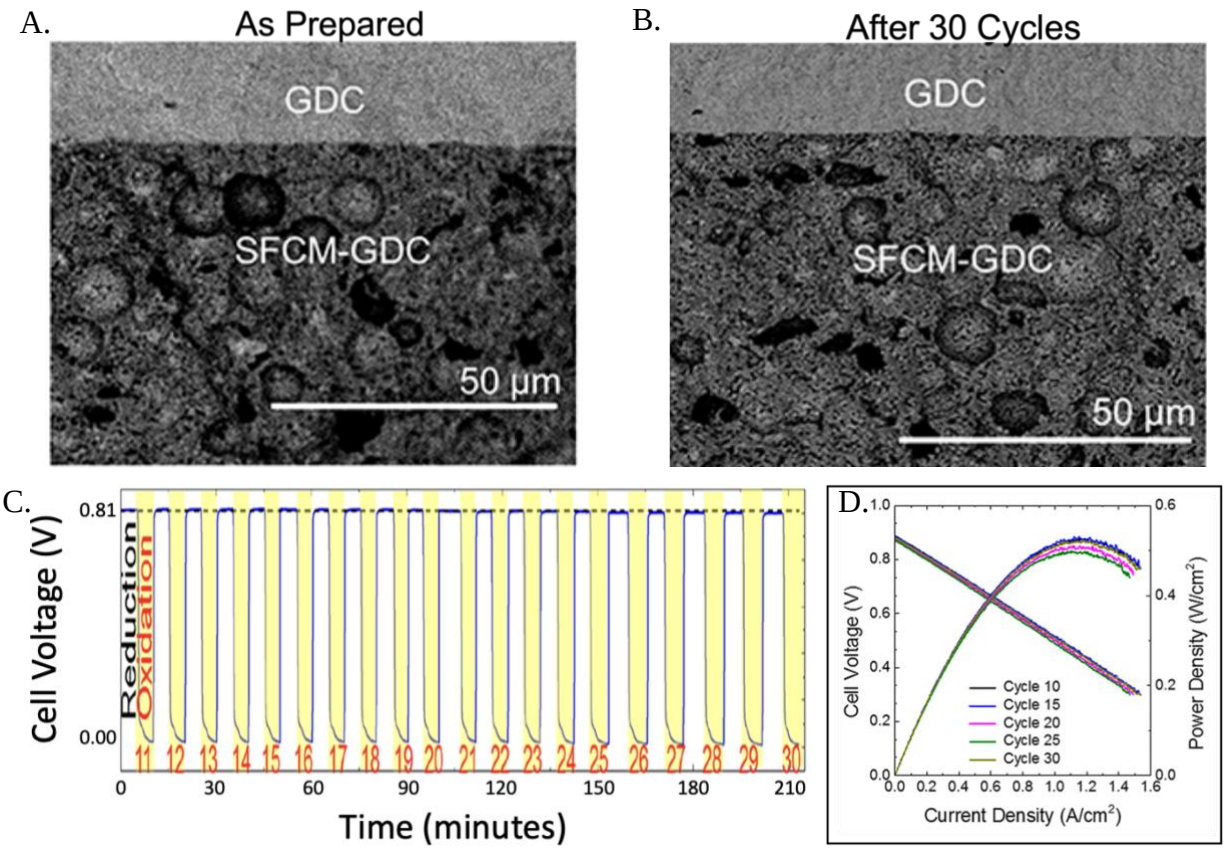

Figure 34. Red-ox stability of SFCM-based ceramic anode button cell (#BC5) tested at 600 °C showing A) as prepared microstructure, B) microstructure after 30 red-ox cycles (between humid H_2 and dry N_2), C) cell voltage versus time during and after each red-ox cycle (constant 0.2 A/cm^2 when in the reduced state), and D) cell current-voltage-power density characteristic comparison for increasing number of red-ox cycles.

While electrochemical performance and red-ox robustness with button cells was very encouraging for the SFCM-based ceramic anode SOFCs, the stresses experienced in a stack and difficulties associated with scaling up the size of large format cells (e.g., 5 cm by 5 cm to 10 cm by 10 cm) are non-trivial and required much optimization.

Improved Performance for Large Format Cells. Much of the work in this project involved optimizing the electrochemical performance (e.g., higher power density) of the SFCM-based ceramic anode SOFCs, while also maintaining/improving the red-ox cycling robustness and general stability of the cells. Moreover, this work was done at Redox primarily while scaling the size to a large format size (i.e., 5 cm by 5 cm to 10 cm by 10 cm). Note that while the performance of the large format cells is tied to the fabrication process and is discussed in part with respect to

the cell performance results, most of the processing details and fabrication challenges related to scaling up the cell size are discussed in **Section 6.1**.

To explore the red-ox stability of the large format SFCM-based ceramic SOFC, we cycled the anode of an operating cell using dry H_2 and industrial N_2 (< 1% O_2), as well as with air. The cell architecture was that of **Figure 8**A, but this cell did not have the cathode functional layer (CFL) and had a relatively low anode porosity as a tradeoff for increased mechanical strength. No pore former was used in the anode of this cell and the cell was fired toward the higher end of fabrication temperatures for the SFCM-based ceramic anode cells. The porosity of the fabricated cell was determined to be ~20 vol% by the Archimedes method. The cell was tested for over 400 hours and included periods at open circuit voltage, constant current, and red-ox cycling as shown in **Figure 35**. Taking into account small fluctuations in the test kiln temperature, the OCV was mostly constant during the entire test, including during red-ox cycling.

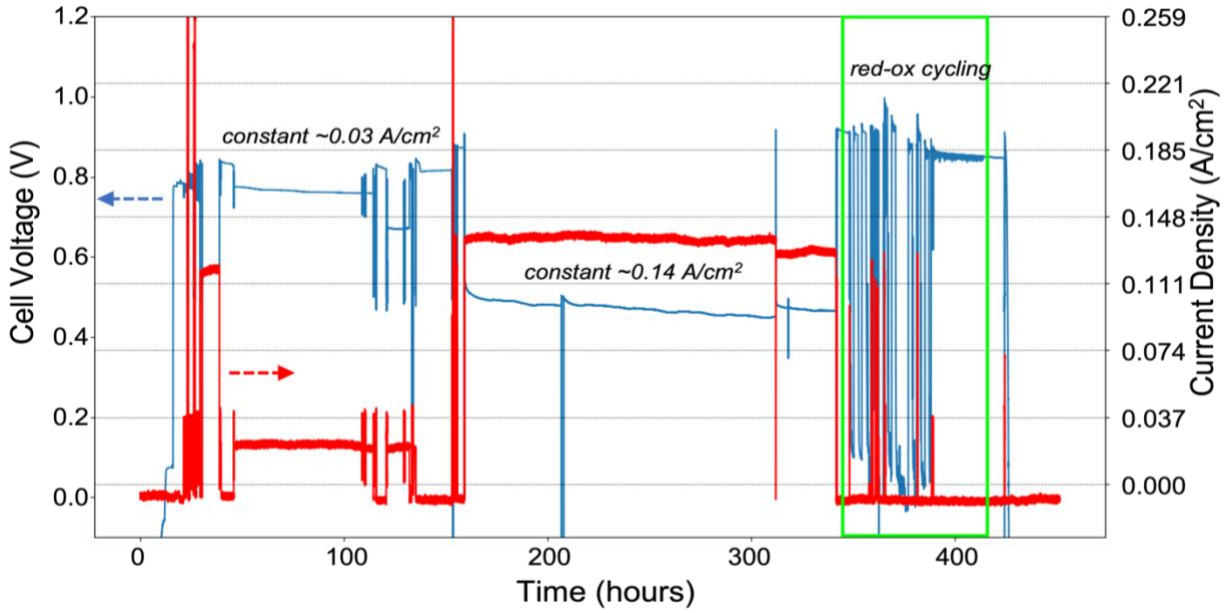

Figure 35. Cell voltage and current density versus time for full test of 5 cm by 5 cm (low-porosity) SFCM-based ceramic anode cell including periods with constant current and red-ox cycling between dry H_2 and industrial N_2 (< 1% O_2) or air at 550 °C.

The cell voltage and current density measured during red-ox cycling between H_2 and industrial N_2 at 550 °C is shown in **Figure 36**. The voltage starts off at ~0.9 V in H_2, then as soon as N_2 is introduced, it drops to ~0.1 V. After cycling back to H_2, the voltage rises initially higher than the

original value, but eventually levels off to the original value. Note that soon after entering oxidation during the 3rd red-ox cycle, the voltage measurement equipment experienced a fault leading to some artificial spikes in the voltage data. The cell voltage response to the same current density loads is very similar throughout the entire test. Note, that the cathode exhaust temperature was approximately 1 °C lower in the oxidizing environment compared to the reducing environment. The reproducibility of these results further indicates good red-ox stability of the SFCM-based ceramic anode.

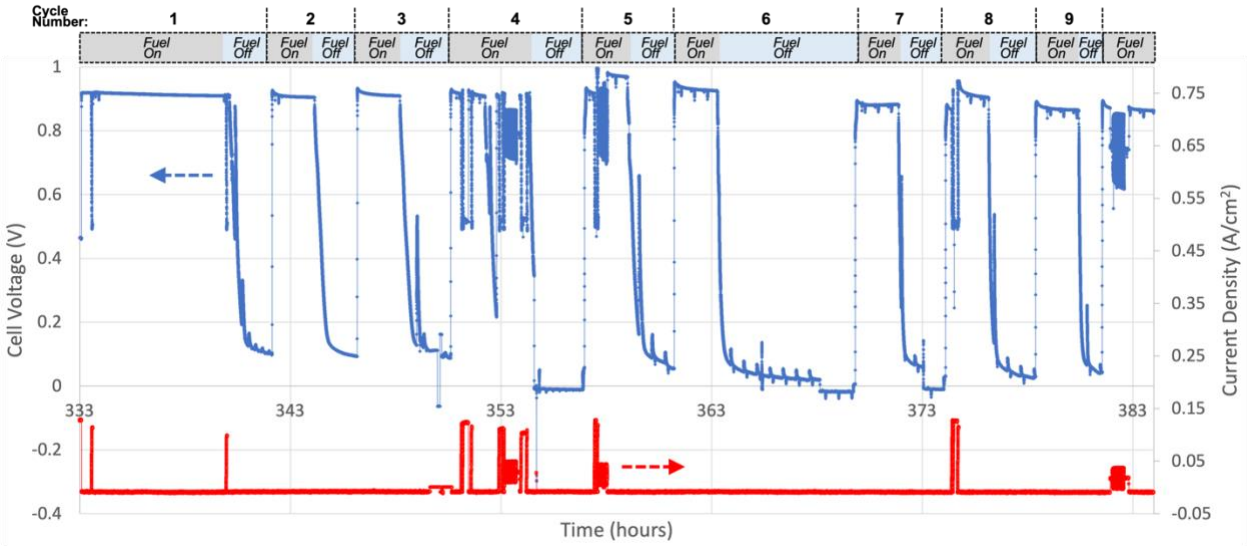

Figure 36. Cell voltage at open circuit conditions of a 5 cm by 5 cm (low-porosity) SFCM-based ceramic anode cell versus test time during nine red-ox cycles switching between dry H_2 and industrial N_2 feed (< 1% O_2) at 550 °C.

A more detailed assessment of the voltage response reveals that the cell voltage and power density versus current density characteristics are nearly identical prior to red-ox cycling (**Figure 37**A) and even after the 3rd cycle (**Figure 37**B). As expected, the power density is relatively low due to lack of porosity and correspondingly low catalyst loading (~4 wt%). Due to the low porosity, the catalyst may not have deeply infiltrated the anode to reach the triple phase boundary with the electrolyte. The area-specific resistances (ASRs) extracted from these current-voltage characteristic curves for the baseline and after the 3rd red-ox cycle are ~3.5 Ω-cm^2 and ~3.2 Ω-cm^2, respectively. The power density similarly improved slightly from ~55 mW/cm^2 at ~0.1 A/cm^2 before red-ox cycles as compared to ~60 mW/cm^2 after. Therefore, there was a slight improvement

in performance with cycling within the first three cycles. In general, the OCV and ASR remained mostly unchanged across the 9 red-ox cycles (50-hour period).

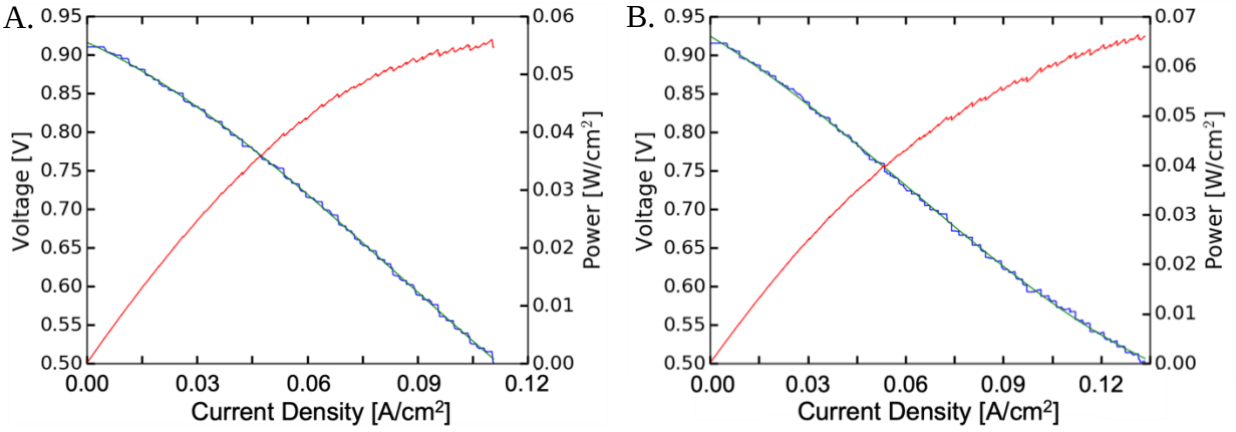

Figure 37. Cell voltage and power density versus current density A) before (cycle 0) and B) after the first three red-ox cycles for the 5 cm by 5 cm (low-porosity) SFCM-based-ceramic anode cell measured in dry H_2 at 550 °C.

The 5 cm by 5 cm (low porosity) SFCM-based ceramic anode cell was also evaluated for red-ox cycles between dry hydrogen and air at the anode side. The cell's OCV drops to zero Volts in air (**Figure 38**A), which is due to the lack of an oxygen chemical potential gradient across the electrolyte. In the case of industrial N_2 as the oxidizing state (e.g., the first three red-ox cycles in **Figure 36**), the OCV of ~0.1-0.15 V corresponds to an oxygen partial pressure of ~100-800 ppm (0.01-0.08%) O_2. During the evaluation of red-ox cycling stability of seal materials (*see Section 5.2*), we estimated that in this case there was ~0.01% to 0.02% O_2 in the industrial nitrogen using gas chromatography. Note, however that the specification for the industrial N_2 is simply < 1% O_2 and therefore the actual O_2 content can change slightly, depending on the particular gas cylinder being used during a test. The current-voltage sweep recorded after the air red-ox cycle is shown in **Figure 38**B. After the red-ox cycle in air, the open circuit voltage briefly increased substantially from ~0.9 V to ~1.0 V for a short period. Despite the ASR briefly increasing back to ~3.5 Ω-cm^2, the power density at ~0.1 A/cm^2 remained about ~60 mW/cm^2 due to the higher OCV. The cathode exhaust temperature was about twice as low during the first cycle with air (4th cycle overall) when in the oxidizing condition versus the reducing condition, which is the probable cause for the temporary increase in OCV and ASR.

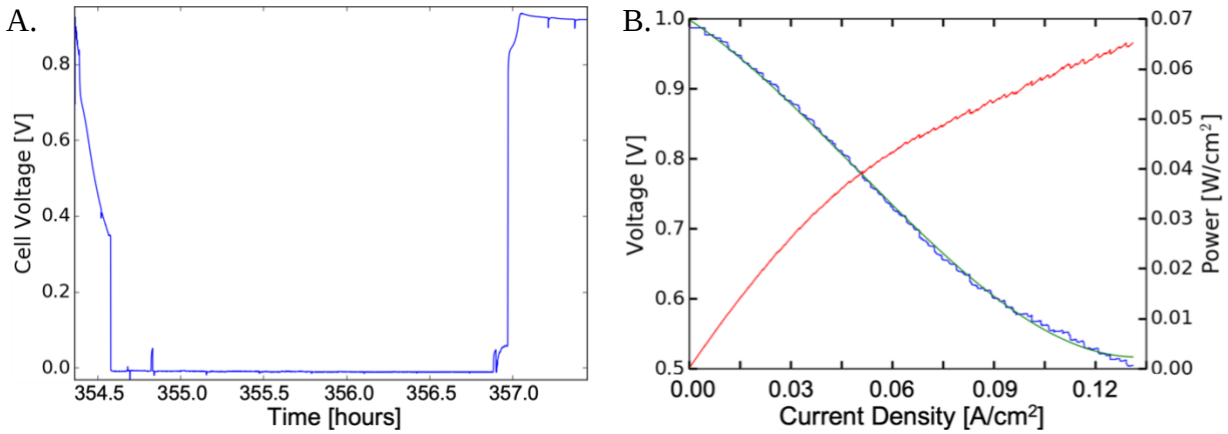

Figure 38. Exemplar result of red-ox cycling at the anode from dry H_2 to dry air at 550 °C for a 5 cm by 5 cm (low-porosity) SFCM-based ceramic anode cell, showing A) cell voltage at open circuit condition during one red-ox cycle, and B) voltage and power density versus current density after the red-ox cycle.

As shown in **Figure 35**, prior to red-ox cycling the 5 cm by 5 cm (low-porosity) SFCM-based ceramic anode cell was held at a constant current of ~0.03 A/cm^2 for ~72 hours and at ~0.14 A/cm^2 for ~155 hours. At the lower current density (~44 hours to ~116 hours), the operating voltage decayed initially at a rate of ~61.5%/1000 hours, then at 18.4%/1000 hours, and finally at ~5%/1000 hours, where the degradation rate was extrapolated linearly from the measurements. Therefore, the rate of decay plateaued over time. While at 0.14 A/cm^2 the same plateauing of the decay rate occurred, the decay rates were higher (e.g., after ~155 hours, the decay rate was still ~24%/1000 hours). Therefore, unlike with the button cells (see **Figure 6**), the large format cells seemed to experience relatively fast degradation. Moreover, this degradation was often found to be worse for higher current densities. There are multiple reasons why degradation rate might be tied to current density, including increased thermal stress at a higher current density and increased residual stress (and in general greater stress during operation) for large format cells. We therefore decided to continue with performance optimization while looking for additional signs of degradation during testing.

Following from these results, we worked to optimize the electrochemical performance of the SFCM-based ceramic anode cell, primarily through increased porosity and increased catalyst loading in the anode. Two identical 5 cm by 5 cm SFCM-based ceramic anode cells were prepared using pore former in the anode for increased porosity. The cells were also fired at a lower

temperature, which together resulted in an increased catalyst loading of ~12 wt% for each cell. These cells also included the CFL, which resulted in higher OCV and helped reduce ASR. The voltage and power density versus current density characteristic curves for cell #1 are shown in **Figure 39**A, while the measured impedance spectrum is shown in **Figure 39**B. The performance curves and impedance spectrum for cell #2 are shown in **Figure 39**C and **Figure 39**D, respectively. The OCV of cell #1 was ~0.92 V, while that of cell #2 was ~0.90 V. The power density at ~0.5 A/cm2 was approximately 0.33 W/cm^2 for cell #1 and 0.25 W/cm^2 for cell #2. Therefore, while the OCV of cell #2 was only ~2% lower than that of cell #1, the power density of cell #2 was 25% lower. The air-to-fuel crossover (via gas chromatography) was found to be ~0.2% for cell #1 and ~1.1% for cell #2. This may have part of the reason for the lower cell performance of cell #2. However, while the cell designs were identical and the cells were prepared in the same way, there may have been slight differences in the microstructure or more likely differences in mechanical strength. A third cell (#3) was prepared with an identical structure and found to have an OCV closer to cell #1, but a power density closer to cell #2 (data not shown). The total ASR at 600 °C was ~0.53 Ω-cm^2 for cell #1 and 0.80 Ω-cm^2 for cell #2. Even though the crossover was probably lower than that of cell #1 (half the relative humidity in the cathode exhaust), the total ASR for the third cell was ~0.79 Ω-cm^2. Note, even though all three cells were 5 cm by 5 cm, the cathode for the third cell was ~6 times smaller surface area than for cell #1 or cell #2. This suggests the difference in performance between the cells was not entirely due to differences in crossover leaks.

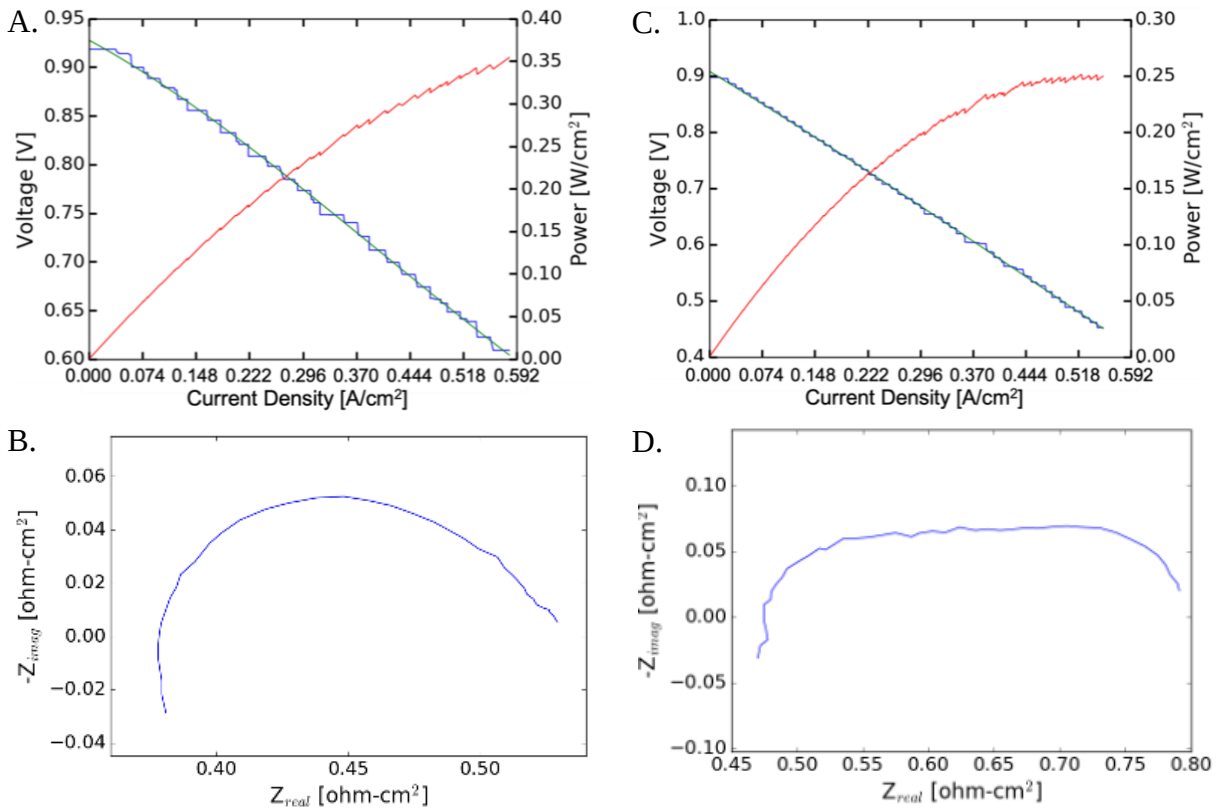

Figure 39. Performance of two identically prepared, initially optimized SFCM-based ceramic anode cells tested in dry hydrogen fuel and air at 600 °C, showing A) voltage and power density versus current density and B) impedance spectrum for cell #1; and C) voltage and power density versus current density and D) impedance spectrum for cell #2.

For better comparison with the low-porosity cell (e.g., **Figure 37** and **Figure 38**B), the performance of (initially optimized) cell #1 at 550 °C is shown in **Figure 40**. This demonstrates that cell #1 had a maximum power density that was about 4.5 times larger than the low-porosity cell. At 550 °C, cell #1 had an ASR of ~1.9 Ω-cm^2 at 550 °C, or about 50% lower than the low-porosity cell. The higher maximum power density of cell #1 was also a result of the relatively high OCV, which was about 12% higher than that of the low-porosity cell.

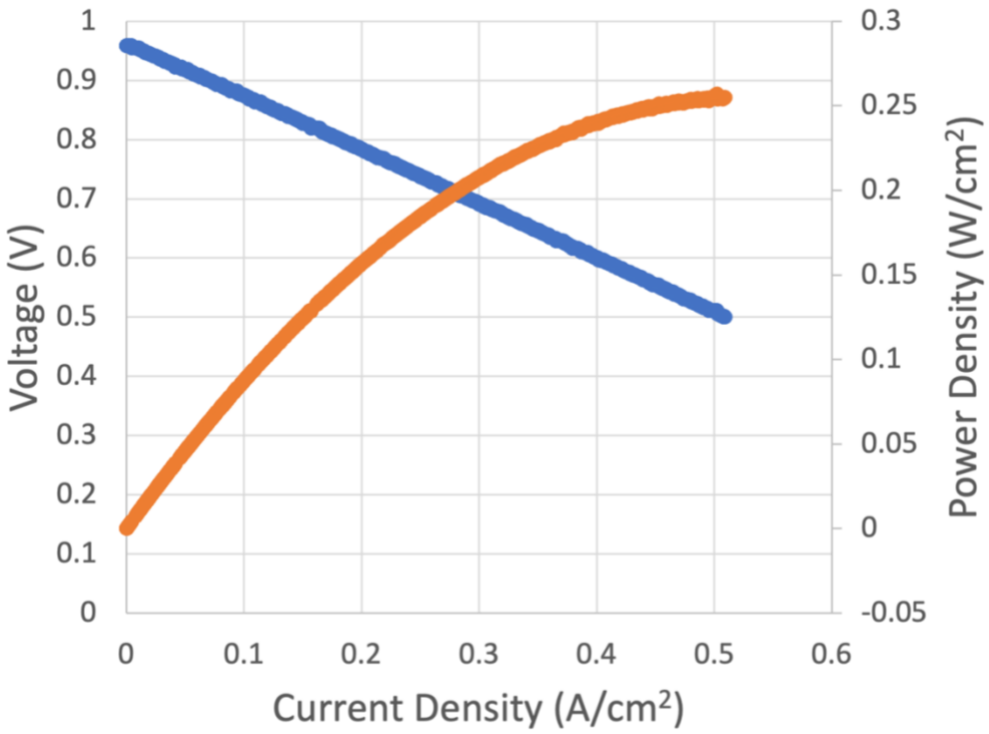

Figure 40. Voltage and power density versus current density of initially optimized SFCM-based ceramic anode cell #1 in dry hydrogen fuel and air at 550 °C.

The low-porosity 5 cm by 5 cm cell had a uniform anode composition, which was a composite of SFCM and ceria materials. The cell architecture for cells #1, #2, and #3 was similar to that shown in **Figure 8**B, where there were two different compositions making up the anode. Each layer was a composite of ceria and SFCM materials but the layer closer to the electrolyte had more ceria material than SFCM compared to the layer further away from the electrolyte. While the initially optimized cells (#1, #2, and #3) were tested only at 550 °C, another 5 cm by 5 cm cell (#4) was made using the same cell architecture (configuration, layer thickness, compositions, and sintering temperatures) and tested at 600 °C using humidified hydrogen fuel. As shown in the voltage and power density versus current density curves of **Figure 41**, this cell performed very well due to a catalyst loading of ~13 wt% and the slightly higher operating temperature. The area-specific-resistance (ASR) of the cell at ~600 °C was 0.2 Ω-cm^2 and the open-circuit-voltage (OCV) was ~0.9 V. At an operation voltage 0.75 V, the power density was ~0.6 W/cm^2. Note, the half-cell was made partly from commercially produced tape cast layers (e.g., in production environment on ~50-75-feet long tape caster), whereas the remaining layers were made using a pilot-scale tape

caster (i.e., < 20-feet long). For large format SFCM-based ceramic anode cells made using only production tape cast layers, the highest power density achieved at an operation voltage of 0.75 V was ~0.3 W/cm^2 (not shown). The maximum power density of cell #4 was ~0.9 W/cm^2. R_{Ohmic} was 0.13 Ω-cm^2 while R_{pol} was ~0.07 Ω-cm^2. Compared to cells #1, the Ohmic resistance of cell #4 was almost 3 times smaller. The electrode polarization resistance, on the other hand, was about 50% smaller. The likely reason for the much lower Ohmic resistance is that cell #4 had a silver contact covering the entire cathode, whereas cells #1 (as well as cell #2 and #3) had a silver screen printed grid. A possible reason for the difference in the polarization resistance is the fact that cell #4 had a slightly higher catalyst loading.

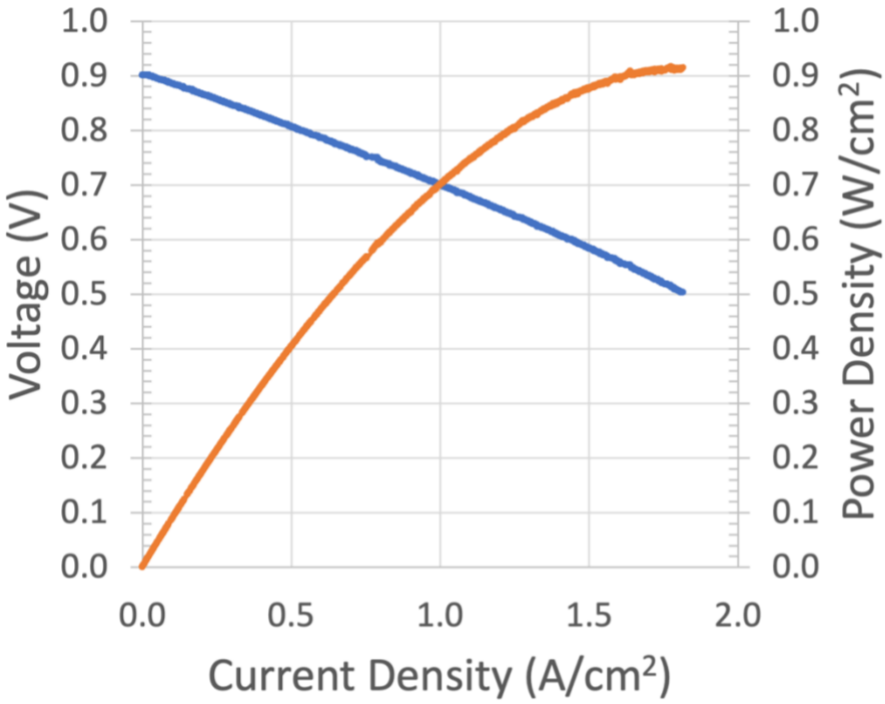

Figure 41. Voltage (blue) and power density (orange) curves for an optimized 5 cm by 5 cm SFCM-based ceramic anode cell (#4) tested at 600 °C in humidified hydrogen and air (~0.6 W/cm^2 at 0.75 V and a maximum power density of ~0.91 W/cm^2).

Another cell (#5) with this same structure as cell #4 and using the same tapes (including a silver contact covering the entire cathode) was tested at 600 °C and found to have an OCV of ~0.88 V and a maximum power density of ~0.93 W/cm^2 (not shown). Despite a slightly lower OCV than cell #4, the ASR of cell #5 was slightly lower (~0.19 Ω-cm^2) which is why the maximum power density was a little higher than that of cell #4. This cell was also tested at ~515 °C at a constant

current of 0.2 A/cm^2 as shown in the time series of **Figure 42**. Note, the cell voltage decreases from hour 25 to around hour 75 because the cell was still equilibrating (exhaust temperature decreasing by about 10 °C). Between about hour 75 and hour 85 the air flow rate decreased, causing some slight fluctuations in voltage. For the remainder of the measurement temperature was steady and the cell operating voltage remained constant.

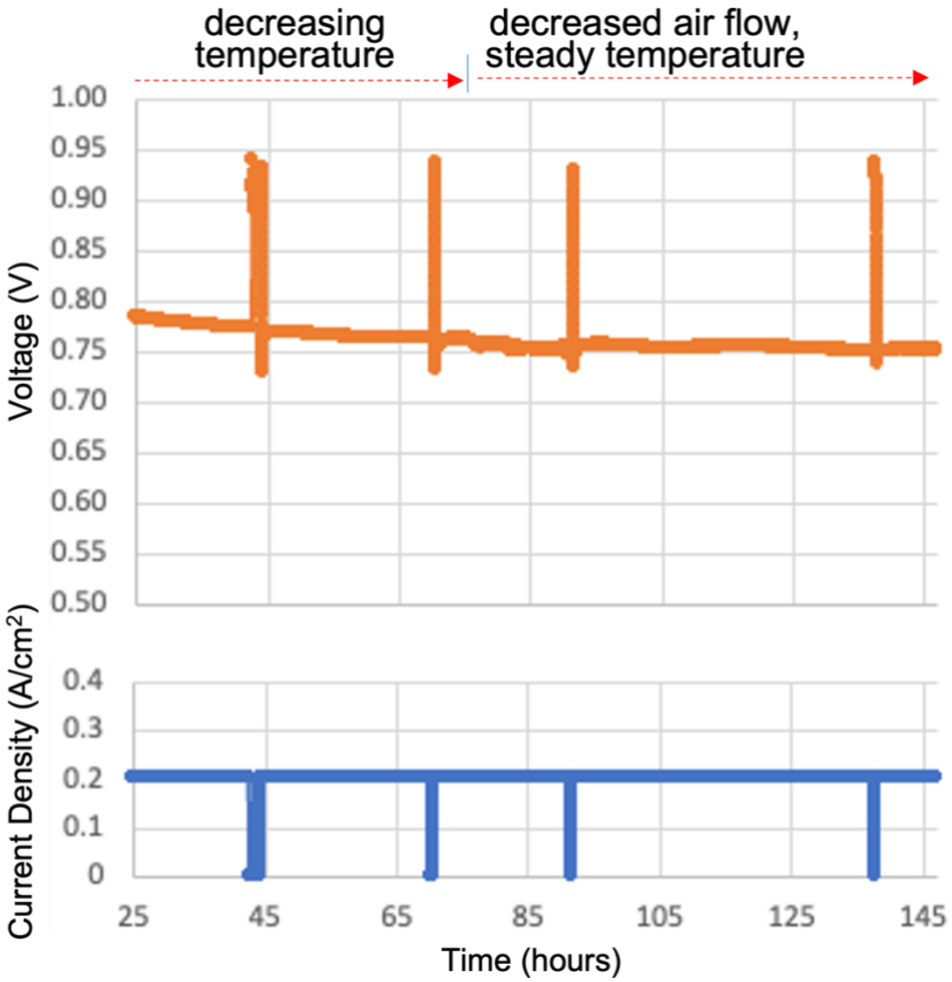

Figure 42. Cell voltage and current density versus time for an optimized 5 cm by 5 cm SFCM-based ceramic anode cell (#5) tested at ~515 °C in humidified hydrogen and air.

While some cells with this structure showed relatively stable performance over time, others did not. In some cases, cells that degraded showed delamination at the anode interface with the electrolyte (e.g., see **Figure 43**A), whereas in other cases there may have been a crack. On the other hand, some large format cells did not show issues with delamination (**Figure 43**B). Mechanical issues, and in particular issues involving delamination, pointed to weak bonding at the

interface between the anode and electrolyte as a feasible way to improve general long-term stability.

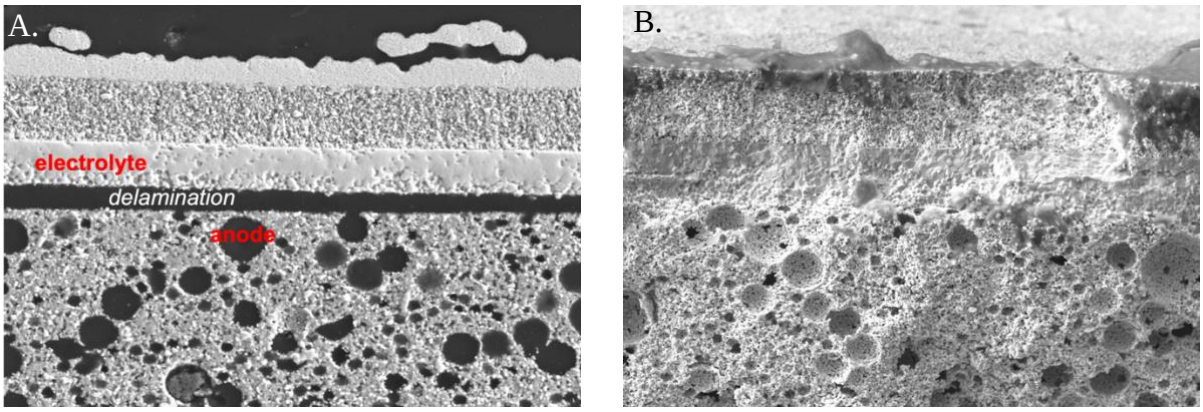

Figure 43. SEM micrographs of post-test cell cross-sections showing A) an example of delamination of the anode from the electrolyte for a 5 cm by 5 cm SFCM-based ceramic anode cell having the same structure and composition as cells #1 through #6; and B) the 5 cm by 5 cm cell #4.

As part of the optimization process, therefore, a priority shifted to the prevention of delamination and improvement of long-term stability for the large format cells. In the first instance, we fired the cell structure of cells #1 through #5 at a higher sintering temperature (cell #6) to increase the particle-to-particle bonding as well as the bonding between the anode and electrolyte. When tested at ~600 °C, cell #6 had an OCV of ~0.82 V, despite having a CFL. The cathode-to-anode crossover (N_2 measured in the fuel exhaust) was less than 0.5%. A possible reason for the lower OCV may be a relatively larger number of pinholes in the electrolyte, which can affect the OCV while not resulting in a measurable difference in the crossover leak measurement. The Ohmic ASR of cell #6 was ~ 0.17 Ω-cm^2 and the total ASR was ~0.69 Ω-cm^2 (or about 3.4 times higher than cell #4 and cell #5) because the higher sintering temperature reduced the porosity and resulted in a catalyst loading of only 7.5 wt%. While the stability was improved (e.g., OCV and ASR changed by no more than ~1% over > 80 hours of testing), the use of a higher sintering temperature alone was determined not to be the best solution due to the lower cell performance.

The evidence suggested that a combination of sufficiently high porosity and bonding strength (particle-to-particle within a given layer and between layers) was necessary to yield high electrochemical performance and stability. Therefore, in light of other processing constraints (e.g.,

see Section 6), we modified the cell structure to include an SFCM-based AFL, such that the cell architecture was like that of **Figure 8**C. Therefore, the new cell (#7) had two different SFCM-based layers as in **Figure 8**B, but the layer closer to the electrolyte was much thinner than the other (i.e., the ASL). The ASL had the same ceria to SFCM materials ratio as for cell #1 through cell #6, while the AFL used a larger amount of the ceria material. The bonding of the anode to the electrolyte was improved not only by the increased ceria content, but also by decreasing the pore size in the AFL in an attempt to increase the catalytically and electro-catalytically active surface area (increased triple phase boundary length). The cell was fired at the lower sintering temperature (i.e., the same as cells #1 through #5). Cell #7 had a catalyst loading of ~9.4 wt%, but note the relatively low weight gain was because one less infiltration step was performed than compared to the process used on cells #1 through #5. A different cell with the same structure as cell #7, but where the same number of infiltration steps were used, yielded the more typical catalyst loading for cells fired at the lower sintering temperature (i.e., ~12 wt%). **Figure 44**A shows the voltage and power density versus current density for cell #7 in humidified H_2 at ~600 °C. The OCV was only ~0.87 V likely due to a higher-than-normal number of pinholes, while power density at 0.75 V was only ~0.27 W/cm^2. **Figure 44**B shows OCV of the cell during red-ox cycling between H_2 and industrial N_2 (starting at ~20 hours). The cell experienced 11 red-ox cycles, with the gas environment switching every 2 hours. The OCV remained constant during the 65 hours of testing. After ~7 cycles the OCV started to show behavior that deviated substantially from the previous cycle. The cathode exhaust humidity data shown in **Figure 44**C, which is an indicator for the degree of anode-to-cathode crossover (as leaking H_2 combusts to form water in the cathode compartment), shows reproducible behavior until about cycle 3 or 4, after which point the cathode humidity begins to increase progressively. Moreover, the voltage of the cell during the N_2 exposure portion of the red-ox cycle drops from about ~0.1 V for the first ~4 cycles, to progressively lower values down to ~0.05 V during the 11th red-ox cycle. Such a decrease in voltage means that additional oxygen (increased cathode-to-anode crossover) is present in the anode compartment during the N_2 exposure portion of the red-ox cycle. This indicates that there was an approximately 20 times higher PO_2 in the anode compartment relative to the baseline in industrial H_2. This evidence suggests damage to the cell, such as delamination or fracture under the repeated red-ox cycles. The impedance spectra for cell #7 as the red-ox cycles progress is shown in **Figure 44**D.

The right-most, low-frequency intercept of each curve represents the total area-specific-resistance (ASR), which upon the first cycle (from curve *0* to curve *1*) exhibits a decrease from ~0.4 Ω-cm^2 to ~0.36 Ω-cm^{2}and then increased following the next two cycles (from curve *1* to curves *2* and *3*) to ~0.44 Ω-cm^2. The Ohmic contribution (left most, high-frequency intercept) appears to have changed more than the electrode polarization contribution during the red-ox cycles. These changes in ASR are small relative to those experienced with the previous large-format cells. After the 3rd cycle, however, the ASR increased much more (not shown), which is consistent with the relatively large increase in cathode humidity.

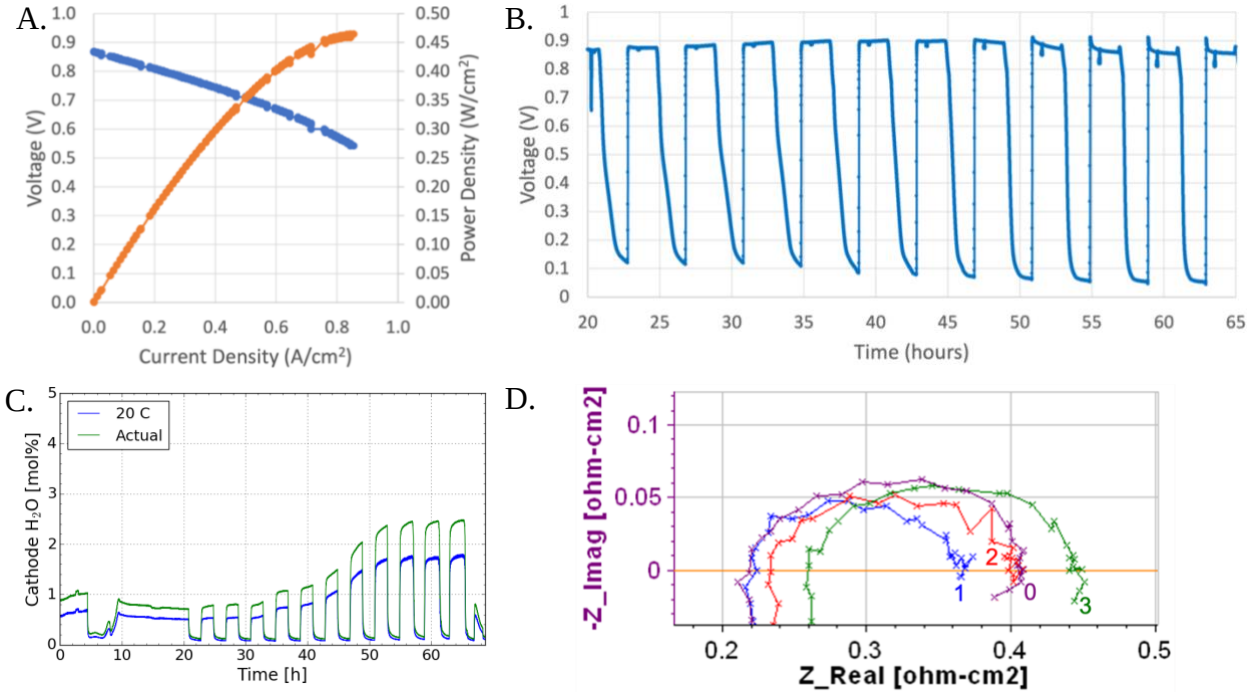

Figure 44. Cell performance at 600 °C with humidified H_2 fuel for a 5 cm by 5 cm SFCM-based ceramic anode cell (#7) with a modified anode structure for improved red-ox cycling showing A) voltage and power density versus current density; B) cell voltage versus time during red-ox cycling between humidified H_2 and industrial N_2; C) cathode exhaust humidity level (mol%) versus time; and D) impedance spectra taken before the red-ox cycles (label *0*) and after the first three red-ox cycles (*1*-*3*).

While similar, additional modifications were also made and tested, including at smaller cell sizes (e.g., 4 cm by 4 cm cells tested with a smaller cathode area than 5 cm by 5 cm cells), these too led to similar observations of degradation. The most common mode of degradation was delamination (e.g., see **Figure 43**A). Further investigation of such cells (post-test) revealed that in one case (cell

#8), a white-colored phase appeared underneath the delaminated electrolyte as shown in a Keyence VHX-2000 microscope image in **Figure 45**A. The white substance was concentrated in the region coinciding with the location of the Ag grid cathode contact. SEM micrographs revealed features above the anode surface (where delamination occurred), which were ~5-10 μm and had a microstructure different from the surrounding anode material (**Figure 45**B). SEM-EDS evaluation showed the white-colored phase to be very high in Sr content but also consisting of GDC (**Figure 45**C). One hypothesis for the presence of this phase is that Sr may have evolved at the anode-electrolyte interface from one of the SFCM-based ceramic anode components during operation, leading to delamination between the two layers. Milliken et al. found that Sr precipitation and diffusion in SrO-doped CeO_2 may result in delamination of the electrolyte from the anode [55]. In that work, a region of porosity formed within the electrolyte and along the anode interface. The electrolyte also displayed microcracks extending into the electrolyte from the anode. Along the interface with the electrolyte, the anode had an accumulation of Sr, which while chemical distinction was beyond the quantitative chemical analysis (electron probe microanalysis, or EPMA) resolution was thought to be SrO, SrOH, or $SrCO_3$. As SrO is unstable in humid reducing environments, strontium hydroxides and carbonates are likely to have formed. Milkien et al. also found that the Sr-precipitates were larger when an external current was applied to the cell. The fact that the white-colored phase was most highly concentrated on the SFCM-based ceramic anode (where the electrolyte had delaminated) in the vicinity of the Ag cathode contact, suggested that a similar process as with Miliken et al. may be related to the observed delamination mode of degradation. However, among other notable differences, the cells in the studies of Miliken et al. showed relatively stable performance at 750-800 °C for several hundred hours followed by degradation at 5-10% per 1,000 hours until about 800-1,200 hours before ASR abruptly increased. OCV was stable during the entirety of their SOFC tests. The large-format SFCM-based ceramic anode cells, on the other hand, had much more rapid degradation.

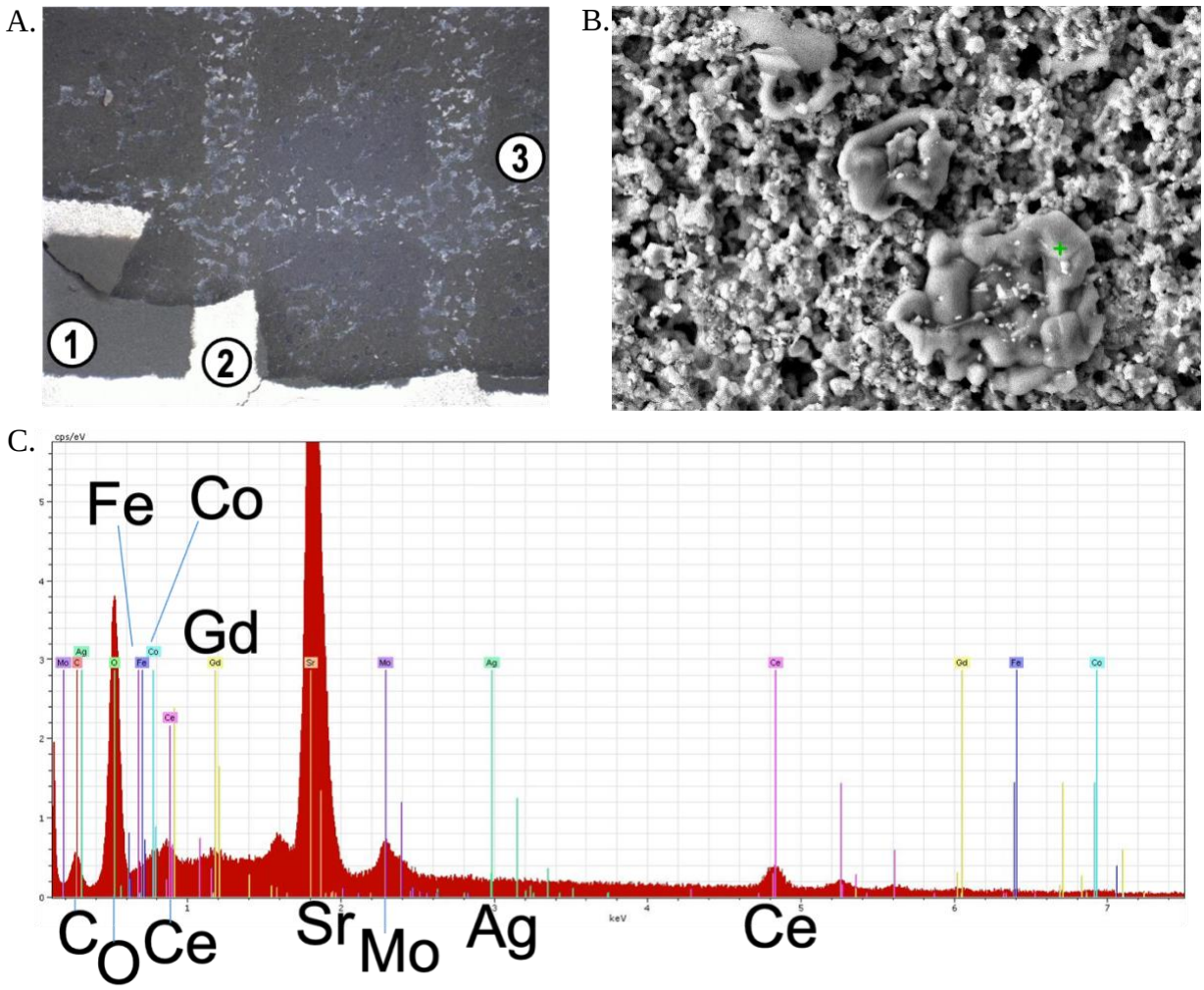

Figure 45. Post-test analysis for 5 cm by 5 cm SFCM-based ceramic anode cell #7 (sintered at the lower temperature) showing A) a Keyence microscope optical image of the cell surface where most of the electrolyte delaminated (remaining electrolyte and cathode shown in location 1 and 2) and with a white-colored phase appearing most concentrated in the vicinity of the Ag grid cathode contact (location 2 and 3); B) SEM micrograph of the anode surface including the white-colored phase (location 1); SEM-EDS analysis results showing a high concentration of Sr along with GDC.

A possible secondary phase was only observed one other time in post-test analysis of operated large-format SFCM-based SOFCs, as shown in **Figure 46**. This 5 cm by 5 cm SOFC (#8) had a similar structure and composition as cell #6 and #7. This cell showed a similar pattern of behavior as cell #7 and ultimately experienced delamination of the electrolyte as shown in the post test photograph of **Figure 46**A. An optical image from a Keyence VHX-2000 microscope (**Figure 46**B) revealed white-colored residue across the surface of the anode where the electrolyte had delaminated. Upon closer inspection, this residue appears to be much larger (~25-150 microns

across) than the white-colored phase on the anode where the electrolyte delaminated for cell #7. The operating current of cell #8 was no larger than that of cell #7, suggesting that the location of the highest concentration of secondary phase in cell #7 (i.e., coinciding with silver grid) may have only indirectly to do with current density. For instance, since more heat is locally released at higher current densities this results in greater thermal gradients and higher thermal stress. Therefore, one possibility is that damage to the electrolyte occurred around the area of the high current density, which (assuming the white-colored phase is strontium carbonate) may have allowed CO_2 from the air to react with the strontium to form $SrCO_3$.

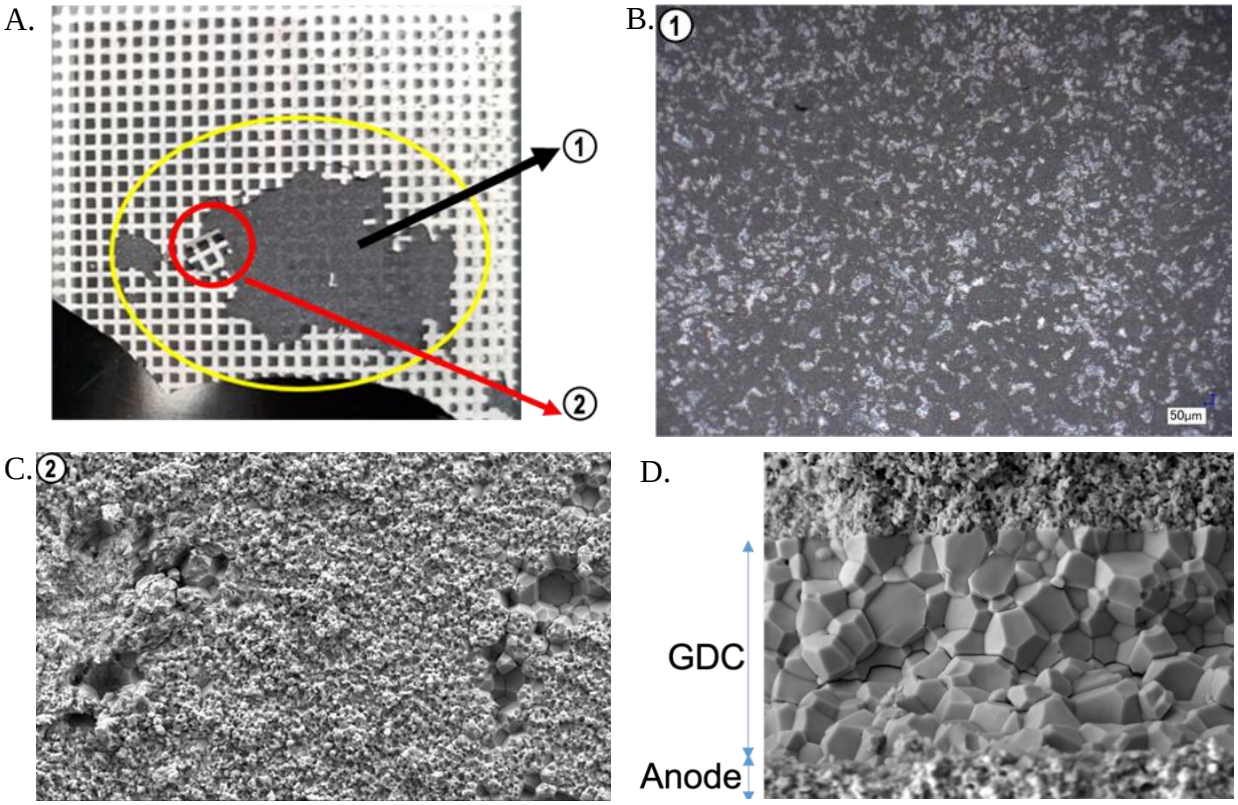

Figure 46. 5 cm by 5 cm SFCM-based ceramic anode cell #8 (sintered at the higher temperature) and damaged during operation showing A) a photograph of the cell with Ag grid and missing electrolyte region; B) an optical image from a Keyence microscope showing the possibility a secondary phase or GDC electrolyte remnants on the surface of the anode at region 1 where the electrolyte delaminated; C) an SEM micrograph of the electrolyte at a site of delamination from the anode (underneath region 2); and D) an SEM cross-sectional micrograph of the cell.

Inspection of the cross-section of cell #8 near the region of delamination shows nothing out of the ordinary (e.g., no secondary phases or unusual porosity) along the anode/electrolyte interface

(**Figure 46**). Note, that initially one thought was that SrO formed due to elemental diffusion and resulting phase instability during cell fabrication. This hypothesis was initially formed after a lower ASR degradation was observed in a few cells sintered at lower temperature compared to cells sintered at higher temperature. However, this hypothesis is likely wrong as not enough identical cells were tested to know if the differences in degradation were due to the cell or due to something else (e.g., stack assembly). Moreover, there does not seem to be any trend in the amount of the white-colored phase observed relative to the sintering temperature. For instance, while there is some difference in the amount of white phase in certain portions of cell #7 (sintered at lower temperature) versus cell #8 (sintered at higher temperature), another cell (#9) that was sintered at the higher temperature had relatively low amounts of the white-colored phase on the AFL (**Figure 47**) when the electrolyte delaminated after testing.

Figure 47. An optical image of the AFL surface of 5 cm by 5 cm SFCM-based ceramic anode cell #9 (sintered at the higher temperature) after test in which the electrolyte and cathode have peeled off completely.

Since the appearance of the whitish phase was possibly related to the observed degradation during test, single-atmosphere chamber anneals were performed with half-cell components to better understand their origin. **Figure 48** shows a cross-sectional SEM micrograph of an SFCM-based ceramic anode half cell annealed in *highly humidified* (30% steam) H_2 for about 50 hours at 650 °C. Steam levels were maintained using a temperature-controlled bubbler feeding into a glass

chamber which held the sample. After testing, the half cell cracked into pieces and exhibited a whitish precipitate on the electrolyte surface. The cross-section shows the precipitate materials (identified as rich in Sr by EDS) are also on the surface of the fractured electrolyte. This led to a hypothesis that the Sr may exsolve from the SFCM during operation, which results in the formation of cracks in the GDC. The Sr may then migrate through cracks in the electrolyte. Such a mechanism may result from exposure to H_2, high humidity, or both conditions.

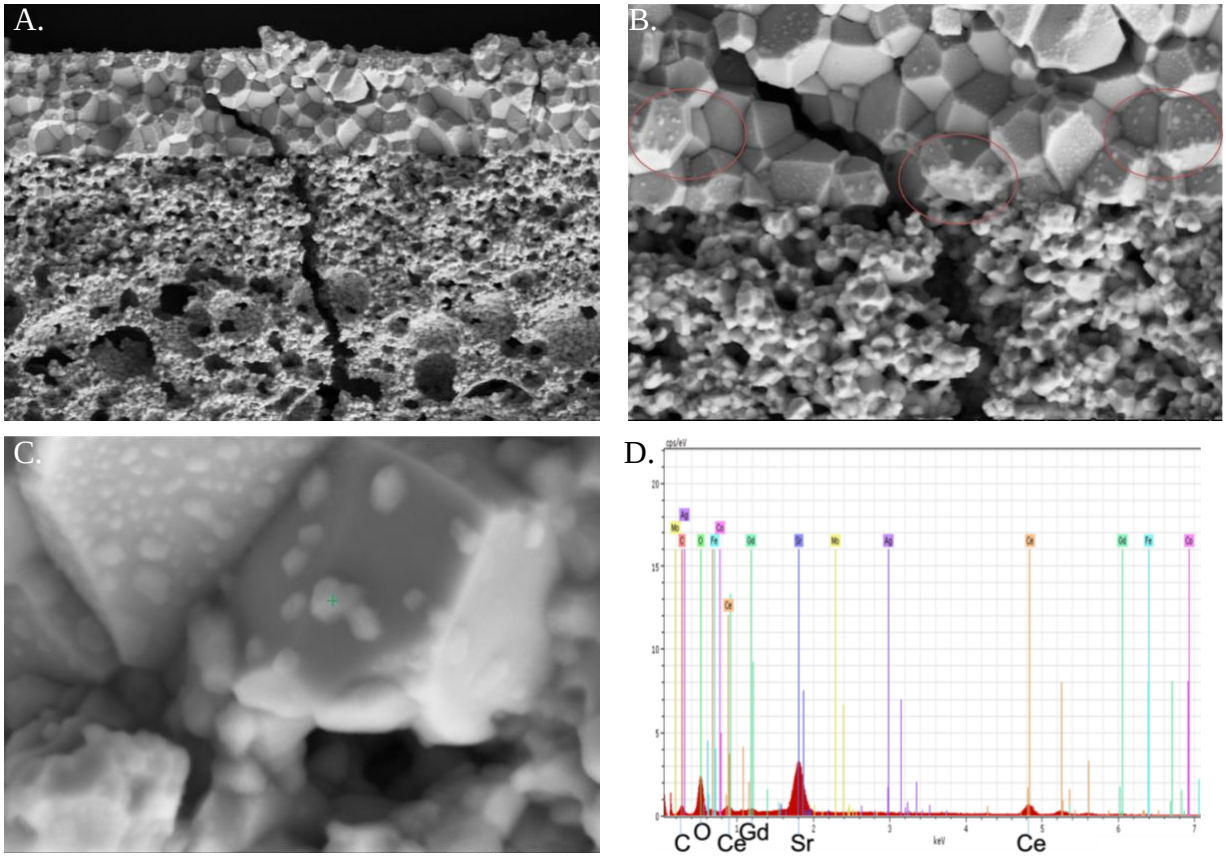

Figure 48. SEM of fractured cross-section of an SFCM-based ceramic anode half-cell after annealing at 650 °C in 30% steam/70% H_2 for ~50 hours showing A) SFCM-based anode, SFCM-based AFL, and GDC electrolyte (baseline, low magnification); B) 1.6-times higher magnification region highlighting areas with Sr-rich particles in the GDC grain boundaries (red circles); 8.3-times higher magnification of GDC grain with green cross indicating the location of the EDS measurement; and D) EDS spectrum illustrating that the white-colored precipitate is Sr-rich.

To better understand the exact mechanism associated with these changes, another SFCM-based ceramic-anode half cell was annealed in *dry* H_2 at 600 °C for 50 hours. **Figure 49** shows a photograph and SEM micrographs of the cross-section and electrolyte surface of the post-test

sample. As seen in **Figure 49**A, just as in testing in 30% humidified H_2 (**Figure 48**), the half-cell sample cracked after testing in dry H_2. We, therefore, concluded that the cracking was due to the use of a single chamber atmosphere test setup in which the entire half cell (i.e., SFCM-based anode and GDC electrolyte) under test was reduced in H_2. The stress (albeit relatively small stress) that results from chemical expansion when the entire electrolyte is reduced seems to have exceeded the strength of the cell, and thus resulted in cracks. In a typical SOFC arrangement (i.e., one in which the cathode side is always exposed to an oxidizing environment such as air), cells do not crack in this manner. Note, during operation of an SOFC system if red-ox cycles occur (e.g., if there is a fuel outage), both sides of the cell are only exposed to air. Therefore, the condition of the entire SOFC exposed to reducing conditions (and thus resulting in cracking), as was the case with the single chamber anneal tests, will not occur in a properly designed system. **Figure 49**B shows an SEM micrograph of the sample's electrolyte surface (higher magnification), while **Figure 49**C and **Figure 49**D show the SEM micrographs of the cross-section at 50% lower magnification and higher magnification, respectively. There is no evidence of the Sr-rich secondary phase that was previously observed in humidified conditions (**Figure 48**). As a result, we concluded that the Sr-rich impurity phase formation is primarily related to humidity. However, while the Sr-rich impurity was not always observed in large format cells up to the point of these anneal tests, the fact remains that in some cases the white-colored precipitates formed during operation. While possibly occurring in button cells made during the initial development of the SFCM-based ceramic anode cells, the Sr-rich precipitates were not observed or at least noticed in post-test analyses of the button cells. There was a slight difference in the composition used in the large format cells made up to this point in the project and the original button cells made during the initial development. This relatively small difference was done, in part, to adjust shrinkage during sintering of the large format cell, which as described in Section 6 is far more challenging than sintering button cells.

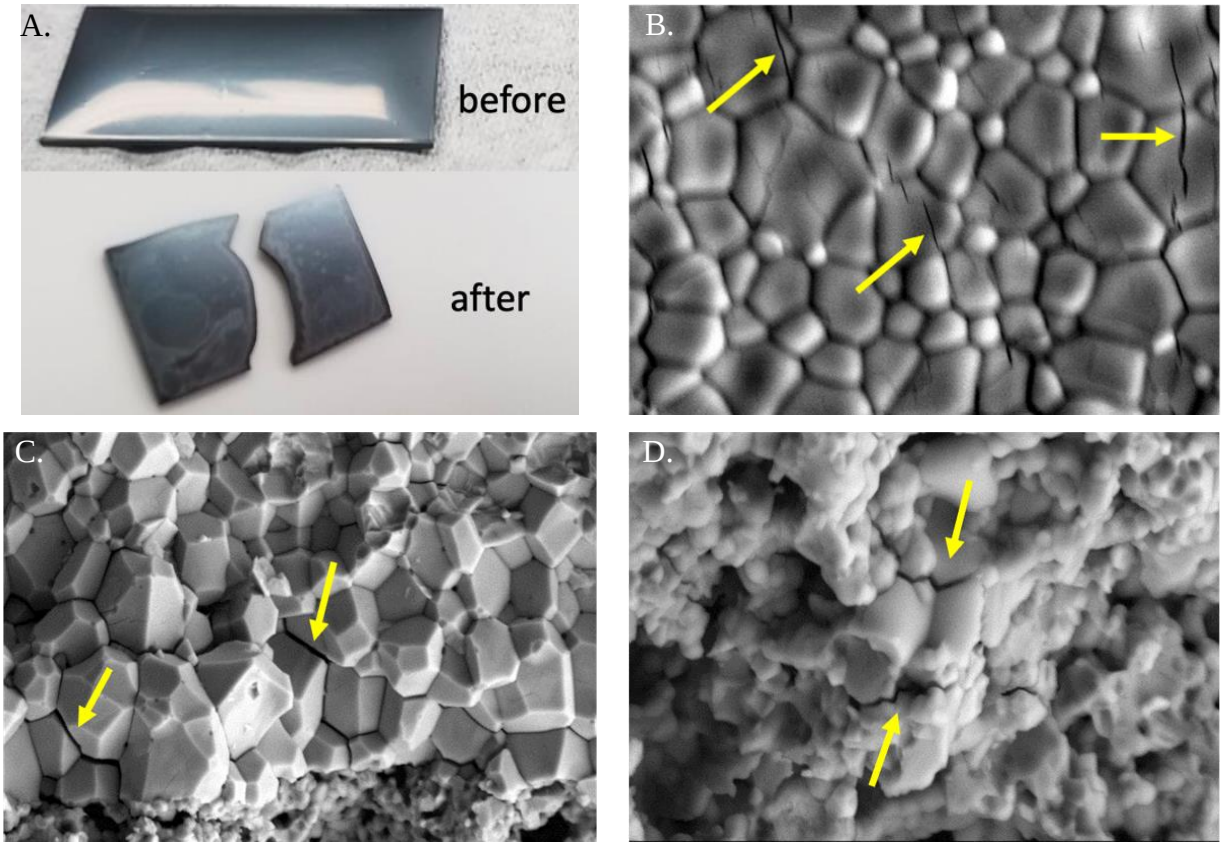

Figure 49. SFCM-based ceramic anode half-cell sample annealed inside of a single chamber setup with flowing dry H_2 for 50 hours, showing A) a photograph of the sample before and after the annealing test; B) an SEM micrograph (higher magnification) of the electrolyte surface after annealing (yellow arrows indicate presence of cracking); C) an SEM cross-sectional image (50% lower magnification) of the sample indicating cracking in the electrolyte; and D) an SEM cross-sectional image (higher magnification) of the composite SFCM-based anode indicating cracking.

As there was uncertainty as to whether the electrolyte delamination in the large format SFCM-based ceramic anode cells was due to the Sr exsolution, we decided to fabricate cells using the exact same structure and composition as the button cells used in the original development efforts. Due to the fabrication issues with that structure/composition, this limited the size of the cells to approximately 2.5 cm by 2.5 cm. Prior to testing a full SOFC, we repeated the single-chamber anneal tests with pressed and sintered bars made from composites of the original button-cell anode composition, the initial large format cell anode composition, and A-site deficient SFCM with GDC. The bars were sintered at the higher sintering temperature. All samples were exposed to 30% steam (balance hydrogen) for at least 50 hours. Some samples were cooled to room temperature in the same environment, while others were cooled in dry hydrogen. **Figure 50**A-B

and **Figure 50**C-D show the SEM micrographs for the initial large-format cell anode composition (Type A composite) and original button-cell anode composition (Type-B composite), respectively, after the sintered bars were annealed in 30% steam (balance H_2) for 50 hours and cooled in *humid* H_2. As seen in the higher magnification images of, an exsolved phase can be found on all surfaces for the Type-A (**Figure 50**B) and Type-B (**Figure 50**D) composites. These precipitates are Sr-rich as seen in the EDS spectra of **Figure 51**. The Type-B composite is the same composition as what was used in developmental button cells. Cobalt is a transition metal that incorporates into the SFCM material, and the excess cobalt can be introduced during the material preparation (e.g., Co-GDC). This makes the perovskite phase A-site deficient, which should make Sr-exsolution less favorable. However, as **Figure 50** and **Figure 51** demonstrate, both the Type-A and Type-B composites lead to the formation of Sr-rich precipitates.

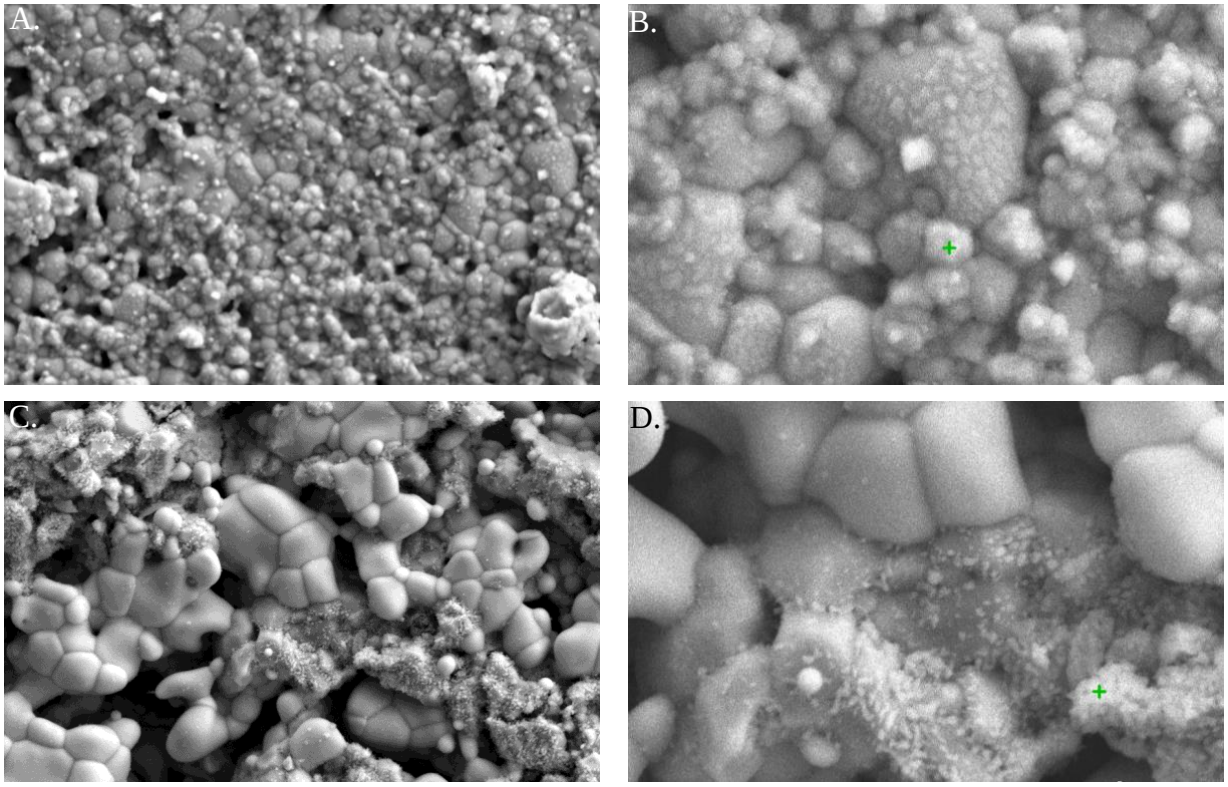

Figure 50. SEM micrographs of pressed and sintered bars of SFCM composites using the initial large-format cell anode composition (Type A) and the original button-cell anode composition (Type B) that were annealed in 30% steam (balance H_2) for ~50 hours and cooled in *humid* H_2, showing the surface of A) the Type-A composite at lower magnification and B) 3-times higher magnification; and the surface of the Type-B composite at C) lower magnification and D) 3-times higher magnification.

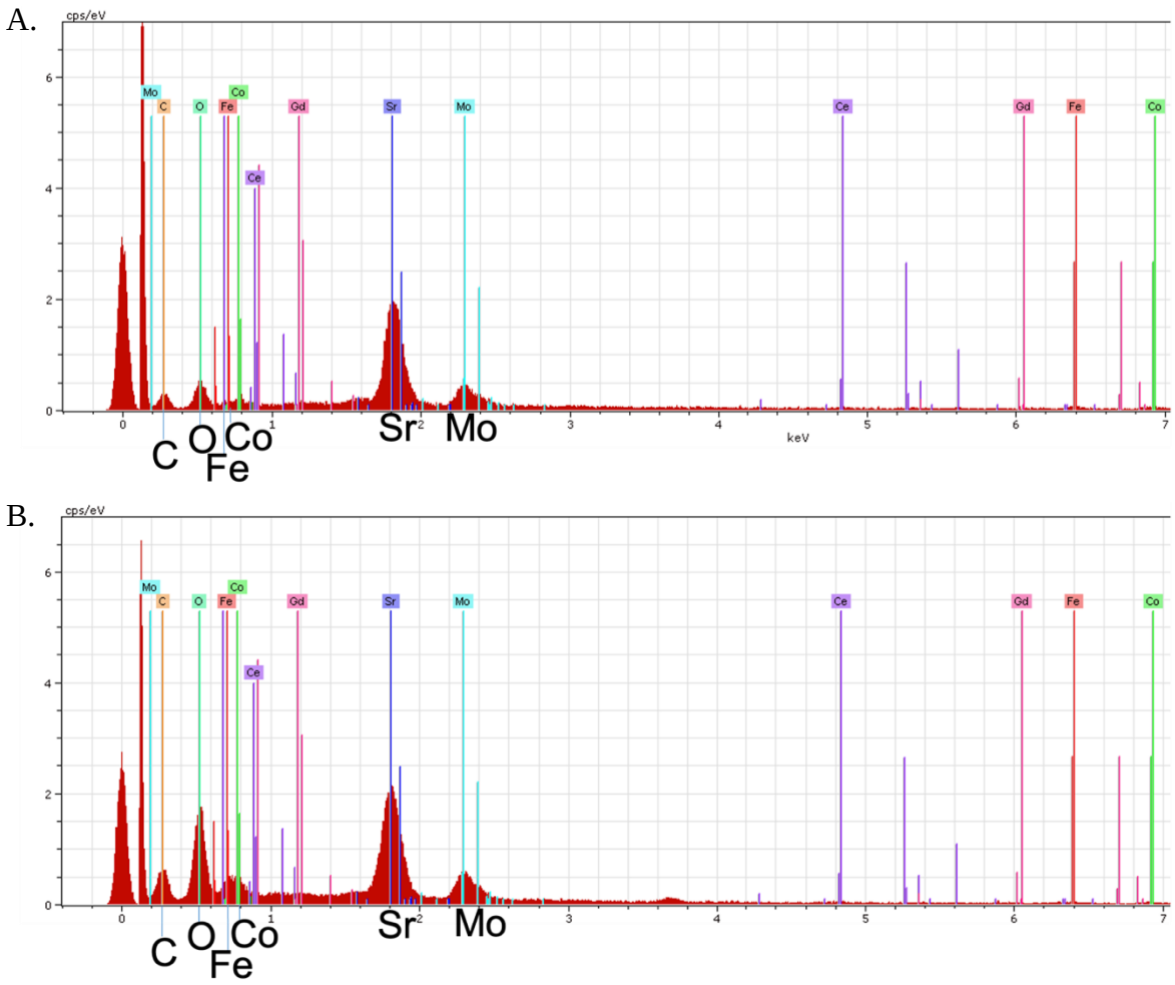

Figure 51. EDS spectrum illustrating that the exsolved phase is Sr-rich for pressed and sintered bars of A) an initial large-format cell anode composition (Type A) and B) an original button-cell anode composition (Type B), which were both annealed in 30% steam/70% H_2 and cooled in the same *humid* gas environment.

To further evaluate the cause of the Sr exsolution, we synthesized A-site deficient SFCM using the glycine–nitrate process (GNP) combustion synthesis method. Note, all other SFCM used in this project was made via solid-state synthesis. A pressed and sintered bar of a composite of GDC and the A-site deficient SFCM was made and annealed in 30% steam (balance H_2) for 50 hours and cooled in humid H_2. As seen in **Figure 52**, once again a phase precipitated on the surface of the SFCM and the GDC. EDS confirmed that the exsolved phase is Sr-rich.

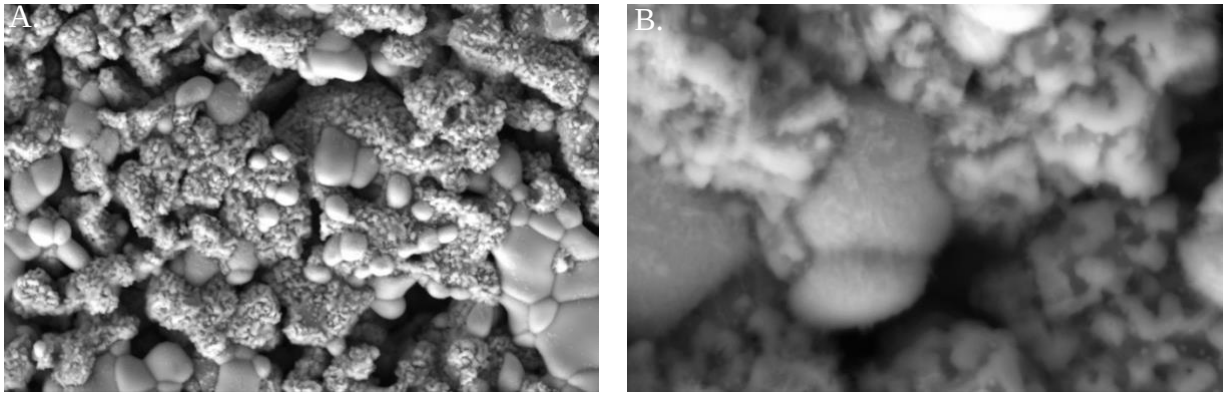

Figure 52. SEM micrographs of pressed and sintered bar of a composite of A-site deficient SFCM with GDC that were annealed in 30% steam (balance H_2) for 50 hours and cooled in *humid* H_2, showing the surface at A) lower magnification and B) 5-times higher magnification, highlighting the formation of exsolved Sr on the A-site deficient SFCM and GDC.

We prepared two pressed and sintered bars of single-phase SFCM in the same fashion as the other bars, but in this case while the bars were still annealed in 30% steam (balance H_2) for more than 50 hours, they were cooled in *dry* hydrogen. **Figure 53** shows a photograph of a fresh bar of SFCM that has not been annealed in comparison with SFCM bars that have both been annealed for 70 hours in 30% steam (balance H_2), one of which was cooled in 30% humidified H_2 (left) while the other was cooled in dry H_2 (right). The bar that was cooled in 30% humidified H_2 clearly has a white-colored residue over the entire surface, whereas the bar that was cooled in dry H_2 looks no different from the fresh SFCM bar. **Figure 54** shows the SEM micrographs of two different SFCM bars that were annealed in 30% humidified H_2 and cooled in dry H_2. There was no obvious precipitated phase on the surface of either sample, and the bars looked similar to fresh SFCM bars.

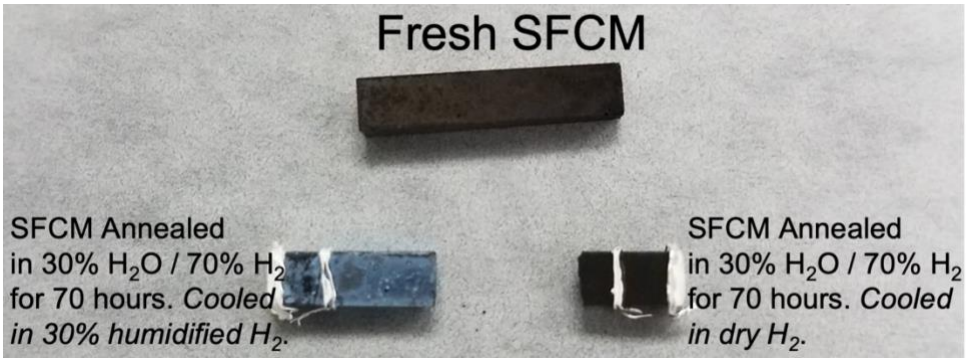

Figure 53. Photograph showing a fresh pressed and sintered bar of SFCM, and similar bars annealed in 30% steam (balance H_2) for 70 hours, where one was cooled in dry H_2 (right, no white precipitates) and the other was cooled in 30% humidified hydrogen (left, white precipitates).

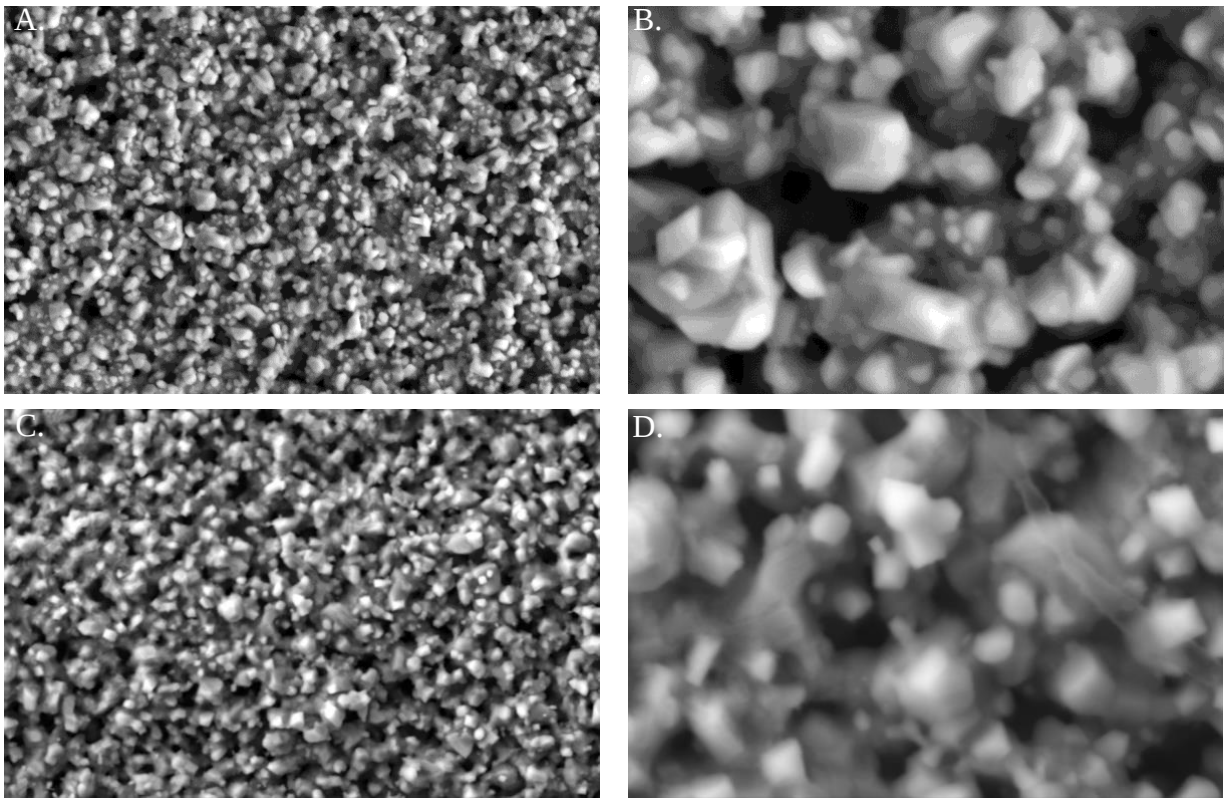

Figure 54. SEM micrographs of two different pressed and sintered bars of SFCM that were annealed in 30% steam (balance H_2) for 70 hours and cooled in *dry* H_2, showing the surface of the first bar at A) lower magnification and B) 4-times higher magnification; and the second bar at C) lower magnification and D) 4-times higher magnification.

The bar-anneal tests demonstrated that the likely cause for the formation of the white-colored Sr-rich precipitates was exposure to steam at low temperatures rather than a process that occurred at elevated temperature. We have confirmed that SFCM decomposition can occur from room temperature (i.e., 25 °C) to at least ~80 °C with the formation of SrO precipitates (*see APPENDIX B*). This suggests that the Sr-rich precipitates that formed on the anode at the interface with the electrolyte are not the cause of the delamination in the large format cells. The delamination may have instead resulted from other events, such as damage during assembly due to high camber or excessive stress creation during operation (e.g., thermo-mechanical stress). Note that in button cell tests, typically 3% humidified or dry hydrogen is used and due to the nature of the test setup, the fuel utilization is very low. Therefore, a possible reason why a Sr-rich exsolved phase was not observed in the initial developmental button cell tests is that any water that formed during operation was quickly removed and the hydrogen streams were always effectively dry or had only

a very small amount of water. When the large format cells are operated, the fuel utilization is much higher, which locally creates a more humid gas stream. Moreover, if damage to the electrolyte occurs during operation of large format cells, the leaked hydrogen can combust and create large amounts of water, which if still present at lower temperatures can cause Sr exsolution.

In further support of the conclusion that the Sr exsolution was unlikely the cause of delamination, we also tested many approximately 2.5 cm by 2.5 cm cells, which used the original button-cell anode composition (Type B). These button-like cells were configured as depicted in **Figure 8**A and tested in the smallest size stainless steel stack hardware available at Redox (i.e., sized for 4 cm by 4 cm cells) with a slightly modified assembly configuration. Though fabricated at approximately the size of a typical button cell, these 2.5 cm by 2.5 cm cells had a relatively large amount of camber. This is in part why the structure was modified slightly to fabricate the large format cells up to this point in the project. While this amount of camber would not normally impact typical testing of a button cell which is cemented to an alumina tube reactor and has current collectors (e.g., silver or platinum mesh) lightly adhered with paste, we used stainless steel components that along with the other stack hardware (e.g., interconnect and current collectors) were compressed during assembly. Due to the camber, we had to increase the height of the current collector mesh and reduce the load on the cell after assembly compared to normal cell/stack assemblies. Note, all the large format SFCM cells also required a load on the stack assembly lower than what is used with typical Ni-cermet cells, but the button-type cells required even less load due to the high camber, which acts as a stress concentrator and can easily lead to cracks in the cell.

A 2.5 cm by 2.5 cm SFCM ceramic-anode SOFC with the original button-cell composition/ structure was fabricated (fired at the higher sintering temperature) and tested at 600 °C in humidified H_2. **Figure 55** shows operating voltage versus time for the cell at a fixed current density of 0.3 A/cm^2. This button-type cell still showed degradation, though less degradation than the 5 cm by 5 cm cells with a configuration as shown in **Figure 8**B and **Figure 8**C. However, the button-type cell ASR degradation rate (~160% per 1000 hours at 600 °C and 0.3 A/cm^2) was about 3 times higher than that of the low-porosity 5 cm by 5 cm cell having configuration of **Figure 8**A which had no anode pore formers added (e.g., see **Figure 35**). Note, the low-porosity 5 cm by 5 cm cell was operated at 550 °C and about half the current density of the 2.5 cm by 2.5 cm button-

type cell. There were a few other 5 cm by 5 cm (non-button-type) cells that had similarly relatively low degradation rates, and yet did not use the original button-cell anode composition. Additional button-type cells were fabricated and fired at lower sintering temperatures, but these had an even higher degradation rate when tested under the same operating conditions. Note, all the button-like cells were heated and cooled in 3% humidified H_2 during testing.

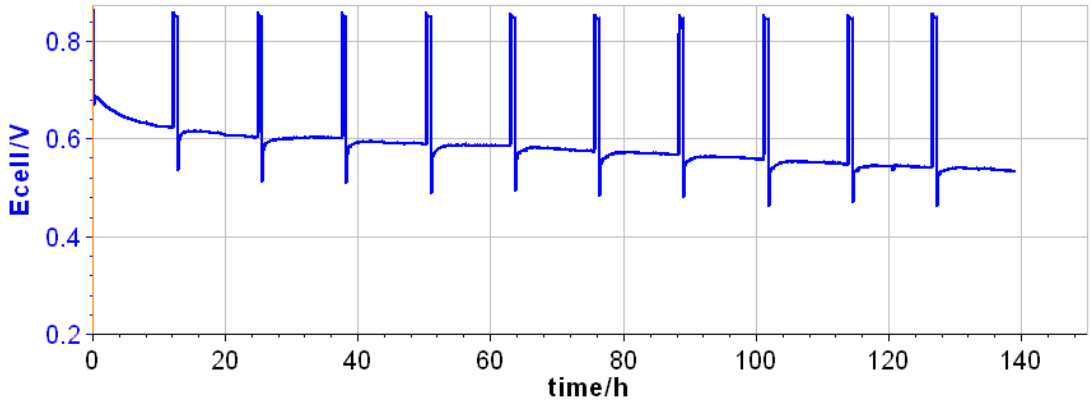

Figure 55. Cell voltage versus time for a 2.5 cm by 2.5 cm button-type ceramic anode SOFC tested at 600 °C with a fixed 0.3 A/cm^2 in humidified H_2.

Figure 56 provides SEM cross-sectional micrographs of the button-like cell that was fired at higher sintering temperatures (data shown in **Figure 55**). At low magnification (**Figure 56**A), much of the electrolyte interface appears intact, though upon closer inspection there are regions of the interface that delaminated. **Figure 56**B shows a higher magnification SEM micrograph of the interfacial region exhibiting delamination, which appears very similar to that observed with the large format cells. Note, in almost all cases for the large format cells, when observed, full delamination of the electrolyte from the anode happened only upon removal of the mesh current collector from the cell. After SOFC operation, the mesh current collector was usually bonded very well to the silver (cathode) contact layer. Therefore, damage to the electrolyte may have started, or at least was made worse, during post-test analysis when the interconnects were removed from the cell. As the mesh usually adhered strongly to the cell, delamination often became obvious only after the mesh was removed from the cell, in which case the delaminated portion adhered to and came off with the mesh. As described above, the button-like cells were assembled with a much lower compressive load than the (non-button-type) large format SFCM-based SOFCs due to a higher camber, which resulted from the use of the original button-cell anode composition. The

lower compressive load resulted in the mesh not adhering as much to the silver contact layer, which is likely why delamination was not observed until an SEM analysis was conducted. Delamination may have similarly not been reported for the development stage button cells as no compressive force is applied to the cells during testing — in the typical button cell test arrangement, mesh current collectors are adhered to the anode and cathode using a paste (e.g., nickel, silver, or platinum).

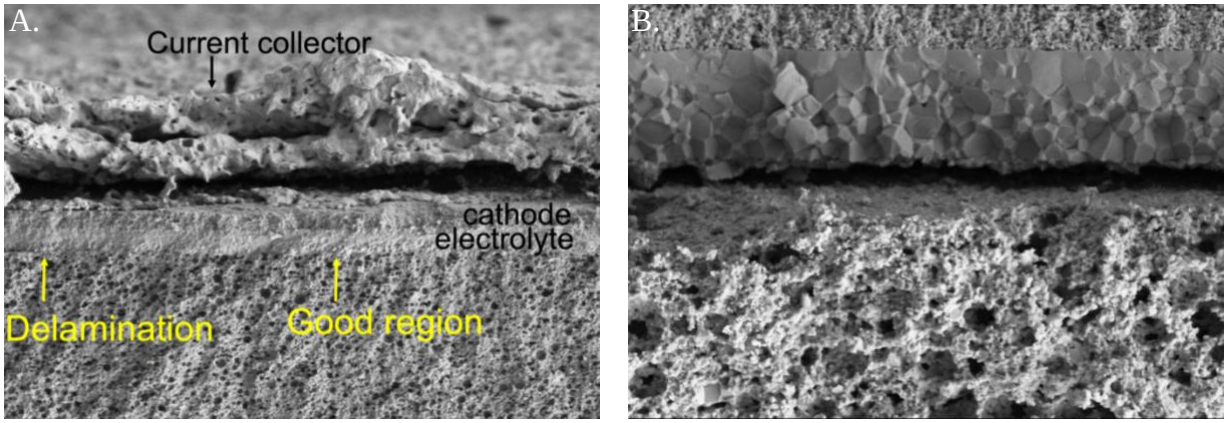

Figure 56. SEM micrographs of a 2.5 cm by 2.5 cm button-type SFCM-based ceramic anode cell after long-term test, showing the cross-section at A) a lower and B) higher magnification.

Even though studies in the literature suggest that Sr-containing perovskite materials can suffer from strontium exsolution and delamination when operated under high humidity within a certain temperature range (Milliken et al.), the majority of the experimental evidence from this project suggests that the presence of Sr-rich precipitates was not the cause of delamination [55]. Rather, the Sr exsolution more likely resulted from the humid, post-delamination conditions (i.e., due to localized fuel combustion) and/or from the presence of water in the anode at low temperatures (e.g., due to a humidified gas inlet stream). While the evidence for delamination ultimately pointed to a cause of overall low mechanical strength and weak bonding of the electrolyte to the anode, we ultimately chose to further modify the anode composition of the structure shown in **Figure 8**C (i.e., an SFCM-based ASL with an AFL) in a way that reduced the possibility for Sr exsolution at the anode/electrolyte interface. In fact, no exsolved strontium was found at the interface of any cells of this further modified type.

An initial version of this SFCM-based ASL with an AFL was fabricated as a 5 cm by 5 cm cell that had some edge cracks and cut smaller to yield a 2 cm by 2 cm cell (cell #10). The cell had an SSC-GDC cathode with a silver cathode contact but no CFL. The catalyst loading in the anode was ~6.3 wt%. The cell was tested using 4 cm by 4 cm stainless steel cell/stack hardware at 600 °C in humidified hydrogen. During a long-term stability test, the cell was held mostly at ~0.3 A/cm^2 but was occasionally dropped to 0 A/cm^2 to check OCV. As shown in **Figure 57**, the OCV was ~0.85 V and the initial ASR at the start of the long-term measurement was ~0.8 Ω-cm^2. Note, that ~20 hours prior to the start of the long-term measurement, cell #10 registered an ASR of ~0.55 Ω-cm^2. The initially lower ASR likely resulted from a higher cell temperature before the cell fully equilibrated after the heat-up process. The OCV was stable for about 250 hours, though there was a very slight decline in OCV that began around 200 hours. ASR was stable for just over the first 100 hours, but then began to increase and reached ~1.1 Ω-cm^2 after ~250 hours.

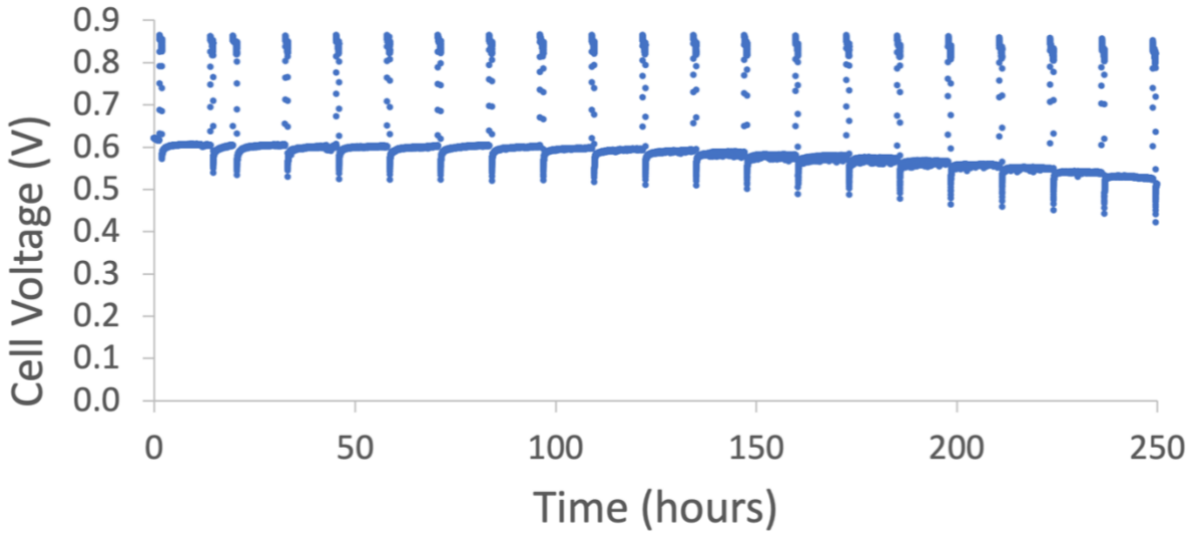

Figure 57. Cell voltage versus time for a 2 cm by 2 cm, modified-composition SFCM-based ASL with AFL (SSC-GDC cathode and silver contact but no CFL; *lower GDC content AFL at the lower sintering temperature*) SOFC (#10) that was operated at 600 °C in humidified H_2 with a fixed current density of ~0.3 A/cm^2 for ~250 hours.

A second cell with the modified-composition, SFCM-based ASL with AFL configuration was fabricated. This cell (#11) was 2.5 cm by 2.5 cm SOFC (also cut from a 5 cm by 5 cm cell with edge cracks) and had a CFL, LSCF-GDC cathode, and silver cathode contact. As shown in **Figure 58**, when operated at 600 °C in humidified hydrogen, cell #11 (red curve) resulted in a high OCV,

similar to that of the best performing SFCM-containing ceramic anode cell, which is shown in the dark gray curves (note, the full performance characteristic curves for cell #4 are provided in **Figure 41**). Also shown in **Figure 58** are the performance curves of the best large format, SFCM-based ceramic anode SOFC that used commercially produced tape cast layers (no CFL; cell configuration as shown in **Figure 8**B). Note, this initial test with the modified-composition, SFCM-based ASL with AFL configuration did not have optimized anode infiltration, which means additional power density improvements are possible.

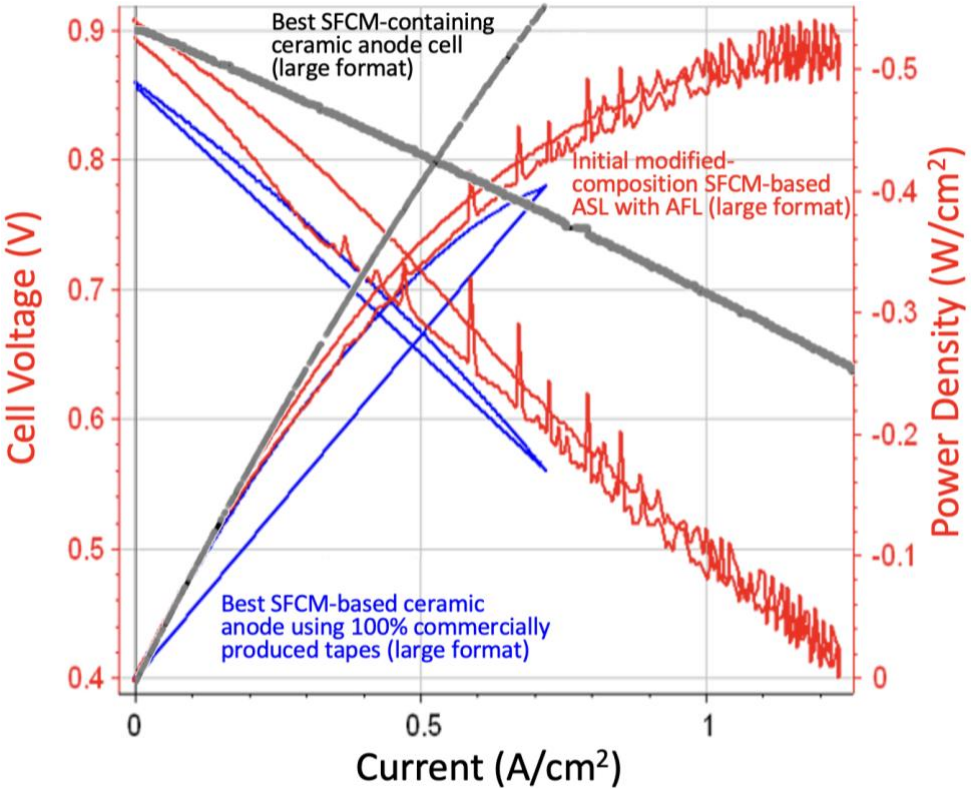

Figure 58. Cell voltage and power density versus current density at 600 °C in humidified hydrogen for the best performance, 5 cm by 5 cm SFCM-based ceramic anode SOFC (dark gray); best performance, 5 cm by 5 cm SFCM-based ceramic anode SOFC using 100% commercially produced tapes (blue curves); and a 2.5 cm by 2.5 cm (modified-composition) SFCM-based ASL with AFL (*lower GDC content AFL at the lower sintering temperature*) SOFC (red curves; cell #11).

As shown in **Figure 59**, when this initial (modified-composition) SFCM-based ASL with AFL cell was operated at 0.3 A/cm^2 at 600 °C for an extended period there was no change in the OCV. The catalyst loading in the anode was ~6.3 wt%. The initial OCV was ~0.9 V due to the CFL,

while the initial ASR was ~0.4 Ω-cm^2. ASR degradation was much lower (i.e., ~35% per 1000 hours for the period in which OCV was stable) than observed with most of the large format SFCM-based ceramic anode cells up to this point in the project. Note, however, that after ~200 hours OCV began to decrease. Also, note that the initial ASR of cell #11 was lower than that of cell #10, though each cell had the same anode configuration and catalyst loading. A possible reason for this is that cell #11 had less camber than cell #10 at the center of the cell, which may have resulted in better contact with the current collectors and stainless-steel interconnect. The Ohmic resistance of cell #11 was only ~12% lower than that of cell #10. Though both cells were sintered in the same firing batch, another possibility is that the actual sintering temperature of each cell was slightly different. Note, while we eventually improved the temperature uniformity of the high temperature sintering furnace as described in Section 6, the processing optimization had not yet been completed when cells #10 and #11 were fabricated.

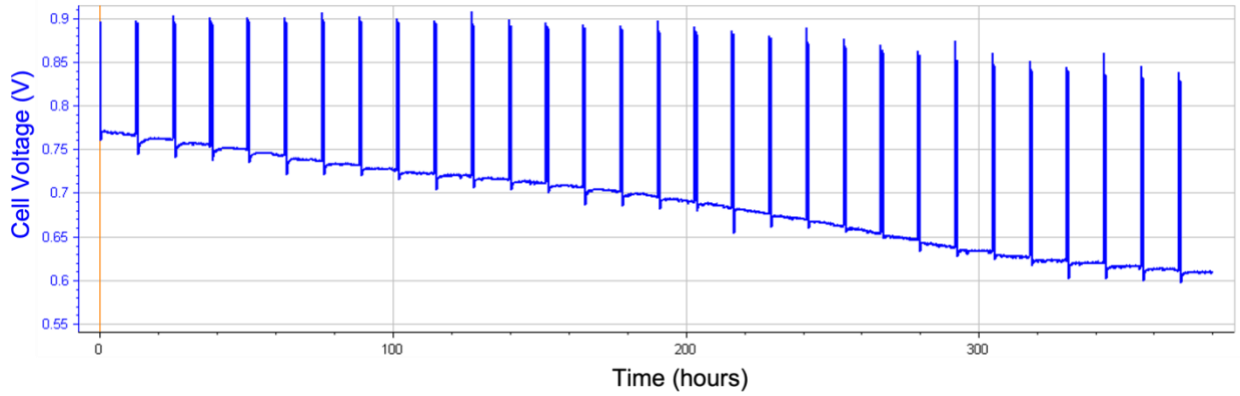

Figure 59. Cell voltage versus time for a 2.5 cm by 2.5 cm (modified-composition) SFCM-based ASL with AFL (*lower GDC content AFL at the lower sintering temperature*) SOFC (#11) operated at 600 °C in humidified H_2 with a fixed current density of 0.3 A/cm^2 until about 250 hours before current density was periodically.

Several approximately 2.5 cm by 2.5 cm cells with the same (modified-composition) SFCM-based ASL with AFL configuration were tested, and each displayed nearly identical behavior. Additionally, each of these cells utilized a silver contact. Silver contacts are thought to be a contributing cause for the delamination that occurred in the previous SFCM-based ceramic anode cells (e.g., cells #1 through #9) due to the strong bond between the silver contact and mesh current collector. While delamination may have initiated during testing of those cells (i.e., resulted in increasing OCV and/or increasing ASR over time), the most obvious delamination (i.e., complete

delamination the electrolyte from the anode) usually occurred during post-test disassembly and removal of the mesh current collector. Cells with the (modified-composition) SFCM-based ASL with AFL configuration did not experience this same delamination. Moreover, there were no instances with the new configuration where the OCV increased during testing, but rather the OCV decreased over time for these cells. Post-test analyses of these cells included SEM-EDS line scans of cell cross-sections as shown in **Figure 60**, which shows the concentration of silver along the indicated (green) line in the cross-section. There is a strong peak at the interface of the cathode/electrolyte, indicating that silver migrated from the cathode contact, through the cathode, and concentrated at the interface. The EDS line scan also indicates that the Ag diffused into the electrolyte, which is therefore concluded as being the likely cause for the decreasing OCV over time.

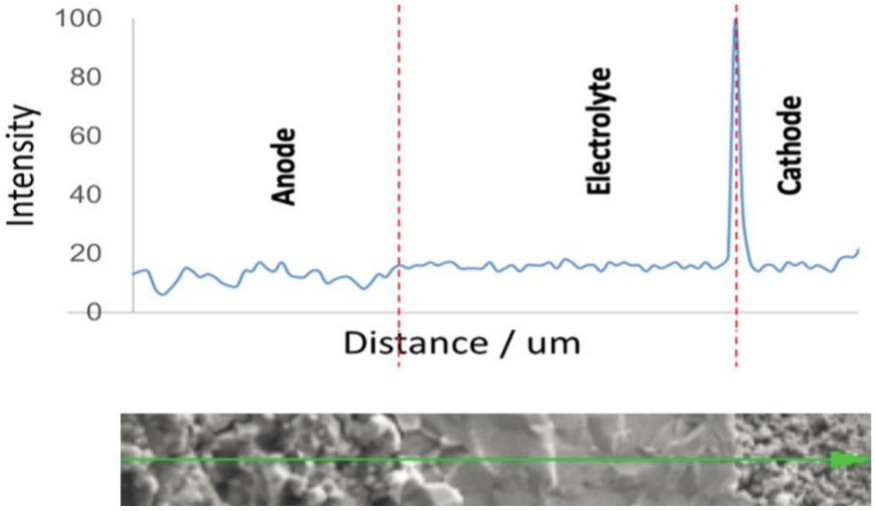

Figure 60. EDS line scan across a post-tested (modified-composition, SFCM-based ASL with AFL; *lower GDC content AFL at the lower sintering temperature*) large format cell demonstrates the presence of Ag at the cathode/electrolyte interface and within the electrolyte, indicating Ag migrated from the contact during operation and caused a decreasing OCV over time.

For comparison with the (modified-composition) SFCM-based ASL with AFL cell configuration, **Figure 61** shows an example of increasing OCV (blue curve) over time at a fixed current density for an earlier version of a 5 cm by 5 cm SFCM-based ceramic anode cell as the electrolyte delaminated from the anode. The OCV (blue curve) increased from about 0.88 V to over 1 V over a period of more than 100 hours in which the cell was mostly under a fixed current density of around 0.1 A/cm^2 (red curve). This is very different behavior than was observed for the (modified-

composition) SFCM-based ASL with AFL cells, likely due to the improved bonding between the anode and electrolyte.

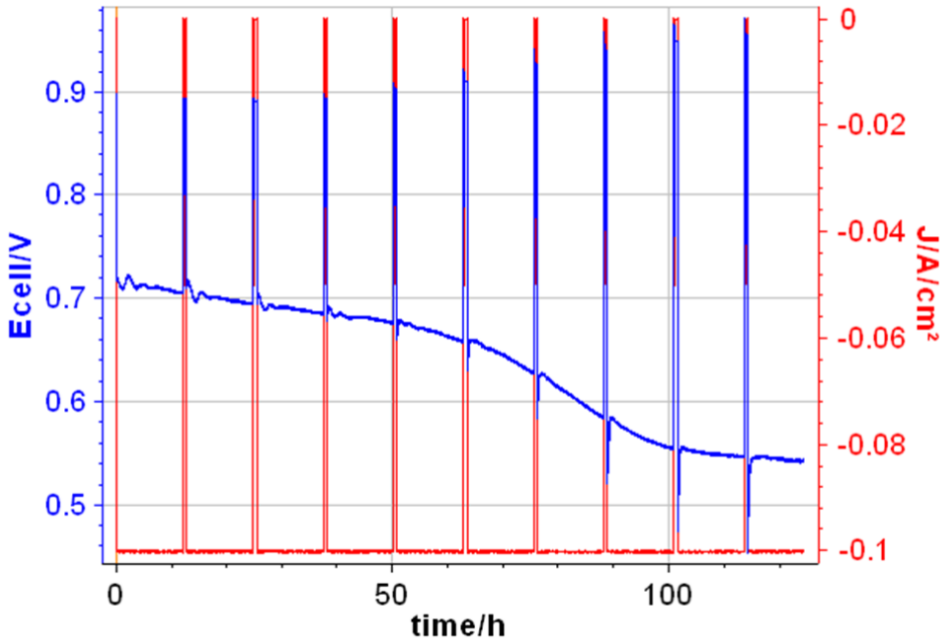

Figure 61. Example of increasing open circuit voltage (blue curve; OCV measured every 10 hours) observed over time with an earlier version of 5 cm by 5 cm SFCM-based ceramic anode cell configuration at 600 °C in humidified H_2 at a fixed current density of 0.1 A/cm^2 (red curve; goes to zero briefly for the periodic OCV measurement).

A 5 cm by 5 cm cell (#12) was made using the same (modified-composition) SFCM-based ASL with AFL configuration and SSC-GDC material, but a ceramic-based cathode contact was used rather than silver. The ASR increased ~6.5 times from the initial baseline after 60 hours when operated at 600 °C in humid hydrogen at fixed current density that was initially 0.4 A/cm^2 and later changed to 0.05 A/cm^2 (**Figure 62**). While extensive delamination did not occur (as happened with the earlier versions of SFCM-based ceramic anode cells), post-test SEM analysis indicated some possible points of delamination rather than separation across the entire electrolyte/anode interface. Note, that this cell had a particularly large amount of camber (more than twice the normal amount for the large format SFCM-based cells) and there is some indication that cracking occurred in the location of delamination (e.g., a black mark indicative of combustion during operation). Therefore, there is the possibility that cracking happened first due to a greater amount of stress in this region and that the resulting combustion increased the stress and led to localized points of

delamination. With this additional data, we decided to further increase the bonding strength between the electrolyte and AFL layers to further improve stability. We also avoided using cells that had such high camber.

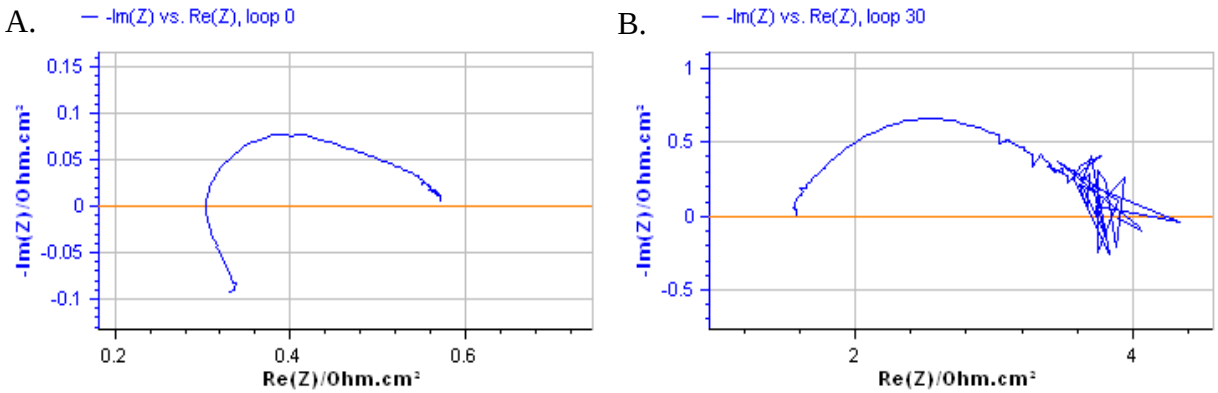

Figure 62. EIS data measured at OCV for 5 cm by 5 cm (modified-composition) SFCM-based ASL with AFL (*lower GDC content AFL at the lower sintering temperature*) SOFC (#12) operated at 600 °C in humidified H_2 (held mostly at fixed current density of initially 0.4 A/cm^2, and then lowered to 0.05 A/cm^2), showing data for A) Loop 0 (shortly after OCV stabilized) and B) Loop 30 (60 hours later) which showed an ASR increase of ~6.5 times higher than the initial value.

To achieve further increased bond strength between the electrolyte and AFL layers, the ceria content of the AFL was increased. As-fabricated porosity was also decreased. Initially, 5 cm by 5 cm half cells were still fired at the lower sintering temperature. As shown in **Figure 63**A, the initial ASR of this cell (#13) was ~1.6 times higher than the 5 cm by 5 cm (modified-composition) SFCM-based ASL with AFL cell that had the AFL with lower GDC content and higher as-fabricated porosity (*see **Figure 62**A*). While part of the increased ASR was a result of an increased Ohmic contribution, the major cause was a higher electrode polarization, which was likely due to decreased catalyst loading in the anode (~3.9 wt% versus ~7.4 wt%). Because the as-fabricated porosity of the AFL was decreased, less catalyst was able to penetrate the AFL and reach the AFL/electrolyte interface. Note, the use of vacuum infiltration can result in an increased catalyst loading for the lower porosity AFL. Despite the larger ASR, this cell's higher-GDC content and lower as-fabricated porosity of the AFL resulted in a much lower ASR degradation rate (~2 times increase from baseline Loop 0 measurement after 60 hours) as shown in **Figure 63**B when compared to that of the lower-GDC content and higher porosity AFL cell shown in **Figure 62**B (~6.5 times increase after 60 hours).

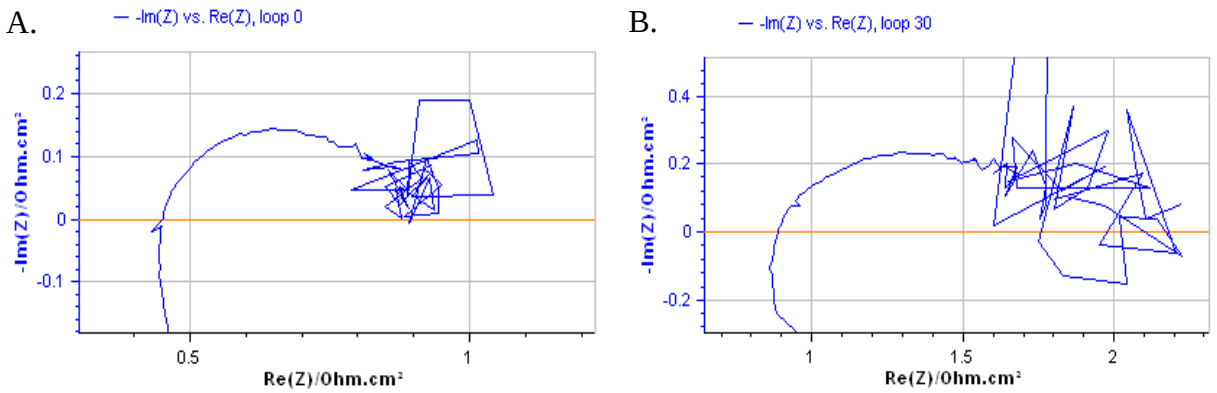

Figure 63. EIS data measured at OCV for 5 cm by 5 cm (modified-composition) SFCM-based ASL with AFL (*higher GDC content AFL at the lower sintering temperature*) SOFC (#13) operated at 600 °C in humidified H_2 (held mostly at fixed current density of initially 0.4 A/cm^2, and then lowered to ~0.2 A/cm^2), showing data for A) Loop 0 (shortly after OCV stabilized) and B) Loop 30 (60 hours later) which showed an ASR increase of ~6.5 times higher than the initial value.

Figure 64 shows the post-test SEM micrographs for a different 5 cm by 5 cm (modified-composition) SFCM-based ASL with AFL (*higher GDC content AFL at the lower sintering temperature*) which had even lower degradation. This cell (#14) operated at ~550 °C and had an approximately 1.6x ASR increase over 60 hours. The SEM micrographs demonstrate that there were no cracks or delamination observed in the electrolyte or at the electrolyte/anode interface for this (modified-composition) SFCM-based ASL with AFL SOFC. In other words, the higher-GDC content and lower as-fabricated porosity in the AFL resulted in better bonding between the electrolyte and the anode. Though the ASR degradation rate was still too high, these results demonstrated that improved electrolyte/AFL bonding strategy had a significant impact on degradation and indicated that the bonding was the leading cause for the degradation. While performance improvements are possible through vacuum infiltration and/or further optimization to the anode pore morphology, the next step of optimization involved continued improvement in bonding between the electrolyte and anode using a higher sintering temperature.

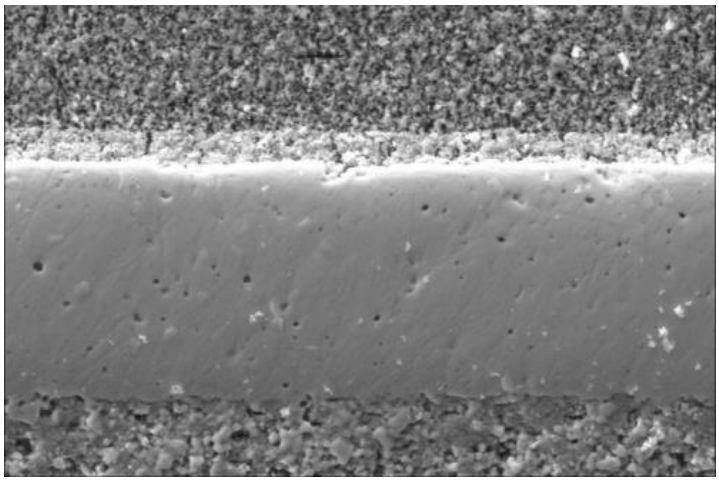

Figure 64. Post-test SEM cross-sectional micrograph of a 5 cm by 5 cm (modified-composition) SFCM-based ASL with AFL (*higher GDC content AFL at the lower sintering temperature*) SOFC (#14) operated for >140 hours at 550 °C in humidified H_2 (held mostly at fixed current density of initially 0.2 A/cm^2, and then lowered to ~0.1 A/cm^2).

Using the same level of (decreased) porosity and (higher) ceria content, a 5 cm by 5 cm (modified-composition) SFCM-based ASL with AFL cell (#15) was fired at a *higher* sintering temperature for even better bonding of the anode to the electrolyte. This cell had no CFL and used an SSC-GDC cathode with ceramic-based contact. The cell was operated for more than 60 hours at 600 °C in humidified H_2, cycling between open circuit voltage and the same fixed current density (~0.35A/cm^2). **Figure 65** shows the cell operating voltage versus time for this cell. Since the open circuit voltage was essentially constant, the ASR was stable as well since the operating voltage (at the same fixed current) did not change. Note, the ASR is relatively high for this cell in part due to a relatively low anode-catalyst loading, but also likely because of relatively high camber. The Ohmic resistance was relatively high (> 0.6 Ω-cm^2) and high camber can lead to poor contact with the current collector. Regardless, the better electrolyte/AFL bonding that resulted from the higher GDC content, lower porosity, and higher sintering temperature improved cell stability significantly.

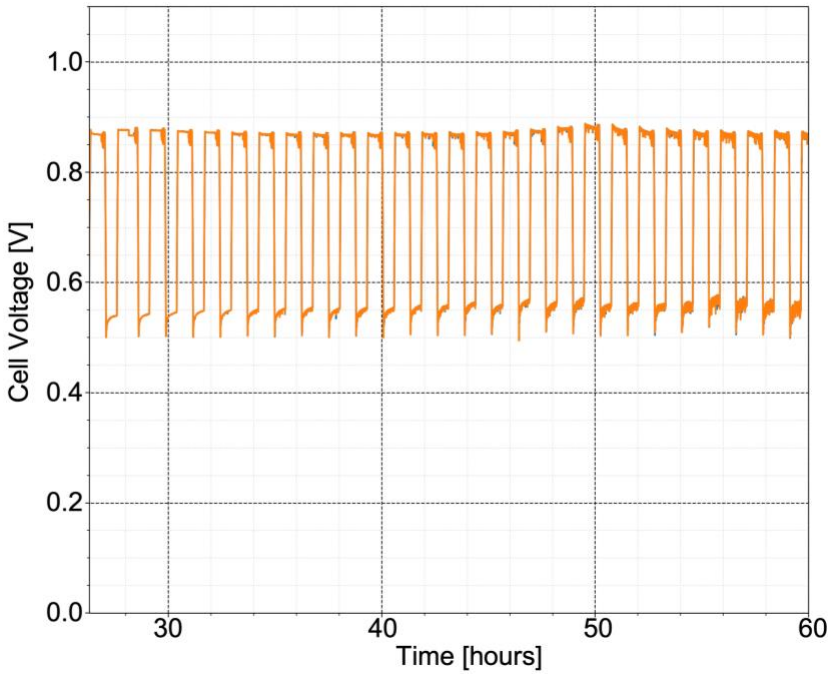

Figure 65. Cell voltage versus time for (modified-composition) SFCM-based ASL with AFL (*higher GDC content AFL at the higher sintering temperature*) SOFC (#15) operating at 600 °C for over 60 hours with humidified H_2 and with current density periodically cycled between a fixed current density of ~0.35 A/cm^2 and open circuit voltage to assess stability.

Throughout this project, we have shown that the SFCM-based ceramic anode SOFCs are capable of reduction-oxidation stability. We have also shown that through proper tuning of the anode, a high performance is possible (e.g., 0.6 W/cm^2 at 0.75 V when operated at 600 °C as shown in **Figure 41** and **Figure 58**). As discussed in Section 6, during the scale-up of cell size, we encountered difficulties (e.g., matching shrinkage between the half-cell layers) and had to modify anode compositions, degree of porosity, and half-cell sintering temperature to achieve flat cells. Some of these modifications seem to have significantly decreased the bonding strength between the anode and the electrolyte. While there was some evidence for Sr exsolution and formation of SrO, SrOH, or $SrCO_3$ in the anode near the interface with the electrolyte, we ultimately concluded that weak bonding and relatively low mechanical strength caused the delamination observed in earlier large format SFCM-based cells, which in some cases led to the formation of Sr precipitates in the presence of water at lower temperatures (e.g., during heating or cooling in humid anode gas streams). Additional results regarding the formation of Sr precipitates for SFCM-based anodes are presented in APPENDIX B. In our efforts to understand the cause for the delamination, we

explored the use of modified cell structure that included a thicker SFCM-based ASL combined with a thinner AFL. Cell stability was greatly improved when testing the modified structure, but to further improve stability we had to increase the ceria content and decrease the as-fabricated porosity of the AFL. In doing so, the amount of catalyst infiltrate in the anode decreased and resulted in lower cell performance. However, performance greater than or equal to that of the best performing large format SFCM-based cell (i.e., see **Figure 41** and **Figure 58**) is possible using vacuum infiltration and/or with an optimized anode pore microstructure (without weakening the electrolyte/anode interface) to increase the catalyst loading. Red-ox cycling robustness with the (modified-composition) SFCM-based ASL with AFL SOFCs was also demonstrated in stacks, as presented in Section 5.

5. OPTIMIZATION OF A RED-OX ROBUST STACK

To develop a red-ox robust stack, there must be a red-ox stable SOFC. Furthermore, since the red-ox cycling occurs in the anode compartment the balance of stack with respect to the anode must also be red-ox stable. Evaluation of the stack components' red-ox cycling robustness therefore focused on materials within the anode-compartment of the stack. The fuel interruption experienced during real world red-ox cycling could be caused by a disruption in the fuel flow, or mechanical failure of the cell, seal, or gasket material to allow internal direct mixing of fuel and air at the anode. Similarly, materials on the cathode would only be subjected to a reducing ambient by a mechanical failure in the cell or gasket/seal material allowing fuel to enter the cathode compartment. Such mechanical failures are not typical of normal stack operation and would potentially lead to total stack failure requiring stack replacement and should therefore be avoided in a well-functioning stack design. Thus, reduction oxidation stability of cathode materials was not investigated in this project. However, as the anode side of the stack experiences oxidizing conditions during the oxidation portion of a red-ox cycle, we did evaluate the red-ox robustness of some interconnect coatings typically used in the cathode compartment (e.g., $Mn_{3-x}Co_xO_4$, or MCO). Any stress that occurs due to red-ox cycling-induced chemical expansion of any of these materials cannot increase cell degradation or otherwise cause failure.

5.1. Evaluation of Stack Component Red-Ox Robustness

While there are various stack designs, all stacks consist of several key elements including interconnect, seals, and cells. **Figure 66A** shows a generic stack in an exploded view, whereas **Figure 66B** depicts a typical cross-section. Often there is a spacer (or window frame) around the permitter of the cell with multiple seals between the various components (e.g., between the cell and spacer, or between the spacer and the interconnect or separator plate). A stack is made up of many repeating units (or cassettes), where the cell, spacer, seals, and an interconnect make up the stack repeat unit (SRU). Generally, while SOFC stack seals can be glass or ceramic based and applied as a coating or layer during stack assembly, seals may also be gaskets (e.g., mineral gaskets comprising mica or vermiculite). There can be other components within the stack, such as current collectors (e.g., conductive mesh or foam as in **Figure 66B**) as well as coatings in different locations to provide, for instance, oxidation resistance, high conductivity contacts, and/or block chromium from becoming volatile and potentially poisoning the cathode. Metal interconnect parts have flow field channels and current collecting ribs optimized for the stack mechanical, electrical, chemical, and electrochemical constraints and the system design points and operating conditions. During the project, we evaluated the red-ox stability of these various components making up the stack using various means, such as dilatometry and seal leak tests. Improvements were made as necessary to match the characteristics of the SFCM-based ceramic anode SOFCs. Additionally, to characterize sources of long-term degradation in stacks for the SFCM-based ceramic anode, long-term anneals of different cell components (e.g., cathodes and contacts, and assembly components) were also undertaken.

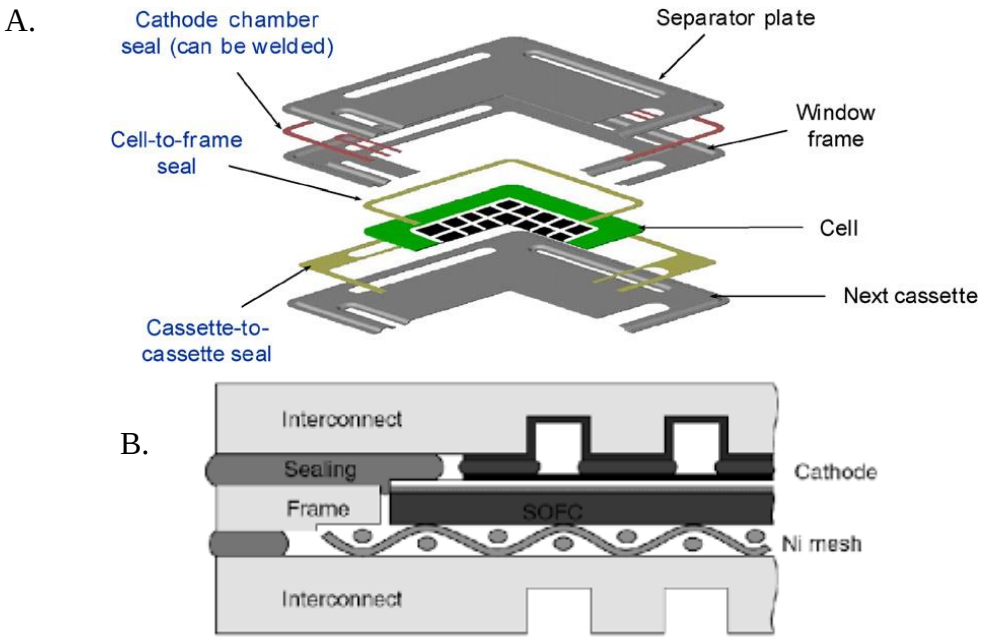

Figure 66. Examples showing the components within an SOFC stack with A) an exploded view [56] and B) a cross-section view [57].

Dilatometry. Various stack components were investigated for red-ox robustness both as separate components (when feasible) and coupled together to see differences in stress states when components are in a more "stack-like" configuration. These investigations used the vertical pushrod dilatometer shown in **Figure 12** to evaluate seal materials and interconnects.

The thermal expansion in air of glass sealing materials was evaluated using dilatometry. The glass materials were pressed into individual pellets and lightly sintered before. After loading a pellet into the dilatometer, temperature was ramped while expansion measurements were recorded. The results are shown in **Figure 67** for three different glass materials with the corresponding coefficients of thermal expansion (CTEs) reported in **Table 3** along with literature values. The glass transition temperature (T_g), where glass becomes significantly less viscous, is marked by a steep increase in the thermal expansion behavior. A sample of 400-series stainless steel interconnect material was also evaluated and included for comparison in **Table 3**. The glass materials have a similar CTE as the 400-series stainless steel. These CTEs are also similar to most SOFCs (e.g., Ni-cermet cells and SFCM-based ceramic anode cells), which serves to minimize the thermal stress during heat-up, operation, and thermal cycling of the stack. Similarities in CTEs between sealing materials and the cell and/or interconnect is also important for maintaining a high-

quality and leak-free seal. This initial assessment of CTE in air served as a baseline for subsequent red-ox cycling evaluations of sealing materials.

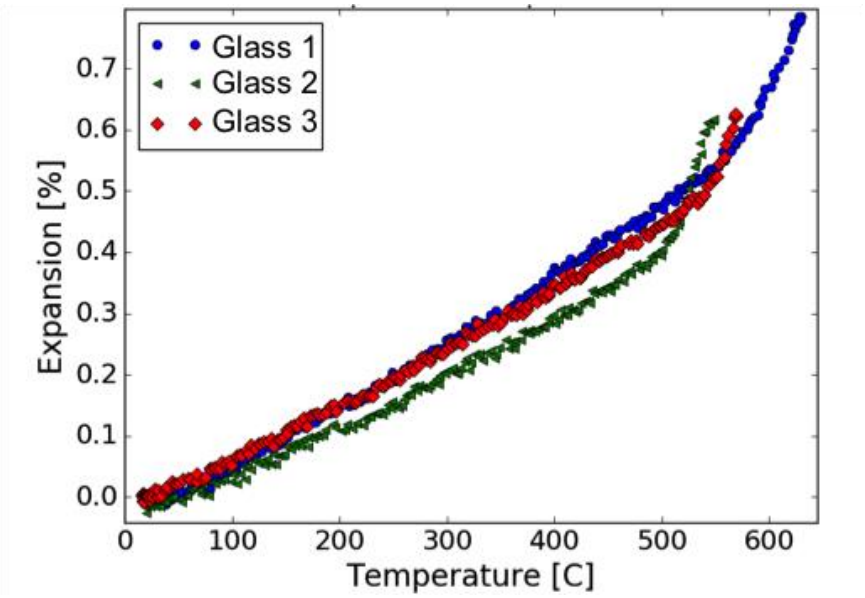

Figure 67. Thermal expansion during heating of sealing glasses measured in air, where the sudden increase in expansion above ~500 °C marks the glass transition temperature for each glass.

Table 3. Coefficient of thermal expansion (CTE) measured in air of glass and interconnect (400 series stainless steel) components used in the stack.

	Measured Value		**Literature Value**	
	CTE [ppm/°C]	**T range** [°C]	**CTE** [ppm/°C]	**T range** [°C]
400 series stainless steel	11.1	22-538	11.4	0-538
Glass 1	10.2	20-500	9.5	n/a
Glass 2	8.5	20-500	9.7	n/a
Glass 3	9.3	20-500	9.8	n/a

Dilatometry was also used to evaluate the mechanical stability of sealing components under red-ox cycling. **Figure 68** shows the expansion behavior for a mineral-based gasket material, which undergoes a relatively fast expansion during the initial exposure to reducing conditions of each red-ox cycle (i.e., humidified 3% H_2 / balance N_2). The gasket material subsequently displays long-term shrinkage behavior. Upon oxidation in dry air, the sample shrinks quickly but then stabilizes. Overall, each red-ox cycle induced a < 1% shrinkage of the gasket material. Moreover, the shrinkage effect seems to decrease as the number of cycles increases.

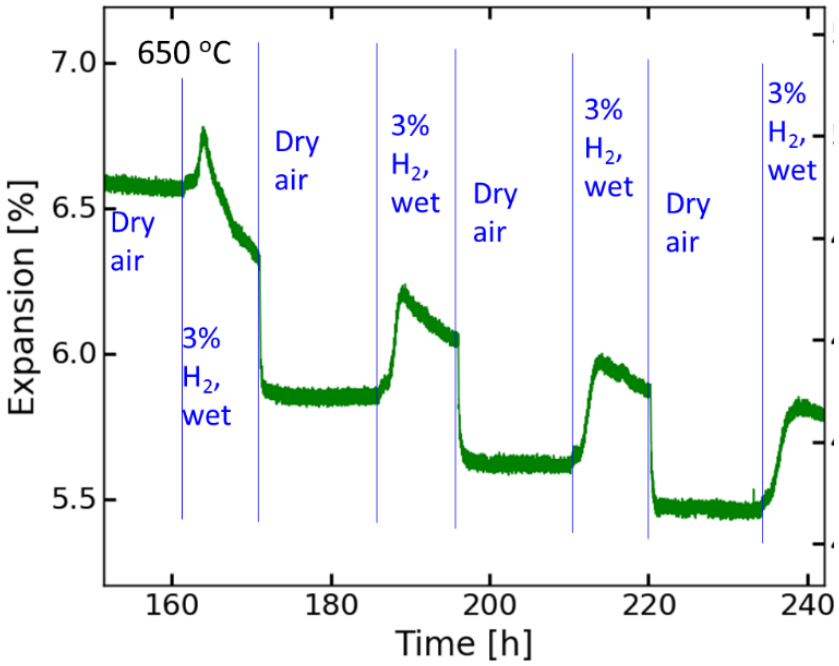

Figure 68. Length change measurements during red-ox cycling of gasket material at 650 °C display a gradual decrease in length of the sample with increasing red-ox cycle number.

Glass seal materials, on the other hand, do not exhibit any measurable dependence on red-ox cycles as shown in **Figure 69**. Very little change in expansion is observed when cycling between wet 5% H_2/balance N_2 and dry air. However, long-term shrinkage is observed for both air and reducing conditions (H_2 or N_2) for the first approximately 35-40 hours and is likely related to creep of the glass. Sudden dips in the measured expansion occur periodically and are subsequently recovered because of fluctuations in temperature following gas changes during red-ox cycling. Note, the mineral-based gasket materials have a similar CTE as the glass materials despite the observed differences in expansion upon red-ox cycling.

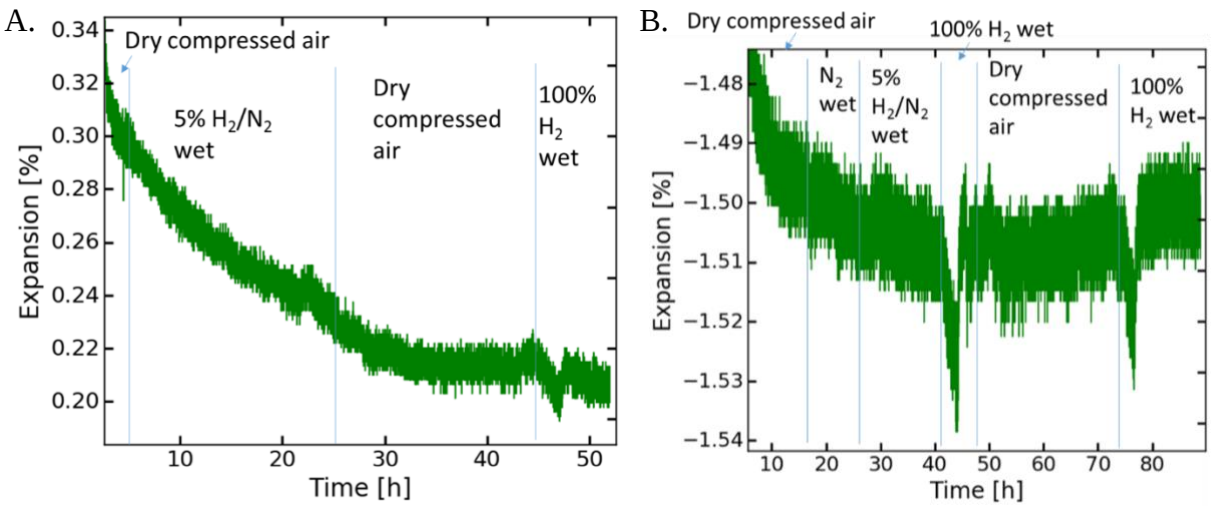

Figure 69. Length change measurements during red-ox cycling of two different glass compositions A) and B) measured at 650 °C.

Figure 70 shows the length change (expansion) of a stack of gasket material during red-ox cycling. The same red-ox conditions were used as in **Figure 18** for the SFCM-based ceramic anode half-cell, but with 3% H_2 (instead of 5%) during the reducing state. As observed for the single piece of gasket material shown in **Figure 68**, upon exposure to reducing conditions the gasket expands while switching to air causes the gasket to shrink. The shrinkage is more than the expansion on each cycle, leading to an irreversible shrinkage of the gasket. The rate of irreversible shrinkage seems to be more rapid within the first 8 cycles, then slows to a lower but approximately constant rate per cycle for the rest of the measurement. Over the entire 22 redox cycles, the gasket shrank by a total of 2%. Note that the magnitude of expansion and the irreversible behavior is consistent with the result in **Figure 68**. The starting expansion (due to heating from room temperature) for the stack of gasket material is almost the same as the previous measurement of a single piece of gasket material, showing good reproducibility in the experimental technique and sample behavior. Also note that at ~30 hours (the 4th cycle), the flow rates were doubled to evaluate if sufficient purge of each gas occurred between changes in the gas environment. The peaks became flatter as a result of the higher flow rate, presumably reaching equilibrium more quickly and indicating that the initial flow rate was insufficient to equilibrate the gas composition during the purge, and therefore confirming similar suspicions in the data of **Figure 18**.

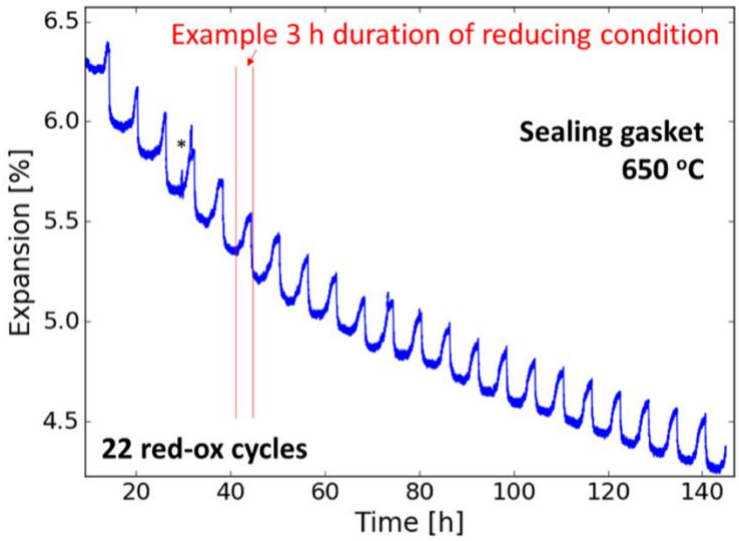

Figure 70. Impact of red-ox cycling (from dry air to humidified 3% H_2 in N_2) on length of a stack of gasket material. The peaks left and right of the asterisk at 30 hours correspond to a sudden fluctuation of temperature due to a controller instability.

Red-Ox Stability of Stack Coatings. We evaluated the red-ox stability of stack coating materials used to ensure good contact is made between the anode-side interconnect and the fuel cell. Two different coating materials were evaluated, namely Ag and $Mn_{1.5}Co_{1.5}O_4$ (MCO). While MCO is more commonly used on the cathode side as a Cr diffusion and oxidation barrier, it is of interest for the anode side in this work to potentially serve as an oxidation barrier during oxidizing conditions in the red-ox cycled stack. Both Ag and MCO materials were applied in slurry form to different interconnect samples and thermally annealed prior to testing. Each material was tested separately with two samples of the same coating placed face-to-face and clamped in a stainless-steel fixture. Area-specific-resistance (ASR) was measured using reference electrodes in contact with the interconnect samples, thereby ensuring ASR is measured through the coatings of interest. The first part of the test involved annealing the samples in humidified 100% H_2 for >100 hours at 600 °C. The samples subsequently underwent red-ox cycling between dry air and humidified 100% H_2 with 3 hour holds in each condition. The Ag-coated samples had an ASR that was too low to measure with the setup, though based on specifications the ASR is estimated to be less than 1 mΩ-cm^2 through the coating and indicating a very conductive coating. Throughout the course of the long-term reducing anneal and 8 red-ox cycles, the ASR for the Ag coating remained below the measurement limit, indicating this coating is highly tolerant of red-ox cycling.

The ASR for the MCO coated samples during the thermal anneal and red-ox cycling are shown in **Figure 71**. For the first 100 hours, ASR increased from ~100 mΩ-cm^2 to ~200 mΩ-cm^2, but then seems to have saturated. Note that the measurement exhibits a significant amount of noise and that the ASR values are relatively high. At this temperature, values of ~50 mΩ-cm^2 are more typical for similarly processed MCO coatings. The high ASR and noise in the data are most likely related to poor interfacial contact between the face-to-face MCO coated samples as no other contact material was used between the two samples. This contrasts with the silver coated samples which, due to the ease of Ag migration, tend to bond with each other and in fact the Ag samples were stuck together at the end of the measurement of that coating material. Despite the poor contact, the general trend in the MCO data is useful for qualitative evaluation of coating ASR. At ~110 hours, red-ox cycling was started on the MCO coated samples and some repeated, consistent fluctuations in ASR were observed. Also note that temperature fluctuated during the red-ox cycles (as indicated in the blue trace of **Figure 71**) due to cycling between air and H_2 gas streams and differences in their respective thermal conductivities. The MCO coating did not show any obvious degradation in ASR after three red-ox cycles.

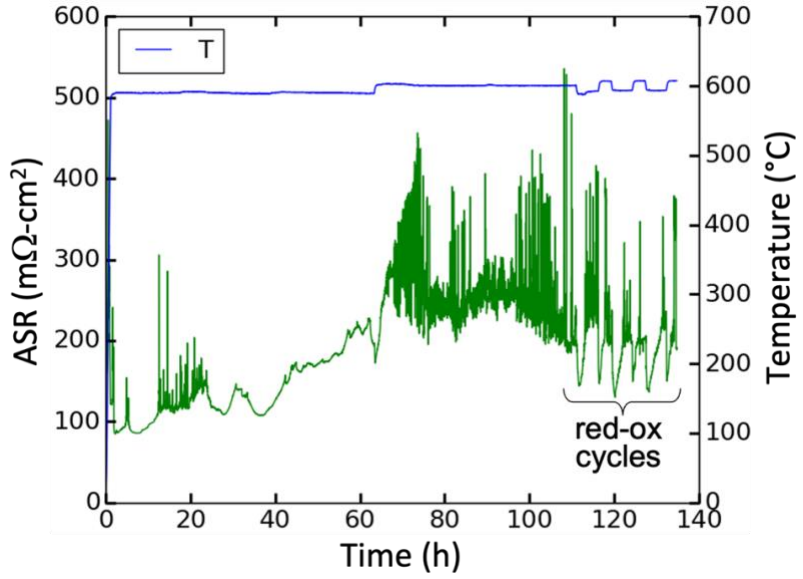

Figure 71. ASR (green) and temperature (blue) during the MCO thermal anneal and red-ox cycling measurements — at ~110 hours, red-ox cycling was initiated, resulting in small oscillations in temperature that in turn resulted in corresponding changes of sample ASR.

5.2. Stack Leak Evaluation During Red-Ox Cycling

The dilatometry studies of the various seal materials showed only a relatively minor impact of red-ox cycling on dilation. To better understand how this translates to seal performance we performed red-ox cycling studies using 10 cm by 10 cm stack hardware. The stacks were fabricated using our standard assembly procedures. We evaluated seals using both a dense alumina sheet as a mock cell and a Ni-YSZ cermet-based half cell (i.e., no cathode), each with a similar thickness. For the alumina mock cell, the anode compartment was cycled between 100% dry H_2 and shop air, while the cathode compartment remained in a constant flow of air at 650 °C. Gas chromatography, volumetric flow meters, and humidity sensors were used to evaluate crossover of gases from the cathode compartment to the anode compartment (i.e., cathode-to-anode (or air) crossover), and vice versa (i.e., anode-to-cathode (or fuel) crossover). The standard timing of the cycling in these tests (used between cycles 0 and 16) was 4 hours in the reducing condition and 4 hours in the oxidizing condition, with an approximately 25-minute N_2 purge between cycles. Cycle 7 had a deviation wherein the air step was held for 37 hours. Between cycles 17 and 22, the oxidizing and reducing conditions were held for only 2 hours during each step. The more rapid red-ox cycling was used to decouple other degradation modes versus time and degradation due to red-ox cycling. A less aggressive schedule of 100% dry H_2 alternating with industrial N_2 (~0.01-0.02% by gas chromatography) was adopted on the Ni-YSZ cermet half cell to see how such a cell handled less aggressive oxidizing conditions. The crossover leak rate summary versus number of red-ox cycles is shown in **Figure 72**. The crossover leak rate values are normalized to the largest value observed (cycle 3 of the Std. Ni-YSZ cermet half cell fuel crossover). The gap in data points between cycle 17-22 for the alumina sample cover a more rapid red-ox cycling frequency where experimental data could not be reliably gathered. Note, see Section 4.4 for a more detailed explanation of the use of industrial N_2 as an oxidizing gas during red-ox cycling.

Figure 72 clearly shows that the crossover increased dramatically for the Ni-YSZ cermet half cell, which as the anode support contains Ni is known to be susceptible to red-ox cycling instabilities. After the test, we verified that the Ni-YSZ cermet half cell exhibited significant cracking in the electrolyte. This occurred after only 3 red-ox cycles even though much gentler oxidizing conditions were used. The alumina mock cell, on the other hand, showed only a small increase in crossover even after more than 20 cycles of red-ox cycling using the more aggressive oxidizing

conditions. The slight increase in the crossover leak rate with cycling in **Figure 72** for the alumina mock cell may be related to the reversible and irreversible expansion behavior of the seal materials as was observed in dilatometry measurements (e.g., see **Figure 68** through **Figure 70**). Overall, this result indicates that the seal system for the stack offers a reasonable and acceptable red-ox cycling robustness.

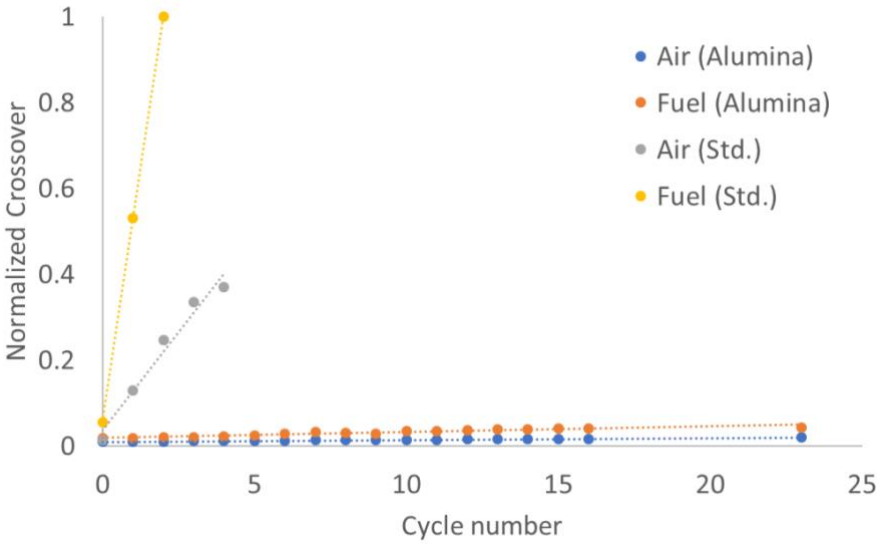

Figure 72. Normalized cathode-to-anode (air) and anode-to-cathode (fuel) crossover during red-ox cycling of an alumina sheet mock cell and a standard (Std.) Ni-YSZ cermet half cell at 650 °C.

We also ran a similar seal evaluation test using an SFCM-based ceramic anode SOFC (configuration as shown in **Figure 8**A) using 5 cm by 5 cm stack hardware. As the 5 cm by 5 cm hardware is essentially identical to the 10 cm by 10 cm hardware, these test results can be compared to those of the alumina sheet mock cell and Ni-cermet half cell which were collected using the 10 cm by 10 cm stack hardware. A comparison of the results for these tests is provided in **Figure 73**. All crossover leak rates have been normalized to the largest value observed (i.e., that of the Ni-YSZ cermet half cell). After 4 cycles the Ni-cermet cell exhibited a large amount of cathode-to-anode (N_2) crossover. The ceramic anode test, in comparison, showed about 90% lower leakage rate after 4 cycles. Moreover, the SFCM-based ceramic anode cell accomplished this despite having a slightly higher baseline (cycle 0) leakage rate than in the case of the Ni-cermet cell.

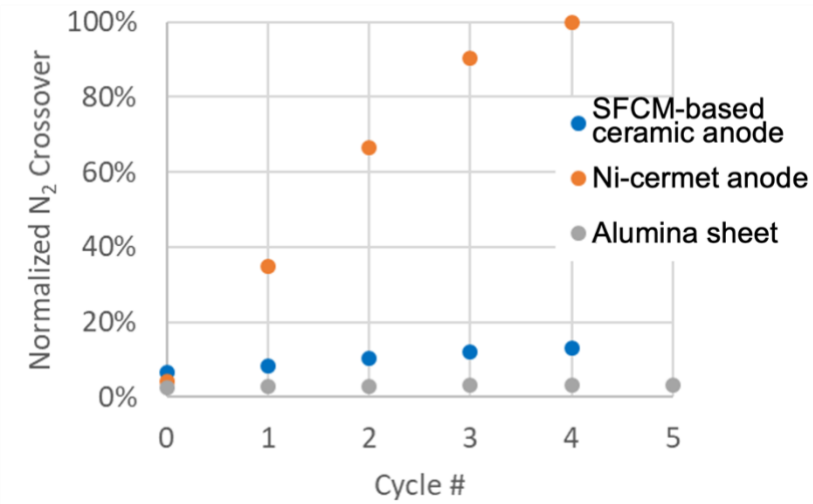

Figure 73. Normalized cathode-to-anode (N_2) crossover during red-ox cycling of a 5 cm by 5 cm SFCM-based ceramic anode SOFC at 600 °C (cycles between H_2 and industrial N_2 with ~0.01-0.02% O_2) compared to measurements made using a 10 cm by 10 cm half cell with a Ni-cermet anode (cycles between H_2 and industrial N_2 with ~0.01-0.02% O_2) and a 10 cm by 10 cm alumina sheet mock cell (cycles between H_2 and air) at 650 °C.

The OCV of the SFCM-based ceramic anode SOFC also showed good stability after each red-ox cycle, which was between 0.86 V and 0.87 V during each cycle. Impedance spectroscopy was used to evaluate changes in the ASR as the number of red-ox cycles increased. Measurements were made in the reducing condition. As shown in **Figure 74**, the high frequency (Ohmic) and low frequency (non-Ohmic or electrode) components of the ASR increased with increasing number of red-ox cycles. The large increase in ASR does not seem to correlate with red-ox cycles, which were performed every 4 hours, but rather seems to be related to another degradation mode. Similar SOFC tests of large format (i.e., ≥ 5 cm by 5 cm) or smaller (e.g., 4 cm by 4 cm) SFCM-based ceramic anode SOFCs also showed relatively high degradation rates as described in Section 4.4. Such degradation was ultimately linked to low mechanical strength of SFCM-based SOFCs and poor bonding between the anode and electrolyte, and solutions were described and presented in that section. Nonetheless, these stack leak evaluation tests demonstrate that the red-ox stability of the SFCM-based ceramic anode SOFCs is dramatically superior to the Ni-cermet anode cell. These tests also further demonstrated the red-ox robustness of the stack design and materials in general.

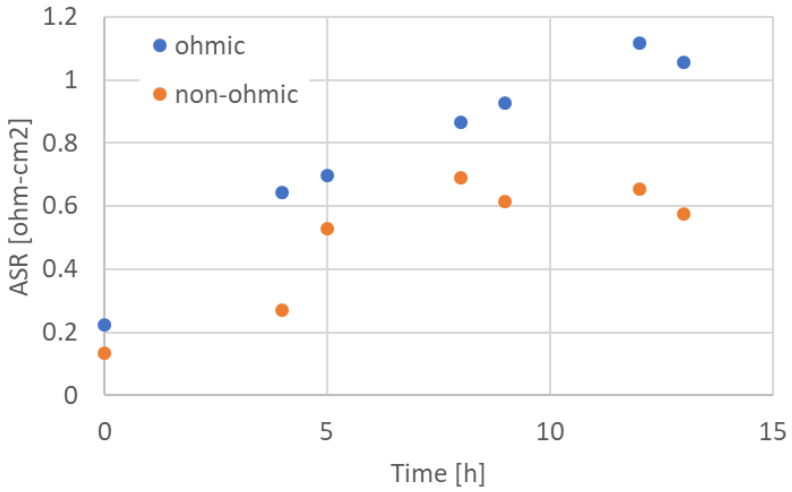

Figure 74. ASR of the 5 cm by 5 cm SFCM-based ceramic anode SOFC measured by impedance spectroscopy during stack leak evaluation/red-ox cycling tests.

5.3. Red-Ox Robust Stack Modeling

SOFC systems can ultimately fail due to red-ox cycling induced degradation at the stack level but can have a root cause from extrinsic sources such as a fuel shortage, emergency shutdown, and/or bad controls. Alternatively, root causes may come from an intrinsic source such as crossover at the seal or gasket between the anode and cathode streams. Each time a conventional Ni-cermet anode experiences a switching between oxidizing (air) and reducing (fuel) conditions represents a chance for damage and ultimately failure. To aid in the design of the red-ox robust stack, we modified Redox's proprietary multi-physics model to include the necessary coupling of thermo-mechanical and chemical-mechanical physics to capture the stresses that arise during heat-up, reduction, and operation of a ceramic anode-supported SOFC stack, including what happens during red-ox cycling.

The reliability of SOFCs depends not only on the stability of electrochemical and chemical performances, but also integrity of the SOFC components. This means that the SOFC must withstand mechanical stresses during cell fabrication, stack assembly, and system operation and shutdown conditions. For planar anode-supported SOFCs, the anode support layer (ASL) typically dominates the mechanical strength because the thickness is much larger than the other layers. Thus, complete stack failure is possible if the ASL experiences mechanical failure (e.g., buckling). Mechanical failure can even happen during stack assembly when the cells undergo various degrees of mechanical loading at the different contact regions within SRUs. For example, the stress will

be different between gasket/seal and cell than between the electrode and current collector contacts. Additional mechanical stresses will be created if there is any mechanical flattening of the cell to ensure sufficient compressive sealing and good electrical contact. Simulation results indicate that thermal expansion (CTE) mismatch can also greatly influence stress distributions in the components of the stack such as cell, contact mesh, and interconnect [58]. Therefore, it is critical to capture the combined residual stress from assembly and cell flattening together with CTE mismatch. Key parameters for a porous anode-supported cell (such as the SFCM-based ceramic anode SOFC) are mechanical strength, stiffness, and fracture toughness, all of which tend to decrease with an increase in porosity [59-60]. A decrease in Young's modulus can also occur during red-ox cycling when there is a large volumetric expansion, such as occurs with Ni-based anodes [61]. Therefore, irreversible cell damage may occur when the mechanical properties change due to the volume change experienced during a red-ox cycle.

Compared to button cells, when large format size cells (e.g., 5 cm by 5 cm to 10 cm by 10 cm) are operated at elevated temperature, the thermo-mechanical properties of the SOFC become very important due to non-uniform temperature distributions and resulting increases in localized stress. The localized stress can be even greater when the large format cells are assembled in a stack [62-63]. The temperature gradient depends strongly on the stack design, the operating conditions, and the gas flow configurations (e.g., co-flow versus cross-flow). Moreover, stack performance degradation is often a result of the degradation of the cell component materials themselves together with related effects due to concomitant re-distributions of fuel and temperature inside stacks [64]. Along the direction of the fuel flow in the channel with the consumption of fuel, the concentration of fuel decreases from inlet to outlet. For poor flow field designs there will be fuel rich and fuel lean channels. Areas of the cell exposed to fuel lean conditions may experience damaging oxidizing conditions. This may also occur during high fuel-utilization operation.

Redox's multi-physics model couples the mechanical, thermal, electrical, electrochemical, and chemical energy domains. For instance, the model simulates electron and oxide ions charge transfer, porous-media gas transport, and electrochemical reactions. The model contains expressions for the fundamental kinetics of both the anode (e.g., Ni-cermet) and cathodes (e.g., LSCF-GDC) via the Butler-Volmer expression and heterogeneous internal reforming reactions in

the anode [65]. The kinetic rates of reforming reactions for the SFCM-based ceramic anode largely depend on the infiltrated catalytically active particle and resulting microstructure. We therefore incorporated into the model the key parameters related to the new electrochemistry and heterogeneous chemistry. We used available results from the literature and experiments (e.g., fixed-bed (quartz tube) catalytic reactor) to fit the kinetics expressions within the model, capturing any differences in catalytic and electro-catalytic properties of the modified SFCM-based ceramic anodes.

Chemo-mechanical modeling. During the project, we prepared a multi-physics model to predict the stress in SOFCs due to reduction-oxidation cycling and acquired initial simulation results. The first test case involved modeling the reduction rate of NiO to Ni, the change in strain, and corresponding stress in a constrained system for a Ni-cermet based cell. This test case allowed us to verify the simulation results against the well-known behavior of Ni-cermet anodes. The SFCM-based ceramic anode was expected to have a significantly lower stress during reduction and oxidation as compared to the Ni-cermet, as suggested by dilatometry and other results (e.g., see Section 4.2). The model was later extended to predict the stress in an SFCM-based ceramic anode cell upon red-ox cycling. Thus, the expanded capability of the multi-physics model served as an aid in the development and design of red-ox robust cells and stacks.

The chemical-mechanical model is based on the nickel reduction/oxidation process, which has been well studied in the literature [66]. The first step in building the model was to implement a 0-D model for a reversible nickel reduction/oxidation reaction under isothermal conditions. The reaction kinetics were appropriately adjusted for each temperature studied (i.e., 600 °C, 650 °C, and 750 °C). **Figure 75** shows the degree of oxidation of NiO during an exemplar reduction process at different temperatures over a period of 300 minutes (5 hours). At higher temperatures, the reduction rate is much faster and the NiO is reduced (i.e., degree of oxidation approaches zero) relatively quickly.

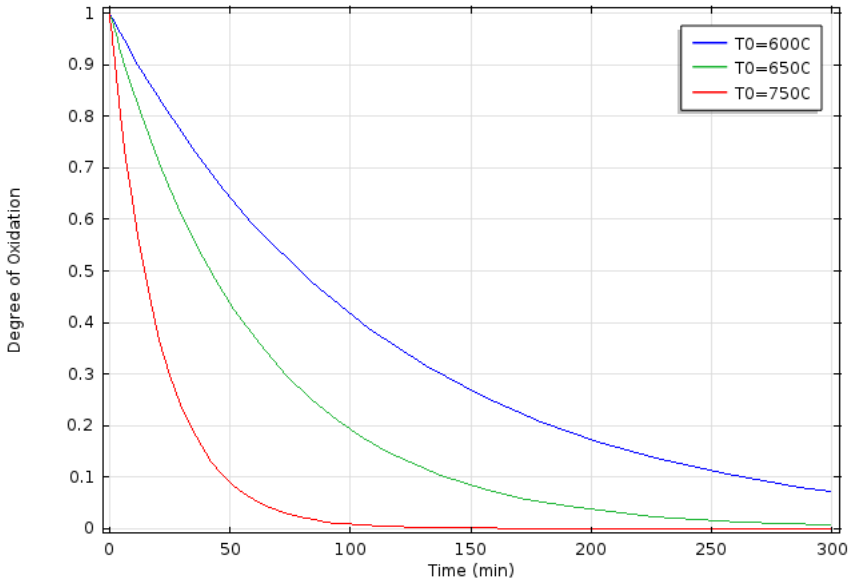

Figure 75. Degree of oxidation during reduction of a NiO-cermet anode cell for three different temperatures (0-D case).

The next model development step involved taking account of space dependencies by linking kinetics to a single channel geometry for the half cell, shown in **Figure 76**A. The complete model includes mass balance, energy balance, and momentum balance. The model also considers the impact of the change in anode porosity (e.g., impact on catalyst activity and flow dynamics). A test case simulation of the reduction process using the single channel model (**Figure 76**A) was performed. As with the 0-D model, the simulation result for the single channel model (**Figure 76**B) shows the total change in NiO to Ni concentrations across the entire cell during reduction, though now appropriately accounting for the cell and stack design. The YSZ concentration is also shown to remain flat since there is no chemical change to the YSZ phase in the Ni-cermet during reduction.

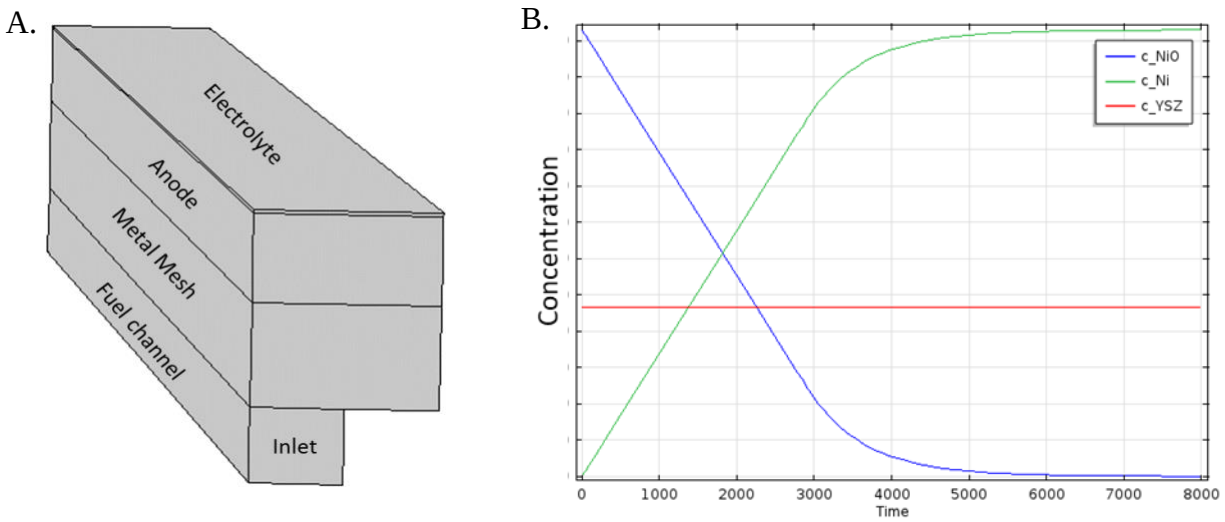

Figure 76. A) Single channel model showing half-cell layers and B) concentration changes of solid phase during cell reduction for the single channel model.

Transient studies of the evolution of NiO concentration during the reduction process were also evaluated. An example of a three-dimensional (3-D) concentration profile along the channel is shown in **Figure 77**. The faint patterns on the surface are due to the metal mesh current collector. The NiO concentration distribution within the anode is shown at 30 minutes into the reduction process (**Figure 77**A) with red representing more NiO and blue representing more Ni metal. A gradient in the NiO concentration through the thickness (top to bottom) is created due to exposure of the cell to H_2 on only the fuel side of the half-cell as is experienced under normal SOFC operating conditions. A second gradient is developed from the gas inlet to outlet (back to front in the figure), with greater Ni content near the inlet, as expected due to consumption of H_2 along the channel from inlet to outlet. **Figure 77**B shows the normalized concentration of pores within the anode after 30 minutes of reduction, where red represents a higher concentration of pores while areas with more blue colors have less porosity. The regions near the top show less porosity than the bottom of the anode because the reducing gas must first create porosity in the outer region of the anode before the inside portions can begin to reduce and become porous.

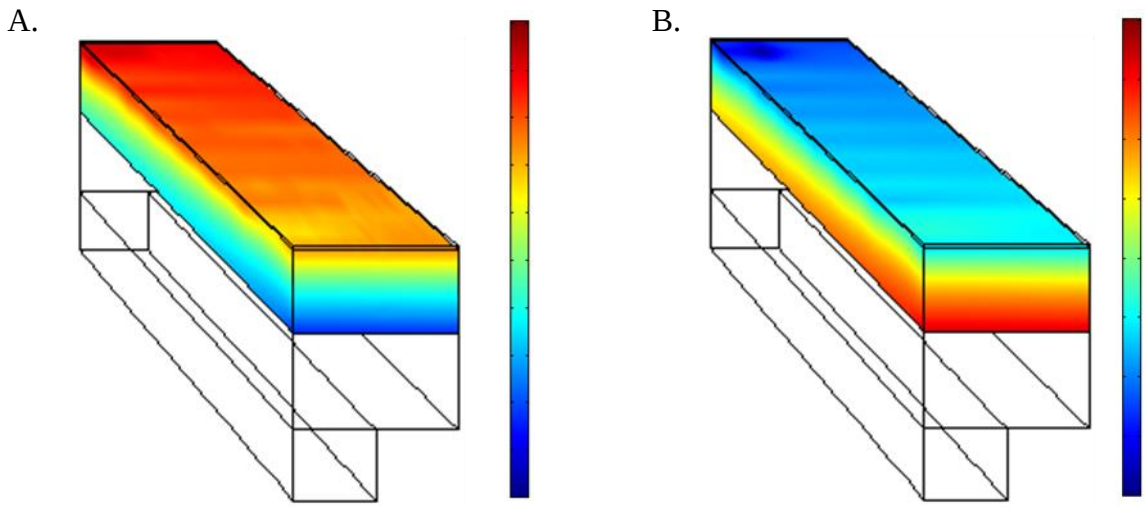

Figure 77. A 3-D concentration profile along the channel with a Ni-cermet cell, showing A) normalized anode NiO concentration and B) normalized porosity in the anode 30 minutes after reduction starts.

Hooke's law (Equation 1) was implemented in the model to evaluate the stress created during reduction. The thermal and chemical stress are included using the thermal ($\alpha\Delta\theta$) and chemical strain ($k\Delta\omega$) deformations in the strain tensor. Initially the model only considered chemical strains, but thermal strains were introduced later in the project.

$$\sigma = \sigma_0 + C:(\varepsilon - \varepsilon_0 - \alpha\Delta\theta - k\Delta\omega) \quad (1)$$

Figure 78 shows an example of the internal stress change during the reduction process in an isothermal condition. These results demonstrate a working chemo-mechanical model framework for a Ni-cermet anode.

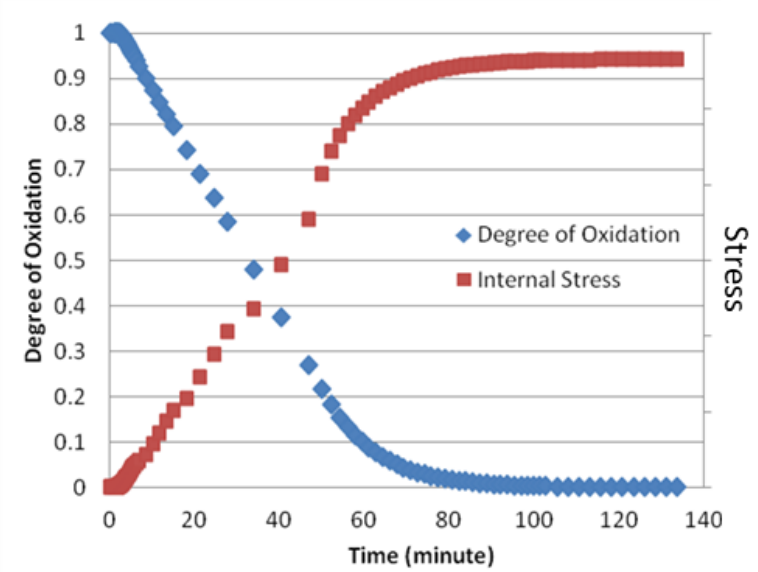

Figure 78. Stress developed in response to a nickel oxide chemical state change during the reduction process (Ni-cermet cell in a single channel model).

Thermo-chemo-mechanical modeling of a Ni-Cermet SOFC. The chemo-mechanical model framework was used initially to study mechanical stress developed during reduction of Ni-cermet based SOFCs. This was expanded to a thermo-chemo-mechanical model framework as shown in the **Figure 79** schematic. Note, though not indicated in the figure, the ceramic anode constitutes a solid phase and undergoes similar thermo-chemo-mechanical changes as those indicated within the framework schematic.

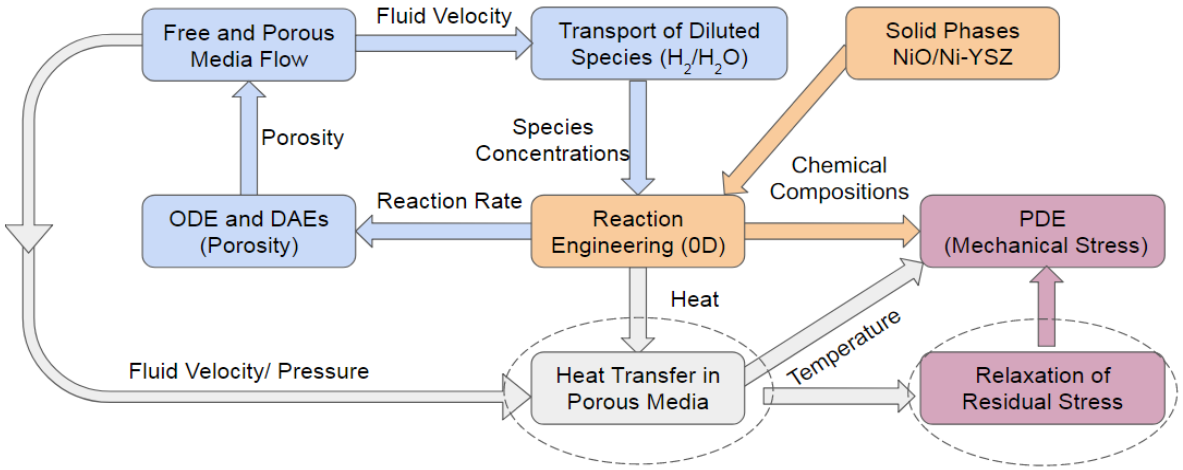

Figure 79. Schematic of the physics contained within the thermo-chemo-mechanical model, shown for a Ni-cermet cell but similar changes occur for the ceramic anode.

The first expansion to the framework was the addition of the heat transfer and energy balance physics to the simulation. In the previous version of the model, the simulated domains were held isothermally at 650 °C. In the expanded version, we accounted for heat released from nickel oxide (NiO) reduction and hydrogen oxidation based on reaction rates to evaluate the impact of non-uniform thermal expansion and resulting stresses during reduction. The second update to the model was the addition of both temperature- and time-related residual stress. When the cell is subjected to stresses at a (relatively) high operation temperature, internal stresses tend to relax and decrease over time. The rate at which this occurs is dependent on temperature and the degree of oxidation within the anode (i.e., metallic Ni will relax more than the oxide). Because of the time-dependent nature of stress relaxation, the total stress depends on how quickly the anode reduction reaction takes place. Similarly, reduction and oxidation reactions in the SFCM-based ceramic anode are expected to exhibit some degree of stress relaxation. If the anode is quickly reduced, there may not be enough time for the initial residual stresses to relax. Therefore, this feature allows the model to account for time-dependent stresses.

Several other minor changes were made to expanded thermo-chemo-mechanical model to more accurately represent the physics of reduction and oxidation compared to the original chemo-mechanical model. These include the following updates:

- The reaction kinetic equation was updated with the reaction rate correlated to both local temperature and solid phase (e.g., NiO) concentration.
- The diffusivity of the fluid was updated so that the effective diffusivity within the porous media is calculated based on local porosity.
- The mesh grid was updated to capture the large variations in the flow at the inlet and outlet.

Figure 80 shows the degree of oxidation (DoO) of the anode at different operation temperatures based on the updated reaction kinetic expression. Note, this result is from the 0-D model using only the updated NiO reduction reaction kinetics. The results agree well with available literature data at 600 °C and 750 °C [66]. Reaction rates in between these two temperatures (e.g., at 650 °C) were interpolated to investigate reduction of SOFC anodes and related chemo-mechanical stress across the full range of relevant operation temperatures.

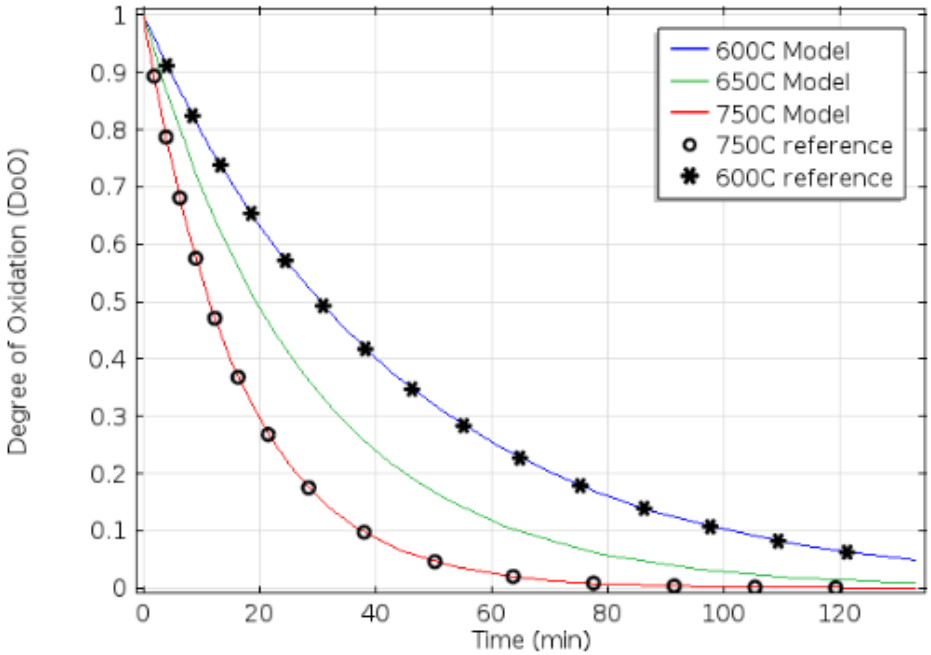

Figure 80. Degree of oxidation (DoO) plot with updated kinetics compared with reference data [66] (Ni-cermet half cell in a single channel model).

As the reaction progresses, the porosity increases and the NiO concentration decreases. Five minutes after reduction starts, the NiO concentration is predicted to be about 85-90% of the initial value. In a snapshot during the reduction process, the porosity varies with position and as expected is higher near the reducing gas inlet (red portion in the foreground of **Figure 81**A). Note, the results of **Figure 81** are for the fully updated 3-D thermo-chemo-mechanical model. The boundary condition before reduction (t = 0 seconds) is a uniform temperature of 650 °C for the modeled sample (see **Figure 76**A). Note, **Figure 81**A is noticeably different from the corresponding **Figure 77**B due to the differences in the updated thermo-chemo-mechanical model compared to the chemo-mechanical model. In short, as the process evolves, the increased porosity allows for faster reduction. Due to the overall exothermic process of NiO reduction with H_2, the sample heats up as the reaction progresses. The degree of oxidation is shown in **Figure 81**B at five minutes after the start of reduction with red representing a larger degree of oxidation (i.e., less reduction to Ni metal). **Figure 81**C shows that the inlet temperature is 650 °C due to convective cooling and increases gradually over the length of the stack. The temperature gradient during reduction is small (< 5 °C).

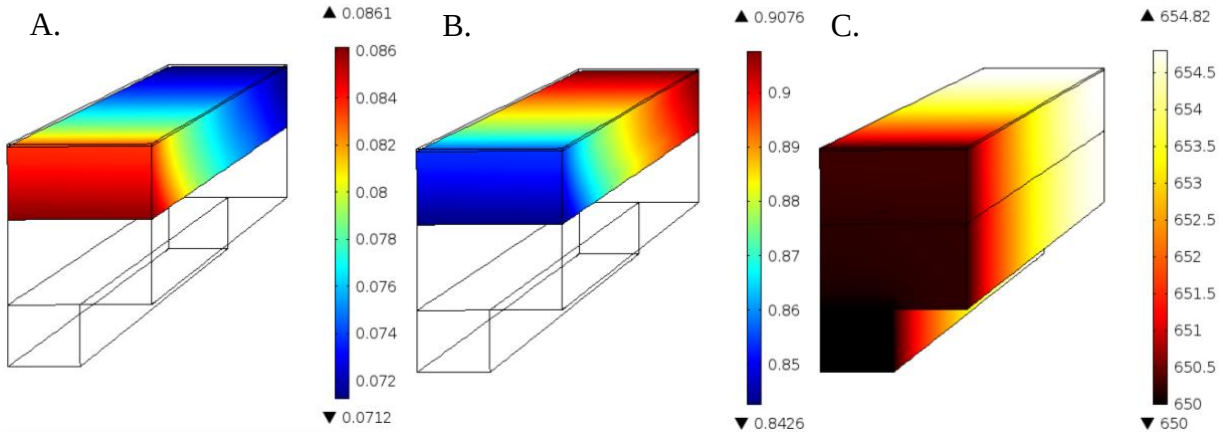

Figure 81. 3-D plots of A) porosity, B) degree of oxidation (DoO), and C) temperature (°C) at five minutes after reduction starts (Ni-cermet cell in a single channel model).

As reduction progresses, the NiO concentration decreases, and thus the heat generated from reduction decreases. The temperature spikes during the initial reduction period and then begins a steady decline as the amount of reduction (and the DoO) decreases as shown in **Figure 82**A. In combination with the large volume decrease of NiO to Ni during reduction, this temperature difference leads to the development of a thermo-chemo-mechanical stress in the anode. The maximum von Mises stress experienced in the sample (e.g., occurring within the anode or at the anode electrolyte interface) is used to show the impact of reduction on stress. **Figure 82**B shows the von Mises stress developed as the sample is reduced. Note that there is a spike in stress in the first five minutes (**Figure 82**B inset) due to the jump in temperature followed by a more gradual increase in peak stress as the anode contracts from reduction. The von Mises stress for the anode contraction is clearly much larger than that from the rise in temperature. While not investigated during this project, in the future the updated tool can also be used to evaluate where the stress occurs within the sample and used to predict failure based on relevant mechanisms of failure (e.g., anode fracture, electrolyte fracture, layer delamination, etc.).

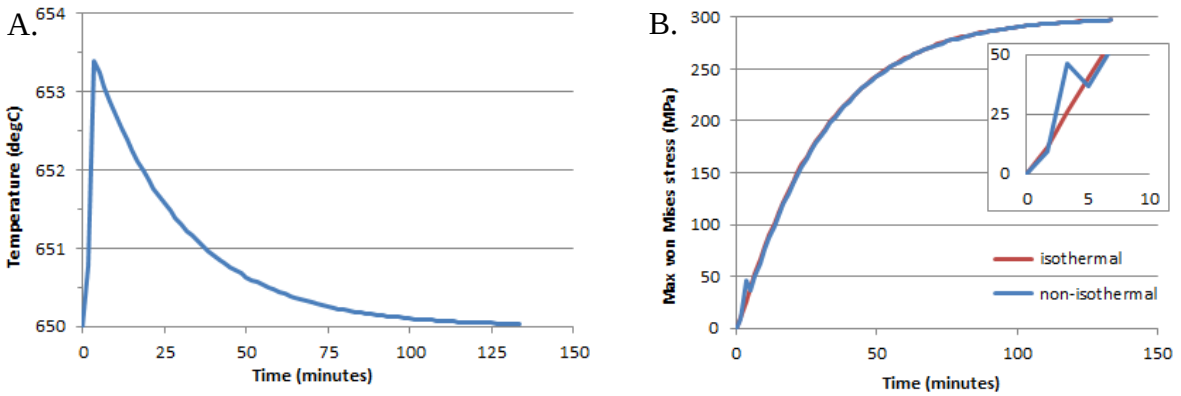

Figure 82. Transient plots showing A) the temperature profile after onset of reduction in a non-isothermal study and B) stress at non-isothermal versus isothermal conditions for a Ni-cermet cell in a single channel model.

To evaluate the stress within components of the cell, the relationship between curvature and residual stress was examined. We also investigated residual stress relaxation with respect to stress development in the composite layers. The SOFC is a layered composite which typically consists of an anode support layer (ASL), anode functional layer (AFL), electrolyte, and cathode. The layers are rigidly bonded during sintering and therefore any mismatch in thermal expansion of the materials results in residual stress. In unconstrained sintering, a manifestation of the residual stress is cell curvature, which if large enough may cause mechanical failure during stack assembly.

Figure 83A shows the simulation result for curvature of an unconstrained Ni-cermet half-cell at room temperature (25°C) after cooling down from sintering temperature (e.g., 1400 °C). The predicted curvature (i.e., camber height) is the same order of magnitude as that observed for Ni-cermet cells having the same layer geometry. Simulation results from a parametric study of residual stress using the multi-physics model also agree well with both X-ray diffraction experimental measurement and analytical calculations via curvature in the literature as shown in **Figure 83**B [67]. The minus sign suggests a compressive residual stress of the thin-film electrolyte on the anode.

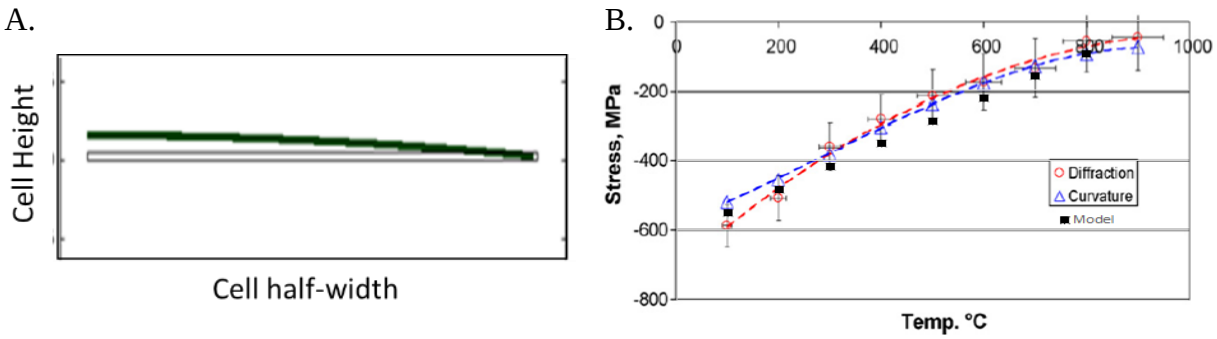

Figure 83. Results of unconstrained Ni-cermet half-cell curvature study showing A) predicted camber height after sintering and B) predicted residual stress from the multi-physics model compared to experimentally determined (XRD) and calculated residual stress [67].

During operation or reduction, relaxation of residual stress changes as a creep process. For ceramics creep can be described by the empirical Norton Power Law in Equation 2. Key parameters are from the literature [68-69].

$$\frac{d\varepsilon}{dt} = k_0 \sigma^n \exp\left(-\frac{E_a}{RT}\right) \quad (2)$$

Therefore, we additionally incorporated relaxation of residual stress into the thermo-chemo-mechanical model to study the combined effect of residual stress and increased chemical stress on relaxation and to determine the resulting total stress at different temperatures. **Figure 84** shows the relaxation of residual stress, thermo-chemo-mechanical stress, and total von Mises stress during reduction at 650 °C and 700 °C. Significantly different trends are seen between the two temperatures. The initial residual stress is higher at 650 °C (**Figure 84**A) than at 700 °C (**Figure 84**B). The residual stress relaxation rate, on the other hand, is lower at 650 °C. Even though chemo-mechanical (von Mises) stress increases more significantly at 700 °C due to faster reduction of NiO, the total stress from the combined effects at 700 °C during reduction of a cell is lower than that at 650 °C.

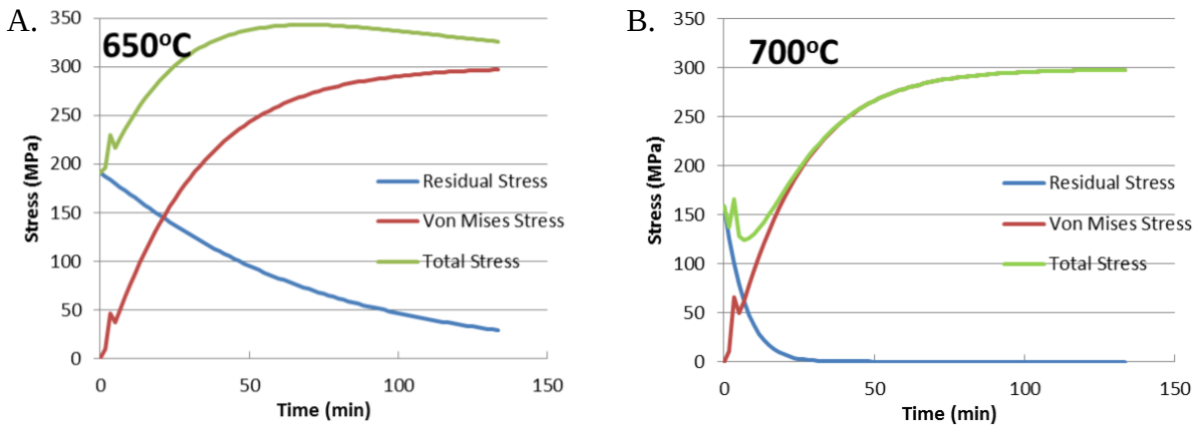

Figure 84. Comparison of combination on chemo-mechanical stress and relaxation of residual stress at A) 650 °C and B) 700 °C.

In summary, we incorporated both energy balance analysis and residual stress calculations into the thermo-chemo-mechanical model to study temperature-related stress as well as both temperature- and time-related stress relaxation. The model was shown to both quantitatively and qualitatively predict accurate results when compared to other studies in the literature. For instance, predicted cell reduction time scales are comparable with those in references [66] and [5]. Additionally, predictions of cell stress are similar to literature values (e.g., see **Figure 83**B), while cell curvature predictions are consistent with measurements of Ni-cermet as well as SFCM-based ceramic anode cells fabricated at Redox. Note, the 3-D modeling results predicted that there is not much impact by varying channel width (not shown) and thus results from the 2-D model should not substantially differ from those in a 3-D model. Studies using the 2-D model are less computationally intensive and allow the model to be used for more practical cases such as modeling the cells in a stack.

Thermo-chemo-mechanical modeling of ceramic anode SOFCs. The framework of the Ni-cermet chemo-mechanical model was used to predict reduction/oxidation reaction kinetics and mechanical behavior that occurs in the SFCM-based ceramic anode cell. While some mechanical test data was measured in this project, relevant material properties data for SFCM-based ceramic anode component materials was still limited. Therefore, to obtain additional reduction-oxidation and other properties inputs to the thermo-chemo-mechanical model, we conducted literature reviews of relevant materials and conducted some additional in-house tests at Redox. This allowed us to run various modeling studies for the SFCM-based ceramic anode cells. For instance, **Figure 85** shows the predicted curvature of an unconstrained SFCM-based ceramic anode half-cell at

room temperature (25 °C) after cooling from high temperature during sintering. The predicted curvature (i.e., camber height) is representative of surface profile measurements of sintered SFCM-based ceramic anode cells.

Another study was intended to determine the curvature and related residual stress within a half-cell after sintering and additional stresses and the evolution of stress during assembly of the cell in a stack. The multi-physics model can be used to determine the relationship between as-fabricated curvature of the cell and cell mechanical failure during assembly which helps to guide new assembly methods and identification of critical cell curvature and strength. Such modifications to the stack assembly can be critical for new cell technologies, such as the SFCM-ceramic anode cells, which have a mechanical strength that is ~4-6 times lower than conventional Ni-cermet cells (depending on the as-fabricated porosity of the SFCM-based ceramic anode). This study considered a 10 cm by 10 cm half-cell geometry with anode and electrolyte layers. The model utilized solid mechanics with built-in thermal expansion considerations. To reduce computational time, the model used 2-D geometry with a symmetric plane in the middle. **Figure 85**A shows the downward curvature of half (of the symmetric plane) of the half-cell in the as-fabricated state due to a greater thermal expansion coefficient of the anode as compared to the electrolyte. This matches observations in real-world sintering of SFCM-based ceramic anode half cells. In **Figure 85**B, the cell is shown in a stack assembly configuration at 10x magnification of the cell curvature with the cell sandwiched between interconnects and endplates. During assembly, the interconnect and endplates are pushed together, which flattens the cell.

Figure 85. Curvature of a A) half-cell at room temperature after sintering and B) the cell placed in a stack assembly with curvature magnified 10x.

At room temperature, the larger thermal expansion of the anode causes the anode to be in tension, while the electrolyte is placed in compression. Upon loading and compression in the stack assembly, these stresses are expected to change. The color map in **Figure 86**, shows the distribution of the in-plane stress within the cell during loading/compression in the stack assembly. Loading the cell in the assembly increases the compressive stress in the electrolyte layer from 160

MPa (see the minimally loaded electrolyte in **Figure 86**B) to 245 MPa, as shown by the dark blue in **Figure 86**C. In contrast, the anode exhibits a much lower stress, with 30 – 48 MPa tensile stress in the compressed assembly. As expected, the tensile stress in the anode increases from near the electrolyte to the free side of the anode (a maximum tensile stress shows dark red color in **Figure 86**C). These results demonstrate that the stack-assembly model with consideration of the initial cell curvature and residual stress allows studies of the stress evolutions of the SFCM-based ceramic anode cells upon assembly in the stack.

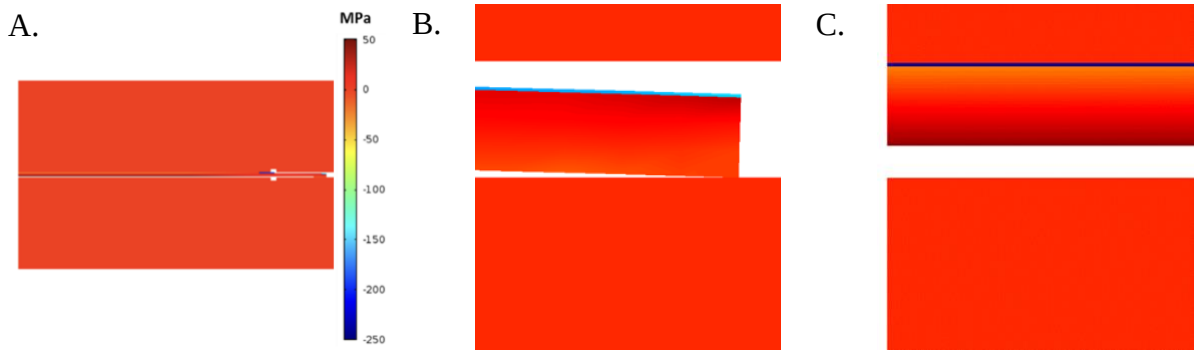

Figure 86. In-plane of cell stress (given by color map) evolution of A) the cell assembly, B) a magnified portion near the edge, and C) a magnified portion near the center.

To study the specific red-ox characteristics of the SFCM anode and the resulting chemo-thermo-mechanical stress of an SFCM-based cell during fabrication and in the stack assembly, a 2-D isothermal model of the SFCM anode of a 10 cm by 10 cm SFCM-based ceramic anode cell was set up with detailed material properties (**Figure 87**A). The oxygen storage capacity of the ceria is thought be an important part of the red-ox stable characteristics of the composite SFCM-GDC anode. Therefore, the thermodynamics and red-ox kinetics of the cerium oxide material (i.e., Ce_2O_3 concentration or reduction state of ceria as a function of oxygen partial pressure) were added to the chemo-thermo-mechanical framework. The rate equation of ceria reduction/oxidation was also incorporated into the model to study transient stress response of the cell. Ce_2O_3 concentration changes (as Ce^{4+} becomes Ce^{3+}) and resulting chemical expansion and mechanical stress of the SFCM anode were simulated as a function of time after the reducing gas (H_2) was introduced in the fuel channel. **Figure 87**B shows Ce_2O_3 concentration quickly responded to the reducing gas at 0 seconds and increased quickly for the first 400 seconds at 650 °C. The Ce_2O_3 concentration plateaued at 3.9% around 1200 seconds. The mechanical stress increased as Ce_2O_3 concentration

increased due to chemical expansion (because a Ce^{3+} cation has larger radius than a Ce^{4+} cation). Upon full reduction, chemical expansion of the SFCM anode can be as high as 0.6% (lattice expansion), which the simulation predicts will result in 66.7 MPa chemo-mechanical stress (von Mises) within the anode at 650 °C as shown in **Figure 87**C. In comparison, Ce_2O_3 concentrations upon full reduction decrease at lower temperatures (1.8% at 600 °C and 0.7% at 550 °C) and the resulting chemo-mechanical (von Mises) stress within the anode due to chemical expansion is predicted to be 30 MPa and 12.3 MPa, respectively. Therefore, the chemo-mechanical stress in combination with residual stress from the stack assembly may damage the cell. Note, SFCM-based ceramic anode half cells were shown to experience cracking in the electrolyte when red-ox cycled at temperatures higher than normal operation (e.g., **Figure 23** shows evidence for electrolyte cracking when red-ox cycles occurred at 700 °C, but this was not observed at 600 °C).

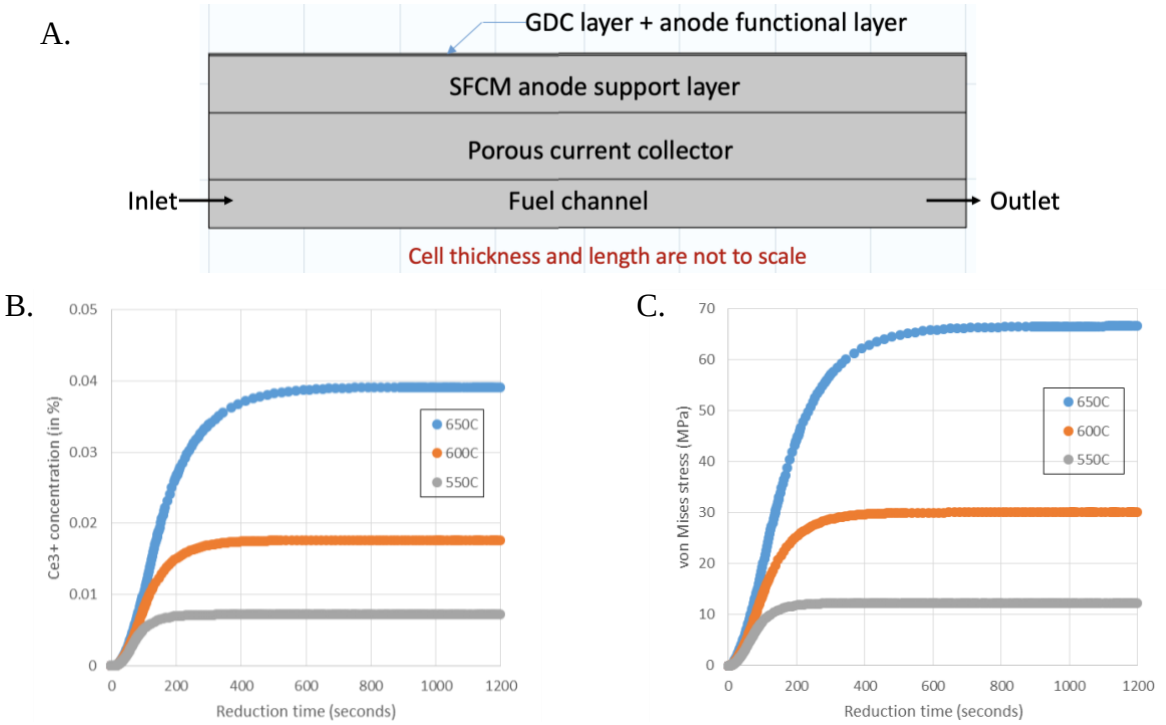

Figure 87. Modeling details showing A) a 2-D model showing half-cell layers and flow; B) concentration changes of reduced ceria in the SFCM half-cell during cell reduction; and C) chemo-mechanical (von Mises) stress changes associated cell reduction.

5.4. Stack Testing

3-cell Stack. Stack testing was conducted at various points throughout the project and used cells which had the configuration (e.g., see **Figure 8**) that was most mature at the time. Stack tests were

conducted using the equipment and methods described in Section 3.1. For example, **Figure 88** shows the stack voltage and power density versus current density for a 3-cell stack using 5 cm by 5 cm SFCM-based ceramic anode cells. These cells were similar to cells #1, #2, and #3 that were described in Section 4.4. The average total ASR of each cell was 0.19 Ω-cm^2 at 600 °C, which is a very good value for the relatively low temperature at which the assessment was made. In fact, this ASR is 40% lower at the same temperature than that demonstrated in the button-cell studies that investigated the impact of Ni:GDC ratio for the infiltrated catalyst (e.g., see **Figure 30** through **Figure 32**). Note that while these 3 cells had a CFL, the CFL thickness was smaller than the ~12 μm CFL used in button cell tests. Additionally, the catalyst loading for the 5 cm by 5 cm cells used in the 3-cell stack was between ~13-14 wt%, whereas the button cells had only ~5 wt%. The initial performance of the cells in the 3-cell stack was similar to that of the highest performing large format, SFCM-based cell (see **Figure 41**). However, while having similar total ASR at 600 °C, the latter had an OCV of approximately 0.9 V. At 600 °C, the initial OCV and operating voltage variation was between ~10-20 mV. After characterization at 600 °C for ~20 hours, the operating temperature was lowered to ~500 °C. Performance at this temperature was compared in both 100% H_2 and 10% CH_4/90% H_2, with only ~7% lower power output in the latter case (not shown).

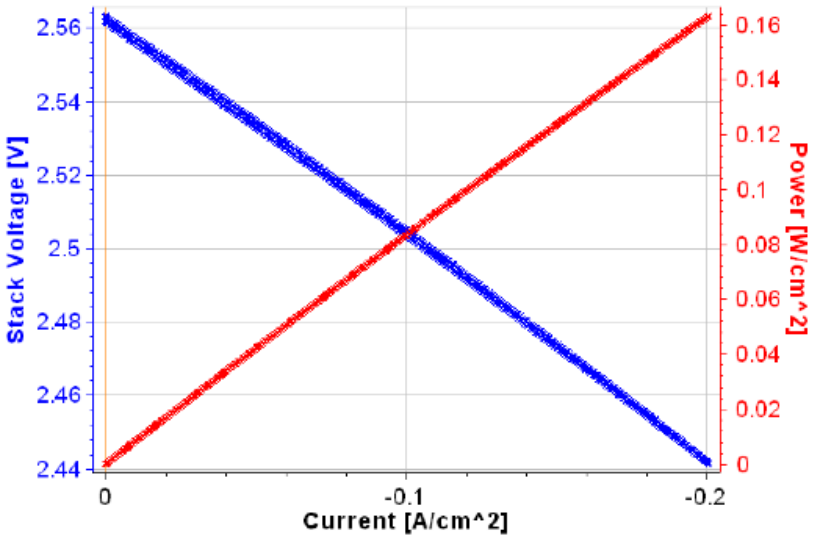

Figure 88. Stack voltage and power density versus current density for a 3-cell SFCM-based ceramic anode stack consisting of 5 cm by 5 cm cells operated at ~600 °C in hydrogen.

The 3-cell stack was held at a constant current of 0.1 A/cm^2 at 500 °C to assess cell stability. This lower temperature was chosen for the stability assessment, due to observations in other cell tests

in which degradation was sometimes greater at higher operation temperature. As shown in **Figure 89**, Cell 1 and Cell 2 had extensive degradation over an 85-hour period, while Cell 3 was relatively stable. The OCV of Cell 3 (red trace) decreased slightly (~20 mV) over 85 hours, while the ASR degradation rate of this cell was only ~35% per 1000 hours. The OCV of Cell 1, on the other hand, decreased ~400 mV over 85 hours, while that of Cell 2 was ~230 mV lower. As the green voltage trace in **Figure 89** shows, the OCV for Cell 2 decreased more rapidly than the operating voltage at 0.1 A/cm^2 for most of the measurement period, which when compensating for the decrease in OCV yields an ASR degradation rate of around 170% per 1000 hours, where the degradation rate was extrapolated linearly from the measurements. Similarly, the ASR degradation rate of Cell 1 (compensated for OCV degradation) was ~325% per 1000 hours, where the degradation rate was extrapolated linearly from the measurements. The relatively high degradation rates of Cell 1 and Cell 2 are thought to be due to damage (e.g., progressive cracking) that occurred throughout the test. Depending on the location of the damage, such cracking can result in fuel consumption (via combustion) without greatly increasing the temperature of the cell.

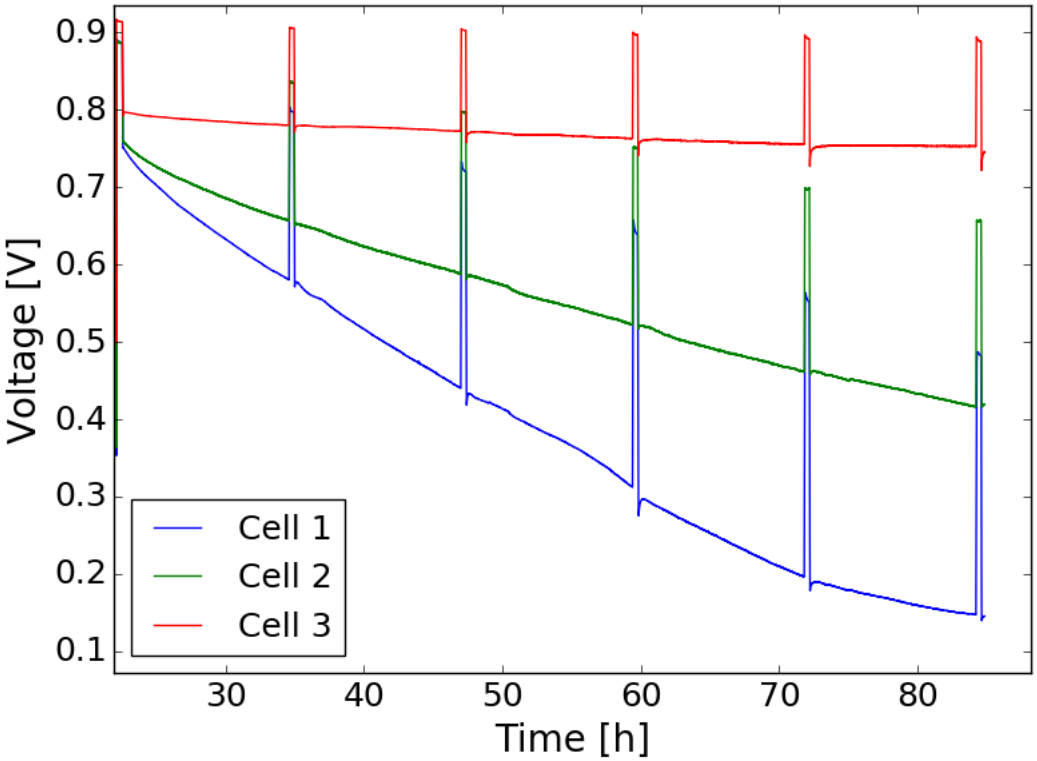

Figure 89. Cell voltage versus time for individual cells in a 3-cell stack of 5 cm by 5 cm SFCM-based ceramic anode SOFCs operating at 500 °C and a fixed current density of 0.1 A/cm^2 in H_2.

The stack was operated for a total of ~300 hours at 500 °C at a fixed current density of 0.1 A/cm^2 (not shown). During this time, the OCV of Cell 1 and Cell 2 continued to decrease and dominated the drop in operating voltage, though the degradation of both cells plateaued. At the end of the ~300 hours, the operating voltage of Cell 1 was ~0.1 V while that of Cell 2 was ~0.15 V. After about 150 hours at 0.1 A/cm2, the OCV of Cell 3 also began to decrease, though at a much slower rate than that observed for the other cells in the stack. At the end of the ~300 hours, OCV was 0.84 V for Cell 3, while the operating voltage had decreased to ~0.64 V. **Figure 90** shows impedance spectroscopy data (measured at OCV) for Cell 3 over a period of ~160 hours, which was collected during the 300-hour period mostly at 0.1 A/cm^2 at 500 °C for the 3-cell stack. As shown in **Figure 90**A, the shape of the Nyquist curves remained mostly unchanged over the ~160 hours. As indicated in the plot, there were changes in the location of the high-frequency intercept (Ohmic) impedance (red star) and at the intermediate frequency (~500 mHz) indicated by the blue star. **Figure 90**B shows how the Ohmic impedance and intermediate frequency contribution change over time. The Ohmic impedance increased slightly but then plateaued. The intermediate-frequency feature first increases slightly, but then decreased to a value slightly less than at the beginning of the measurement period. The low frequency contribution (shown to the right of the intermediate-frequency feature in **Figure 90**A) progressively increased throughout the measurement period, but given the relatively small changes in impedance, the decreasing OCV of Cell 3 was clearly the dominant mode of degradation. This is similar to the conclusion for Cell 1 and Cell 2 with respect to the initial 80-hour measurement period as shown in **Figure 89**.

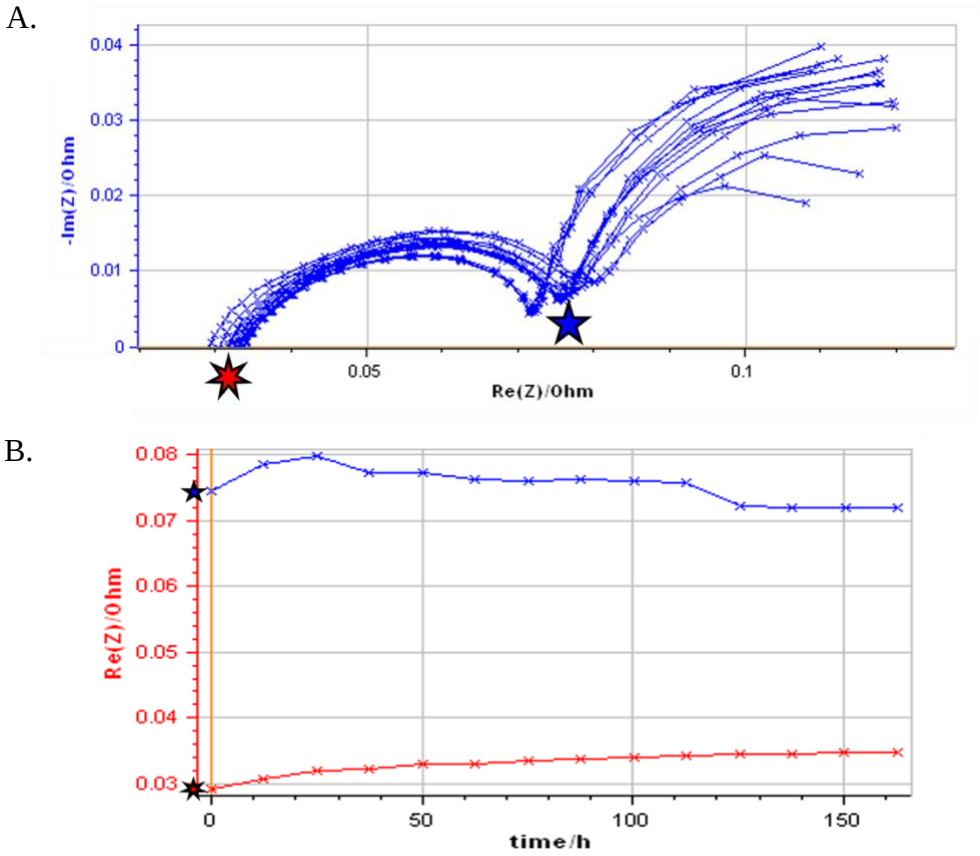

Figure 90. EIS data for *Cell 3* of a 3-cell stack of 5 cm by 5 cm SFCM-based ceramic anode SOFCs operating at 500 °C in H_2, showing A) Nyquist curves measured at OCV over >160 hours in which the cell was mostly held at 0.1 A/cm^2; and B) real impedance versus time for the Ohmic impedance (x-axis intercept) at high frequency (~987 mHz — red, 7-point star) and impedance at low frequency (~500 mHz — blue, 5-point star).

10-cell Stack. A 10-cell stack using 10 cm by 10 cm SFCM-based ceramic anode SOFCs was operated at 600 °C with H_2 fuel and air. The stack voltage and current density versus time is shown in **Figure 91**. The cells were made from commercially-produced tape cast layers and had a configuration as shown in **Figure 8**B. The cells did not have CFLs. The half cells were fired at a lower sintering temperature. The anode catalyst loading for the cells was between 10-11 wt% and the cells used a silver grid for the cathode contact. The stack was operated for a period of almost 250 hours. Initial characterization during the first ~10 hours included current density sweeps and assessing the red-ox cycling stability of the stack.

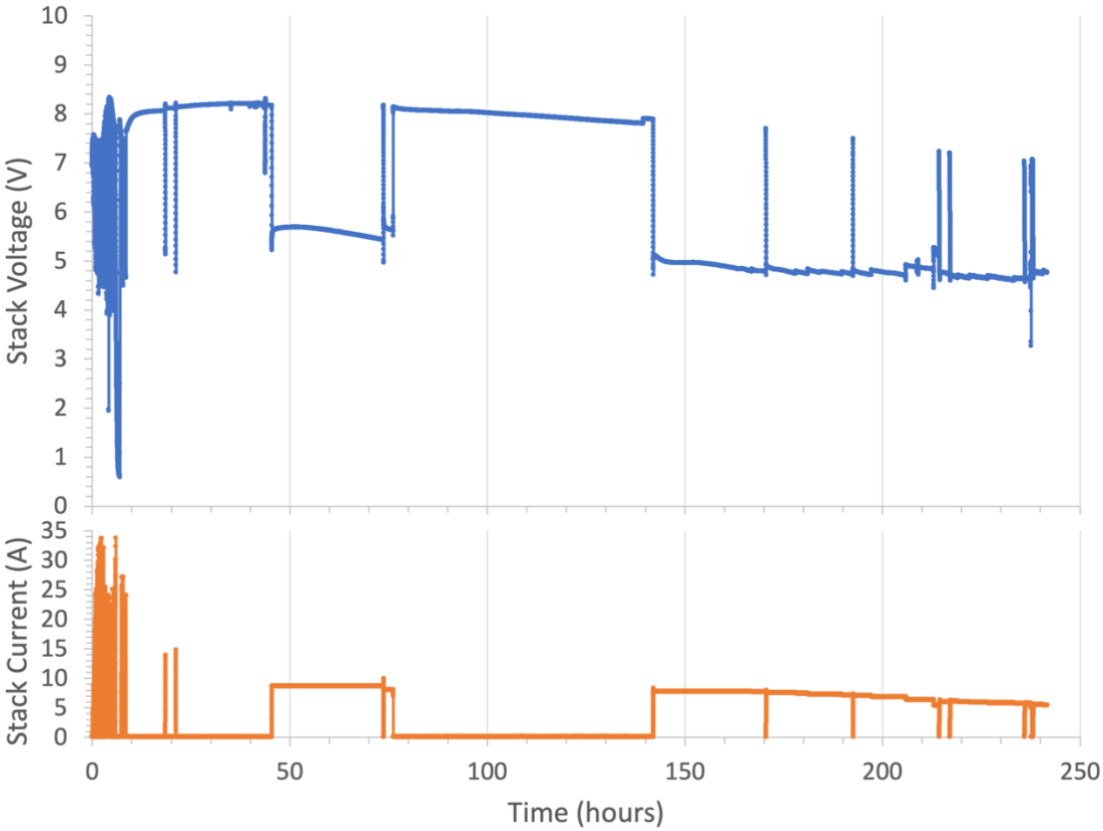

Figure 91. Stack voltage and current density versus time for a 10-cell SFCM-based ceramic anode stack (using 10 cm by 10 cm cells made from production tape cast layers) at 600 °C in H_2.

Stack voltage and power versus current for the 10-cell, 10 cm by 10 cm SFCM-based ceramic anode stack is shown in **Figure 92**. The stack achieved a maximum power of 155 W at 600 °C. The open circuit voltage of each cell in the stack was relatively low (e.g., ~0.75 V) and fluctuated slightly during the initial 10 hours of characterization likely as a result of temperature variations during current loading and return to open circuit voltage as seen in **Figure 91** and **Figure 93**. The low OCV values may have been a result of a relatively high degree of pinholes in the electrolytes of the cells. As seen in **Figure 93**, while the OCV for most of the cells were similar to each other, the spread in ASR was quite large and did not follow a trend with location in the stack. For instance, Cell 5 showed the highest ASR and incidentally the lowest OCV. Cell 1 showed the second highest ASR. However, as Cell 5 was at the center of the stack, the ASR is expected to have been lower than Cell 1, which was at the outside of the stack where heat loss should have been greater. This is mainly attributed to possible differences between the cells. As the cells used materials tape cast

on a production tape caster in large batches, the likely cause for differences between the cells is during the high-temperature sintering process rather than differences in the tapes. Due to temperature gradients in the sintering furnace (e.g., *see Section 6*), the most obvious difference in the cells was in their camber. The cells in the 10-cell stack had anywhere from approximately 4-20 times higher camber than normal for Redox's Ni-cermet cells. While the stack assembly process was modified to accommodate a smaller compressive load on the stack, some of the cells may have been damaged due to the high camber. Such damage may have happened during the assembly process, during the stack heat-up sequence, and/or during the initial reduction as discussed in Section 5.3. Another possible consequence of the high camber may have been differences in the quality of the contact between interconnect, current collectors, and cell. Such differences can result in variations in the Ohmic ASR and lead to the spread in ASR seen in **Figure 93**.

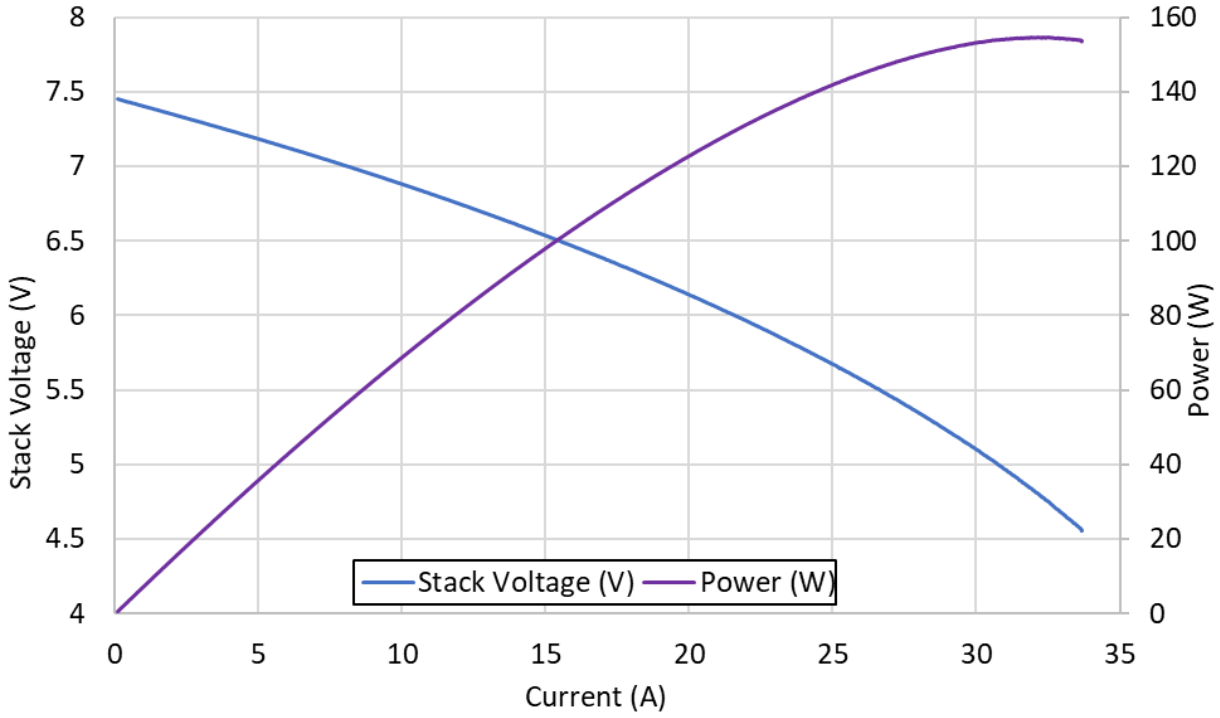

Figure 92. Stack voltage and power versus current for a 10-cell (10 cm by 10 cm) SFCM-based ceramic anode stack (production-made, non-optimized tape cast layers) measured at 600 °C in H_2.

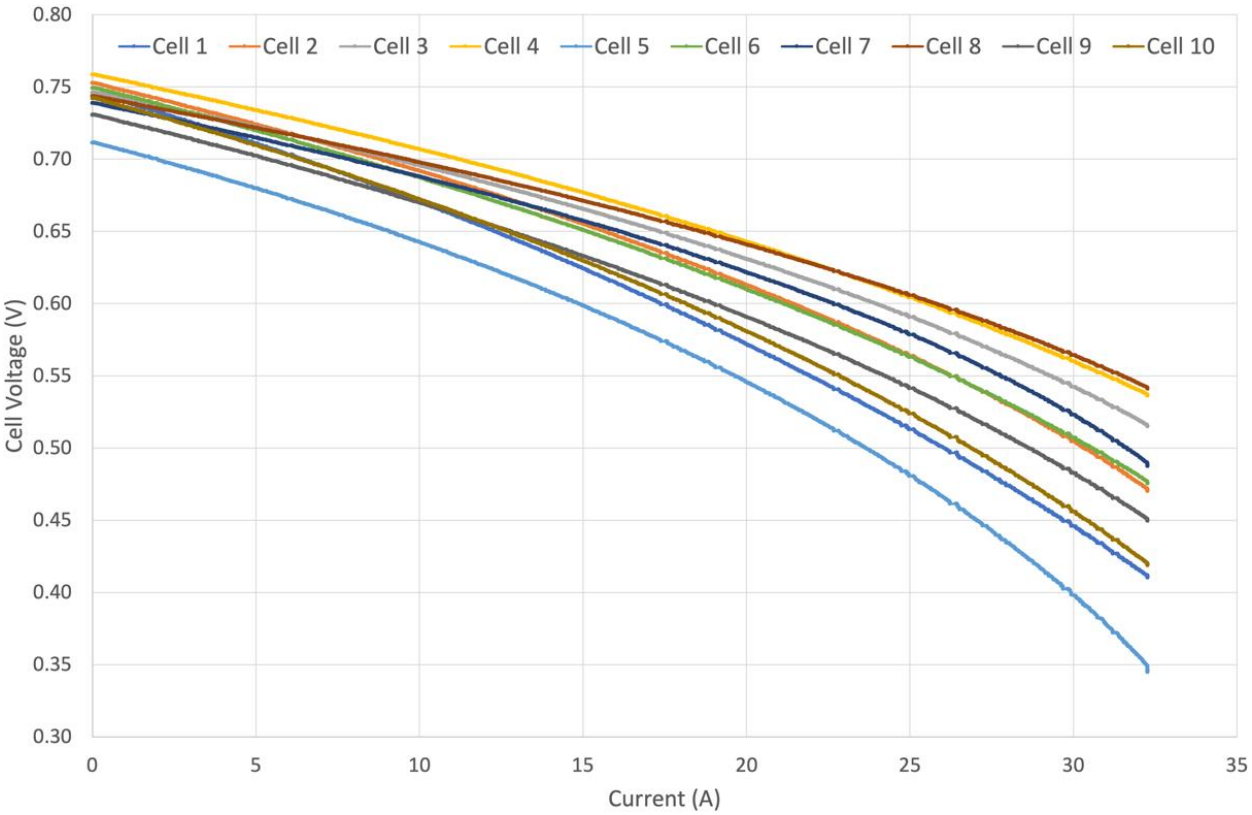

Figure 93. Cell voltage versus current for each cell in a 10-cell 10 cm x 10 cm SFCM-based ceramic anode stack (production-made, non-optimized tape cast layers) measured at 600 °C in H_2.

The 10-cell stack was also red-ox cycled at ~6 hours into operation after first unloading the current and then switching the H_2 anode input stream to industrial N_2 (> 0.01-0.02% O_2). As shown in **Figure 94**, this resulted in the stack voltage decreasing from ~7.8 V to ~0.6 V after about 1 hour. Note that the voltage in the industrial N_2 equilibrates to ~60 mV/cell, which is many orders of magnitude more oxidizing than H_2 as explained in Section 4.4. In fact, the value for the voltage per cell suggests there was ~1% O_2 in anode, which is at the upper end of the specification for the industrial N_2. When H_2 was reintroduced around 7 hours into operation, the OCV recovered to the original value before the oxidizing gas was introduced.

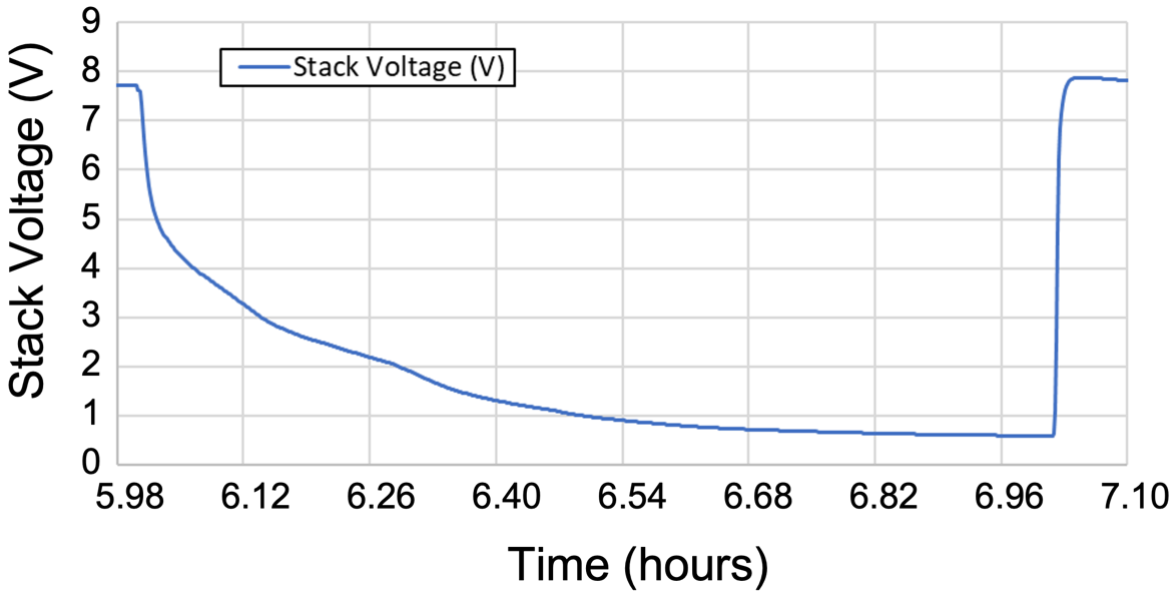

Figure 94. OCV of a 10-cell SFCM-based ceramic anode stack measured during red-ox cycling. OCV starts at ~7.8 V in H_2, then rapidly drops in N_2, but fully recovers when H_2 restarted.

Figure 95 shows stack voltage and power versus current at different points in time during operation of the 10-cell stack, where the 1st set of curves (P_1, V_1) was near the beginning of characterization, the 2nd set (P_2, V_2) was just before the red-ox cycle, and 3rd set (P_3, V_3) was just after the red-ox cycle. Note, the maximum power just before the red-ox cycle was ~145 W, which is ~7% lower than the beginning of operation. More than likely, similar degradation (e.g., mechanical damage) was occurring as was observed in other single cell and stack tests of SFCM-based ceramic anode cells using a similar cell configuration. Note, the temperature for the second data set was a little lower than at the beginning of operation, which is likely why the OCV was a slightly higher just before the red-ox cycle. While the industrial N_2 was flowing to the anode during the red-ox cycle, stack temperature also decreased. When the H_2 was turned back on, the temperature of the stack increased. As result the temperature of the stack after the red-ox cycle when the 3rd data set was collected was similar to the temperature for the 1st data set, possibly because equilibrium had not yet been reached. The average cell ASR before the red-ox cycle was ~0.74 Ω-cm^2, whereas after the red-ox cycle the ASR was ~0.77 Ω-cm^2. When combined with the lower OCV after the red-ox cycle, this resulted in a lower maximum power output for data set three (~130 W). While unclear whether the slightly higher ASR was a result of the red-ox cycle or due to the degradation that occurred throughout the test, the fact that the 10-cell stack with 10 cm

by 10 cm SFCM-based ceramic anode cells showed only a very small change in ASR represents a significant improvement in the red-ox robustness over conventional Ni-cermet cells.

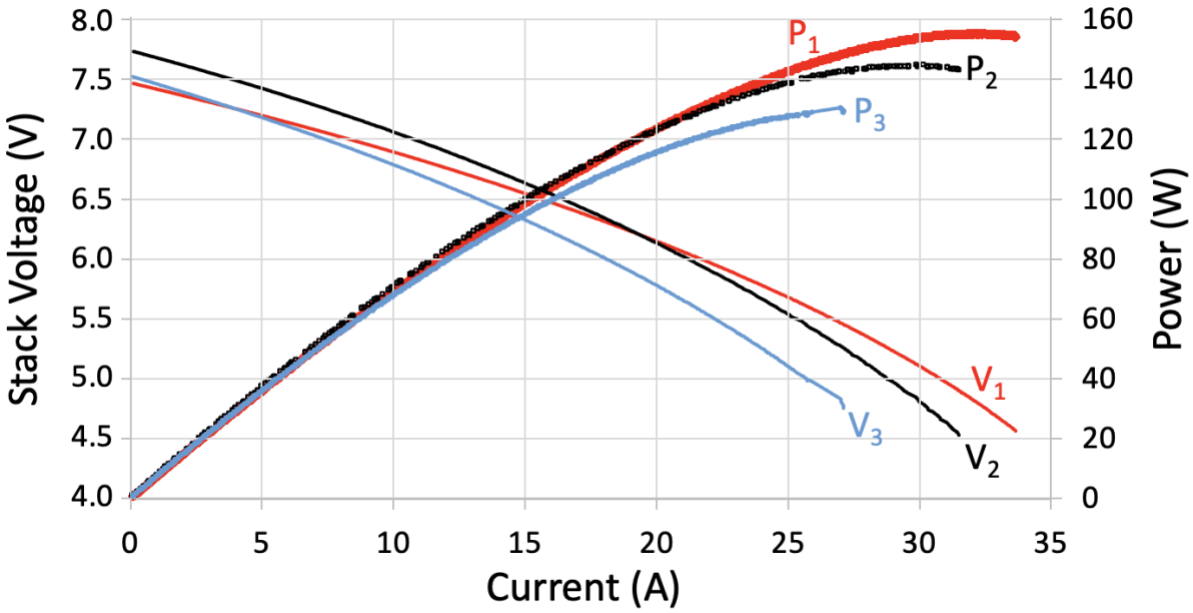

Figure 95. Stack voltage and power versus current measured at different points in time for a 10-cell (10 cm by 10 cm) SFCM-based ceramic anode stack (production-made, non-optimized tape cast layers) measured at 600 °C in H_2, where the 1st set of curves (P_1, V_1) was near the beginning of characterization, the 2nd set (P_2, V_2) was just before the red-ox cycle, and 3rd set (P_3, V_3) was just after the red-ox cycle.

Note, several single cell and 3-cell stacks were tested before and after the 10-cell stack test using similar production-type 10 cm by 10 cm SFCM-based ceramic anode SOFCs (data not shown). These had a similar performance level as the 10-cell stack, indicating that the 10-cell stack of 10 cm by 10 cm cells performed similarly to smaller size stacks. While the performance was consistent between full stack and short stack or single cell tests, the need to increase power density required the optimization of the anode microstructure. As discussed in Section 4.4, the production-type cells were not optimized and the maximum power density achieved for such cells was ~0.4 W/cm^2 at 600 °C, versus 0.9 W/cm^2 for a more optimized structure (e.g., see **Figure 41** and **Figure 58**). The more optimized structure was fabricated using tapes made with Redox's pilot-scale tape caster. Note, for comparison, using more-optimized anode microstructures, a 1-kW stack would need only around eighteen to twenty 10 cm by 10 cm SFCM-based ceramic anode cells operating at 0.75 V. Unfortunately, the baseline-stability problem led to delays that prevented us from

demonstrating the targeted 1-2 kW stack. Given that we ultimately solved the baseline stability problem (as described in Section 4.4), and the fact that the 10-cell stack of 10 cm by 10 cm SFCM-based ceramic anode cells showed similar performance as smaller size stacks, the foundation toward continued improvement and demonstration of a ≥ 1-kW stack (with approximately eighteen to twenty 10 cm by 10 cm cells) has been set.

Impact of Reformed Natural Gas. A single cell test was conducted to compare performance in H_2 and reformed natural gas using a 10 cm by 10 cm SFCM-based ceramic anode cell (no CFL). The 10 cm by 10 cm SFCM-based ceramic anode SOFC was assembled in a single cell stack and tested in H_2 and reformed natural gas. The natural gas was reformed using the facilities and equipment described in Section 3.1. Due to a malfunction in the steam supply, the steam content used was more than three times the target value. Three fuel compositions were used, dry H_2, high steam content H_2 (H_2O:H_2 ~ 10:1), and steam reformed natural gas (i.e., a syngas consisting of H_2, H_2O, CO, CO_2, and CH_4 — also with ~10:1 steam:fuel). Note, the cell did not include a CFL and had a structure of the SFCM-based ceramic anode SOFC similar to that of cell #7 (i.e., see **Figure 8**C). Note, this cell was also used in a different test that was found to have an obstruction in the gas manifold after heating the stack up. After cooling, the cell was re-assembled with new stack hardware and heated again.

The electrochemical performance of the 10 cm by 10 cm cell at ~600 °C is shown in **Figure 96**. As expected, the SOFC exhibited the highest power density and OCV in pure H_2. The thin SFCM-based layer closest to the electrolyte was relatively dense due to a lower amount of pore former and a higher sintering temperature. Therefore, the catalyst loading was relatively low, which resulted in a relatively high ASR. Additionally, there was an error during startup which resulted in flooding of the cell near room temperature with liquid H_2O. Upon introduction of high steam content in H_2, the OCV dropped slightly, while the power density decreased significantly (i.e., the ASR increased significantly). In reformed natural gas, the ASR was larger than in both conditions using H_2. The large increase in ASR upon introduction of high steam content is believed to be due to a significant dilution of the H_2 fuel reaching the active electrochemical sites in the anode (i.e., concentration polarization). Similarly, the reformed natural gas contained significant levels of steam which dilutes the fuel. Much less steam is typically used (e.g., steam-to-carbon or steam-to-

fuel ratio of 2.5-4.0). The steam dilution effectively means that in these two cases the fuel had a much lower energy density than the dry H_2 case. In operation with more reasonable levels of steam, the impact on cell ASR is expected to be much less. This was, for instance, the case for the 3-cell stack using 5 cm by 5 cm cells when tested in 10% CH_4 / 90% H_2 at ~500 °C (i.e., only ~7% lower ASR), as described above.

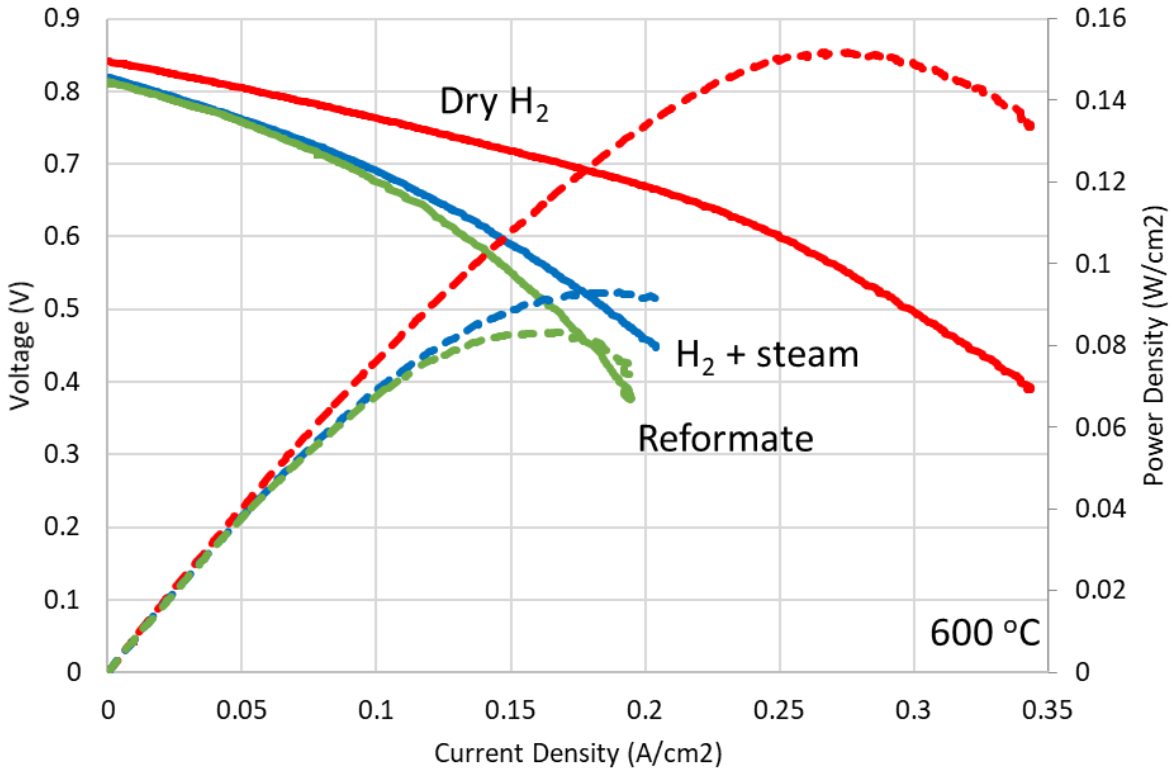

Figure 96. Cell voltage and power density versus current density for a 10 cm by 10 cm SFCM-based ceramic anode cell evaluated at ~600 °C using dry H_2, H_2 with high steam content (10:1 steam-to-H_2), and reformed pipeline natural gas (10:1 steam-to-fuel).

The stability of the 10 cm by 10 cm cell for the different fuels is shown in **Figure 97**. After reaching 600 °C, the cell was initially held at OCV and voltage increased with time until about hour 20. The cell operation under load (at ~0.2 A/cm^2) was then evaluated in dry H_2 and remained largely stable with time. At ~20.75 hours, the fuel was gradually changed to high steam-containing H_2 and performance decreased as steam content increased, likely due to a more dilute fuel mixture as explained above. At ~22.4 hours, the fuel was changed to reformate (10:1 steam-to-fuel) and held under load (~0.14 A/cm^2) for ~5 hours. During this time, the cell exhibited no decrease in operating voltage, but rather the operating voltage increased slightly with time while at constant current.

This result indicates that much like the 5 cm by 5 cm and button cell results, 10 cm by 10 cm SFCM-based ceramic anode SOFCs exhibit essentially no difference in stability when reformed natural gas is used instead of hydrogen fuel streams.

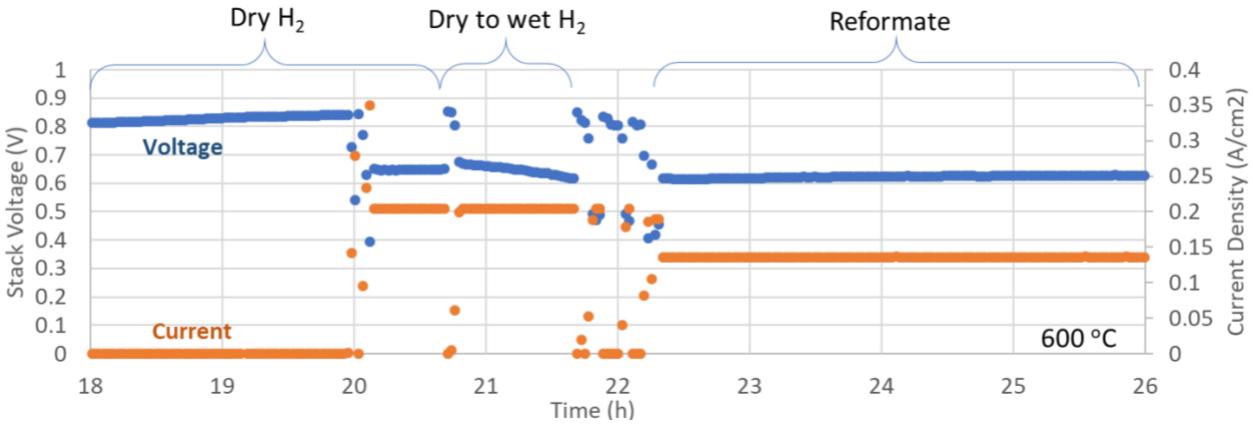

Figure 97. Stack voltage and current density versus time for a 10 cm by 10 cm SFCM-based ceramic anode cell at ~600 °C using dry H_2, H_2 with high steam content (10:1 steam-to-H_2), and reformed pipeline natural gas (10:1 steam-to-fuel).

The 10 cm by 10 cm cell was operated for a total of ~180 hours as shown in **Figure 98**. The steam for the fuel reformer dropped out at ~27 hours and lasting until ~32 hours. As a result, during this time the fuel processor was fed natural gas without any steam. Under these conditions the reformer experienced coking. From ~32 hours to ~69 hours, wet hydrogen fuel was fed to the cell. Following this, dry hydrogen was used for the remainder of the test. Also note, an instrumentation problem occurred between 47-62 hours, which resulted in a noisy cell voltage signal.

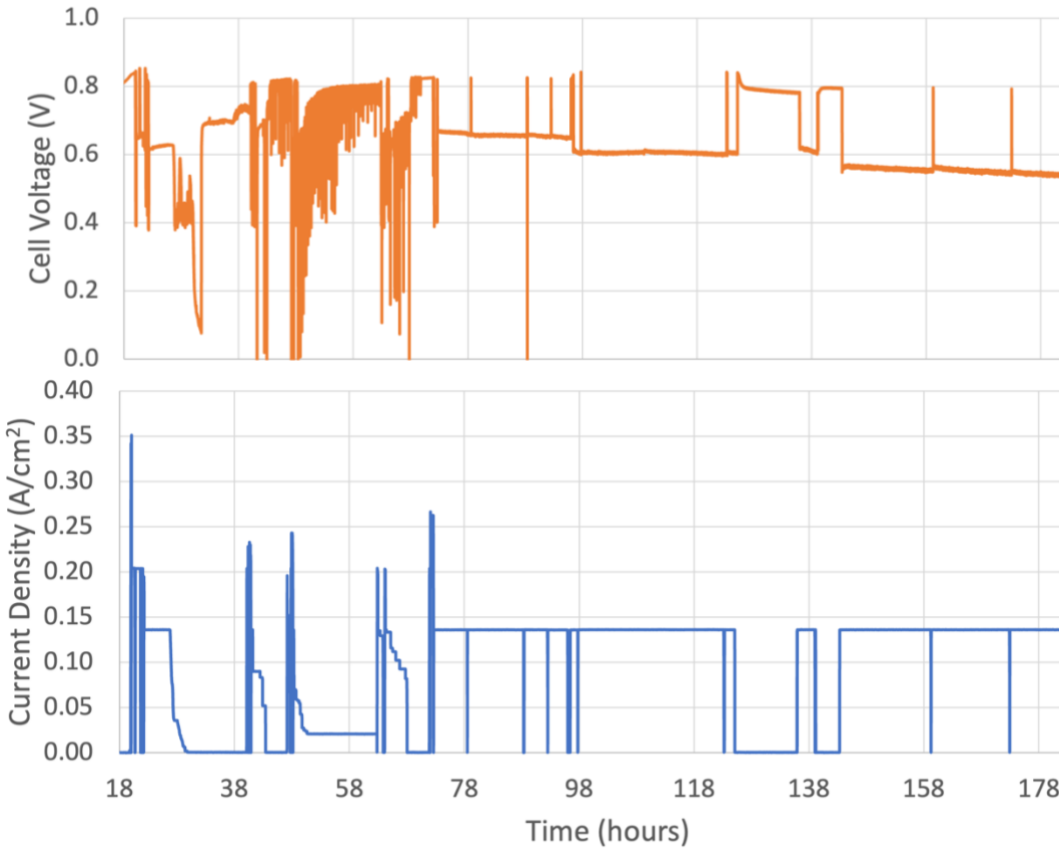

Figure 98. Cell voltage and current density versus time between ~18-180 hours of operation for a 10 cm by 10 cm SFCM-based ceramic anode cell at an average temperature of ~600 °C in both hydrogen and reformed natural gas.

The impact of operation temperature was evaluated for the 10 cm by 10 cm cell from about hour 73 to hour 141 (**Figure 98**). At 600 °C, between hour 73 and hour 96, the cell was loaded at a fixed current density of ~0.14 A/cm^2. During this time, the operating voltage was mostly unchanged with only a decrease of ~17 mV over the 23-hour period. From around hour 96, temperature was dropped to ~575 °C, while maintaining a constant ~0.14 A/cm^2. At this temperature, the operating voltage was stable and did not vary for ~30 hours. At hour 126 temperature was increased to ~625 °C with the cell maintained at OCV until about hour 136 when the cell was loaded to ~0.14 A/cm^2. The current was then kept constant until hour 140 when the cell returned to OCV. Though under load for only 4 hours at this temperature, the operating voltage decayed more rapidly than when originally at ~600 °C (i.e., ~15 mV). After this, the cell temperature was lowered back to ~600 °C and the current density was returned to ~0.14 A/cm^2 at about 143 hours and maintained until ~185

hours. Over this ~42-hour period, the operating voltage decayed slightly (i.e., ~23 mV). Compared to the period before the variations in operating temperature (i.e., from about hour 40 to hour 73), this was a slightly slower degradation rate (about 25% slower). The degradation rate clearly showed a trend with increasing temperature. Note, even at 600 °C, this was a relatively high degradation rate but is similar to that observed for cells with the same cell configuration as described in Section 4.4. Moreover, after the steam stopped and coking occurred within the reformer, there appears to have been a change in cell performance. For example, comparing **Figure 99** and **Figure 96**, at 600 °C in dry hydrogen the power density at ~0.14 A/cm^2 dropped ~10% after the coking event. While some of this decrease may have been due to the normal (i.e., mechanical stress-induced) degradation often observed for this cell configuration, additional reasons may include a change to the stack hardware (e.g., carbon/coke build up in the flow field that may have reduced the flow uniformity across the cell) or potential damage to the cell. **Figure 99** also summarizes the change in electrochemical performance for operation between 575 °C and 625 °C. Note that even though the ASR at 625 °C is decreased compared to that at 600 °C, the power output is lower due to the much lower OCV.

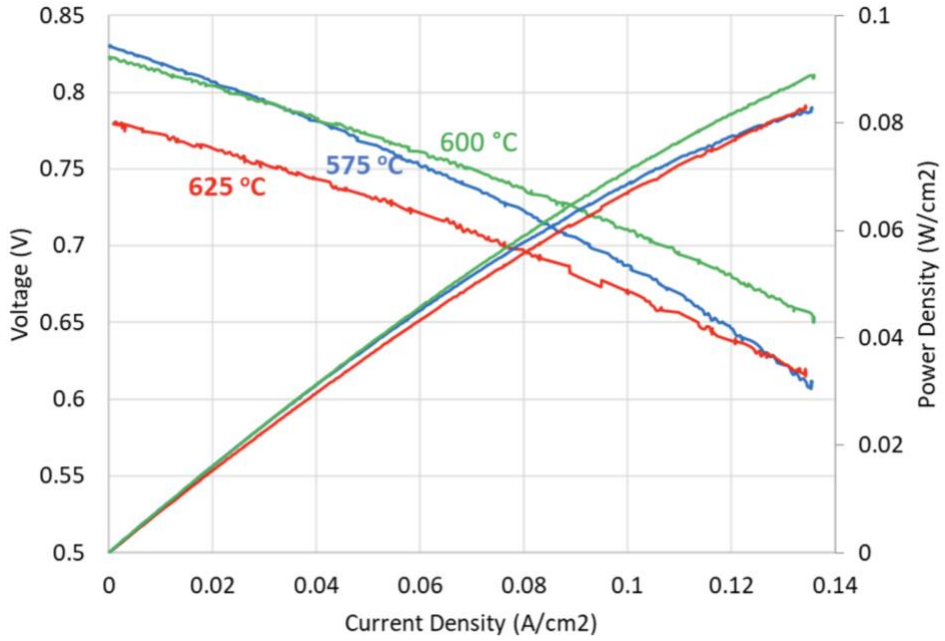

Figure 99. Cell voltage and power density versus current density for a 10 cm by 10 cm SFCM-based ceramic anode cell evaluated from 575 °C to 625 °C (hour 73 to hour 141) using dry H_2.

Red-ox Cycling of Stacks Using SFCM-based ASL with AFL SOFCs. As discussed in Section 4.4, cells made using the configuration shown in **Figure 8**C using an SFCM-based ASL with an AFL had good stability at OCV and under load, especially when the half cells were sintered at higher temperature (e.g., see **Figure 65**). Therefore, we assembled a 3-cell stack using cells made with the same configuration and fabrication process. Note, the cells did not have a CFL. The anode catalyst loading was ~5-6 wt% since non-vacuum infiltration was used. The stack was tested at 600 °C in humidified hydrogen. The red-ox cycling test profile consisted of running the cells at OCV until thermal equilibrium was reached, and then subsequently loading the cells to a fixed current density and holding for a period of time for a combined time of ~30 minutes in the reducing gas environment. The stack was then unloaded (i.e., brought back to OCV) before the anode stream was switched from humidified H_2 to (humidified) industrial N_2. As explained in Section 4.4, industrial N_2 has up to ~1% O_2 and has been shown to cause the same damage as air when used with conventional Ni-cermet cells, thus providing a surrogate for air that is simpler and safer to use in red-ox cycling tests. The stack was held under industrial N_2 for ~30 minutes before switching back to humidified H_2 and repeating the cycle. Therefore, each red-ox cycle lasted for around 1 hour.

Figure 100 shows the cell voltage for each cell in the stack versus time. Note, the performance of each of the cells is slightly different from one another. The cells experienced slightly different amounts of shrinkage during sintering, possibly due to variations in the local temperature in the furnace or differences in the weight of the top setter plate used in constrained sintering. The highest camber cell had ~2x the camber of the lowest camber cell. As discussed above, the SFCM-based cells are relatively low strength (compared to typical Ni-cermet cells). Therefore, even though the stack assembly load was decreased for SFCM-based cells, there is still an increased risk of damaging a higher camber cell, and there remains the possibility for the current collectors to not make contact completely with the electrodes and interconnect. Differences in the amount of catalyst loading (as well as how deep the catalyst infiltrated into the anode) may also be related to the differences in ASR. Impedance spectroscopy results confirmed that Ohmic resistance dominated the ASR for the three cells, whereas electrode polarization amounted on average for only ~0.14 Ω-cm^2. Cell 2 had about a 25% lower ASR than the single cell 5 cm by 5 cm test of the same configuration (i.e., **Figure 65**). The ASR of Cell 3 was about 25% higher, while Cell 1 was

the worst performing and had about 75% higher ASR than the single cell 5 cm by 5 cm test. Regardless, across the 16 cycles shown in **Figure 100**, the performance of each cell remained essentially unchanged relative to each cell's baseline at the beginning of the red-ox cycle test. The red-ox cycling did not affect the OCV or the ASR of the cells. While **Figure 100** shows the individual voltage response for 16 cycles, the stack experienced a total of 50 red-ox cycles.

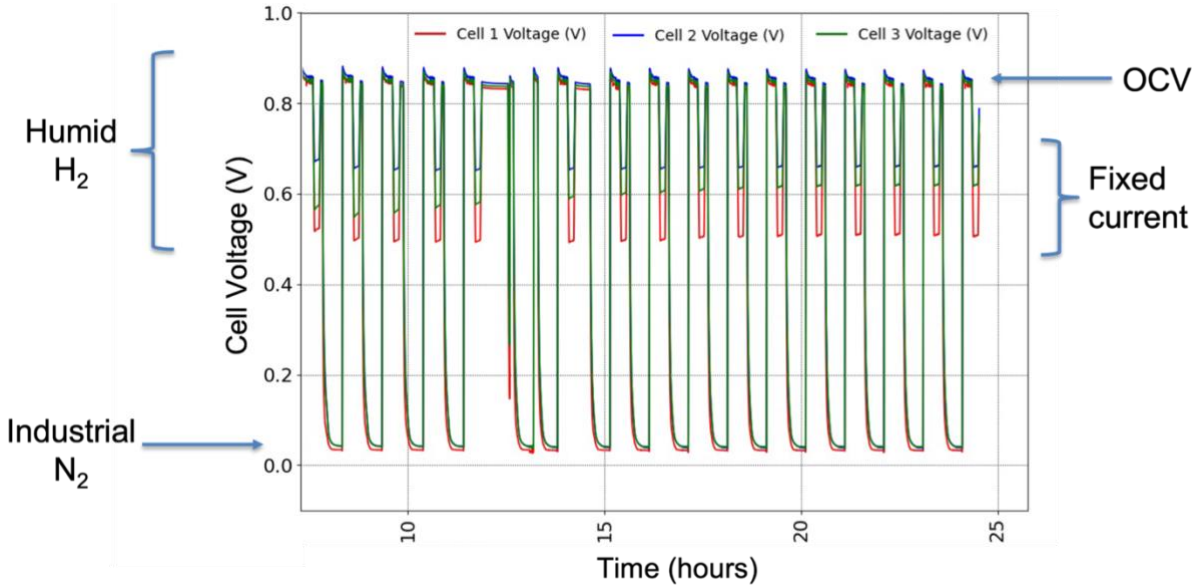

Figure 100. Cell voltage versus time for 3-cell stack using 5 cm by 5 cm SFCM-based ASL with AFL (*higher GDC content AFL at the higher sintering temperature*) and operating at ~600 °C during first 16 red-ox cycles, switching between humidified H_2 and humidified industrial N_2 (< 1% O_2) — the fixed current in H_2 was 0.21 A/cm^2.

Figure 101 shows the stack voltage versus time for the 3-cell stack as 50 red-ox cycles were completed over a period of ~60 hours. The cycle numbers (red) are shown in the bottom of plot. The average operating voltage at ~0.21 A/cm^2 was essentially unchanged through cycle 38. After cycle 38 (hour 47), three current sweeps were performed and yielded the same response as was observed prior to this point in time. After this point in time (hour 50), there potentially appears to be some ASR degradation between red-ox cycles 40 and 50. However, note that due to syncing errors between the current loading and red-ox cycling, there were several instances in which current was loaded while the anodes of the cells were exposed to the oxidizing environment. Green stars in the plot indicate when these events occurred, starting at red-ox cycle 19. These spikes in current were determined to have occurred because the sequence synchronization errors resulted in (potentiostatic) impedance spectroscopy measurements being made while in the oxidized state,

rather than in the reduced state at OCV as intended. This resulted in the measurement equipment increasing current beyond the constant current of 0.21 A/cm^2 in the reduced state (as high 0.6 A/cm^2) to maintain a voltage close to zero volts. Note, in the reduced state when impedance spectroscopy measurements were made at OCV, the bias current was normally only several mA.

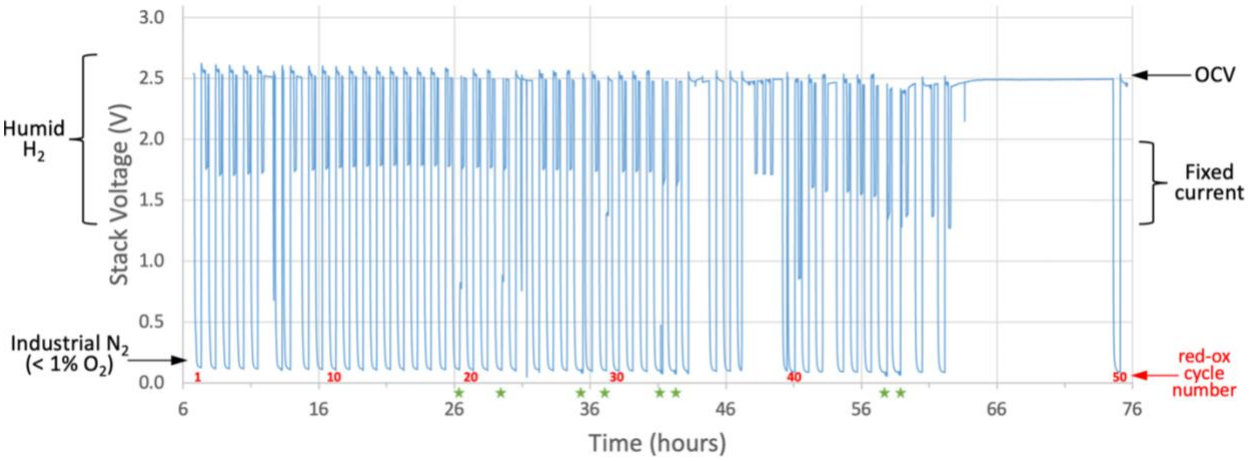

Figure 101. Stack voltage versus time for 3-cell stack using 5 cm by 5 cm SFCM-based ASL with AFL (*higher GDC content AFL at the higher sintering temperature*) and operating at ~600 °C during 50 red-ox cycles, switching between humidified H_2 and humidified industrial N_2 (< 1% O_2) — the fixed current in H_2 was 0.21 A/cm^2, but green stars indicate when current was accidentally loaded to as high as 0.6 A/cm^2.

When a current load is pulled from an SOFC that has no fuel at the anode, oxygen pumping still brings oxygen ions across the electrolyte to the anode. However, in this case as there is no fuel to oxidize, the oxygen ions can instead oxidize the materials in the anode (e.g., the GDC and SFCM). This can change the electrochemical potential of the different phases in the anode, resulting in different oxidation states. In other words, when the anode is in an oxidizing environment (e.g., humidified N_2 with 1% O_2) and a current is drawn from the cell, the degree of oxidation for these phases can be greater than without the current [70-71]. Moreover, the increased oxidation of these phases can result in chemical expansion greater than experienced during red-ox cycling and in the oxidizing state. As the ionic current with no fuel present can lead to an increase in the degree of oxidation, the result will be increased chemo-mechanical stress. These phenomena can result in permanent damage to the cell with increased ASR.

Upon closer inspection of the data between hour 46 and hour 65 (**Figure 102**), additional observations can be made. First, as the yellow star symbol between red-ox cycles 40 and 41 (hour

51-52) indicates, there was an anomalous low ASR measurement where the operating voltage was less than half the value of the previous measurements even though the current density was the same. Due to the hydrogen-to-industrial N_2 gas switching sequence becoming out of sync with the current loading portion of the test, as well as an unrelated error, there were two back-to-back red-ox cycles (numbers 39 and 40, between hour 50 and hour 51) with only a short period in between when H_2 was flowing. Moreover, right after this event, rather than flowing 100% H_2 in the reducing state, the anode stream anomalously consisted of a humidified 50% H_2/50% N_2 mixture, before returning to humidified 100% H_2 during the subsequent red-ox cycle. As with other large format cell tests in which red-ox cycling was conducted, the temperature of the stack (measured at the top stack endplate) decreased when switching from hydrogen to the oxidizing gas environment. The temperature decrease was typically registered as ~15 degrees lower when the anode stream was switched to the industrial N_2. However, as the red-ox cycle switching occurred in a relatively short time (i.e., every ~30 minutes), the temperature decrease did not fully equilibrate. As such, during the back-to-back red-ox cycles (numbers 39 and 40), the endplate temperature decreased further. Moreover, this meant that the endplate temperature was $\leq$ 590 °C when current was loaded between hours 51 and 52 (yellow star in **Figure 102**). Therefore, during this portion of the measurement, the cells were at a lower operating temperature and only half the fuel was flowing (i.e., the fuel was more dilute). Therefore, the ASR at that point of time was lower likely because the cells were operating at a lower temperature and because of increased concentration polarization. An impedance spectroscopy data comparison was made before this event (near hour 49.2), directly after the back-to-back red-ox cycle event and before the current loading (yellow star symbol) at around hour 51.2, and subsequently during the next scheduled impedance measurement (near hour 52.2). Note that the anode stream was 50% H_2/50% N_2 only for the measurement at around hour 51.2, whereas 100% H_2 was flowing for other two measurements. Relative to the measurement at hour 49.2, the Ohmic and electrode impedance at hour 51.2 had increased 1.87x and 2.18x, respectively. At hour 52.2, the ASR had decreased but still displayed an Ohmic and electrode impedance that was 1.19x and 1.18x, respectively, higher than that measured at hour 49.2. Another similar increase in ASR occurred after red-ox cycles 46 and 47, though in this case current spiked in the reduced state due to impedance spectroscopy measurements that occurred while in the oxidized state (i.e., industrial N_2 flowing in the anode stream). Just before red-ox cycle 46 (at hour

56.8), the Ohmic and electrode impedance were both similar to that at hour 52.2 (i.e., just after the incident indicated by the yellow star symbol). However, immediately after the incident that occurred in red-ox cycles 46 and 47, at hour 59.2, the Ohmic and electrode impedance were 1.07x and 1.32x, respectively, higher than the measurements at hour 56.8 (i.e., before the incident indicated by green stars between hours 58-59). The next two impedance measurements at hours 61.1 and 62.2 showed Ohmic impedance that were 1.12x and 1.16x higher than at hour 56.8, indicating a relatively slow increase of ~3% per hour (during the period in which 2 additional red-ox cycles had occurred). The electrode ASRs at hours 61.1 and 62.2, on the other hand, had increased to 1.28x and 1.7x, respectively, higher than at hour 56.8. Thus, after the incident at red-ox cycles 46 and 47 (green symbols), the electrode impedance was increasing much more rapidly than the Ohmic impedance (i.e., at ~13% per hour, during the period in which 2 additional red-ox cycles had occurred. This is slightly different behavior than occurred after the incident at hour 49.2 (yellow star symbol), perhaps indicating multiple types of damage beginning to happen to the cell as the stress from the extreme oxidative states (e.g., high current events — green star symbols).

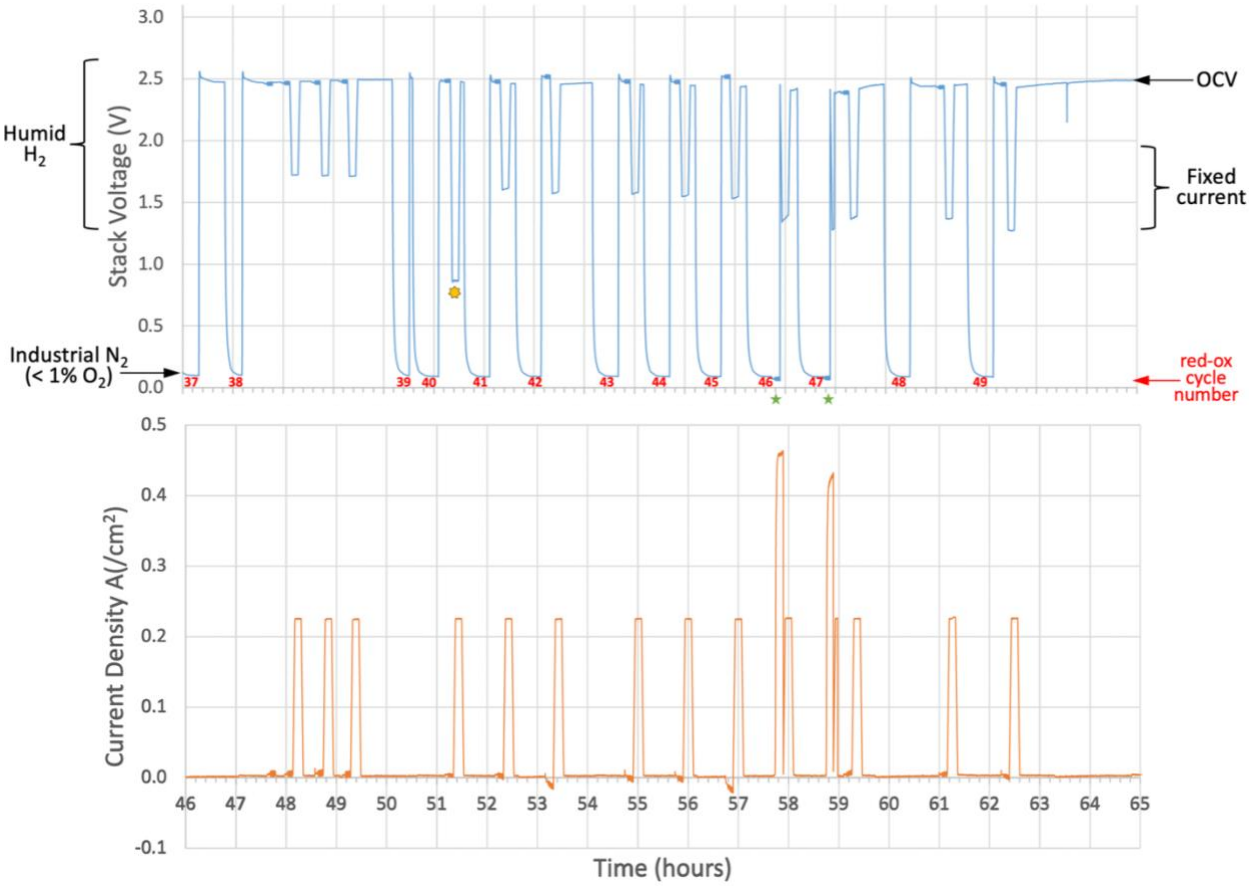

Figure 102. Stack voltage and current density versus time for a 3-cell stack using 5 cm by 5 cm SFCM-based ASL with AFL (*higher GDC content AFL at the higher sintering temperature*) and operating at ~600 °C between hours 46 and 65 when red-ox cycles 37 through 49 occurred, switching between humidified H_2 and humidified industrial N_2 (< 1% O_2) — the fixed current in H_2 was 0.21 A/cm^2, but green stars indicate where current was accidentally loaded to >0.4 A/cm^2. The yellow star between cycles 40 and 41 indicates an anomalously high ASR due to a decreased operating temperature after back-to-back red-ox cycles 39 and 40 as well as decreased fuel flow.

In addition to the temperature variations leading to anomalous operating voltages at 0.21 A/cm^2 during certain parts of the test, **Figure 102** reveals that starting around red-ox cycles number 40 or 41, OCV values in the reduced state were observed to decrease. Upon closer inspection, however, this does not appear to be directly related to a degradation phenomenon, as the OCV recovers after cycle number 49 and especially between hours 63 and 65 when more time has passed after a current loading but without additional red-ox cycles. Rather, this seems to also be a result of the event sequencing errors which led to the unsynchronized timing of the current loading and red-ox cycles. While upon reduction the cell voltage increases quickly, reaching a fully

equilibrated OCV takes some time, especially if temperature has not yet equilibrated. In most cases, the OCV recovered more quickly after a red-ox cycle than a current loading (e.g., see **Figure 101**), likely due to localized heating while under load with H_2 fuel. However, directly after and for some period of time after an incident in which the stack was loaded while the anode stream was oxidizing (green star symbols in **Figure 101** and **Figure 102**), the OCV after the red-ox cycle appears to have been much slower.

The initiation of a prolonged period of decreased OCV from around hour 52 until about hour 62 appears to begin with the current loading at decreased temperature which happened because of the back-to-back red-ox cycles (yellow star symbol in **Figure 102**). When this occurred the operating voltage of Cell 1 dropped below zero Volts. When combined with the current spikes at around 58 hours and 59 hours while industrial N_2 was flowing in the anode stream, the cells appear to have taken extra time to equilibrate after both switching to reducing conditions and loading the cell in H_2. While the OCV eventually recovered after enough time, these events may have also resulted in some damage to the cell due to the additional chemo-mechanical stress as discussed above.

In summary, this 3-cell stack red-ox cycling test successfully demonstrated that large format SFCM-based ceramic anode cells can operate in a stack without performance degradation for at least ~40 red-ox cycles. The test also revealed that damage may occur when the anode is in the oxidized state if cell is current loaded. An even more mechanically strong SFCM-based ceramic anode cell is highly desirable (e.g., so that a larger mechanical load can be applied during stack assembly) but may also have the benefit of yielding cells that are more robust to such a condition. While literature evidence backs this conclusion, the simplest way to prevent such degradation is to ensure the SOFC system disconnects the load as fast as possible in the event of a fuel disruption.

Throughout this project, SFCM-based ceramic anode SOFCs have been shown to be capable of reduction-oxidation stability. Moreover, proper tuning of the anode can yield a high-performance large format SOFC (e.g., > 0.6 W/cm^2 at 0.75 V). As described in Section 6, difficulties were encountered in scaling up the cell size (e.g., matching shrinkage between the half-cell layers), which required modification of the degree of porosity and half-cell sintering temperature to achieve flat cells. In doing so, the bonding strength between the anode and electrolyte was unfortunately decreased. As described in Section 4.4, in finding a solution for increasing the

bonding strength one tradeoff (primarily because of the decreased porosity) was lower initial performance. The lower porosity increased the difficulty for the catalyst solution to infiltrate deeply into the anode. One way to overcome this challenge is to apply vacuum during catalyst infiltration and/or to optimize the anode's pore morphology in future efforts. Taken all together, the path for further optimization of SFCM-based cells and stacks is clear and the potential still strong for high-performance, robust SOFC stacks operating at lower temperatures (≤ ~600 °C).

6. CERAMIC-ANODE CELL FABRICATION SCALE-UP

6.1. Scale-up of Ceramic-Anode SOFCs to Large Format Size

There are several requirements for large format SOFCs (e.g., 5 cm by 5 cm to 10 cm by 10 cm), including the need for a flat cell (e.g., 50-100 μm per cm) with low camber and no edge curl to prevent stress concentrators during stack assembly and operation. Moreover, the large format cells must be stronger than smaller button cells as they must be assembled in a stack, usually under varying degrees of compressive load. The large-format SFCM-based ceramic anode cells must also have a relatively high degree of as-fabricated porosity for catalyst infiltration, which is a requirement that runs counter to the strength requirement (i.e., as porosity increases, strength decreases).

Based on these requirements, there are several challenging aspects to increasing the size of SFCM-based ceramic anode cells. For instance, shrinkage mismatch is challenging and normal methods for characterization (e.g., dilatometry) cannot always be relied upon to guide design and processing optimization. This in part is due to the diffusion of elements (e.g., cobalt), between the SFCM-based ASL layer or layers, any AFL that may be present, and the GDC electrolyte. Dilatometry is often used to derive the sintering curves for the individual layers, in part so that that the sintering process may be fine-tuned to best accommodate different shrinkage rates of the layers making up the half cell during high temperature firing. The sintering curves are also typically useful for adjusting tape cast recipes (e.g., changes to the phase composition, including ceramic powders and pore formers) to better match the shrinkage of the layers. As the shrinkage of the individual layers can be different when elements diffuse into or out of the layer, the sintering curve/dilatometry tool was less useful for SFCM-based ceramic anode cells than with normal Ni-cermet based SOFCs.

Nonetheless, the sintering curves still served as a tool for generalized observations as a balance was made between pore-former size/amount, composite anode composition, layer thickness, and sintering process to achieve acceptable cell strength, flatness, and electrochemical performance. This meant that increasing the size of the SFCM-based ceramic anode cells was more difficult than with Ni-cermet cells.

For SFCM-based ceramic anode SOFCs, a cell shrinks more as the firing temperature increases. The increased firing temperature also helps improve mechanical strength through a higher degree of particle-to-particle necking within a layer, as well as increased bonding between layers. Unfortunately, all else the same, a higher sintering temperature decreases the as-fabricated porosity and thus a trade-off is lower catalyst infiltrate uptake. A study was conducted to gauge the impact of sintering temperature (low, medium, and high) on cell performance. The shrinkage rate was lowest at the "low" sintering temperature, which resulted in the highest anode catalyst loading after several infiltration cycles without vacuum — during each cycle a dropper was used to soak the anode in a nitrate solution of Ni and GDC, followed by heat treating the cell to decompose the nitrates. The cells were approximately 4 cm by 4 cm after sintering. A relatively large difference in shrinkage rate occurred in going from the "low" sintering temperature to a "medium" temperature. When going to the "high" sintering temperature, however, the shrinkage rate was only slightly higher than at the "medium" temperature. Less catalyst infiltrate (about 25% lower) was able to be loaded into the anode of the cells fired at "medium" and "high" temperatures even though more infiltration cycles were used. The less efficient the catalyst infiltration process (i.e., the more cycles needed), the more expensive the process. Additionally, the need for vacuum infiltration can greatly increase the cost of infiltration and, therefore, there is a great deal of motivation to not use such a process. As seen in **Figure 103**, the cell fired at the "medium" sintering temperature resulted in the best performance (i.e., the lowest total impedance at ~0.3 Ω-cm^2). While the "high" sintering temperature resulted in approximately the same Ohmic impedance as the "medium" sintering temperature cell, and despite having the same catalyst loading, the decreased anode porosity of the "high" sintering temperature cell likely resulted in less catalyst reaching the triple phase boundary at the anode/electrolyte interface. The "low" sintering temperature cell, on the other hand, had a much higher Ohmic resistance but a similar electrode impedance as the "medium" temperature cell. While in this example, the "medium"

temperature cell is the most optimized, the strength of cells fired at that temperature was ultimately found to be too low for large format size cells (e.g., 5 cm by 5 cm or 10 cm by 10 cm) to operate reliably.

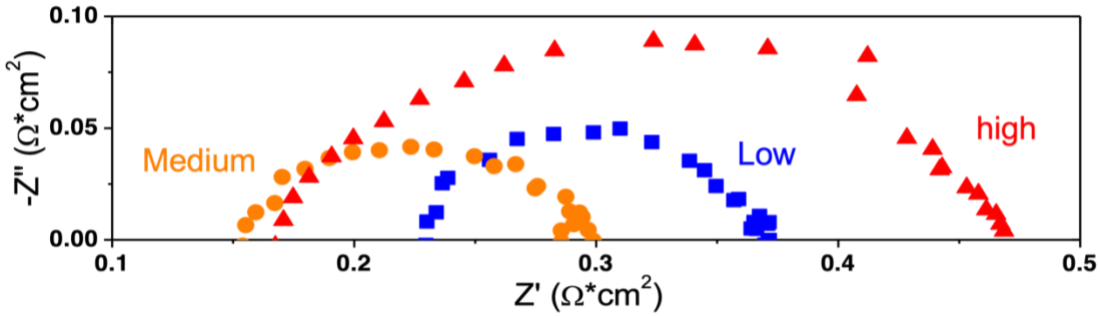

Figure 103. Summary of the impact of sintering temperature on 4 cm by 4 cm SFCM-based ceramic anode cell performance (Nyquist plot of impedance spectra) at 600 °C in hydrogen for low, medium, and high sintering temperatures.

As discussed in Section 4.4, during performance optimization many of the configurations explored for the SFCM-based ceramic anode cells resulted in delamination at the interface between the anode and electrolyte. This is thought to have generally occurred due to the build-up of stress that resulted from mismatched sintering shrinkage, thermal expansion, and chemical expansion between the layers. While initially we thought the presence of exsolved Sr at the anode for some configurations was the primary cause for delamination, we ultimately concluded that several factors contributed to the degradation observed with large format SFCM-based ceramic anode SOFCs. The mismatch in thermal expansion and chemical expansion were most likely to cause problems during operation of cell/stacks as described further in Sections 4.4 and 5.3. Additionally, the degree of camber and other high points on the cell (e.g., edge curl) increased the localized stress in the cell after assembly with stack hardware.

As discussed in Section 4.3, the mechanical strength of SFCM-based ceramic anode half cells is as much as 10-times lower than Ni-cermet half cells. During the project we briefly investigated the use of additives to improve the strength of the SFCM, but at higher sintering temperatures while strength may have improved there were also reactions between the materials that created undesirable secondary phases. At lower sintering temperatures, while no secondary phases resulted, the mechanical strength improvement was negligible. Moreover, in all cases the resulting material had unacceptably low electrical conductivity (i.e., at least an order of magnitude lower),

which was attributed to insulating phase formation in the materials that had reactive secondary-phase formation. While a solution for improved strength may be possible with additional work, our efforts in the remainder of the project were focused on increasing the bonding strength between the layers as much as possible and finding ways to lower the load on the cells during stack assembly.

Because of these fabrication issues, every time the cell configuration was modified or the composition of the layers was changed (e.g., amount of pore former and metal/ceramic phases), a lot of work was required to increase the cell size. For instance, a series of sintering shrinkage curves for SFCM-based composites is shown in **Figure 104** for various ASL samples. The ASL samples had different compositions and amounts of pore former. The lowest shrinkage sample (red diamonds) was a sample made from SFCM and one of the strengthening additives mentioned above. Conclusions resulting from investigation of the sintering curves included the observations that increased pore former decreased shrinkage, whereas smaller particle size and amount of the ceria-based phase increased the degree of sintering. Additional sintering curves for the AFL (when used) and electrolyte were similarly created and we made the necessary tradeoffs to match shrinkage rates as much as possible during sintering.

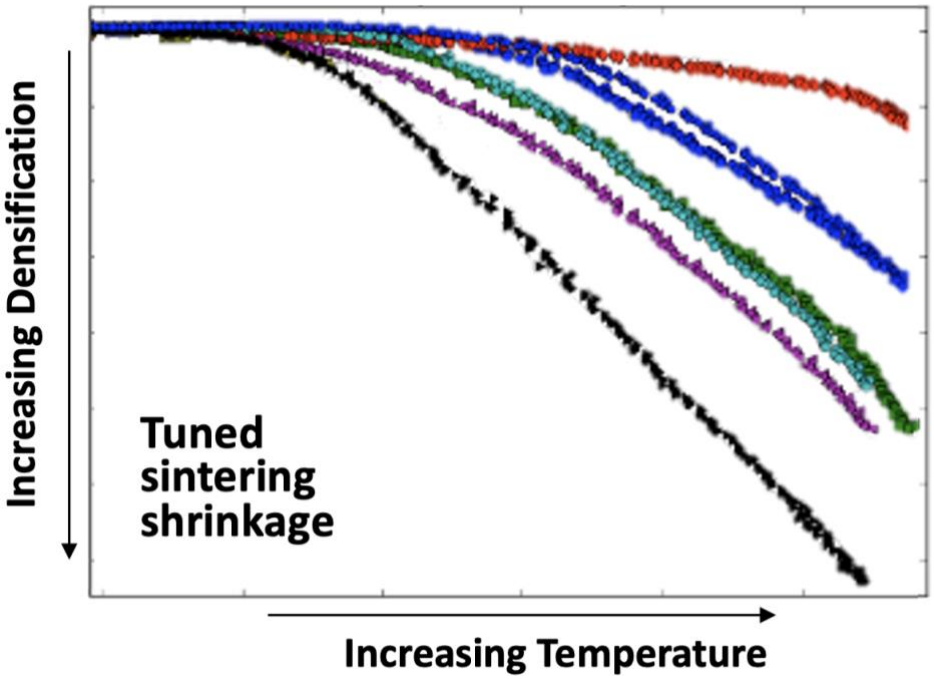

Figure 104. Example of sintering curves for various SFCM-based ceramic anode support layers (ASLs) with variations in composition and amount of pore former.

As mentioned in Section 4.4, the initial configuration and composition for the SFCM-based ASL were modified slightly from that of the original button cells used in the baseline development efforts in order to achieve flat, crack-free large format half cells. The baseline large-format cell configuration (i.e., see **Figure 8**A) for a porous SFCM-based ceramic anode supported half-cell was successfully fabricated at a large format size of 10 cm by 10 cm, as shown in **Figure 105**. The electrolyte layer was dense and without any cracks. The ASL formulations and fabrication procedures (e.g., firing schedule and constrained sintering weight) were optimized to reduce the cell camber for large format cell size. As shown in **Figure 106**, the initial cell configuration yielded a flat cell that met the target specification from maximum to minimum height variation across the entire cell.

Figure 105. Example of 10 cm by 10 cm SFCM-based ceramic anode supported half cell with the anode and electrolyte co-fired at high temperature.

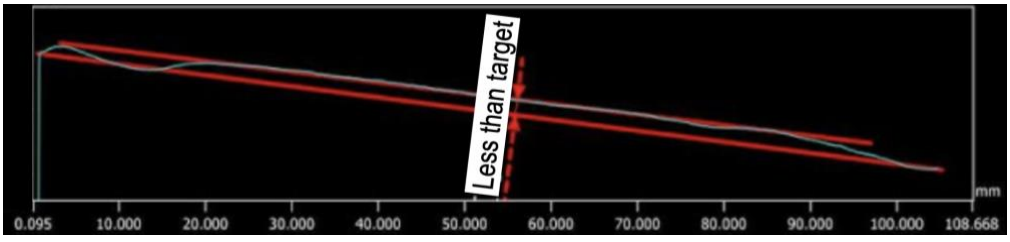

Figure 106. Example of cell camber for a 10 cm by 10 cm SFCM-based ceramic anode half cell (note, the sample was not entirely flat on the stage, resulting the tilted profile) — the maximum of from high to low spots for the cell was found to meet the target specification.

For other cell configurations, to achieve a sufficiently flat cell at a large format size greater than or equal to 5 cm by 5 cm generally required a lower sintering temperature due to shrinkage mismatch between the layers. This lower sintering temperature, however, resulted in lower strength. This is just one example of the challenges faced in scaling up the size as the cell configuration was optimized for performance (e.g., > 0.6 W/cm^2 at 0.75 V and 600 °C as in **Figure 41**), long-term stability, and red-ox stability.

6.2. Fabrication Scale-Up for Increased Batch Production

To make stacks with the SFCM-based ceramic anode SOFCs, a larger number of cells were needed and the characteristics and performance of the cells should be similar to each other. During the initial portion of the project, Redox had successful tape casts of SFCM-based ceramic anode cell components (i.e., cell configuration shown in **Figure 8**A) with a commercial manufacturing partner. Development casts of the SFCM-based ceramic anode were produced and used to fabricate >30 half-cell laminates sized for 10 cm by 10 cm cells. Note, some of the laminates were subsequently cut to make 5 cm by 5 cm cells. The laminates were fired both at a production partner's facility and at Redox. The larger kiln used at the production partner had a very good temperature uniformity. Four cells were spread out from the top and bottom to the middle of the furnace to evaluate temperature non-uniformity impacts on cell firing. All cells survived firing without cracking or undesirable deformation. While the electrochemical performance of these SOFCs was relatively low, the cell stability was relatively good (see **Figure 35** through **Figure 38**). Additional modifications were made to the anode tapes with the production tape casting partner and at 600 °C yielded a cell performance of only ~0.25 W/cm^2 at 0.75 V (see **Figure 58**).

Cell fabrication optimization. While working with smaller batches of tapes in the cell optimization process, the dedicated SFCM-based cell sintering furnace at Redox was found to have non-optimal temperature uniformity, due in part to the smaller size as compared with the furnace at the production partner's facility. As cells are fired on multiple tiers within a high temperature box furnace, cells on certain levels were found to always yield a better firing result than the other levels. For example, this led to issues with cracking of cells on certain levels in the furnace. To increase yield, the furnace was modified to promote convection and improved temperature uniformity. During the first few trials after the modification was made, the furnace temperature

uniformity between the tiers was much better than before. Due to the unintended consequence of the furnace modification resulting in a change to the average temperature profile of all the tiers, each step of the thermal profile needed to be adjusted.

Thermocouples were used on each of the levels in the furnace to fully characterize the temperature uniformity, which was found to have improved dramatically after the furnace modification with the temperature variation among the different levels brought to within ≤ 5 °C of each other at all steps of the firing schedule. The furnace and sintering process optimization was also subsequently found to yield 5 cm by 5 cm cells without cracks as shown in **Figure 107**.

Figure 107. Example of 5 cm by 5 cm SFCM-based ceramic anode half cell without cracks as a result of an optimized firing profile and improved temperature uniformity in the furnace.

After optimizing the cell performance and stability for the large format SFCM-based ceramic anode SOFCs, using the commercial-scale tape casting equipment for all the half-cell layers was no longer an option in this project. Therefore, Redox's pilot-scale tape caster was modified to achieve greater uniformity across the fabricated green tape (e.g., thickness variation — side to side and front to back) and between different tape cast batches. Prior to improvements, the tape cast slurry was manually poured into the doctor blade reservoir at the beginning of the tape casting process, which resulted in a variable head pressure as the slurry level in the reservoir varied. This tended to result in tapes that are thicker near beginning of the tape, and gradually decreasing in thickness toward the end of the tape. For instance, the previous process had, in certain instances, resulted in a thickness at the start of the tape that was approximately twice that of the end of the tape. Such a large variation in tape thickness may not impact the small size cells (< 5 cm by 5 cm)

made one at a time but can cause problems for larger size cells made in large batches. Additionally, an IR temperature sensor was used to characterize the tape caster bed temperature, which was found to not be uniformly heating. This can result in different drying rates for different portions of the same tape, which can lead to cracking or other undesirable defects. From our analysis of the overall process, a plan was developed to improve the tape caster bed temperature uniformity and to obtain a more-uniform head pressure during feeding of the slurry to the doctor blade reservoir. The improvements yielded a thickness difference between the beginning of the tape and the end of the tape within ±5% of each other. Lastly, the tape casting process was optimized to increase the amount of tape created in a single batch. Unlike the 50-75 feet long tape production tape casters, the pilot-scale tape caster was only ~15 feet long. When using the pilot-scale tape caster, a relatively thick tape (e.g., ASL) might not have time to dry before reaching the end of the tape caster bed. Therefore, the ASL tape casting process was modified such that the layers were thinner and were able to fully dry before reaching the end of the tape caster bed, which enabled the tape to be rolled up in a continuous process that yielded much more tape in a single batch. The thinner tapes were still strong enough that they were able to be removed from the carrier film and laminated together with the other layers in the half cell prior to sintering. After several trials, the optimized thickness was found to be about 50% the previous ASL thickness. The tape is much thinner, but still thick enough allow the ASL to be easily removed from the Mylar carrier film, transported, and stacked together for lamination. Moreover, the ASL tape is sufficiently thin that the ASL is dry by the time the tape reaches the end of the tape caster and therefore can be rolled up and made in larger batches. The image of the new, thinner tape casted ASL is shown in **Figure 108**. A fired 5 cm by 5 cm cell using the new (thinner) tapes is shown in **Figure 109**. There were no cracks and the cell was flat with a shiny electrolyte.

Figure 108. Photograph of a thinner SFCM-based ceramic ASL tape that enabled the fabrication of larger batch sizes as the tape dried more quickly and was able to be rolled up at the end of the pilot-scale tape caster, as shown on the right side of the image.

Figure 109. Sintered 5 cm by 5 cm SFCM-based ceramic anode half cell made with thinner ASL was found to be flat and without cracks.

7. TECHNO-ECONOMIC ANALYSIS

7.1. Manufacturing Cost Modeling

The techno-economic analysis (TEA) goal for the project was to reduce the system capital equipment costs normally associated with a safety gas anode-protection system. The target stack cost after optimized performance and development in high volume production (≥ 500,000 units/year) was ~$225/kW with a cell power density of >0.75 W/cm^2 at 0.75 V (at ~600 °C).

The manufacturing process for the SFCM-based cells was modeled by CALCE as a sequence of process steps that are executed in a specific order. The steps and their sequence are referred to as

a process flow. Process-flow modeling emulates a real manufacturing process. Process-flow modeling is generally thought of as a *bottom-up* approach to cost modeling. In a bottom-up model the overall response or characteristic of a product is decided by accumulating the properties (responses and characteristics) of each individual action that takes place while manufacturing the product. The opposite of a bottom-up approach is the *top-down* method, in which high-level attributes are used to determine the responses or characteristics of the object without considering the constituent parts or the processes used to create the object.

In process-flow models, an object accrues cost (and other properties) as it moves through the sequence of process steps. Each process step starts with the state of the product after the preceding step ("Inputs"). The step then modifies the product, and the output is a new state ("Outputs"), which forms the input to the process step that follows, and so on. When multiple process steps are sequenced together, a process flow is created. A linear sequence of process steps is called a "branch." The process flow for a complex manufacturing process may consist of one or more branches. Multiple branches imply that independent sub-processes are taking place that eventually merge to form the complete product.

The process flow for SFCM-based ceramic anode cells was formulated using an easily accessible spreadsheet format. Each step was modeled by one or more process steps. Each process step was (in general) be characterized by the following:

- Process time
- Operator utilization (how many people, or how much of one person is dedicated to the step)
- Capacity (number of identical items processed in parallel)
- Material cost
- Tooling cost
- Equipment (capital) cost
- Equipment operational time (fraction of the time the equipment is expected to be available)
- Defect density introduced or Yield
- Fault coverage (test/inspection steps only)

In addition, general information (applicable to all steps) includes labor rate, labor burden, depreciation life, and other unit conversion information. Using this information, the labor, material, tooling, and equipment costs associated with each process step can be determined. In

addition, the impact of the step on the yield of the product can be found. The process costs and yield can then be accumulated to determine the final product cost (e.g., in the unit of $/cell or $/kW) and yield. The manufacturing process flow model includes a Monte Carlo analysis (various inputs can be represented as probability distributions). When the Monte Carlo analysis is performed, the resulting costs and yields are probability distributions. The model has been populated with the appropriate data.

The model includes material, labor, tooling and capital equipment costs. The first 10 steps of the ASL, AFL and Electrolytic branches were split from the main process flow and formed into three separate (sub-)process flows, each of which represents the manufacturing process for the particular type of powder. A "Raw Materials" model option was also added, which allows the user to choose to either make or buy each type of powder and estimate the material cost per sheet for each type of powder. For example, if one powder is chosen to be made, that powder making process is enabled, and the overall fabrication process starts from the first step of the powder model; if the powder is chosen to be bought directly, the powder process will be disabled, and the overall fabrication process will start from the first step of the updated "ASL" process, which is purely the material cost per sheet if powder is bought.

Including the three newly created powder processes, all process step costs are converted into the effective cost per cell for comparison purposes. The model also tracks defect density and yield through all the process steps. Test/inspection steps determine the amount of product scrapped based on a fault coverage and the defect density and/or yield of the product when the test step is encountered. Additionally, the model generates the cell yield.

The initial process-flow analysis model for SFCM-based ceramic cell manufacturing was subsequently updated to include the following significant extensions:

1. **Hours per Year** – "Hours per year" was replaced with "Number of shifts" as an input. Four shifts (each with 40 hours) per week are possible. Based on the number of shifts, the hours per year can be determined.
2. **Annual Volume** – The step time of each process step can be converted into hours per cell for comparison purpose. Then the step with the longest step time is the "bottleneck" step that determines how many cells can be produced annually by the process. Therefore, combined with the hours per year calculated from the number of shifts, the annual volume in cells can be calculated.

3. **Final Total Yield** – The non-parametric yield and the defect density are accumulated independently through the process. After the last process step the final total yield is calculated as the product of the final non-parametric yield and the final parametric yield (calculated from the cumulative defect density).
4. **Final Yielded Cost** – Final yielded cost is the final cumulative cost divided by the final total yield. It is the effective cost per good (cell) produced. As a result of the stochastic simulation process (i.e., Monte Carlo analysis), each execution of the model produces a different combination of cost and yield and therefore a unique final yielded cost.
5. **Process Utilization** – The process utilization accounts for the fraction of the total calendar time that the process (process step or particular equipment) is utilized by the product being modeled. This is important because capital costs (equipment) are allocated to each cell (or cell equivalent) based on the fraction of the equipment's total life used up by each cell. Previously, the only input that modeled the utilization was a process-step specific equipment utilization fraction that, when coupled with the hours per year (input), allows a capital cost to be determined for every process step. This concept was refined. The number of shifts determines the production volume of cells that can be produced, but also determines how the equipment is utilized.
6. **Equipment Quantity/Dedication/Sharing** – Features were added to the cost model that allow the number of pieces of equipment used in each process step to be adjusted. Choosing whether the production line is dedicated to the SFCM-based ceramic anode fuel cell manufacturing and choosing whether or not all tape fabrication branches (e.g., electrolyte, anode, etc.) are sharing the same production line, which will affect the equipment cost.

One last update was made to the process-flow analysis model for SFCM-based ceramic anode cell manufacturing. These significant extensions of the model included:

1. **Dedication Process Check** – Both the branch process flows (tape manufacturing) and the main process flow can be chosen to be either dedicated or non-dedicated to the SFCM-based ceramic fuel cell manufacturing branch (they are either exclusively used for SFCM-based SOFC manufacturing, or they are non-exclusive, meaning that they are shared with the production of other parts or products). For each process flow, if it is dedicated and its step time is longer than the total shift time, an error message is generated, and the analysis will terminate.
2. **Equipment Quantity** – The number of pieces of equipment used in each process step can be adjusted, which influences the annual volume as well as the final cost of the cells.
3. **Bottleneck Step Identification** – The step with the longest step time (per cell manufactured) will be the "bottleneck" step that effectively determines the number of cells that can be produced annually. The bottleneck step is automatically identified and highlighted in the analysis.
4. **Final Cost Decomposition** – The four major cost components: material cost, labor cost, equipment cost, and tooling cost were updated so they are accumulated separately

throughout the process flow, and the final cost decomposition can be shown in a form of a pie-chart as given in the example of **Figure 110**.

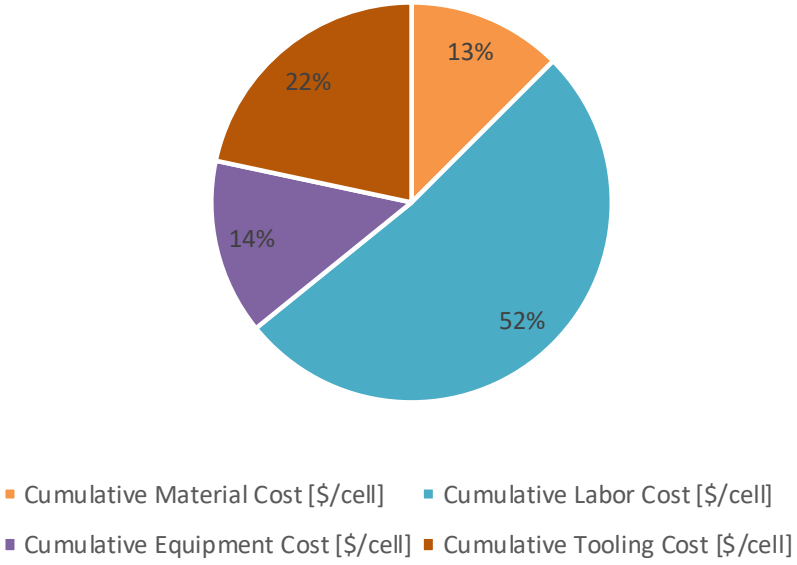

Figure 110. Example of cost breakdown resulting from the manufacturing cost model.

This cell fabrication cost model was ultimately expanded to the stack and system level, to allow the estimation of system level manufacturing costs. Together with past cost models Redox worked on with Strategic Analysis Inc. (DE-AR0000494) that was based on a design for manufacture and assembly (DFMA) approach, the CALCE cost model provides Redox a useful set of tools for estimating the cost of manufacturing all aspects of SOFC power systems. In parallel, CALCE created a natural gas supply disruption model to help quantify the frequency, severity, and duration of natural gas outages to quantify the benefits of the reduction oxidation stack. These two modules provide inputs into the lifecycle cost analysis to show the overall cost benefits of the reduction oxidation stable stack versus incumbent SOFC approaches.

7.2. Discrete Event Simulator

Life-cycle cost modeling generally involves modeling systems that evolve over time. Time-dependent costs usually involve the operation and support of the system. Support costs (e.g., maintenance costs) that occur over time are combinations of labor, equipment, testing, and spare parts. If the life cycle of a system is relatively short (i.e., less than a couple of years), then direct calculation methods work well, however, when the modeled life cycle extends over significant periods of time and the cost of money is non-zero, the calculation of life-cycle cost changes from

a multiplication problem into a summation problem and the dates of cost events become important (e.g., the cost of individual maintenance events differ based on when they occur). Discrete-event simulation (DES) is commonly used to model life-cycle costs that are accumulated over time when time spans are long, and the cost of money is non-zero.

DES is the process of codifying the behavior of a complex system as an ordered sequence of well-defined events. In the context of cost modeling, an event is a particular change in the system's state at a specific point in time, and the change in state generally has cost consequences. Discrete means that successive changes are separated by finite amounts of time, and by definition, nothing relevant to the model changes between events. At each event, various properties of the system can be calculated and accumulated. The property of interest for the SOFC power system is cost. Everything in the DES is uncertain and can be represented by probability distributions. This means that we model the timeline (and accumulate relevant parameters) many times (through many possible time histories) to build a statistical model of what will happen.

A DES model for the SFCM-based ceramic anode SOFC stack was developed. This model includes a set of failure mechanisms that are each characterized with a time to failure distribution and a consequence. The consequence is either a maintenance event (which costs money) or an acceleration in the degradation of the stack (after a prescribed amount of degradation, the stack must be replaced). The DES samples the time to failure distributions to determine the earliest event; moves the system clock to that event; determines the cost of the event (if any); resamples the time to failure for the mechanism that caused the event; determines the next event; and continues the process until the end of support for the system is reached. In parallel with this process, a degradation clock tracks the overall degradation in performance of the stack. When the performance of the stack has reached a prescribed threshold, the entire stack must be replaced.

Figure 111 shows an example analysis from the discrete-event simulator. In this example, the stack is simulated for 4 years with a discount rate of 7%/year. The result of a single time history for the stack is shown in **Figure 111**A, whereas **Figure 111**B shows seven independent time histories. The latter example indicates that the cost of the paths varies due to uncertainties in both the time to failures for the various mechanisms and the cost of resolving those failures. Note, the

data used in the example in **Figure 111** is not specific to the SFCM-based ceramic anode SOFC stack and was meant to illustrate the capabilities of the model.

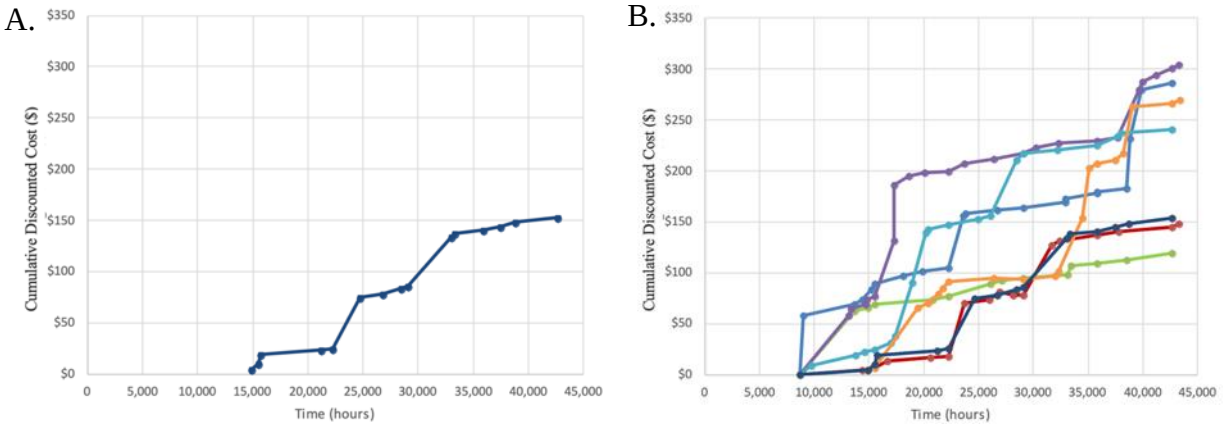

Figure 111. An example of a life-cycle cost simulation of a stack showing A) single time history and B) seven independent time histories.

The disruption of natural gas to a stack is a potential failure mechanism in the field. Therefore, we developed a capability within the DES model that estimates the risk (frequency) of gas disruptions based on historical gas disruption data. Natural gas pipelines are generally divided into production pipelines, gathering pipelines, transmission pipeline and distribution pipelines. The distribution pipelines deliver natural gas from the city gate stations (where the transmission pipelines feed into the lower pressure distribution pipelines) to individual homes and businesses. The distribution pipeline network is the focus of this model. Disruptions to the distribution pipeline network can be divided into the service interruptions and leaks. The former can further be divided into intentional and unplanned interruptions, as described below.

Intentional service interruptions include:

- Planned interruptions for maintenance or upgrade
- Customer request
- Tight gas supply
- Gas supply shortage

Unplanned service interruptions include:

- Malfunction of equipment
- Damage to gas facilities due to natural disasters

- Explosion or fires resulting from failure of gas equipment
- Acts of vandalism, sabotage or civil disturbance
- Gas supply interruptions at the city gate station due to transmission pipeline problems
- Pressure fluctuations caused by human error or equipment failure
- Safety conditions that require shutdown of gas to a customer or area
- Emergency conditions

The typical causes of leaks are:

- Gas pipeline hits or dig-ins by customers, contractors or third parties
- Corrosion and deterioration in pipes or joints
- Material component failure (e.g., caused by weld or material defects)

Figure 112 shows a simplified model of a natural gas distribution pipeline network assumed in the model, in which a large pipeline starts from the city gate station; a middle pipeline starts from some point on the large pipeline; followed by a small pipeline and a local pipeline that ultimately connects to the fuel cell stacks. The average pipeline distances were assumed to be known, and the failure rate data in the unit of number of failures per mile per year were obtained from a pipeline risk analysis by J House Environmental [72]. Using this information, the gas pipeline's time to failure (from the install date) can be estimated using a Monte Carlo simulation as shown in **Figure 112**, which can be can be used as an input to the SFCM-based ceramic cell stack DES model for the life-cycle cost estimation compared to that of a Ni-cermet cell.

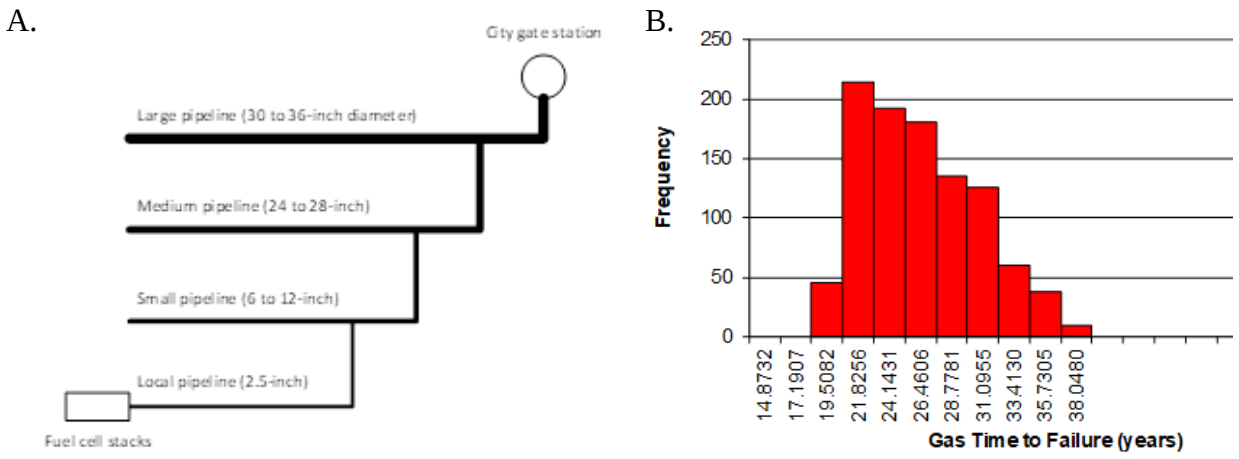

Figure 112. A) Simplified natural gas distribution pipeline network and B) distribution of the simulated pipeline network time to failure (interruption).

The DES model includes a set of user-definable failure mechanisms that are each characterized with a time to failure distribution and a consequence. In general, the consequence is a maintenance event (which costs money) and possibly an acceleration in the degradation of the stack (after a prescribed amount of degradation, the stack must be replaced). The DES samples the time to failure distributions to determine the earliest event; moves the system clock to that event; determines the cost of the event (if any); resamples the time to failure for the mechanism that caused the event; determines the next event; and continues the process until the end of support for the system is reached. In parallel with this process, a degradation clock tracks the overall degradation in stack performance. When the performance of the stack has reached a prescribed threshold, the entire stack must be replaced.

After developing the initial DES model, additional changes and enhancements were made, including:

1. The addition of a realistic system model (shown in **Figure 113**) with reasonable reliability and maintenance data.
2. The enhanced failure mechanism model includes the following inputs for every failure mechanism: time to failure distribution; time to repair distribution; spare parts cost; stack life removed distribution; and a liability duration (e.g., warranty length).
3. The updated deployment model, which defines the size and date of field systems allows deployments to be described by overall system size (from which the number of stacks are calculated). The system model was also extended to allow multiple deployments with different installation dates and assorted sizes.
4. The addition of a variable (time dependent) weighted average cost of capital (WACC) model.
5. The addition of a Levelized Cost of Energy (LCOE) model, which is defined as the ratio of total life-cycle cost and the total energy produced determined by the efficiency of the stack and the change in efficiency as a function of time.
6. A model output of a breakdown of the life-cycle costs by failure mechanism and deployment costs — an example breakdown for a case in which LCOE was $367/MWh is shown in **Figure 114** (the assumed production volume was very low, with the stacks costing $5,000/kW; the weighted average cost of capital (WACC) = 13%/year; system size was 25 kW; support life = 10 years).

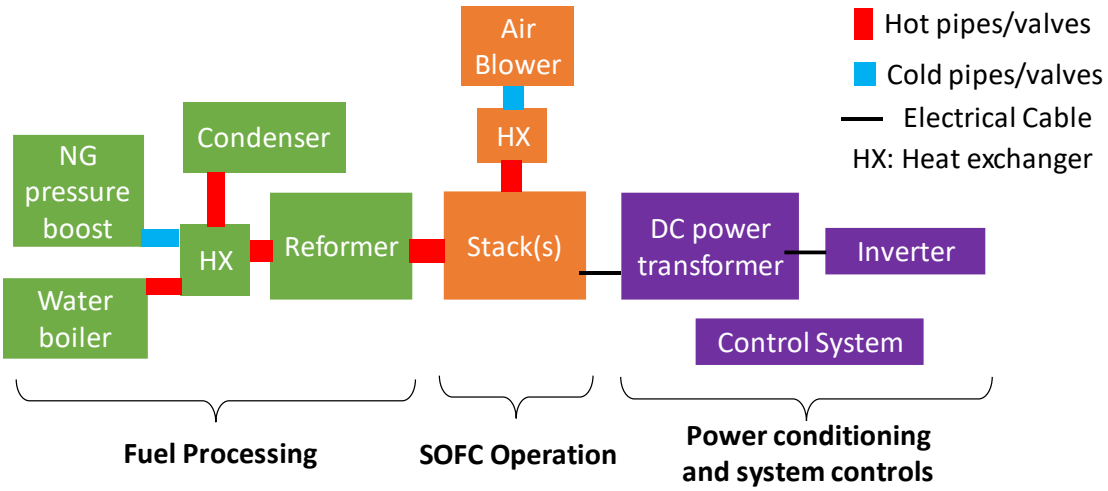

Figure 113. Configuration assumed for discrete event simulator model.

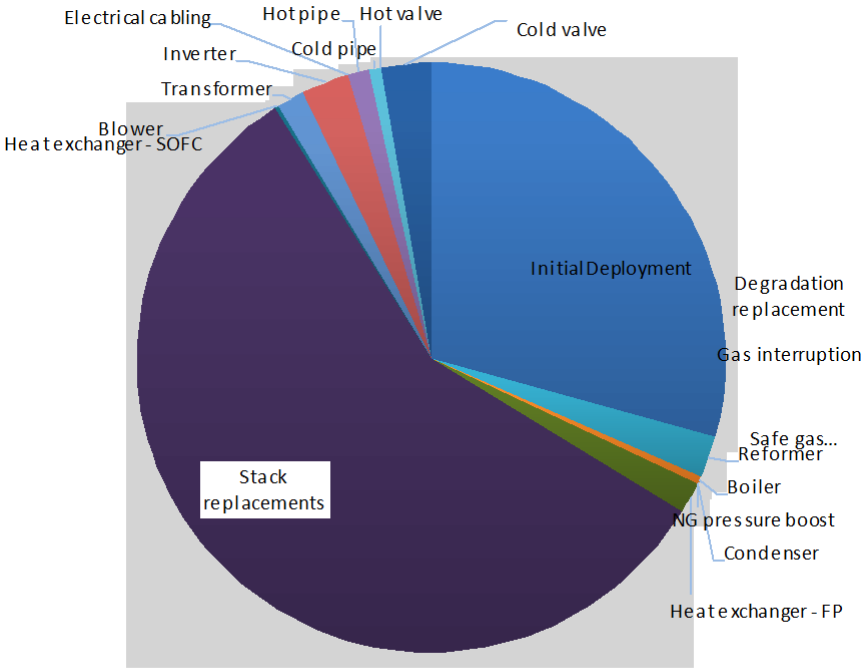

Figure 114. Example output from discrete event simulator showing cost breakdown over warrantied life of system — note, in this example, the system production volume is very low.

Example Discrete Event Simulator Analysis. **Figure 115** shows a 25-kW, 10-year installation example case with a false alarm incidence once per year. Key results are summarized in **Table 4**. Note, the component costs (including cell/stack costs) were modeled at a very low production volume, but still demonstrate the impact of red-ox robust stacks. False alarms are situations where

the system shuts down based on the input from a sensor or safety system, but no actual cause of failure is determined. Such false alarms may arise from, for example, operation of a forklift or other motorized vehicle near a fuel gas sensor. The following four different assumptions were compared: 1) no damage to the stacks caused by false alarms; 2) damage to the stacks from the false alarm that results in stack replacement every 3 years; 3) damage to the stacks from the false alarm that causes stack replacement at every false alarm; and 4) no false alarms. The second case is an example of a red-ox robust (tolerant) stack, representing a drastic improvement in red-ox cycling tolerance over the nickel-cermet based stack in case three. Note, the stacks also accumulate collateral damage from other component failures and may in some cases fail due to other failure modes. This case includes 41 different components/failure mechanisms, a 13%/year discount rate, fuel costs, and an initial 50% energy conversion efficiency.

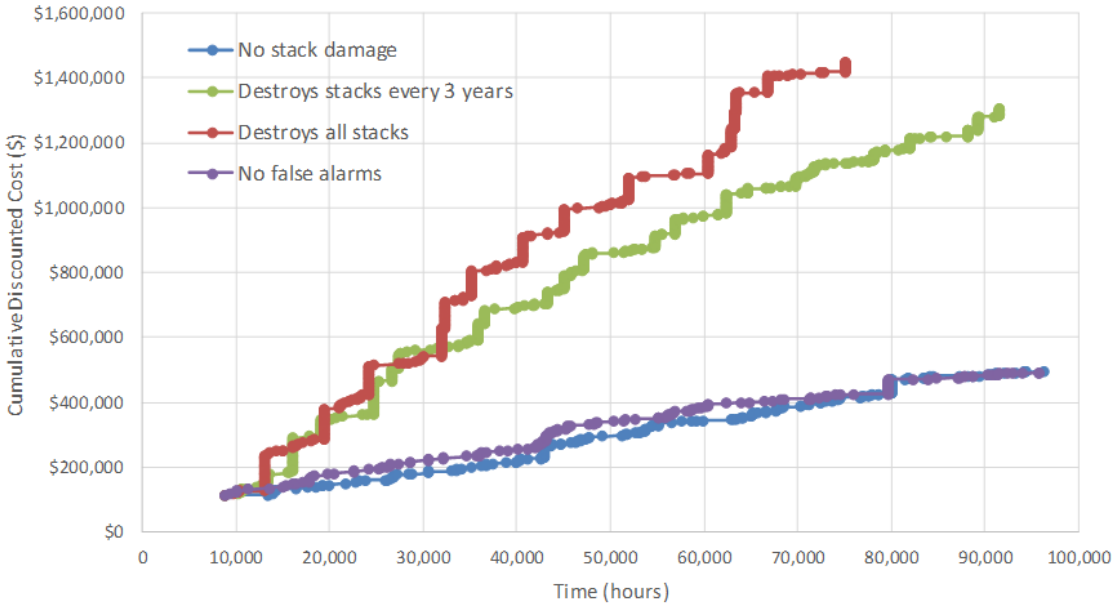

Figure 115. Example of discrete event simulator output for four conditions for a 25-kW system — note, in this example, the system production volume is very low.

Table 4. Summary of data for cases shown in Figure 115 (very low production volume).

	LCOE ($/MWh)	Operational Availability
No false alarms	$287	98.11%
No stack damage	$288	97.96%
Destroys stacks every 3 years	$658	96.54%
Destroys all stacks	$724	95.95%

Obviously, the LCOE is lower when there is no stack damage due to the false alarms and the fact that availability is higher. Note, this is a stochastic calculation that samples from probability distributions; and every time the analysis is run there is slightly different answer.

Logistics Model. A logistics model was created to capture the sparing process for sustaining the system (i.e., a model of the items and quantities must be readily available to maintain system operation with minimal or no downtime). This model was implemented as a parallel simulation (i.e., the logistics model runs in parallel with the DES model) that tracks the spare parts inventory. As maintenance actions take place (which consume spare parts), the spares are drawn from inventories of previously purchased parts. When the inventory level for a part falls below a part-specific and user defined threshold, the inventory is replenished. The inputs to this model include (all are part specific):

- Initial inventory quantity
- Inventory replenishment threshold
- Inventory replenishment quantity
- Lead time for replenishment
- Holding cost
- Shelf life

Specific parts have the option to be bought as needed (rather than inventoried). All the items listed above have differing costs, occur at various times, and can affect the availability of the energy system. Specific outputs from the model include the spares holding cost. The simulation also supplies the total inventory holding costs as a function of time. Specific model options include:

- Use of the inventory model – users can turn off the inventory model. If the inventory model is turned off, all spares are assumed to be bought as needed (on demand).
- Sell back – at the end of the simulation the unused spare parts can be "sold back" at their purchase price. This is equivalent to the transfer of the unused spares to another account. The alternative is no recouping of the cost spent on the unused spare parts.
- Option to pay for the spare parts when received or when ordered.

Figure 116 shows the difference with and without the sparing model. In the case without the sparing model, the assumption is that all spare parts are bought as needed. The cost difference is

due to a non-zero holding cost and the non-zero discount rate (13%/year in this case). While the cost difference may not be as significant as other data and model impacts, the primary value of the logistics model is twofold: 1) the model helps the user determine the size of the spares inventory that is necessary to avoid disruptions in service (i.e., availability degradation), and 2) this model is needed to capture and differentiate various business models that could be used to provide energy to customers. Business models of interest are maintenance contracts, warranties, and various forms of power purchase agreements.

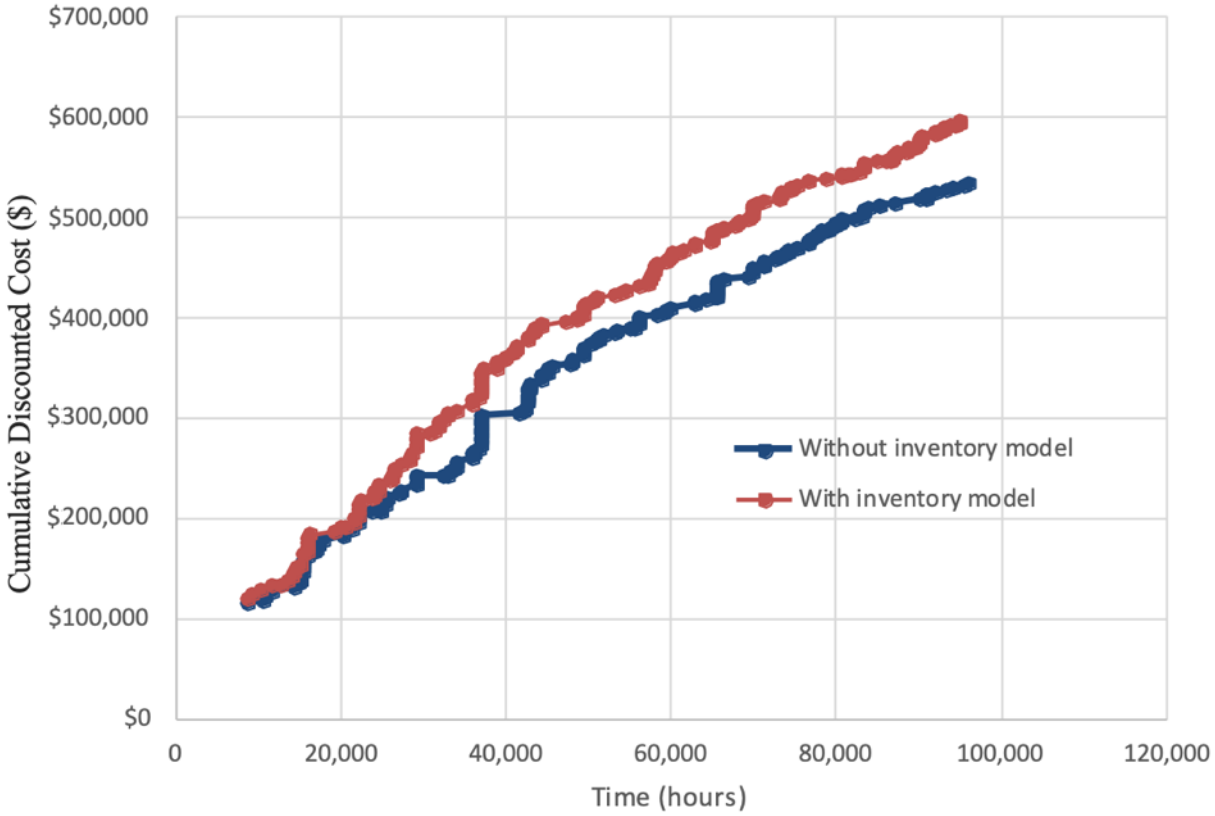

Figure 116. Difference in output for the DES model with and without incorporating spares — note, in this example, the system production volume is very low.

Gas Interruption Downtime Model. The gas interruption model was subsequently enhanced to include downtime. In addition to the frequency of gas interrupt events, the updated model can now estimate the duration of the gas interruption at those events. The model uses historical data of failure types (rupture, hole, pinhole, unknown) for five pipe sizes to determine downtime. The

downtime is a function of the length of each of the five pipe sizes in the non-redundant pipe network that feeds the installation.

The result of the model is a distribution of downtime per year for the relevant gas delivery network. The gas failure downtime per year is divided by the failure rate (failures/year) to construct the downtime per failure event. A distribution of downtimes per failure event is then created and used to model the time to repair or replace input for the gas interruption mechanism in the DES. An example output for the gas interruption model is shown in **Figure 117**.

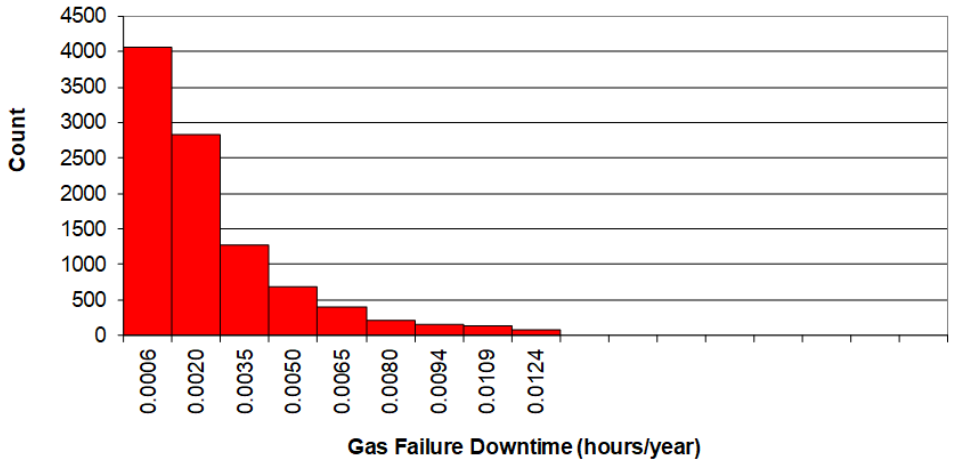

Figure 117. An example of the updated natural gas interruption model output.

Impact of a Red-Ox Tolerant Cell. **Figure 115** shows an example of how a red-ox robust, SFCM-based ceramic anode SOFC will exhibit a much lower lifetime cost than a cell without red-ox stability (and without any fuel backup system). While unexpected natural gas disruptions are relatively rare, estimated to be ~0.22 per year, when they do happen, they can be catastrophic without proper preparation. **Figure 118** shows the results of a DES, which accounts for the costs of multiple failures during the SOFC system lifetime. In **Figure 118**A, each jump in cost represents a result of a failure, with the biggest jumps coming from a natural gas disruption. Each line represents a different run of the simulation. In contrast, **Figure 118**B shows a significantly reduced lifetime cost because natural gas disruptions do not cause failure of the system. Note, a fuel gas-backup system adds to the capital expense (e.g., perhaps as much as 5-10% of the system cost) and operating expense for the system. In the case of a gas disruption event in which there is no gas backup system, all stacks are assumed to need to be replaced. Moreover, even with a fuel backup

gas (e.g., safety gas), damage can occur to Ni-cermet cells. In this case, only a portion of the stacks may need to be replaced or all the stacks will have a relatively large one-time decrease in performance (not shown, but somewhere between the two cases). Therefore, all else the same, the red-ox cycling robust cells can result in the lower lifetime cost of an SOFC power system.

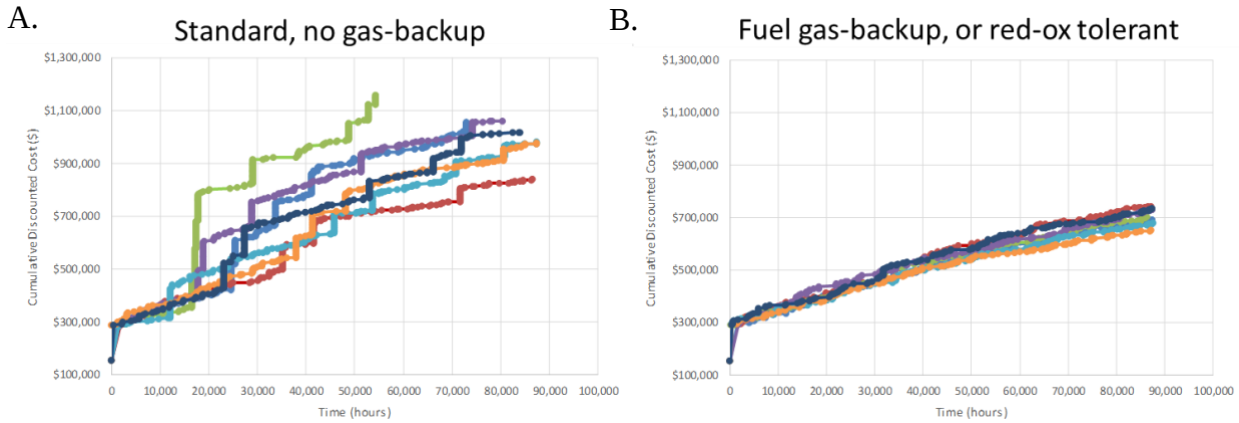

Figure 118. Individual results for Monte Carlo simulations using the discrete event simulator model A) standard Ni-cermet cells without natural gas backup and B) red-ox tolerant anode without natural gas backup — note, in this example, the system production volume is very low.

Separate simulations were run using a higher production volume, lower-cost stack (i.e., $250/kW) to look at the impact of A) a system using a red-ox robust (tolerant) stack without fuel gas-backup, B) a system with a standard Ni-cermet cell and no fuel gas-backup, and C) a system with a standard Ni-cermet cell and fuel gas-backup. In Case C, a one-time performance decrease was assumed to occur in the event of a gas outage, whereas all stacks in the system required replacement for the same type of event in Case B. SOFCs with Ni-cermet anode supports have been shown to experience extensive damage and failure when undergoing red-ox cycles such as during a fuel disruption without a backup gas — for instance see **Figure 3**C and **Figure 72**, as well as references [6-7], [14-15], and [48]. In Case A, no degradation occurred with a fuel gas interruption as the stacks were robust to red-ox cycling (e.g., an SFCM-based ceramic anode SOFC stack). Seven samples of data were collected in a series of Monte Carlo simulations that each ran for an approximately ten-year period. In each case, a higher production volume, lower-cost stack was assumed. A comparison of the different cases found that on average the LCOE for Case A at ~$0.09/kWh was about 6.7% lower than Case B, whereas the LCOE for Case B was about 3.7% lower than Case B. The total non-fuel operating cost for Case A was about 18% lower than that of

Case B, while that for Case C was only 10% lower than that of Case B. Note, due to the stochastic nature of the simulation, some of the non-fuel operating cost difference between the cases can be attributed to the cost of random failures of different components and the impact such failures have on degradation. When considering only the stack degradation cost differences, Case A was found to have a 99% lower cost than Case B. Case C, on the other hand, was found to have around a 95% lower cost than Case B.

8. CONCLUDING REMARKS

While running longer than intended due to unforeseen issues associated with baseline stability of large format SFCM-based ceramic anode SOFCs and difficulties in identifying the root cause for the issues, ultimately the project was successful in demonstrating a highly red-ox robust large format cell in stacks. Moreover, the path for continued improvement has been described. 10 cm by 10 cm SFCM-based ceramic anode SOFCs were fabricated using commercially produced tape cast layers and laminates to produce sintered half cells with very low camber, which is ideal for stack assembly. A 5 cm by 5 cm SFCM-based ceramic anode SOFC was optimized and demonstrated to have very high maximum power density (~0.9 W/cm^2) at ~600 °C with a power density of more than 0.6 W/cm^2 at 0.75 V in hydrogen. The red-ox robustness of stack components was fully evaluated found to be very good with minor adjustments made to the stack assembly process to accommodate the relatively low strength of the SFCM-based ceramic anode cells. As the electrochemical performance of large format cells was optimized, long-term degradation increased, and through an extensive set of studies the cause for the degradation was attributed to a relatively low mechanical strength and weak bonding between the anode and electrolyte. Ultimately this led to the optimization of a red-ox robust cell structure utilizing an SFCM-based ceramic anode support layer combined with a thin anode functional layer. As cell performance was improved throughout the project, we optimized the cell fabrication processes to scale-up cells to a large format size (e.g., 5 cm by 5 cm and 10 cm by 10 cm). To aid in this optimization, various assessments (e.g., dilatometry measurements of tape cast layers) were made to ensure that the scaled-up cells met the specifications for assembly in a stack. Moreover, the cell fabrication processes (e.g., tape casting and sintering) were also optimized to achieve higher manufacturing yields (i.e., a larger number of cells that meet quality control criteria in a single batch) during cell

manufacturing of the larger-format, SFCM-based ceramic anode cells. The red-ox cycling robustness of a 3-cell stack of 5 cm by 5 cm SFCM-based ASL with AFL SOFCs was demonstrated in hydrogen at 600 °C with no OCV or ASR degradation after ~40 cycles. Unfortunately, the stack was unintentionally damaged through current loading when the anode stream was in the oxidized state. The cell was also loaded to higher than intended current densities that caused at least one cell to experience negative voltages. Had these events not occurred the stack is expected to have continued to operate without degradation for additional red-ox cycles. In an SOFC system, such an event can be avoided through the proper system and controls design. As the safety gas system can cost many hundreds of dollars per kW, an SOFC solution that avoids the need for such equipment can greatly reduce the system capital equipment cost. Additional optimization of the anode pore microstructure and use of vacuum infiltration should enable the SFCM-based ASL with AFL SOFCs to achieve the same or better performance as the best performing large format cell demonstrated in this project (i.e., > 0.6 W/cm^2 at 0.75 V). A 1-kW stack with 10 cm by 10 cm cells having this level of performance will require only around 18-20 cells. While not quite as high as the target performance, this will still result in significant cost savings and yield stack costs around $250-$275/kW. Furthermore, there is more room for improvement with additional optimization. The SFCM-based ceramic anode SOFC was scaled to a large format size as large as 10 cm by 10 cm and tested in stacks with as many as 10 cells demonstrating that larger stacks can be assembled and undergo red-ox cycling with minimal impact on performance. Moreover, 10 cm by 10 cm SFCM-based ceramic anode cells were tested with reformed, pipeline natural gas and found to have no difference in performance at an operating voltage of 0.75 V when compared to operation with hydrogen. Therefore, the project successfully demonstrated the advantages of and continued potential for SFCM-based ceramic anode cells to provide a red-ox robust stack for distributed generation.

9. REFERENCES

1. R.S. Wilckens, L.G.J. De Haart, I.C. Vincke, L. Blum, A. Cramer, J. Remmel, G. Blass, F. Tietz, W.J. Quadakkers. Recent Results of Stack Development at Forschungszentrum Juelich. In: S. Singhal, M. Dokiya (Eds.), Proc. of the 8th International Symp. On SOFC, Electrochemical Soc. Proc. Series, Vol. 2003-07, Paris, The Electrochemical Soc. Inc., Pennington, New York, p. 98, April 2003.
2. S. Diethelm, J. Van herle, S. Wuillemin, A. Nakajo, N. Autissier, M. Molinelli. Impact of Materials and Design on Solid Oxide Fuel Cell Stack Operation. Journal of Fuel Cell Science and Technology, 5 (3), 2008.
3. J. Kuebler, U.F. Vogt, D. Haberstock D, J. Sfeir, A. Mai, T. Hocker, M. Roos, U. Hamisch. Simulation and Validation of Thermo-mechanical Stresses in Planar SOFCs. Fuel Cells 10 (6), 1066-1073, 2010.
4. H. Yokokawa, H.Y. Tu, B. Iwanschitz, A. Mai. Fundamental mechanisms limiting solid oxide fuel cell durability. Journal of Power Sources, 182, 400-412, 2008.
5. D. Sarantaridis and A. Atkinson. Redox Cycling of Ni-Based Solid Oxide Fuel Cell Anodes: A Review. Fuel Cells, 7, 246-258, 2007.
6. M. Cassidy, G. Lindsay, K. Kendall. The Reduction of Nickel-Zirconia Cermet Anodes and the Effects on Supported Thin Electrolytes. Journal of Power Sources, 61, 189-192, 1996.
7. T. Klemensø, C. Appel, C., and M. Mogensen. In-situ Observations of Micro-structural Changes in SOFC Anodes During Redox Cycling. Electrochemical and Solid State Letters 9, A403- A407, 2006.
8. W. Wang, C. Su, Y. Wu, R. Ran, Z. Shao. Progress in Solid Oxide Fuel Cells with Nickel-Based Anodes Operating on Methane and Related Fuels. Chem Rev, 113, 8104-8151, 2013.
9. A. Atkinson, S. Barnett, R.J. Gorte, J.T.S. Irvine, A.J. Mcevoy, M. Mogensen, S.C. Singhal, J. Vohs. Advanced anodes for high-temperature fuel cells. Nature Materials, 3, 17-27, 2004.
10. A. Hagen, R. Barfod, P.V. Hendriksen, Y.L. Liu, S. Ramousse. Degradation of Anode Supported SOFCs as a Function of Temperature and Current Load. Journal of the Electrochemical Society, 153, A1165-A1171, 2006.
11. S. McIntosh and R.J. Gorte. Direct Hydrocarbon Solid Oxide Fuel Cells. Chemical Reviews, 104, 4845-4865, 2004.
12. M.Y. Gong, X.B. Liu, J. Trembly, C. Johnson. Sulfur-tolerant anode materials for solid oxide fuel cell application. Journal of Power Sources, 168, 289-298, 2007.
13. Z. Cheng, J.-H. Wang, Y. Choi, L. Yang, M.C. Lin, M. Liu. From Ni-YSZ to sulfur-tolerant anode materials for SOFCs: electrochemical behavior, in situ characterization, modeling, and future perspectives. Energy & Environmental Science, 4, 4380- 4409, 2011.
14. D. Fouquet, A.C. Muller, A. Weber, and E. Ivers-Tiffee. Kinetics of Oxidation and Reduction of Ni/YSZ Cermets. Ionics (Kiel) 9, 103-108, 2003

15. T. Klemensoe, C. Chung, P.H. Larsen, M. Mogensen. The Mechanism Behind Redox Instability of Anodes in High-temperature SOFCs. J. Electrochem. Soc., 152, 2186-2192, 2005.

16. D. Sarantaridis, R.A. Rudkin, A. and Atkinson. Oxidation Failure Modes of Anode-Supported Solid Oxide Fuel Cells. Journal of Power Sources, 180, 704–710, 2008.

17. J. Laurencin, G. Delette, B. Morel, F. Lefebvre-Joud, and M. Dupeux. Solid Oxide Fuel Cells Damage Mechanisms due to Ni-YSZ Re-oxidation: Case of the Anode Supported Cell. Journal of Power Sources, 192, 344-352, 2009.

18. M. Pihlatie. Stability of Ni-YSZ Composites for Solid Oxide Fuel Cells During Reduction and Reoxidation. Ph.D. Dissertation, VTT Technical Research Center, Finland, June 2010.

19. A. Nakajo, F. Mueller, J. Brouwer, J. Van Herle, and D. Favrat. Mechanical Reliability and Durability of SOFC stacks. Part II: Modelling of Mechanical Failures During Ageing and Cycling. International Journal of Hydrogen Energy, 1-18, 2012.

20. A. Hagen, P.V. Hendriksen, H.L. Frandsen, K. Thyde´n, R. Barfod. Durability Study of SOFCs Under Cycling Current Load Conditions. Fuel Cells, 9 (6), 2009.

21. Dikwal, C., Bujalski, W., Kendall, K., The Effect of Temperature Gradients on Thermal Cycling and Isothermal Ageing of Microtubular Solid Oxide Fuel Cells, J. of Power Sources, 193 (1), 2009.

22. Molinelli, M., Larrain, D., Autissier, N., Ihringer, R., Sfeir, J., Badel, N., Bucheli, O., Van Herle, J., Dynamic Behavior of SOFC Short Stacks, J. Power Sources, 154, 394-403, 2006.

23. M. Hanasaki, C. Uryu, T. Daio, T. Kawabata, Y. Tachikawa, S.M. Lyth, Y. Shiratori, S. Taniguchi, and K. Sasaki. SOFC Durability Against Standby and Shutdown Cycling, Journal of the Electrochemical Society, 161 (9), 2014.

24. A. Wood, M. Pastula, D. Waldbillig, and D. Ivey. Initial testing of solutions to redox problems with anode-supported SOFC. Journal of the Electrochemical Society, 153, A1929-A1934, 2006.

25. H. Itoh, T. Yamamoto, M. Mori, T. Horita, N. Sakai, H. Yokokawa, D. Masayuki. Configurational and Electrical Behavior of Ni-YSZ Cermet with Novel Microstructure for Solid Oxide Fuel Cell Anodes. Journal of the Electrochemical Society 144, 641-646, 1997.

26. A. Busawon, D. Sarantaridis, and A. Atkinson. Ni Infiltration as a Possible Solution to the Redox Problem of SOFC Anodes. Electrochemical and Solid State Letters, 11 (10), B186-B189, 2008.

27. R. Leah, A. Bone, A. Selcuk, D. Corcoran, M. Lankin, Z. Dehaney-Steven M. Selby, and P. Whalen. Development of Highly Robust, Volume-Manufacturable Metal-Supported SOFCs for Operation Below 600°C. ECS Transactions, 35 (1), 351-367, 2011.

28. R. Hart. Development of a Thermal Spray, Redox Stable, Ceramic Anode for Metal Supported SOFC. FE0026169 project kickoff presentation. December 2, 2015. Available at: https://www.netl.doe.gov/sites/default/files/2017-12/DE-FE0026189-Kickoff-presentation_0.pdf

29. S. Singhal. High-temperature Solid Oxide Fuel Cells: Fundamentals, Design and Applications, Oxford, Elsevier, 2003.

30. M. Halinen, O. Thomann, and J. Kiviaho. Experimental Study of SOFC System Heat-up Without Safety Gases. Int. J. Hydrogen Energy, 39, 552-561, 2014.

31. M. Weimar, L. Chick, D. Gotthold, and G. Whyatt. Cost Study for Manufacturing of Solid Oxide Fuel Cell Power Systems. Pacific Northwest NL, Report-22732, US-DOE #DE-AC05-76RL01830, Sept. 2013.

32. Office of Electricity Delivery and Energy Reliability U.S. Department of Energy, Year-in-Review: 2014 Energy Infrastructure Events and Expansions, May 2015. Available at: https://www.energy.gov/sites/default/files/2015/05/f22/2014-YIR-05282015.pdf

33. Amercian Gas Association, Natural Gas Pipeline Systems: Delivering Resiliency. A Reslience White Paper, October 10, 2014. Available at: https://www.energy.gov/sites/prod/files/2015/04/f21/AGA%20QER%20Comments%20-%20System%20Resiliency.pdf

34. North American Electric Reliability Corporation, 2013 Special Reliability Assessment: Accommodating an Increased Dependence on Natural Gas for Electric Power Phase II: A Vulnerability and Scenario Assessment for the North American Bulk Power System, Chapter 3: Gas Supply Vulnerabilities, page 26, May 2013.

35. Chicago Metropolitan Area Critical Infrastructure Protection Program, Planning For Natural Gas Disruptions, page 12-14, December 2002. Available at: https://publications.anl.gov/anlpubs/2003/02/45798.pdf

36. G. Xiao, F. Chen. Redox stable anodes for solid oxide fuel cells. Frontiers in Energy Research, 2, 18, 1-13, 2014.

37. J. Karczewski, B. Bochentyn, S. Molin, M. Gazda, P. Jasinski, B. Kusz. Solid oxide fuel cells with Ni-infiltrated perovskite anode. Solid State Ionics, 221, 11-14, 2012.

38. C. Savaniu and J. Irvine. La-doped SrTiO3 as anode material for IT-SOFC. Solid State Ionics, 192, 491-493, 2011.

39. Y.-H. Huang, G. Liang, M. Croft, M. Lehtimaki, M. Karppinen, J.B. Goodenough. Double-Perovskite Anode Materials Sr_2MMoO_6 (M = Co, Ni) for Solid Oxide Fuel Cells. Chemistry of Materials, 21, 2319-2326, 2009.

40. S. Tao and J.T. Irvine. A redox-stable efficient anode for solid-oxide fuel cells. Nature materials, 2, 320-323, 2003.

41. S. Tao and J.T. Irvine. Synthesis and characterization of $(La_{0.75}Sr_{0.25})Cr_{0.5}Mn_{0.5}O_{3-\delta}$, a redox-stable, efficient perovskite anode for SOFCs. Journal of the Electrochemical Society, 151, A252-A259, 2004.

42. S. Tao and J.T. Irvine. Catalytic properties of the perovskite oxide $La_{0.75}Sr_{0.25}Cr_{0.5}Fe_{0.5}O_{3-\delta}$ in relation to its potential as an SOFC anode material. Chemistry of Materials, 16 (2004) 4116-4121.

43. T.H. Shin, Y. Okamoto, S. Ida, T. Ishihara. Self-Recovery of Pd Nanoparticles That Were Dispersed over La(Sr)Fe(Mn)O3 for Intelligent Oxide Anodes of Solid-Oxide Fuel Cells. Chemistry-A European Journal, 18, 11695-11702, 2012.

44. S. Chan, K. Khor, Z. Xia. A complete polarization model of a solid oxide fuel cell and its sensitivity to the change of cell component thickness. Journal of Power Sources, 93, 130-140, 2001.

45. S. Hui and A. Petric. Conductivity and stability of $SrVO_3$ and mixed perovskites at low oxygen partial pressures. Solid State Ionics, Solid State Ionics, 143, 275-283, 2001.

46. K. Zheng, K. Świerczek, N.M. Carcases, T. Norby. Coking Study in Anode Materials for SOFCs: Physico-chemical Properties and Behavior of Mo-Containing Perovskites in CO and CH_4 Fuels. ECS Transactions, 64 103-116, 2014.

47. K.J. Pan, A. Mohammed Hussain, E.D. Wachsman, Alternative Anode for Solid Oxide Fuel Cells, USPTO Provisional Patent Application 62/310,371, filed March 18, 2016.

48. M. Ettler, H. Timmerman, J. Malzbender, A. Weber, and N.H. Menzler, Journal of Power Sources, 195 (17), 5452-5467, 2010.

49. K.J. Pan, A. Mohammed Hussain, E.D. Wachsman, D. Ding, Solid Oxide Fuel Cells Cathode Functional Layer, USPTO Provisional Patent Application 62/310,358, filed, March 18, 2016.

50. S.R. Bishop, D. Marrocchelli, C. Chatzichristodoulou, N.H. Perry, M.B. Mogensen, H.L. Tuller, and E.D. Wachsman. Chemical Expansion: Implications for Electrochemical Energy Storage and Conversion Devices. Annual Review of Materials Research, 2014. 44:205–39.

51. B.M. Blackburn, et al. High Power, Low Cost Solid Oxide Fuel Cell Stacks For Robust And Reliable Distributed Generation. Final report for FE0026189. OSTI ID: 1647299. August 3, 2020.

52. D. Ding, M. Liu, M. Liu. Enhancing SOFC Electrode Performance Through Surface Modification. ECS Transactions, 57, 1801-1810, 2013.

53. D. Ding, Z.B. Liu, L. Li, C.R. Xia. An octane-fueled low temperature solid oxide fuel cell with Ru-free anodes. Electrochemistry Communications, 10, 1295-1298, 2008.

54. T.Z. Sholklapper, H. Kurokawa, C.P. Jacobson, S.J. Visco, L.C. De Jonghe. Nanostructured Solid Oxide Fuel Cell Electrodes. Nano Letters, 7, 2136-2141, 2007.

55. C. E. Milliken, S. Guruswamy, and A. C. Khandkar. Electrochemical Stability of Strontium-Doped Ceria Electrolyte in Solid-Oxide Fuel Cell Applications. Journal of the American Ceramic Society, 84 [7] 1533–38 (2001).

56. K.S. Weil and B.J. Koeppel. Thermal stress analysis of the planar SOFC bonded compliant seal design. International Journal of Hydrogen Energy, 33 (2008) 3976 – 3990.

57. H.P. Buchkremer and R. Conradt. Durable sealing concepts with glass sealants or compression seals. Handbook of Fuel Cells – Fundamentals, Technology and Applications, Ed. by W. Vielstich, H. A. Gasteiger, A. Lamm and H. Yokokawa, 2010 John Wiley & Sons, Ltd.

58. C.-K. Lin, L.-H. Huang, L.-K. Chiang, and Y.-P. Chyou. Thermal stress analysis of planar solid oxide fuel cell stacks: Effects of sealing design. Journal of Power Sources, 192 (2), pp. 515-524, 2009.

59. A. Morales-Rodriguez, A. Bravo-Leon, A. Dominguez-Rodriguez, S. Lopez-Esteban, J.S. Moya, and M. Jimenez-Melendo. High-temperature mechanical properties of zirconia/nickel composites. Journal of the European Ceramic Society, 23 (15), pp. 2849- 2856, 2003.

60. M. Radovic and E. Lara-Curzio. Mechanical properties of tape cast nickel-based anode materials for solid oxide fuel cells before and after reduction in hydrogen. Acta Materialia, 52 (20), pp. 5747-5756, 2004.

61. M. Pihlatie, A. Kaiser, and M. Mogensen. Mechanical properties of NiO/Ni-YSZ composites depending on temperature, porosity and redox cycling. Journal of the European Ceramic Society, 29(9), pp. 1657-1664, 2009.

62. E. Ivers-Tiffee, A. Weber, and D. Herbstritt. Materials and technologies for SOFC-components. Journal of the European Ceramic Society, 21 (10-11), pp. 1805-1811, 2001.

63. A. Atkinson and A. Selcuk. Mechanical behaviour of ceramic oxygen ion-conducting membranes. Solid State Ionics, 134(1-2), pp. 59-66, 2000.

64. H. Yokokawa, T. Horita, K. Yamaji, H. Kishimoto, and M.E. Brito. Degradation of SOFC Cell/Stack Performance in Relation to Materials Deterioration. Journal of The Korean Ceramic Society, 49(1), pp. 11-18, 2012.

65. L. Wang, G.S. Jackson, and B.M. Blackburn. Developing 3-D Model of Intermediate-Temperature SOFC with GDC Electrolyte. Solid Oxide Fuel Cells 13 (Sofc-Xiii), 57(1), pp. 2583-2595, 2013.

66. M.H. Pihlatie, H.L. Frandsen, A. Kaiser, M. Mogensen. Continuum mechanics simulations of NiO/Ni–YSZ composites during reduction and re-oxidation. Journal of Power Sources 195 (2010) 2677–2690

67. J. Malzbender, W. Fischer, R.W. Steinbrech. Studies of residual stresses in planar solid oxide fuel cells. Journal of Power Sources 182 (2008) 594-598.

68. B. Charlas, C. Chatzichristodoulou, K. Brodersen, K. Kwok, P. Norby, M. Chen, H.L. Frandsen. Residual stresses in a co-sintered SOC half-cell during post-sintering cooling. Proceedings of 11th European SOFC and SOE Forum 2014, B1107.

69. H.L. Frandsen, M. Makowska, F. Greco, C. Chatzichristodoulou, D.W. Ni, D.J. Curran, M. Strobl, L.T. Kuhn, P.V. Hendriksen. Accelerated creep in solid oxide fuel cell anode supports during reduction. Journal of Power Sources 323 (2016) 78-89.

70. A. Faes, A. Hessler-Wyser, A. Zryd, and J. Van herle. A Review of RedOx Cycling of Solid Oxide Fuel Cells Anode. Membranes 2012, 2(3), 585-664.

71. L. Wang, Y. Yu, K. J. Gaskell, E.J. Crumlin, Z. Liu, B. W. Eichhorn, and G. S. Jackson. In operando x-ray photoelectron spectroscopy studies of H_2 oxidation and H_2O electrolysis on gadolinia-doped ceria electrodes. Journal of Physics: Energy 3 (2021) 014004.

72. J House Environmental, Pipeline Risk Analysis - Mountain House Specific Plan III, 2004. Available at: http://www.sjgov.org/commdev/cgi-bin/cdyn.exe/handouts-mtnhouse_EIR_Appendix_K_Pipeline_R?grp=handouts-mtnhouse&obj=EIR_Appendix_K_Pipeline_R (accessed October 16, 2017).

APPENDIX A. SFCM PROPERTIES AS A FUNCTION OF PO_2

To better understand the origins of changes in mechanical properties with changes in operating conditions (e.g., air vs. hydrogen), an investigation was conducted to determine the non-stoichiometry, or oxygen content, of the SFCM-based ceramic anode materials. The studies involved measurements of changes in mass of samples with changes in temperature and oxygen partial pressure. Any loss or gain of mass is assumed to be due to loss or gain of oxygen. Consistent with typical non-stoichiometric oxides, the oxygen vacancy concentration increases as the material is exposed to increasingly reducing conditions, as shown in **Figure 119**.

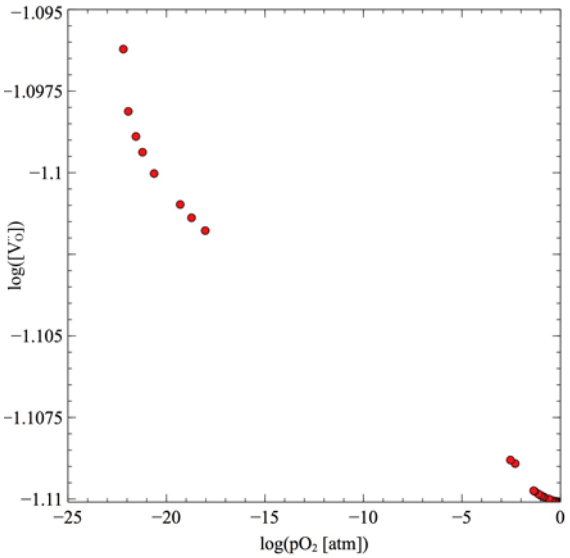

Figure 119. Oxygen vacancy concentration ($V_{O}^{\cdot\cdot}$) in the SFCM-based ceramic anode increases with decreasing oxygen partial pressure (pO_2).

The mass of SFCM was measured at 400, 500 and 600 degrees Celsius, under various oxidizing and reducing gas environments. Results are presented in **Figure 120** and **Figure 121**, and the appropriate slopes and intercepts are in **Table 5** and **Table 6**. At high pO_2, relatively small changes occur in mass as the pO_2 changes. At sub-atmospheric pO_2, higher temperature measurements result in lower oxygen content. But at even higher atmospheric pO_2, higher temperatures show a greater increase in oxygen content. Under reducing conditions lower oxygen content is shown by higher temperature samples. For the linear region, the slopes are all consistent with each other.

There appears to be a point where additional oxygen is lost from the material at the lowest pO_2. This point increases with temperature.

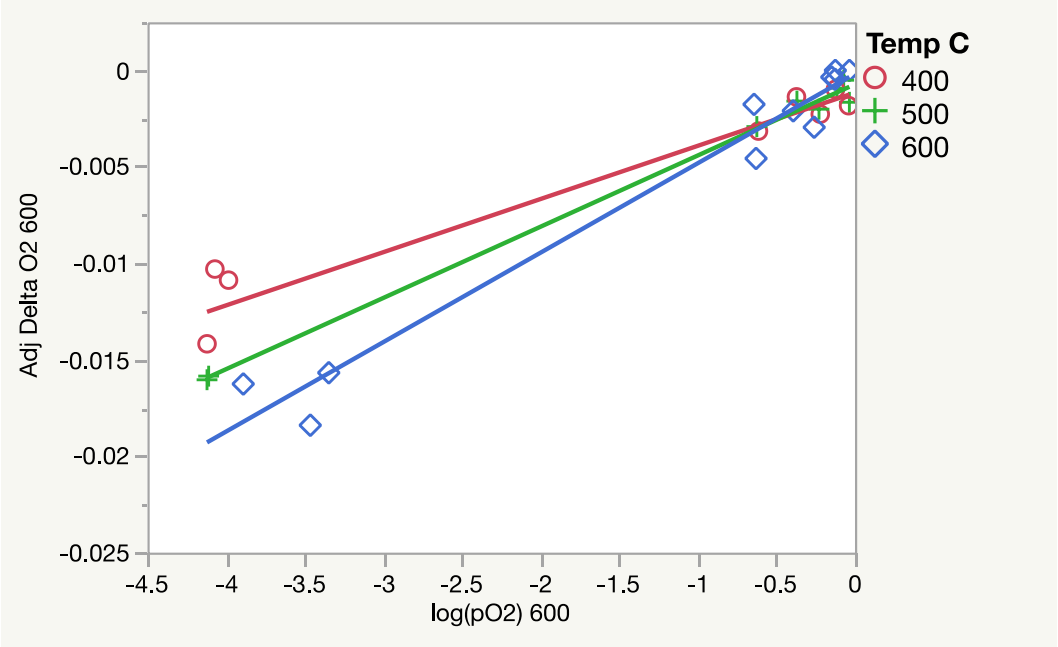

Figure 120. Oxygen non-stoichiometry of SFCM at high pO_2.

Table 5. Linear fit parameters for oxygen non-stoichiometry of SFCM at high pO_2.

Temp (°C)	Slope	Intercept
400	0.002759	-0.001148
500	0.003695	-0.000716
600	0.004639	-0.000174

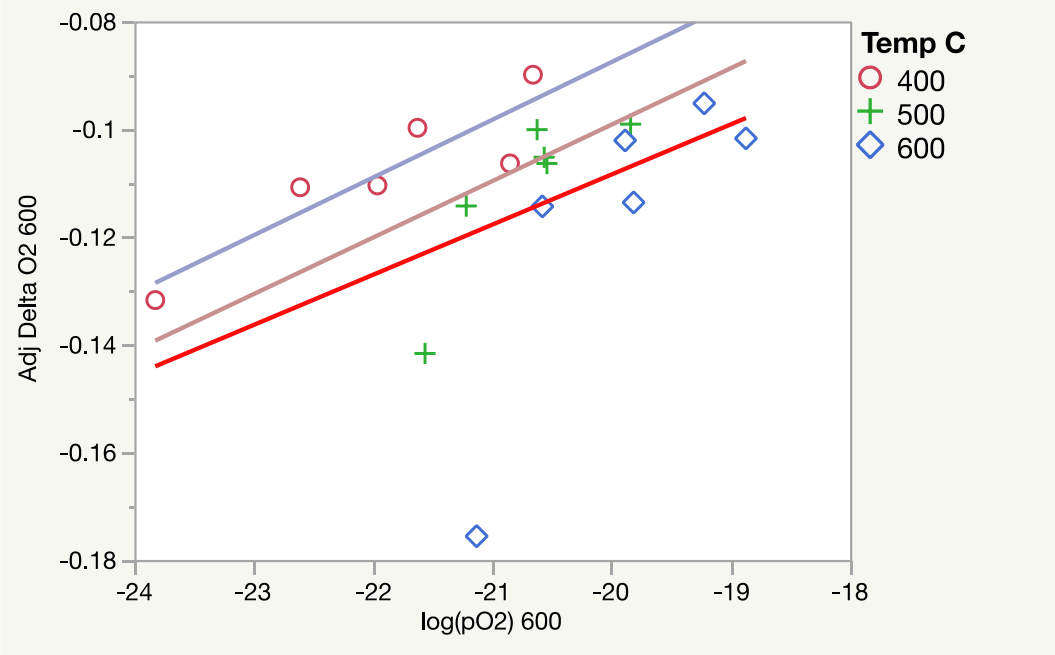

Figure 121. Oxygen non-stoichiometry of SFCM at low pO_2.

Table 6. Linear fit parameters for oxygen non-stoichiometry of SFCM at low pO_2.

Temp (°C)	Slope	Intercept
400	0.0107	0.1268
500	0.0105	0.1106
600	0.0093	0.0778

To study the kinetic properties of SFCM, we constructed an electrical conductivity relaxation (ECR) testing system. ECR is a common technique used to investigate the kinetics of oxygen transport. In order to investigate these properties with ECR samples were placed in a closed environment and the oxygen partial pressure of the environment was rapidly changed to pump oxygen in and out of the sample, resulting in a change of the concentrations of defects, which was measured by changes in the samples electrical conductivity. We then extracted the kinetic parameters to better understand the change in kinetics for SFCM samples under different atmospheres. The schematic drawing of the custom-built testing system is shown in **Figure 122**. A nitrogen and oxygen gas mixture was fed into the reactor using individual mass flow controllers, and the total flow rate was fixed at a high flow rate (100 SCCM) to induce sharp step changes in

the oxygen partial pressure, which was monitored through a yttria-stabilized zirconia (YSZ) oxygen sensor. The conductivity change of individual samples was monitored in real time. The conductivity relaxation profile acquired can be fit with a diffusion equation to extract kinetic parameters.

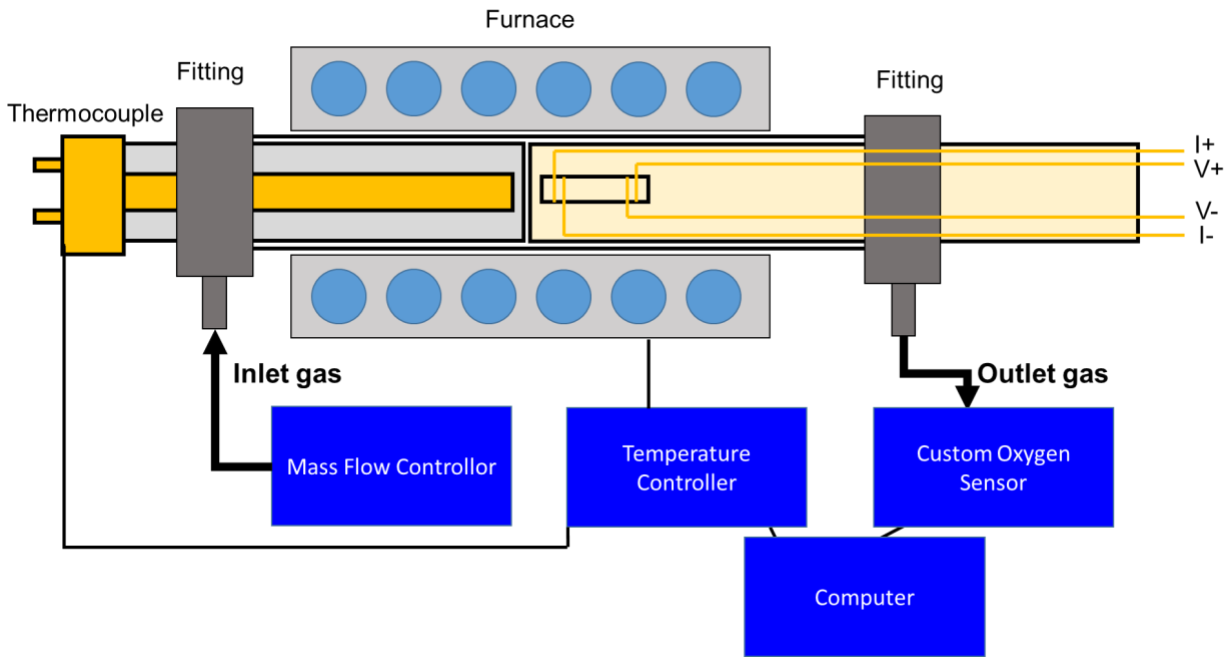

Figure 122. Schematic drawing of ECR reactor

Figure 123 shows the ECR on SFCM under oxidizing conditions with a step change of pO_2 from (a) 1 atm to 0.487 atm and (b) 0.109 to 0.06 atm at 600 °C. The rapid change of the conductivity relaxation curve of SFCM samples (less than 1 minute) during the re-equilibrium process at oxidizing conditions implies that the oxygen stoichiometry of SFCM does not change much under oxidizing environments.

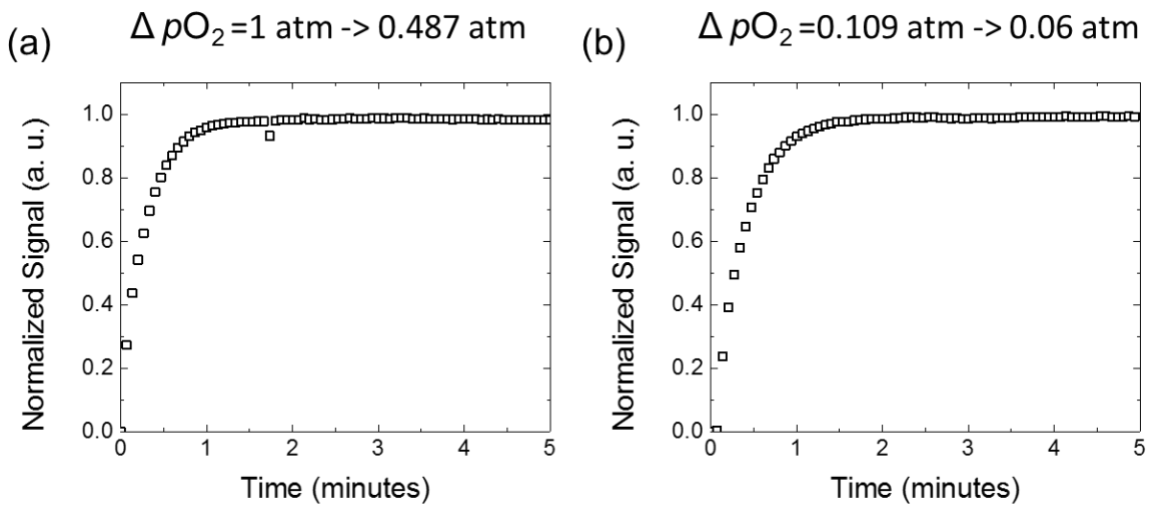

Figure 123. ECR on SFCM under oxidizing conditions with a step change of pO_2 from (a) 1 atm and 0.487 atm and (b) 0.109 and 0.06 atm.

Figure 124 shows the ECR on SFCM under reducing conditions with a step change of pO_2 from $10^{-18.86}$ atm to $10^{-19.662}$. Under reducing conditions, the conductivity change takes hours to get re-equilibrium at 600 °C, suggesting that SFCM slowly releases oxygen from the lattice

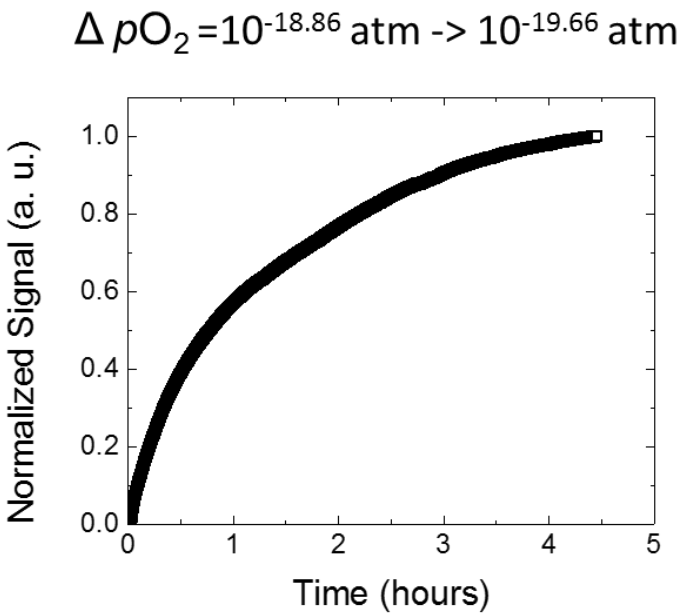

Figure 124. ECR on SFCM at 600 ºC under reducing conditions with a step change of pO_2 from $10^{-18.86}$ atm to $10^{-19.662}$ atm.

The conductivity of SFCM was determined over a wide range of oxygen partial pressure (pO_2). Nitrogen and oxygen gas mixtures were fed into the reactor using individual mass flow controllers,

and the total flow rate was fixed at a high flow rate (100 SCCM) to induce accurate step changes in the oxygen partial pressure, which was monitored through a yttria-stabilized zirconia (YSZ) oxygen sensor. **Figure 125** shows the double log plot of conductivity versus pO_2 at 600 °C. In high pO_2 range, the oxidizing environment (N_2/O_2 mixture), the conductivity of SFCM increases as pO_2 increases, suggesting that SFCM exhibits *p*-type conductivity in this regime. The increase of pO_2 affects the defect chemistry of SFCM, compensating the concentration of total charge carriers. A linear correlation in the double log plot of conductivity versus pO_2 is observed with a slope of 0.07.

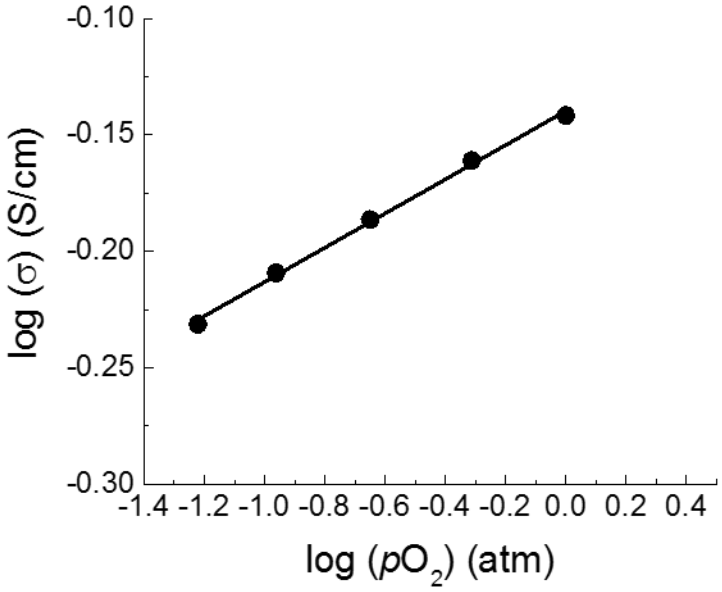

Figure 125. The conductivity of SFCM as a function of oxygen partial pressure under oxidizing conditions

Figure 126 shows the conductivity of SFCM as a function of oxygen partial pressure under reducing conditions at 600 °C. The reducing environment was controlled by a mixture of N_2/H_2 gases. Interestingly, the decrease in pO_2 increases the conductivity of SFCM, which is opposite to the trend in the high pO_2 range, suggesting that SFCM exhibits *n*-type conductivity under low pO_2. The double log plot of conductivity of SFCM versus pO_2 has a linear relationship with a slope of -0.14. Compared the pO_2 dependence on SFCM conductivity in the high and low pO_2 regimes, the slope is doubled in reducing environment, indicating that each ionic defect in SFCM generates two times electronic defect in reducing environment than in the oxidizing environment.

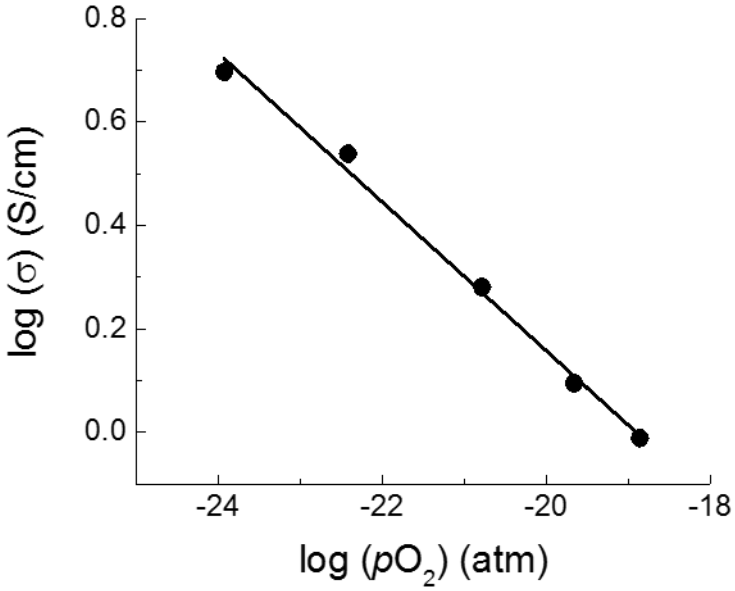

Figure 126. The conductivity of SFCM as a function of oxygen partial pressure under reducing conditions

Electrical conductivity relaxation was performed on SFCM over a wide range of oxygen partial pressure (pO_2) and temperature. Nitrogen and oxygen gas mixtures were fed into the reactor using individual mass flow controllers, and the total flow rate was fixed at a high flow rate (100 SCCM) to induce sharp step changes in the oxygen partial pressure, which was monitored through a yttria-stabilized zirconia (YSZ) oxygen sensor. **Figure 127** shows the electrical conductivity relaxation curves of SFCM under the step change of pO_2 from 1 atm to 0.5 atm at 600 °C, 650 °C, and 700 °C. In high pO_2 range, the oxidizing environment (N_2/O_2 mixture), SFCM exhibits fast change in conductivity while changing the gas environment. The conductivity of SFCM equilibrates with the gas environment in less than 1 minute for all tested temperature. There is no significant difference between the relaxation time for SFCM at different temperatures.

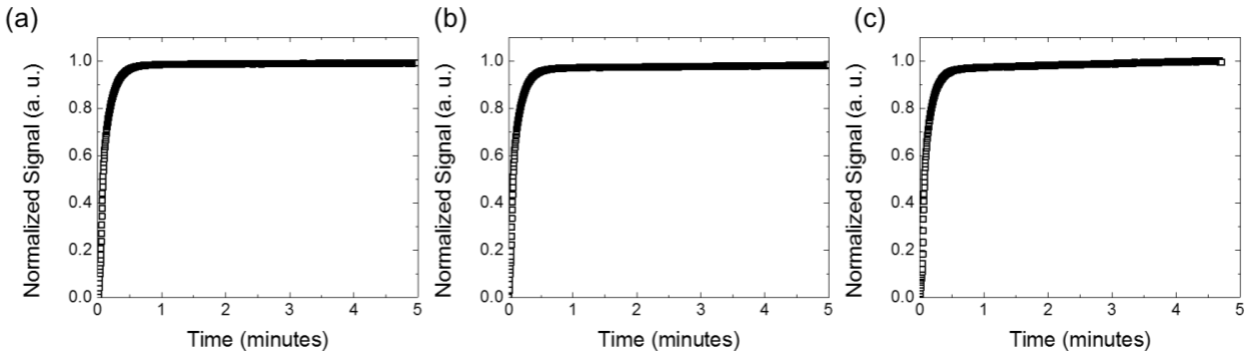

Figure 127. Electrical conductivity relaxation of SFCM under oxidizing conditions from pO_2 =1 to 0.5 atm at (a) 600 °C, (b) 650 °C, and (c) 700 °C.

Figure 128 shows the electrical conductivity relaxation curves of SFCM under the step change of pO_2 from 0.05 atm to 0.03 atm at 600 °C, 650 °C, and 700 °C. In this pO_2 range, SFCM also exhibits a fast change in conductivity while changing the gas environment. The conductivity of SFCM equilibrates with the gas environment in less than 1 minute for all tested temperatures. Compared the changes in conductivity relaxation curves for SFCM at different oxidizing environments, there is no significant difference between the changes in conductivity kinetics for SFCM at different pO_2.

On the basis of these results, the conductivity of SFCM changes as a function of temperature and pO_2. Generally, it requires a relatively long time for the movement of oxygen ion to get equilibrium with the gas environment. Therefore, it is reasonable to assume that the defect concentration in SFCM (i.e., oxygen vacancy concentration) does not change much in the oxidizing environment as evidenced by the fast relaxation time. Due to the presence of multiple transition metals, cobalt, iron, and molybdenum, the change in conductivity may be the results of the changes in stable oxidation states for each element in SFCM. Hence, the *p*-type charge carrier in high pO_2 range may switch from one to the other multivalent metals, resulting in the changes in overall conductivity while maintaining the same concentration of oxygen defects.

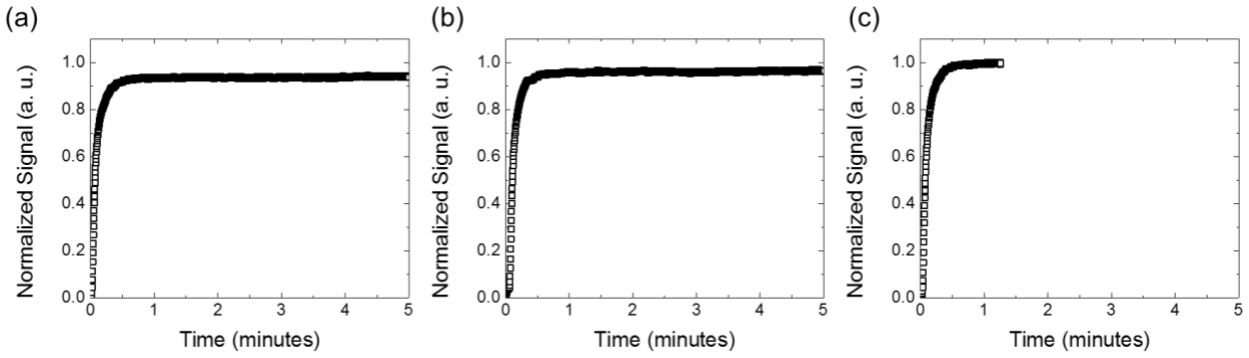

Figure 128. Electrical conductivity relaxation of SFCM under oxidizing conditions from pO_2 =0.05 to 0.03 atm at (a) 600 °C, (b) 650 °C, and (c) 700 °C.

Electrical conductivity relaxation of SFCM under reducing environments (N_2/H_2 mixture) was performed on SFCM as a function of oxygen partial pressure (pO_2) and temperature to identify effects of each experimental variable (temperature, pO_2) on surface exchange kinetics of SFCM. The bar shape of SFCM samples with a dimension of 1.2 cm x 0.3 cm x 0.15 cm was used for this study. **Figure 129** shows the electrical conductivity relaxation curves of SFCM at 600°C during a step change of pO_2 from $10^{-19.6}$ to $10^{-20.3}$, from $10^{-20.3}$ to $10^{-22.7}$, and from $10^{-22.7}$ to $10^{-23.8}$ atm, as shown in red, blue, and black, respectively. In low pO_2 range, the reducing environment (N_2/H_2 mixture), it takes a longer time for SFCM to reach equilibrium with the gas environment at a lower pO_2 after a step change of pO_2. It suggests that the overall exchange rate of SFCM decreases with the decrease in pO_2. The overall reaction is a sequence of reaction process and can be considered as three major steps: (1) mass transfer, (2) surface exchange, (3) oxygen diffusion in SFCM. Our results show that either rate of surface exchange or oxygen diffusion in SFCM decreases as the SFCM is reduced.

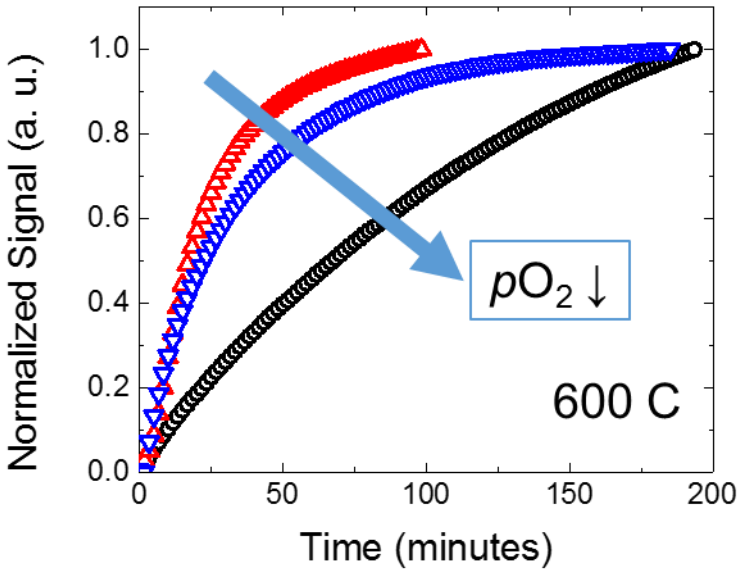

Figure 129. Electrical conductivity relaxation of SFCM under reducing conditions at 600 °C during a step change of pO_2 from $10^{-19.6}$ to $10^{-20.3}$, from $10^{-20.3}$ to $10^{-22.7}$, and from $10^{-22.7}$ to $10^{-23.8}$ atm, as shown in red, blue, and black, respectively. SEM, XRD, XPS, etc.

SFCM anode samples were placed in TGA at three elevated temperatures (575, 625, and 675 °C) for seven cycles between oxidizing and reducing environments. **Figure 130** and **Figure 131** show the mass loss and gain curves at 625 °C, respectively. On reduction, a 1% mass loss was observed in SFCM over the 4-hour period. With each reduction cycle, the mass loss decreased which was mostly (but not completely) gained in the subsequent oxidation cycle. With each oxidation cycle, the total mass increased, but never reached the initial mass before cycling.

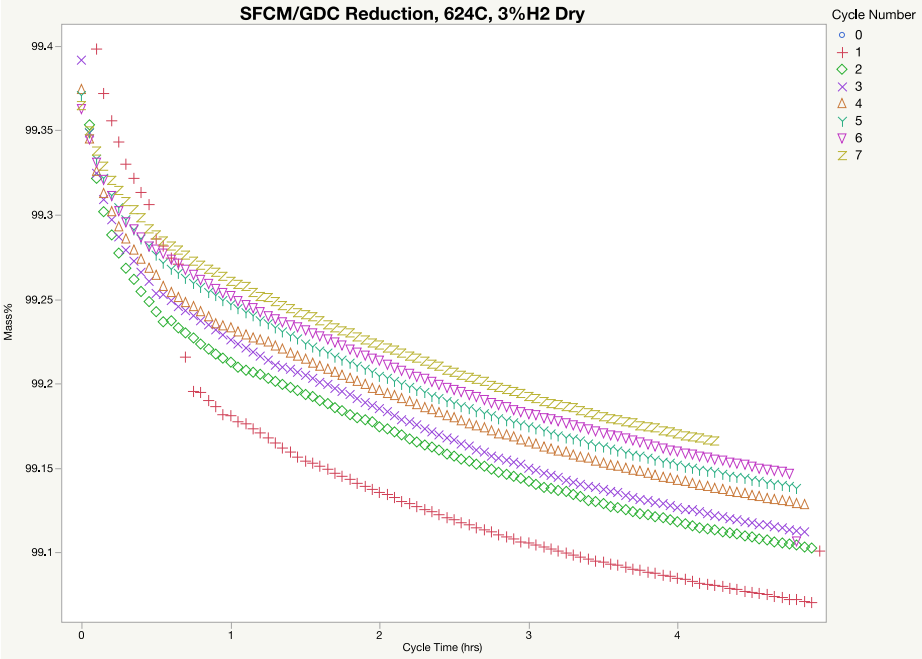

Figure 130. Cycled reduction of SFCM anode.

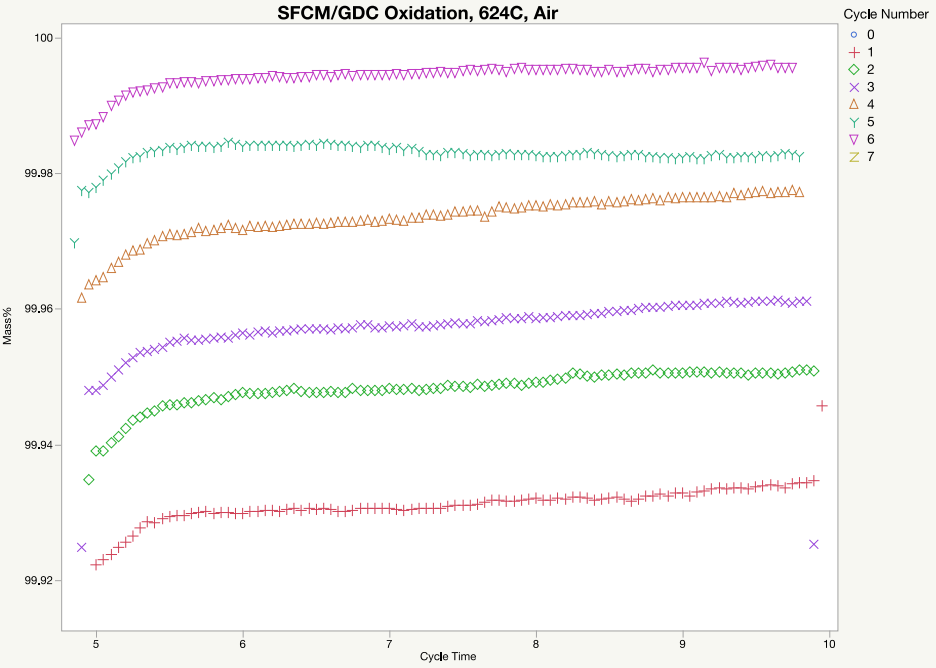

Figure 131. Cycled oxidation of SFCM Anode.

APPENDIX B. OPTIMAL STORAGE CONDITIONS FOR SFCM

Following observations that SFCM shows an interaction with water at room temperature, an evaluation was made to determine the long-term stability of the SFCM ceramic anode material when exposed to high humidity storage conditions. An investigation was also made to determine the impact of humidity on the storage conditions of typical cathode materials, which are known to interact with water under certain operating conditions. While the performance of strontium-based perovskite electrodes of solid oxide fuel cells (SOFCs) at their operating temperatures have been studied extensively, the durability of these electrodes under storage conditions have remained poorly understood. The studies used such techniques as X-ray Florescence (XRF) and Energy Dispersive X-Ray Spectroscopy (EDS) analysis to compare fresh and obviously (visual discoloration) degraded samples.

The degradation modes are appearance of white precipitates and dark black discoloration on the surface of SFCM-based ceramic anodes of SOFCs. This study investigated the physical-chemical, and electrical characteristics of the SFCM anodes when subjected to various temperature-humidity and time conditions. The observed dark-black discoloration due to aging is attributed to combination of additional phases, while the formation of white precipitate is attributed to thick strontium carbonate layer. The temperature-humidity dependent degradation is attributed to strong susceptibility of strontium oxide to chemisorb water vapor and carbon dioxide from surrounding atmosphere in the presence of a favorable temperature (~80 °C) and humidity environment (~60-95% RH).

A test methodology was developed involving visual inspections and 2- and 4-point in-plane resistance measurements of SOFC electrodes. One reference sample was used to validate the discoloration after exposure to a combination of temperature and humidity conditions. After evaluating the resistance performance in a matrix of temperature (25 – 80 °C) and relative humidity (0-95%), a predictive model of resistance was developed. The measurement setup is shown in **Figure 132** for the 2-point measurement, but a similar arrangement was used for the 4-point meaurement.

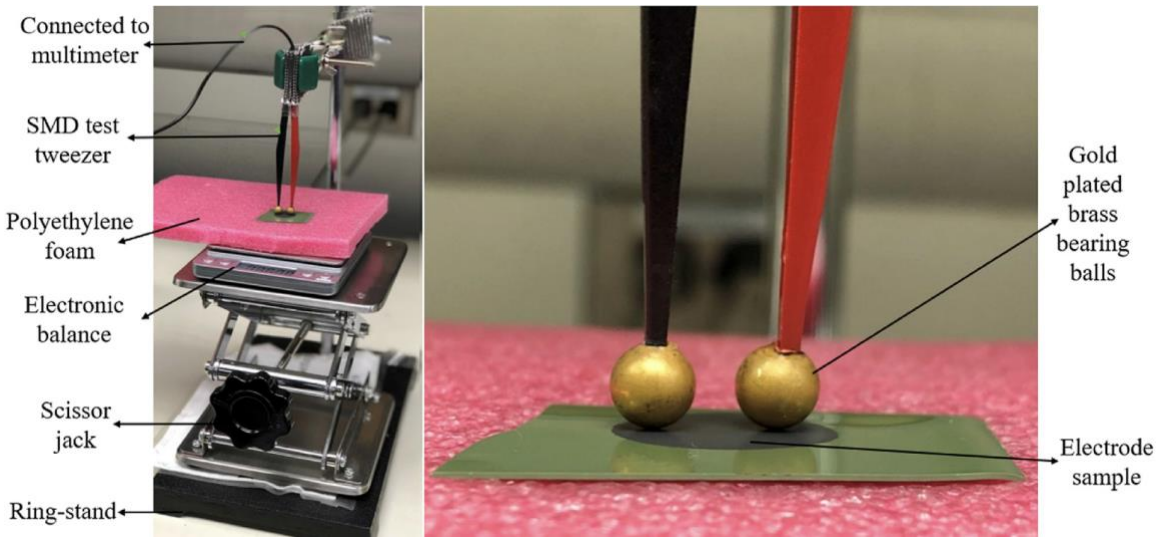

Figure 132. Image of the two-point conductivity measurement setup.

Preliminary data analysis was performed assuming a lognormal distribution, which is based on a multiplicative growth model. This means that at any instant of time, the process undergoes a random increase of degradation that is proportional to its current state. Lognormal distributions are often used for failures due to chemical reactions or degradations, such as corrosion, migration or diffusion. The amount of water that can be adsorbed by the oxide was expected to be proportional to relative humidity. Also, increases in temperature are expected to result in increases in degradation kinetics. This implies there is an interaction between temperature and humidity in degradation of the anode material. That is, certain combinations provide a favorable thermodynamic environment for the degradation. Hence, a generalized Eyring model was used to determine the reliable life because it assumes that there is an interaction between temperature and humidity. The life-stress relationship for the generalized Eyring model is given in Equation 3.

$$L(T, RH) = \frac{1}{T} e^{\left(A + B\frac{1}{T} + C \cdot RH + D \cdot \frac{RH}{T}\right)} \quad (3)$$

Where L is the life of the device, T is temperature, RH is relative humidity, and A, B, C, and D are model parameters. Since the generalized Eyring model has four parameters, there must be data from at least four different combinations of temperature and humidity in order to solve for all the model parameters and to predict the reliable life. Life-stress curves were obtained using the generalized Eyring lognormal model at 25 °C and at different relative humidity levels.

Accelerated testing was performed to characterize the degradation behavior of SFCM-based ceramic anodes during SOFC storage (results shown in **Figure 133**). Due to the consistent observation of dark black discoloration of samples when their room temperature resistance reaches to 5 MΩ and above, the resistance of 5 MΩ was defined as a failure criterion for SFCM anodes. Note, this resistance failure criterion condition depends on sample configuration and use, and served as a metric to guide lifecycle model development.

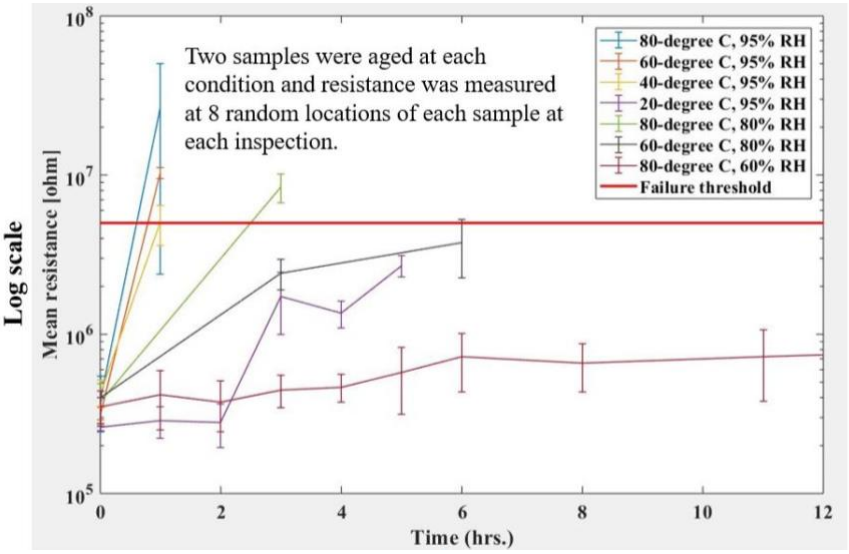

Figure 133. Mean resistance of SFCM ceramic anode samples from each condition measured at each inspection location is plotted against time.

A degradation model was developed to predict the failure time for individual conditions. The requirement of degradation model comes from the fact that the accelerated testing was interval based with more than one conditions having the same failure interval. Linear, polynomial and exponential models have been considered to model the resistance of the SFCM-based ceramic anode as a function of temperature, relative humidity, and time. The linear degradation model outperformed the polynomial and exponential degradation models with R-square of 0.94 as compared to R-square of 0.51 and 0.90 of polynomial and exponential models, respectively. However, since this linear degradation model has been developed using the data from accelerated humidity (above 60%RH), it should not be used to predict the resistance at low humidity conditions, while failure time obtained from this model at high humidity conditions can be used in life prediction model to predict the life of anode at low temperature-humidity conditions because

of the same failure mechanism. Equation 4 provides the resistance of the SFCM-based ceramic anode as a function of temperature, relative humidity, and time.

$$R(T, RH, t) = 0.51\times T + 1.27\times RH + 7.24 \times t + (T-321) \times [(RH-90.6)\times 0.031] + (T-321) \times [(t-1.764)\times 0.28] + (RH-90.6)\times[(t-1.764)\times 0.75] + (T-321)\times[(RH-90.6)\times\{(t-1.764)\times(0.016)\}] - 279.16 \quad (4)$$

R is the two-wire resistance of the SFCM-based ceramic anodes in MΩ at 80 grams of force load in the sample testing setup, T is the temperature in K, RH is the percentage relative humidity, and t is time in hours. The model output is compared with the actual test data shown in Figure 134. It shows that the linear degradation model fits the test data.

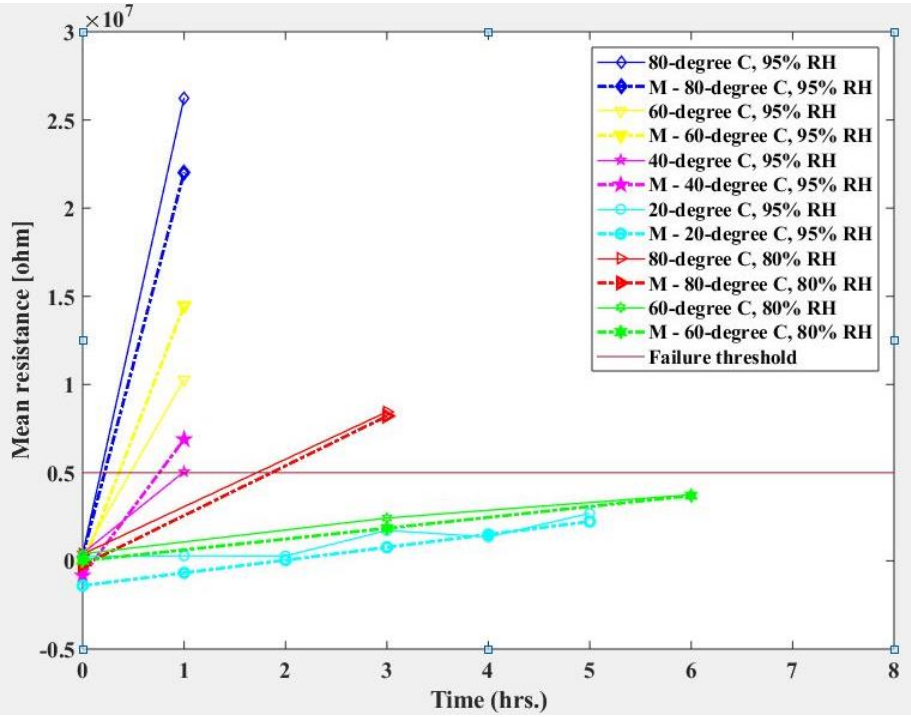

Figure 134. Comparison of actual test data (solid line) with model predicted data (dashed line) for each test conditions

The time to failure was predicted using the linear degradation model and was used in a Generalized Eyring model to assess the reliable storage life. The Generalized Eyring model was found to be the most suitable life-stress relationship model to predict the life of ceramic anodes, since it assumes that there is an interaction between temperature and humidity. The experimental analysis showed a highly significant interaction of temperature and relative humidity on the degradation

rate. Moreover, since the Generalized Eyring model has four parameters, there must be data from at least four different combinations of temperature and humidity to solve for all of the model parameters.

Additionally, a lognormal distribution was used to model a hazard function, since literature suggests that a lognormal distribution is most suitable for failure due to chemical reactions or degradation, such as corrosion, migration, and diffusion. It was found that the life of the SFCM-based ceramic anodes during storage is highly dependent on relative humidity with less effect of temperature (below 80 °C). The effect of temperature on the life of SFCM-based ceramic anodes during storage at 25% relative humidity with 5 MΩ (1500% increase in resistance) as failure threshold is shown in **Figure 135**. Similarly, the effect of humidity on the life of SFCM anodes during storage at 25 °C with 5 MΩ (1500% increase in resistance) as failure threshold is shown in **Figure 136**.

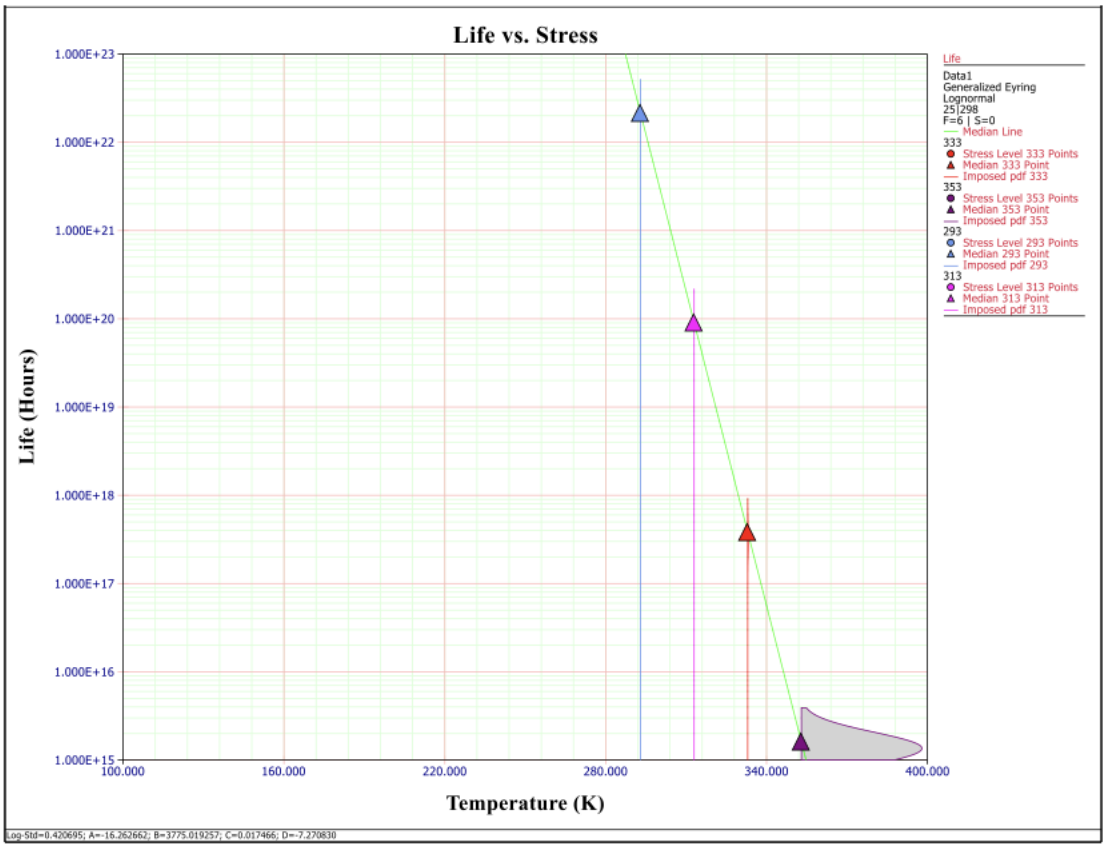

Figure 135. Effect of temperature on SFCM anodes at 25% RH with 1500% increase in resistance as failure criterion.

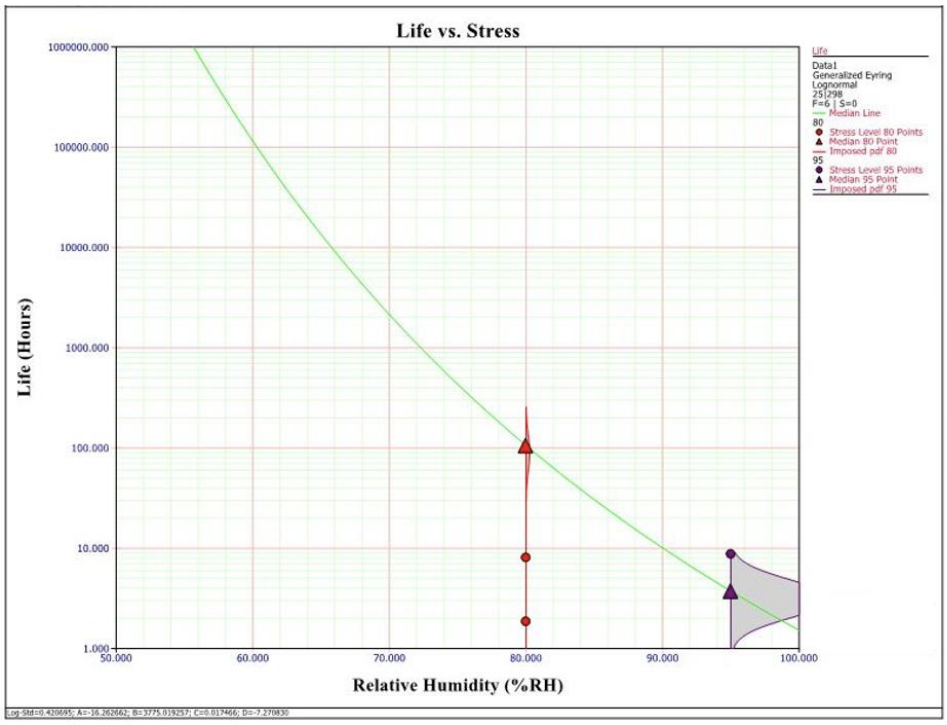

%RH	Life in Hours (95% Reliability)
40	$5.71*10^{10}$
60	57584
80	53
95	2

Figure 136. Effect of humidity on SFCM anodes at 25 °C with 1500% increase in resistance as failure criterion.

Moreover, the comparison of life of SFCM anode with 600 kΩ (100% increase in resistance) and 5 MΩ (1500% increase in resistance) as failure threshold is shown in **Table 7**, while the effect of humidity on the life of SFCM anodes during storage at 25 °C with 600 kΩ (100% increase in resistance) as failure threshold is shown in **Figure 137**.

Table 7. Effect of relative humidity on the life of SFCM anodes with 100% and 1500% increase in resistance at 25 °C.

Effect of RH on Life at 25 °C (% RH)	**100% Increase in Resistance** (Life in Hours (95% Reliability))	**1500% Increase in Resistance** (Life in Hours (95% Reliability))
40	229178	$5.71*10^{10}$
60	170	57584
80	4	53
95	0.7	2

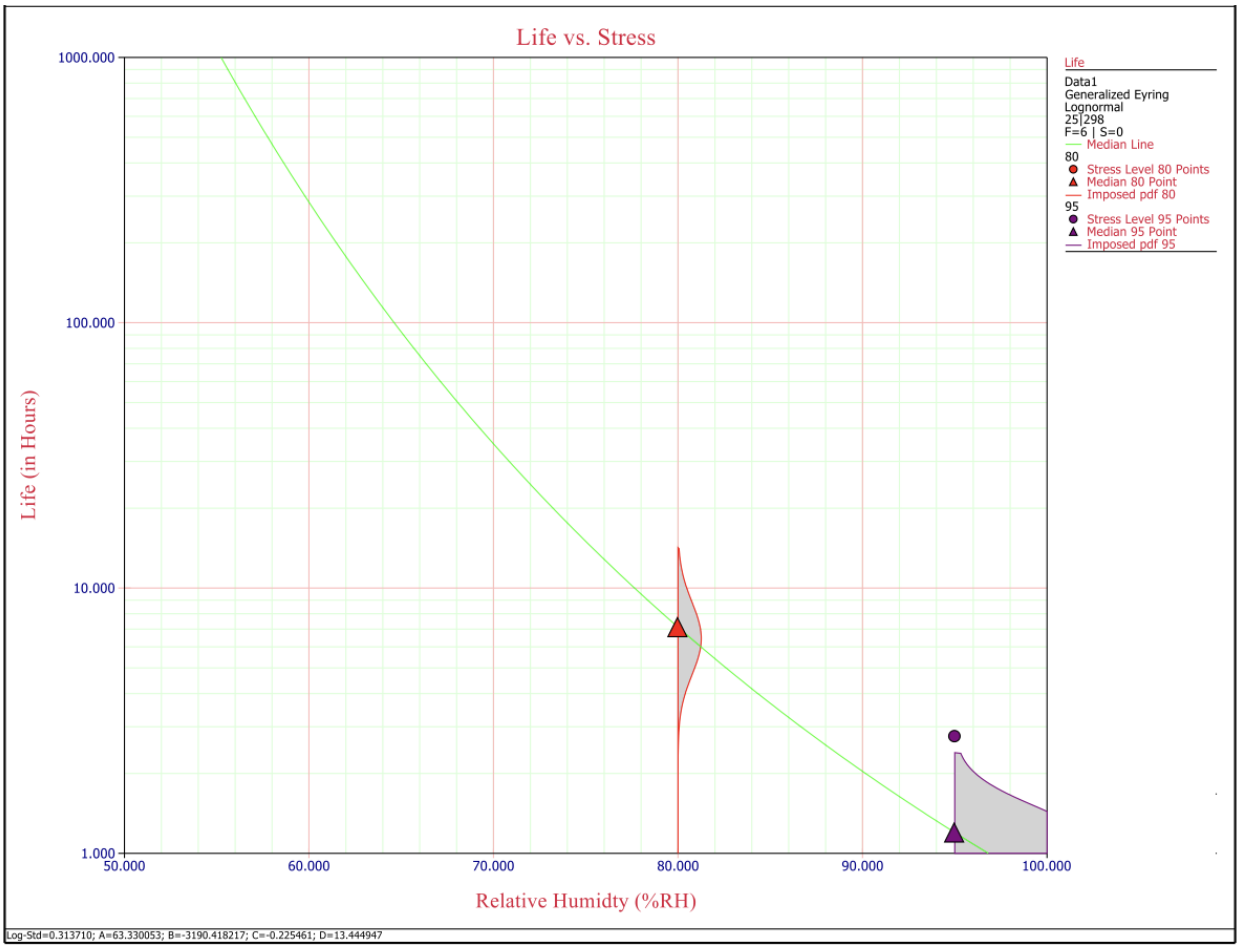

Figure 137. Effect of humidity on SFCM anodes at 25 °C with 100% increase in resistance as failure.

The analytical results suggest that storing the SFCM ceramic anodes at a relative humidity higher than 60% can cause degradation in hundreds of hours, while storage below 40% relative humidity results in less or no degradation. Therefore, the recommended storage of the ceramic anode at low relative humidity (below 40% RH).

Temperature-Humidity Study of Strontium based Perovskite (LSC and LSCF) Cathodes. LSC and LSCF perovskite compounds have been studied extensively in the past because of the interest in the physical properties resulting from the presence of two oxidation states of the metallic cation. The composition of these oxides depends both on the annealing temperature and the oxygen partial pressure maintained during the synthesis, these parameters determining the ratio of oxygen defects.

Two sets of LSC samples (LSC Set A and LSC Set B) and one set of LSCF samples were aged at 80 °C and 80% RH. Elemental composition analysis showed the LSC Set B samples to have higher strontium weight percentage as compared to LSC Set A samples (Figure 138).

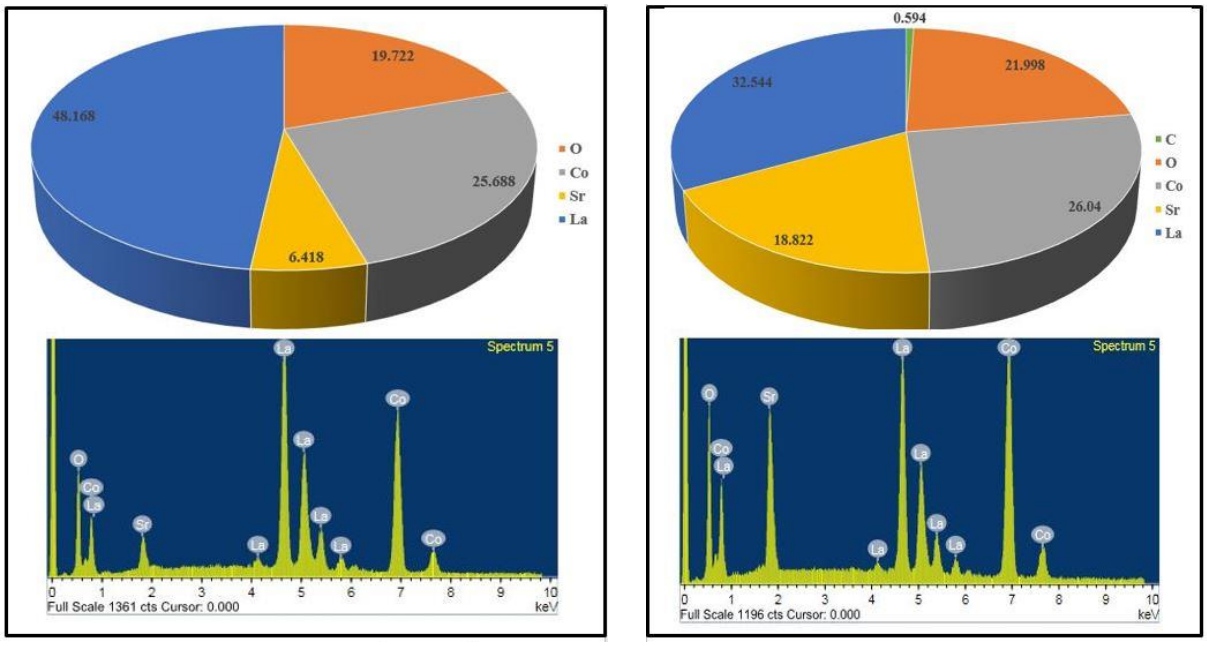

LSC Set A: Unaged Sample **LSC Set B: Unaged Sample**

Figure 138. Elemental composition analysis for LSC Set A and LSC Set B samples

Similar to the SFCM ceramic anode materials, LSC set B samples showed black discoloration due to temperature-humidity exposure while discoloration was not observed in LSC set A and LSCF samples. Besides that, maximum percentage increase in two-wire resistance was observed for LSC set B samples (**Figure 139**).

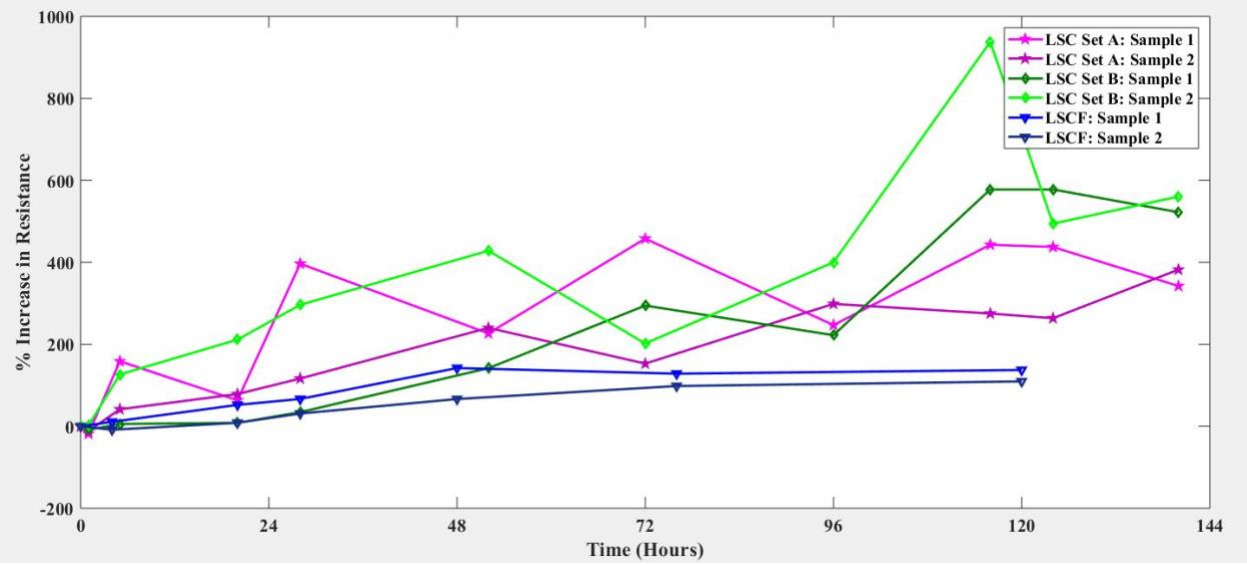

Figure 139. Percentage degradation due to temperature-humidity aging of LSC and LSCF samples.

The low temperature aged samples (i.e., 20-80 °C and 60-95% RH) were subsequently tested at ~650 °C to investigate whether the increased electrode resistance observed at room temperature persists under SOFC operating conditions. All sample resistances were measured using a Van der Pauw 4-point configuration in dry air, were thermally cycled typically 3 times while resistance was measured, and were annealed, or aged, for >100 h in the stated condition. **Figure 140** and **Figure 141** show the resistance measured for two (La,Sr)Co_3 (LSC) samples. Note that the noise in the data is an instrumental artifact. The key point is at typical operating temperature (~650 °C, or ~1.08 on the inverse temperature x-axis scale), the resistance of LSC Sample 1 shows no significant impact for unaged or aged samples. LSC Sample 2 does show a larger resistance at operating temperature (and room temperature), consistent with discoloration effects also observed in the sample after aging (which weren't observed in LSC Sample 1, or LSCF sample). All sample geometries were approximately the same between sample sets, and the multiple sets of lines for each measured sample represent multiple thermal cycles to check for reproducibility.

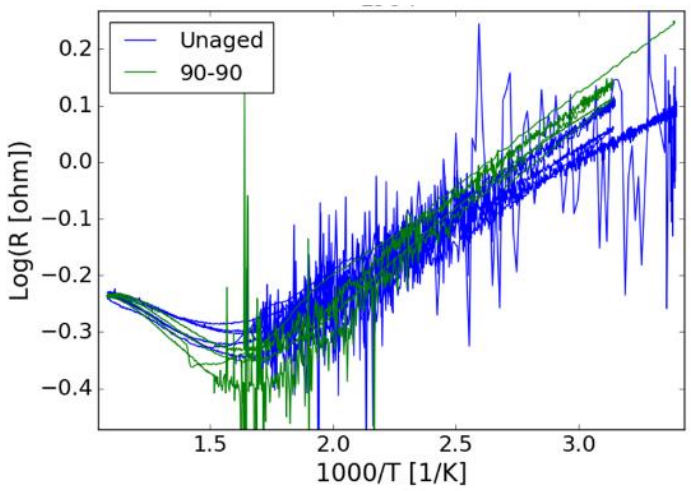

Figure 140. As prepared (unaged) and annealed (90% RH, 90 °C) resistance of LSC Sample 1.

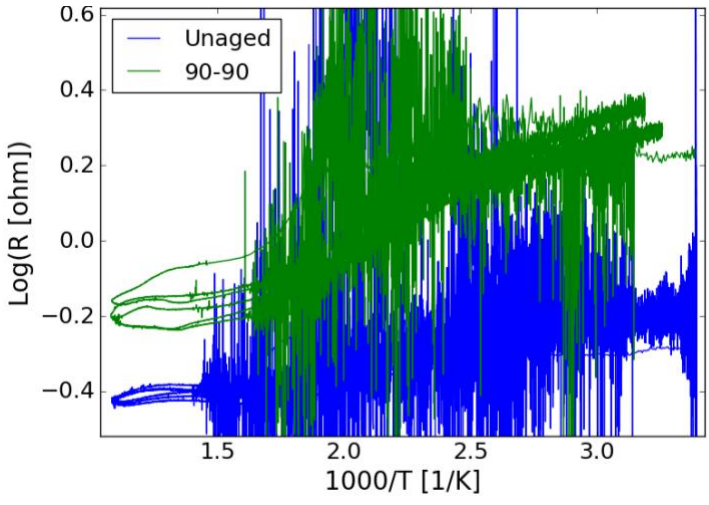

Figure 141. As prepared (unaged) and annealed (90% RH, 90 °C) resistance of LSC Sample 2.

Figure 142 shows the resistance for a (La,Sr)(Co,Fe)O_3 (LSCF) sample. Similar to the LSC sample 1 shown above, the LSCF sample exhibits similar electrical resistance in SOFC operating conditions. The SFCM-based ceramic anode resistance is shown in **Figure 143**. The initial resistance is too large to measure for the first cycle starting at room temperature (shown by noisy data in the upper right portion of the figure) and consistent with the high resistance measured after the humidity and temperature annealing. Upon heating the resistance decreased dramatically, to a value lower than the unannealed sample. The activation energy has also been reduced. The source of the improved performance in operating conditions (in contrast to inferred worse performance from annealing at room temperature alone) is not at this time known.

In summary, we have found a set of cathode materials (LSC and LSCF) that are resistant to harsh storage conditions, and we have found that while the SFCM-based ceramic anode is susceptible to degradation effects in harsh humidity and temperature storage conditions, the electrical conductivity at operating conditions may not be adversely impacted.

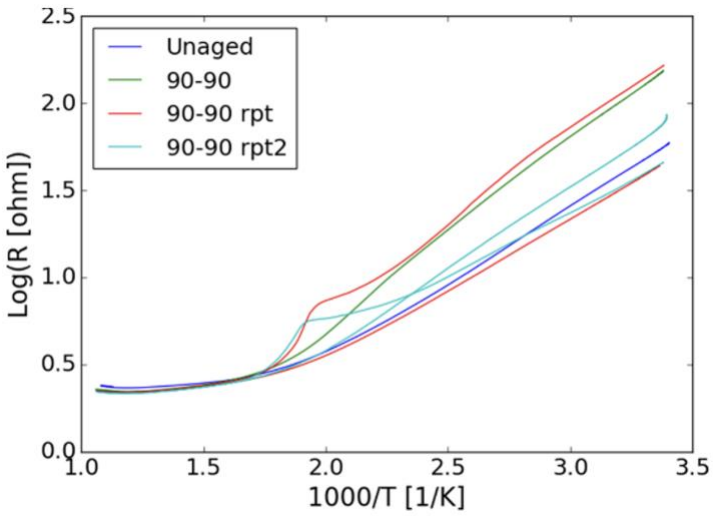

Figure 142. As prepared (unaged) and annealed (90% RH, 90 °C) resistance of the LSCF sample.

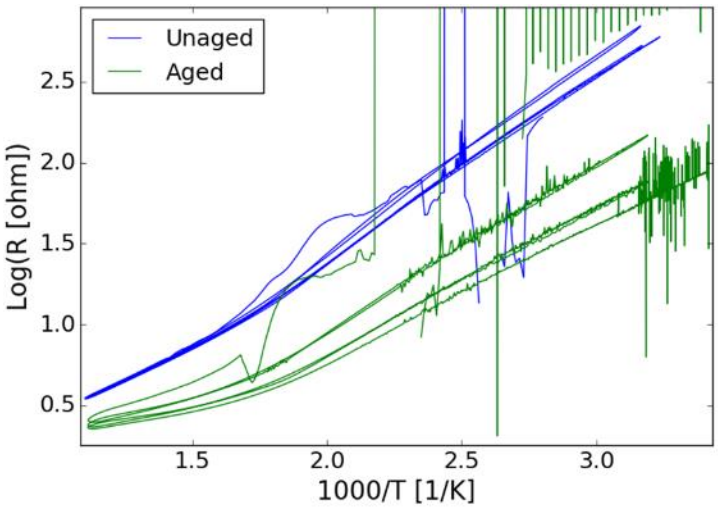

Figure 143. As prepared (unaged) and annealed (aged), in controlled humidity and temperature, resistance of the ceramic anode sample.